

07774



National Library of Canada

Bibliothèque nationale du Canada

CANADIAN THESES ON MICROFICHE

THÈSES CANADIENNES SUR MICROFICHE

NAME OF AUTHOR/NOM DE L'AUTEUR Mr. Donatus K. Uko

TITLE OF THESIS/TITRE DE LA THÈSE The Bauschinger Effect and Applications to the
Manufacture of High Strength Linepipe

UNIVERSITY/UNIVERSITÉ McMaster

DEGREE FOR WHICH THESIS WAS PRESENTED/ GRADE POUR LEQUEL CETTE THÈSE FUT PRÉSENTÉE Ph.D.

YEAR THIS DEGREE CONFERRED/ANNÉE D'OBTENTION DE CE DEGRÉ 1978

NAME OF SUPERVISOR/NOM DU DIRECTEUR DE THÈSE Dr. J.L. Duncan

Permission is hereby granted to the NATIONAL LIBRARY OF CANADA to microfilm this thesis and to lend or sell copies of the film.

L'autorisation est, par la présente, accordée à la BIBLIOTHÈQUE NATIONALE DU CANADA de microfilmer cette thèse et de prêter ou de vendre des exemplaires du film.

The author reserves other publication rights, and neither the thesis nor extensive extracts from it may be printed or otherwise reproduced without the author's written permission.

L'auteur se réserve les autres droits de publication; ni la thèse ni de longs extraits de celle-ci ne doivent être imprimés ou autrement reproduits sans l'autorisation écrite de l'auteur.

DATED/DATÉ June 14, 1978 SIGNED/SIGNÉ 

PERMANENT ADDRESS/RÉSIDENCE FIXE DWOK ESSEN NO: 2, ESSENE,
IKOT ABASI L.G.A.,
CROSS RIVER STATE, NIGERIA.



National Library of Canada

Cataloguing Branch
Canadian Theses Division

Ottawa, Canada
K1A 0N4

Bibliothèque nationale du Canada

Direction du catalogage
Division des thèses canadiennes

NOTICE

The quality of this microfiche is heavily dependent upon the quality of the original thesis submitted for microfilming. Every effort has been made to ensure the highest quality of reproduction possible.

If pages are missing, contact the university which granted the degree.

Some pages may have indistinct print especially if the original pages were typed with a poor typewriter ribbon or if the university sent us a poor photocopy.

Previously copyrighted materials (journal articles, published tests, etc.) are not filmed.

Reproduction in full or in part of this film is governed by the Canadian Copyright Act, R.S.C. 1970, c. C-30. Please read the authorization forms which accompany this thesis.

**THIS DISSERTATION
HAS BEEN MICROFILMED
EXACTLY AS RECEIVED**

AVIS

La qualité de cette microfiche dépend grandement de la qualité de la thèse soumise au microfilmage. Nous avons tout fait pour assurer une qualité supérieure de reproduction.

Si il manque des pages, veuillez communiquer avec l'université qui a conféré le grade.

La qualité d'impression de certaines pages peut laisser à désirer, surtout si les pages originales ont été dactylographiées à l'aide d'un ruban usé ou si l'université nous a fait parvenir une photocopie de mauvaise qualité.

Les documents qui font déjà l'objet d'un droit d'auteur (articles de revue, examens publiés, etc.) ne sont pas microfilmés.

La reproduction, même partielle, de ce microfilm est soumise à la Loi canadienne sur le droit d'auteur, SRC 1970, c. C-30. Veuillez prendre connaissance des formules d'autorisation qui accompagnent cette thèse.

**L'À THÈSE A ÉTÉ
MICROFILMÉE TELLE QUE
NOUS L'AVONS REÇUE.**

THE BAUSCHINGER EFFECT
AND APPLICATIONS TO THE
MANUFACTURE OF HIGH STRENGTH LINEPIPE

by

DONATUS KAISO UKO, B.Sc., M. Eng.

A Thesis

Submitted to the School of Graduate Studies

In Partial Fulfilment of the Requirements

For the Degree

Doctor of Philosophy

McMaster University

April, 1978

© DONATUS KAISO UKO 1978

THE BAUSCHINGER EFFECT
AND APPLICATIONS TO THE
MANUFACTURE OF HIGH STRENGTH LINEPIPE

ACKNOWLEDGEMENTS

The author is sincerely grateful to Prof. R. Sowerby for his advice and guidance during the course of this work. Dr. Sowerby was away on sabbatical leave during the final year of this program of research but continued to participate actively in the program by means of frequent correspondence. During the absence of Dr. Sowerby, Prof. J.D. Embury acted as my supervisor. I would like to thank Dr. Embury for this and above all, for his encouragement and friendship.

Many thanks are also extended to Prof. J.L. Duncan whose continued support and interest in my overall program of studies at McMaster has been a source of real encouragement. The assistance received from my supervisory committee and the frequent discussions with the members of the Mechanical-Metallurgy and Metalworking Research Groups are also appreciated.

The research was funded partly by Noranda Research Centre, Quebec and partly by the National Research Council of Canada. The support for the author by the Department of Mechanical Engineering of McMaster University is acknowledged and special mention is made of the assistance received from the Government of the Cross River State of Nigeria.

The typing skill and patience of Mrs. Lorraine Felbel is also acknowledged.

Finally, I wish to congratulate my wife Seowo, for her patience and understanding, to thank both our parents and families and to dedicate this work to our son and to my father.

DEDICATED TO: IDARA DONALD UKO

and

MY FATHER (1911-1978)

DOCTOR OF PHILOSOPHY (1978)
(Mechanical Engineering - Production)

McMASTER UNIVERSITY
Hamilton, Ontario

TITLE: The Bauschinger Effect and Applications to the
Manufacture of High Strength Linepipe

AUTHOR: Donatus Kaiso Uko, B. Sc., Mech. Eng., (University of
Southampton)

M. Eng., (McMaster University)

SUPERVISOR: Professor R. Sowerby

NUMBER OF PAGES: (xviii), 286

ABSTRACT

The macroscopic stress-strain characteristics of many common engineering materials embraces several complex phenomena which are generally attributed to the dependence on loading history. Certain particular aspects of this history related behaviour may be classified under the general heading, the Bauschinger Effect. Investigations into the Bauschinger Effect have produced a variety of continuum plasticity models to explain the phenomenon. The models vary in their degree of complexity but even the more sophisticated ones have not always shown good agreement with experimental observations. Microscopic theories have also been proposed to describe the work hardening behaviour of alloys composed of a hard second phase in a plastically deformable matrix. The work of Brown and Stobbs is an example in which the Bauschinger Effect is treated as an integral part of the work hardening phenomenon in a two phase material.

This thesis examines three continuum models in some detail in order to determine the role played by internal stresses on the macroscopic behaviour and the Bauschinger Effect. A modification to an existing model is introduced and shown to improve the description of some experimentally determined cyclic stress-strain data.

Furthermore, the microscopic model due to Brown and Stobbs has been studied quantitatively. The original model was proposed based on detailed observations of the plastic deformation of a simple model system of dispersion hardened single crystals of copper-silica. In this

present study, an attempt is made to generalize the model to more complex polycrystalline systems comprised of four spheroidized plain carbon steels which contain different volume fractions of Fe_3C type carbides and three linepipe grade HSLA steels, the microstructures of which are relatively more complex. The experimental inputs to the model were determined from reverse flow experiments performed in a well aligned tension - compression loading fixture.

The final aspect of the work of this thesis was focussed on the study of an industrial application in which the Bauschinger Effect can play a major role. The U-O-E pipe making process was selected for study in this regard.

The general objective of the thesis was to provide a better understanding of the Bauschinger Effect in terms of its causes and practical implications in common structural steels. Certain specific conclusions have been reached in this regard.

TABLE OF CONTENTS

CHAPTER		PAGE
I	GENERAL INTRODUCTION	1
II	LITERATURE REVIEW	6
2.1	Introduction	6
2.2	The Bauschinger Effect	7
2.2.1	The Phenomenon	7
2.2.2	Definitions	10
2.2.3	Suggested Causes	15
2.2.4	Related Studies on Aspects of the Bauschinger Effect	21
2.2.5	Engineering Significance	29
2.3	The Scope and Objectives of Present Investigations	31
III	THEORETICAL MODELS OF THE BAUSCHINGER EFFECT	35
3.1	Introduction	35
3.2	Work Hardening Models of Continuum Plasticity	36
3.2.1	Isotropic and Kinematic Hardening Models	36
3.2.2	Anisotropic and Kinematic Hardening Models	43
3.2.3	Second Order Effects in Plasticity	45
3.2.4	Subsequent Yield Surfaces	47
3.3	Phenomenological Models of the Bauschinger Effect	52
3.3.1	Model Based on Macroscopic Residual Stresses	53
3.3.2	The Masing Type Hardening Model	54
3.3.3	Mroz's Kinematic Hardening Model	54

CHAPTER		PAGE
3.4	Microplasticity Models	58
3.4.1	Experimental Evidence of Back Stresses	59
3.4.2	The Theoretical Derivation of the Mean Matrix Stress	61
3.4.3	The Bauschinger Effect Parameter	67
3.5	Summary	71
IV	MATERIALS AND EXPERIMENTATION	73
4.1	Introduction	73
4.2	Experimental Materials and Metallography	73
4.2.1	Plain Carbon Steels	73
4.2.2	Controlled Rolled HSLA Steels	74
4.2.3	Dual Phase HSLA Steels	84
4.3	Preliminary Experimental Studies	86
4.4	Tension-Compression Loading Equipment and Specimen Geometry	93
4.5	The Reverse Flow Experiments	102
4.5.2	Cyclic Loop Symmetry and Structural Damage	104
4.5.3	Tests for Discontinuous Yielding in Reverse Flow	108
4.6	Experimental Results	113
V	RESULTS AND DISCUSSION	114
5.1	Introduction	114
5.2	Phenomenological Models of the Bauschinger Effect	117
5.2.1	Model Based on Macroscopic Residual Stresses	117
5.2.2	Hardening Model Using Elastic/Plastic Elements	117
5.2.3	The Modification of Mroz's Kinematic Hardening Model	122

CHAPTER		PAGE
VI	THE U-O-E PIPE MANUFACTURING PROCESS	196
6.1	Introduction	196
6.2	The Mechanics of the U-O-E Process	197
6.2.1	The "U" Stage	202
6.2.2	The "O" Stage	204
6.2.3	The "E" Stage	208
6.3	Discussion	211
6.3.1	The Influence of the BE in Pipe Making	211
6.3.2	Pipe Yield Strength Assessment	216
VII	CONCLUSIONS	222
7.1	On the Phenomenological Modelling of the BE	222
7.2	On the Microscopic Model of the BE due to Brown and Stobbs	224
7.3	Implications of Internal Stresses	225
7.4	Discontinuous Yielding in Reverse Flow	226
7.5	Empirical Aspects of the Bauschinger Effect	227
7.6	On a Practical Application: The Bauschinger Effect in Pipe Manufacturing	228
7.7	Recommendations for Further Research	229
APPENDIX A	Metallurgical and Processing Features of Controlled-Rolled HSLA steels	232
APPENDIX B	Supplement to Chapter V, Section 5.8, (Experimental Aspects of the Bauschinger Effect in HSLA Steels)	237
APPENDIX C	Elastic-Plastic Axisymmetric Finite Element Analysis of the Pipe Expansion Problem	250

CHAPTER		PAGE
VI	THE U-O-E PIPE MANUFACTURING PROCESS	196
6.1	Introduction	196
6.2	The Mechanics of the U-O-E Process	197
6.2.1	The "U" Stage	202
6.2.2	The "O" Stage	204
6.2.3	The "E" Stage	208
6.3	Discussion	211
6.3.1	The Influence of the BE in Pipe Making	211
6.3.2	Pipe Yield Strength Assessment	216
VII	CONCLUSIONS	222
7.1	On the Phenomenological Modelling of the BE	222
7.2	On the Microscopic Model of the BE due to Brown and Stobbs	224
7.3	Implications of Internal Stresses	225
7.4	Discontinuous Yielding in Reverse Flow	226
7.5	Empirical Aspects of the Bauschinger Effect	227
7.6	On a Practical Application: The Bauschinger Effect in Pipe Manufacturing	228
7.7	Recommendations for Further Research	229
APPENDIX A	Metallurgical and Processing Features of Controlled-Rolled HSLA steels	232
APPENDIX B	Supplement to Chapter V, Section 5.8, (Experimental Aspects of the Bauschinger Effect in HSLA Steels)	237
APPENDIX C	Elastic-Plastic Axisymmetric Finite Element Analysis of the Pipe Expansion Problem	250

CHAPTER		PAGE
C.1	Introduction	250
C.2.1	Geometric Relations	251
C.2.2	Constitutive Equation	257
C.2.3	The Virtual Work Principle	260
C.2.4	Matrix Notations for the FEM Model	261
C.3	The FEM Program	265
C.4	Listing of FEM Program	266
	REFERENCES	280

LIST OF FIGURES

FIGURE	CAPTION	PAGE
2.1	A schematic representation of forward and reverse flow behaviour in uni-directional straining	8
3.1	A schematic representation of yield surfaces in plane stress: (a) Initial yield surface, (b) Isotropic Expansion, (c) Kinematic Hardening	38
3.2	Initial and subsequent yield surfaces of Al.(19S) alloy, Ivey [73].	49
3.3	Macroscopic residual stress model of the Bauschinger Effect	49
3.4	Material modeled by a parallel connection of elastic-plastic hardening elements.	55
3.5	(a) Piecewise linear stress-strain curve, (b) and (c): Representation of (a) in stress space using nested yield loci (after Mroz [60]).	57
3.6	Schematic two-phase deformation model.	65
4.1	Optical micrographs of SAE 1015 compared in the (a): as received, (b): spheroidized conditions.	77
4.2	Optical micrographs of the HSLA steels: (a): HSLA Steel-A (b): HSLA Steel-B (c): HSLA Steel-C	78 80 81
4.3	Experimentally derived σ - ϵ diagrams of three differently oriented tensile samples of the HSLA steels: (a): HSLA Steel-A (b): HSLA Steel-B (c): HSLA Steel-C	88 90 91
4.4	Experimental tension-compression loading fixture	95

FIGURE	CAPTION	PAGE
4.5	Uniaxial tension-compression specimen	97
4.6	Some parts of the loading fixture of Fig. 4.4 (a): Top holder for specimen and alignment pointer (b): Bottom holder for alignment pointer (c): Alignment pointer	98 99 99
4.7	The complete experimental tension-compression loading arrangement	101
4.8	A typical experimental reverse flow load - extension diagram	103
4.9	An experimental method of assessing the reproduceability of the loading fixture of Fig. 4.4	105
4.10	Tests for cyclic loop symmetry using the HSLA steel-B	107
4.11	The Ludering effect in forward and reverse flow	110
4.12	Interrupted tests used to study the mechanics of Luder's strain propagation in reverse flow: (a): following a tensile prestrain (b): following a compressive prestrain	111 112
5.1	Reverse flow behaviour modified by macroscopic residual stresses	118
5.2	Forward and reverse flow behaviour using two elastic/non-hardening elements: as drawn, $\sigma_2 = 2\sigma_1$	120
5.3	Forward and reverse flow behaviour using two elastic/linear hardening elements: as drawn, $\sigma_2 = 2\sigma_1$, and $E/E_t = 4$	123
5.4	Comparison of experimental data with linear isotropic and a kinematic hardening model	124
5.5	A comparison of experimental data with the combined isotropic and kinematic hardening model for different hardening levels	126

FIGURE	CAPTION	PAGE
5.6	Comparison of experimental data with the combined isotropic and kinematic hardening model	127
5.7	(a): Experimental measurements of permanent softening plotted as a function of prestrain for the spheroidized plain carbon steels (b): A replot of Fig. 5.7(a) as a function of the square root of prestrain in order to verify the theoretical parabolic dependence of permanent softening on prestrain	133 134
5.8	Experimentally derived values of permanent softening plotted as a function of volume fraction of the carbide particles in the spheroidized plain carbon steels	136
5.9	The theoretical BEP as a function of prestrain	138
5.10	A comparison of experimentally determined values of the BEP with the theory due to Brown and Stobbs [86].	140
5.11	(a): A verification of the parabolic relationship between the prestrain and the unrelaxed strain (b): The development of microscopic strain incompatibility (internal stresses) as a function of the imposed deformation in two phase spheroidized and HSLA steels	142 144
5.12	A typical set of forward and reverse flow curves employed to experimentally determine permanent softening	149
5.13	Experimental measurements of permanent softening plotted as a function of prestrain for the HSLA steels	151
5.14	A replot of Fig. 5.13 as a function of the square root of prestrain in order to verify the parabolic relationship of permanent softening with prestrain in the case of the HSLA steels	152

FIGURE	CAPTION	PAGE
5.15	Experimentally determined values of permanent softening plotted as a function of the total volume fraction of non-ferritic products in the HSLA steels	155
5.16	A superimposition of the forward and reverse cyclic curves of Fig. 4.10 used to demonstrate the symmetry of the σ - ϵ loops: (a): second half cycles (b): third half cycles (c): fourth half cycles	163 164 165
5.17	The study of cyclic loop symmetry using the dual phase HSLA steels: (a): the dual phase steel-D (b): the dual phase steel-E	167 168
5.18	The effect of cycling the overstrained material and the reverse flow behaviour following overstraining: (a): loading first in tension (b): loading first in compression	170 171
5.19	A survey of the structural damage produced by the nucleation of voids at the second carbides in spheroidized steels [105]	173
5.20	A schematic representation of discontinuous yielding behaviour	175
5.21	The study of the mechanism of Luder's strain propagation upon loading in (a): the case of initial loading in tension (b): the case of initial loading in compression	177 180
5.22	A comparative plot of the tensile prestress, σ_f and the compressive (reverse) yield stress σ_r as a function of prestrain: (a): for σ_r (.2%) (b): for σ_r (.5%)	186 188
5.23	The Bauschinger Effect measured by the stress difference ($\sigma_f - \sigma_r$) as a function of prestrain and using four offset strain definitions of σ_r	189

FIGURE	CAPTION	PAGE
5.24	The empirical parameterization of the Bauschinger Effect	191
5.25	A qualitative study of roundedness using four first reverse flow curves which are to be compared with the initial tensile curve of the material in Fig. 4.3(b).	193
6.1	A diagrammatic representation of the U-O-E method of pipe forming	198
6.2	A representation of the deformation (strain) history in the pipe wall during forming	199
6.3	The schematic illustration of the deformation cycles imposed on the inside and outside surface elements of a U-O-E pipe during forming	201
6.4	The stress distributions and residual stresses in the pipe wall resulting from the 'U' and 'O' stages of forming	203
6.5	Division of plate thickness into twenty parts	206
6.6	A piecewise linear approximation method of the stress-strain curve for use in the FEM program	210
6.7	(a): The annular finite element model employed in the pipe expansion problem (b): The geometry and boundary conditions employed in the pipe expansion problem	210 210
6.8	Pressure-radial expansion relationship obtained by ascribing different stress-strain behaviour to the various domains of the pipe wall: (a): the HSLA Steel-A (b): the HSLA Steel-B (c): the HSLA Steel-C	212 214 215
6.9	A schematic representation of the accumulation of plastic hinges during the flattening of a transverse section of pipe	218

FIGURE	CAPTION	PAGE
B.1	A comparative plot of the tensile prestress, σ_f and the compressive (reverse) yield stress, σ_r as a function of prestrain:	
B.2		
	B.1: HSLA Steel-B	238
	B.2: HSLA Steel-C	239
B.3	The Bauschinger Effect measured by the stress difference, $(\sigma_f - \sigma_r)$ as a function of prestrain and using four offset strain definitions of σ_r :	
B.4		
B.5		
	B.3: HSLA Steel-A 90° Samples	240
	B.4:(a) HSLA Steel-B, 0° Samples	241
	B.4:(b) HSLA Steel-B, 90° Samples	242
	B.5:(a) HSLA Steel-C, 0° Samples	243
	B.5:(b) HSLA Steel-C 90° Samples	244
B.6	The empirical parameterization of the Bauschinger Effect:	
B.7		
B.8		
	B.6: HSLA Steel A, 90° Samples	245
	B.7:(a) HSLA Steel-B, 0° Samples	246
	B.7:(b) HSLA Steel-B, 90° Samples	247
	B.8:(a) HSLA Steel-C, 0° Samples	248
	B.8:(b) HSLA Steel-C, 90° Samples	249
C.1	Incremental deformation model	252
C.2	Location of a finite element in the pipe wall	258

LIST OF TABLES

TABLE	CAPTION	PAGE
4.1	Mechanical properties and volume fractions of the plain carbon steels	76
4.2	Spheroidization tempering schedule	76
4.3	Rolling practice for the HSLA Steels	82
4.4	Chemical compositions of the HSLA and dual phase steels	83
4.5	Tensile properties of the HSLA Steels	92
4.6	Variations in the through thickness tensile parameters of the HSLA Steel-C	94
5.1	Interpolated and micrographic volume fractions of the HSLA Steels	153
5.2	Dimensional changes in 1045 steel rods due to straightening after cold drawing	160
6.1	Experimental strain amplitudes employed to Simulate the U-O-E forming of a 40" (1016 mm) x 1/2" (13 mm) pipe	200
6.2	Nominal pipe strengths after 1% expansion	220

CHAPTER I

GENERAL INTRODUCTION

The rheological behaviour of many common engineering materials, particularly of metals, is known to depend in a complex manner with the history of deformation processing. One important example of this dependence is found in the Bauschinger Effect (referred to here as BE) which may be defined simply as the strength loss observed in reverse plastic flow following prestraining in the opposite sense. The study of the BE is a useful method of demonstrating some of the aspects of path dependent plastic deformation. In general, the path dependence of the process means that the resistance of the material and the distribution of stresses within the material is determined not simply by the current level of total imposed strain but by the route through which the strain was achieved. Thus, it is necessary to specify not only the cumulative strain but also the history of the straining process in order to adequately define the current mechanical state of the material.

During general deformation processing, the observed material resistance to plastic flow which is attributable to the distribution of stresses inside the material has become known as work or strain hardening. The process of work hardening has been studied widely from two different perspectives. In the macroscopic approach employed in the theory of plasticity, emphasis is placed on the development of mathematical models capable of adequately describing the observed behaviour of materials in a continuum sense. The microscopic approach on the

other hand attempts to provide a description of work hardening plasticity in terms of detailed physical features such as the grain size and morphology, dislocations and the presence of second phase particles in the microstructure. In this thesis, both continuum and dislocation plasticity models will be utilized in an attempt to relate the two formalisms in the context of the description of the Bauschinger Effect as a part of the broader problem of work hardening in engineering plasticity.

The Bauschinger Effect is conventionally studied in experiments where variation in the loading path can be made. In a typical example, forward loading in tension may be followed by plastic loading in compression. It therefore becomes possible to observe and measure any differences between the forward and reverse plastic flow curves in order to quantify the BE. For purposes of illustration, the BE can be defined in this type of test by the stress difference (reduction) between the forward flow stress at the point of unloading and the reverse yield stress in compression. This reduction in strength is generally considered as a consequence of residual stresses in macroscopic terms but also more fundamentally, in terms of the internal stresses developed during the plastic deformation of the material in forward prestraining. The origin of internal stresses is related to the inhomogeneity of the plastic deformation process at a microscopic level. Clearly, on a limited scale, internal stresses may be generated by the non uniform deformation of individual grains in a polycrystalline aggregate. More pronounced however, are the internal stresses due to the interference caused by extensive rigid obstacles in the path of mobile dislocations

in the matrix of the deforming material. This aspect is discussed at length in this thesis. For general purposes here, a material in which a distribution of rigid and undeformable particles embedded in a soft and plastically ductile matrix is visualized. During plastic straining, the particles can only deform elastically while the matrix flows plastically around them. As long as interfacial voiding or particle cracking is not permitted, local stress concentrations occur in the vicinity of the particles and the microscopic strain distribution is consequently inhomogeneous.

Many of the common structural materials, particularly, the dispersion and precipitation hardened alloys belong to this class of two phase materials. For example, in steels, the matrix is composed of ferrite containing a dispersion of cementite and other precipitation hardening carbides which constitute the particle (second) phase. In this thesis, the BE is studied in a range of structural steels containing a complex variety of particle morphologies. The aim is to provide a better understanding of the BE in terms of its natural causes and practical implications in common engineering materials.

The investigations undertaken during the course of this work are reported subsequently in six major chapters. Chapter 2 which follows immediately is devoted to the review of previous research on the various aspects of the BE. A detailed account of the objectives of this present work and the rationale behind these is presented at the end of this chapter.

Chapter 3 is devoted to the discussion of the macroscopic and microscopic models of the BE. Some of the macroscopic models which exist

are shown to serve only to demonstrate the gross phenomenon of the BE without being quantitatively predictive. An important contribution of this work considers the modification of one of these models due to Z. Mroz using a more general context of work hardening to provide a more realistic prediction of material behaviour.

The microscopic theory of the BE attempts to emphasize the physical aspects of the plastic deformation process in terms of the microstructural features and the path dependent nature of the pattern of dislocation accumulation and interaction with structural obstacles. In particular, the dislocation theory for reversible plasticity modelled by Brown and Stobbs after the deformation behaviour of dispersion hardened single crystals of copper-silica alloys is generalized for structural steels and used to quantitatively study the BE in these materials. Several of the dislocation models which exist in the literature enable the description of aspects of work hardening but only in single crystals and polycrystals possessing simple and well characterized microstructures. The development of these models for the more common structural materials is lacking and this present work attempts to make a contribution in this regard.

In Chapter 4, the metallurgical structure of the experimental steels is considered in detail. Details are also provided of the preliminary experiments performed to classify the materials. The chapter concludes with the description of the test device developed for tension-compression reverse flow experiments and of the actual experiments performed to study the different aspects of the BE.

The results obtained from the experiments proposed in Chapter 4

as well as the results obtained in the analyses of the macroscopic and microscopic models of the BE proposed in Chapter 3 are presented and discussed in Chapter 5.

Chapter 6 is devoted to practical aspects of the BE in the manufacture of high strength large diameter linepipe. The strain history of two typical elements in the pipe wall is simulated experimentally and utilized quantitatively in a Finite Element Programme to predict the final pipe properties taking into account the Bauschinger Effect.

In Chapter 7, the significant conclusions derived from this study are listed. Recommendations are made for future research and the thesis is concluded with three appendices. The first one provides some more information on the important class of HSLA - high strength low alloy - steels used in this study. The second appendix presents, for completeness, some of the BE data determined experimentally for the HSLA steels which were excluded from the discussion in Chapter 5. The final appendix discusses the theory of large strain incremental plasticity and the Finite Element Model formulation of the pipe expansion problem. It also includes a listing of the FEM programme used to predict the pressure - radial expansion characteristics of a formed pipe.

CHAPTER II

LITERATURE REVIEW

2.1 Introduction

There has been an extensive interest in the Bauschinger Effect in recent years, both from the theoretical and the practical points of view. Many of the previous investigations of the BE may be broadly classified as either macroscopic or microscopic in approach. The aim of this chapter is to review some of the major contributions in the literature.

Various macroscopic theories have been developed to explain the work hardening behaviour of metals, and even the more sophisticated models provide a description of the BE, only in a qualitative sense. On the other hand, theoretical and experimental studies have shown that the understanding of the microscopic processes of work hardening in two phase alloys can be greatly enhanced by an examination of the BE. In the main, the theoretical studies serve to clarify the engineering significance of the BE, firstly in terms of those processes where the detrimental influence of the BE would be manifested in the reverse plastic strain cycling of structures, and secondly in terms of the characterization and the possible elimination of the effect especially in those industrial materials which rely on a combination of precipitation hardening and work hardening to achieve design strength levels. In this chapter, the phenomenon and the different definitions of the BE will be discussed together with a review of the possible causes and



past research on the BE. Later in the chapter the engineering significance and the scope and objectives of the present investigations are discussed.

2.2 The Bauschinger Effect

2.2.1 The Phenomenon

A common observation in uniaxial plastic deformation is that the elastic limit is often higher for subsequent loading in the same direction as compared with loading in the reverse sense. This type of direction at behaviour was first reported by Bauschinger [1] in 1881 and the phenomenon now carries his name.

Considerable effort has since been devoted by many investigators to account for the observations made by Bauschinger. Their work has combined to illustrate that the directional behaviour in the reverse stress-strain relationship is far more complex than originally envisaged: The measurement of the BE involves observing the plastic flow behaviour of a material when strained in a direction opposite to that imposed during prestraining. One experimental technique is that of uniaxial loading where the prestrain in tension is followed by unloading and then reverse straining in compression (or vice versa). Observations of the behaviour of the material in this kind of test has resulted in the BE being defined in a variety of ways using stress, strain and energy related parameters. The shape of a typical stress-strain curve for reverse straining in compression following prestraining in tension is shown schematically in Fig. 2.1. The behaviour of some real materials is illustrated in this diagram in the following manner. As the imposed tensile strain is increased, the material undergoes elastic deformation along the line OA

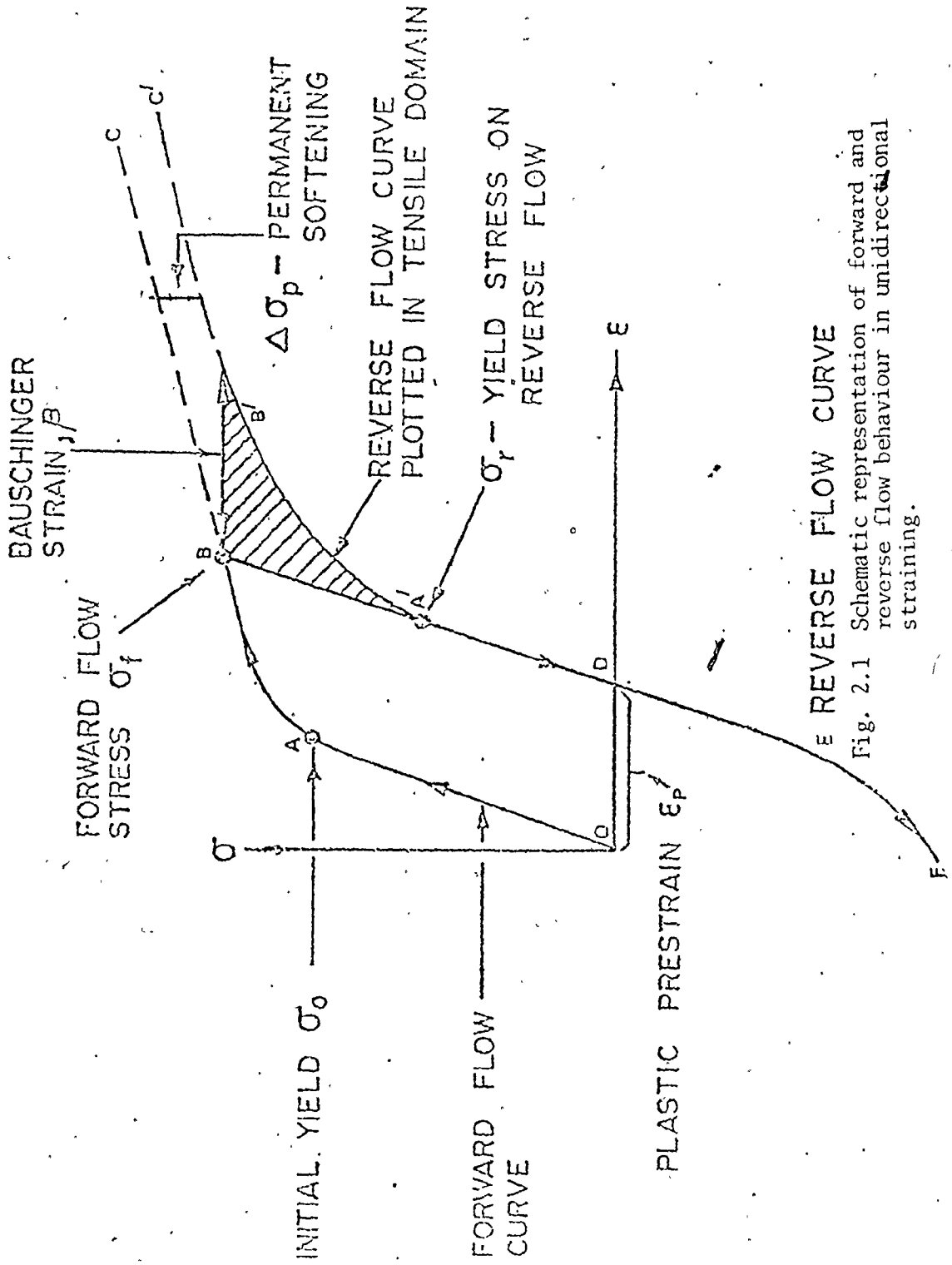


Fig. 2.1 Schematic representation of forward and reverse flow behaviour in unidirectional straining.

and yields at the point A, where the initial yield stress σ_0 is defined. As the amount of plastic strain is increased, the flow stress also increases, usually in a non-linear manner, and the resultant stress-strain curve, ABC, depicts work hardening or strain hardening behaviour.

In the ideal case the specimen behaves in a linear elastic manner if it is unloaded from a typical point B to zero load at D. Upon reloading in tension the elastic line DB (parallel to OA) is followed until the specimen again yields at B. Continued loading takes the specimen along the path BC. In the practical situation there may be a small elastic hysteresis loop rather than the single unloading and loading line DB. Furthermore, there may be some additional rounding of the reloading line as point B is approached on account of the preyield microstrain. However, in general, the new yield strength upon reloading in tension does not differ much from the original forward flow stress, σ_f , at point B.

Now, consider the case of unloading from B to D and instead of reloading along the direction of prior strain as before, the specimen is now immediately loaded in compression. The stress-strain curve obtained would be of the form DEF which may be reflected and redrawn in the tension quadrant as DA'B'C'.

Several interesting features of the reverse deformation are now revealed when a comparison is made with the monotonic loading curve, ABC. Firstly, the elastic limit is lower at A' compared to the point B; it is noted that in real materials a well defined elastic limit is often lacking. Secondly, the reverse flow curve is well rounded in the domain A'B'; the extent of this roundedness depends on the material.

Finally, as reverse straining proceeds, plastic deformation continues to take place but at a reduced level of stress, vis a vis the initial (monotonic) hardening curve. The reverse flow curve may eventually run parallel to the monotonic curve offset by an amount, $\Delta\sigma_p$ which is termed permanent softening.

2.2.2 Definitions

It is possible to define the BE in terms of the reduction of the yield stress shown in Fig. 2.1 as

$$\sigma_f = |\sigma_r| \quad (2.1)$$

where σ_r is the reverse yield stress provided a consistent measure of σ_r is adopted. In view of the rounded nature of the reverse stress-strain curve, σ_r may be measured in the usual way as a proof or offset yield stress, where the offset strain chosen is small, in the order of $0 < \epsilon_r < .5\%$. Besides the obvious approximation involved in computing the reverse yield stress this way, this definition has the additional disadvantage in that it tells us nothing about the subsequent roundedness and permanent softening of the reverse flow curve. However, since some measure of the yield stress in reverse flow following prestraining is one of the major aspects of the BE, this definition has been used by a number of authors, notably Kishi et al [2,3], Taira et al [4] and by Gupta and Kodali [5,6]. Another widely used stress related definition is due to Milligan et al [7]. Milligan also measured the BE in different heat treated structures of 4330 high strength steel using the Bauschinger effect factor, BEF defined as,

$$\text{BEF} = |\sigma_r|/\sigma_f \quad (2.2)$$

More recently, Jamieson and Hood [8] studied the BE in HSLA steels and redefined the BEF in the form,

$$\text{BEF} = (\sigma_f - |\sigma_r|)/\sigma_f \quad (2.3)$$

The definitions given in equations (2.1) to (2.3) are derived from the observed forward and reverse flow behaviour. They are arbitrary and imply nothing about the work hardening behaviour or the origins of the Bauschinger effect. As mentioned briefly in Chapter 1, and discussed at greater length below in the thesis, the BE is a consequence of inhomogeneous plastic straining at the microscopic level. Models have been proposed (and these are discussed later) which relate the extent of the permanent softening, $\Delta\sigma_p$, (see Fig. 2.1) to the back stresses that are developed. Furthermore, these models specify the functional dependence of the overall hardening, $(\sigma_f - \sigma_o)$, and the permanent softening, $\Delta\sigma_p$, on such quantities as the forward plastic prestrain, ϵ_p , and the volume fraction, V_f , of the second phase particles. Consequently, a measure of both $(\sigma_f - \sigma_o)$ and $\Delta\sigma_p$, or the ratio

$$\Delta\sigma_p / (\sigma_f - \sigma_o) \quad (2.4(a))$$

provides a means of testing certain features of the model for different materials. Ibrahim and Embury [9] recognized this fact and introduced what they termed a Bauschinger effect parameter (BEP) along the lines of (2.4(a)) as

$$\text{BEP} = (\sigma_f - |\sigma_r|)/(\sigma_f - \sigma_o) \quad (2.4(b))$$

The determination of σ_r in this equation as proposed by Ibrahim and Embury [9] is discussed in Chapter 3, section 4.3. In references [9] and [10], these authors tested the dependence of eqn. (2.4(b)) on both the prestrain and volume fraction for two b.c.c. metals. A similar (but preliminary) study was undertaken by Filipovic [11] for an HSLA steel.

Another method of specifying the BE is to consider the reverse deformation in terms of strain. In his work on the BE, Woolley, 1953 [12] introduced the Bauschinger strain, β , see Fig. 2.1. Buckley and Entwistle [13] studying the BE in single and polycrystals of pure aluminum used the same approach in 1956. The β -strain in these cases was measured by a reverse stress, $\sigma_r = -n\sigma_f$ where $0 < n < 1$ was a fraction fixed arbitrarily at 0.75 by Woolley and chosen separately at 0.75 and 1.0 by Buckley and Entwistle. In order to characterize the stress and strain related BE definitions, Kumakura [14] investigated the BE in various plain carbon steel structures and concluded that both methods provided representative measurements of the BE.

The representation of the pertinent characteristics of the BE in Fig. 2.1 illustrates the difficulties which must be faced in assessing the magnitude of the BE and consequently explains the existence of an array of definitions in the literature. There is evidence in the literature, Abel [15] and Abel and Ham [16] to suggest that in some cases large β -strain values may be obtainable with a relatively small yield lowering effect, while in other cases, the reverse may be true. In some alloys, it is possible to obtain reverse yielding during unloading followed by rapid work hardening. With this type of reverse flow

behaviour, the BE, as characterized by the β -strain would be smaller in magnitude than the corresponding measurement using one of the stress related parameters. Further complications arise when local regions of the reverse flow curve are concave outwards, i.e. a locally decreased hardening rate with increasing strain, as observed by Stoltz and Pelloux [17] in Al-Cu-Mg (2024-T6) alloys; or when regions of constant flow stress are exhibited by the reverse flow curve as observed by Hasagawa and Yakou [18] in pure aluminum at high temperatures. These kinds of behaviour clearly indicate the complexity of the problem of characterizing the BE. Some recent work by Abel and Muir [19,20,21] deals with this problem in some detail. These authors have proposed the following three parametric representations of the BE.

$$(i) \quad \beta(\epsilon) = \beta/\epsilon_p \quad (2.5)$$

$$(ii) \quad \beta(\sigma) = (\sigma_f + \sigma_r)/\sigma_f \quad (2.6)$$

$$(iii) \quad \beta(E) = (E_s/E_p) \quad (2.7)$$

Equation (2.5) defines a Bauschinger strain parameter as the ratio of the β -strain measured upon fully reversed loading to the pre-stress during forward loading. With this definition, $\beta(\epsilon)$ will be less than 1.0 and although Abel and Muir prescribe a "theoretical maximum" value of $\beta(\epsilon) = 2$, there is no clear evidence why this limitation should be true in general.

Equation (2.6) re-introduces the Bauschinger effect factor, BEF of eqn. (2.3) as the Bauschinger stress parameter, $\beta(\sigma)$ in order to take into account the cases of yielding during unloading. The evaluation of the limiting values of $\beta(\sigma)$ is discussed more clearly by Moan[22].

In the extreme case where a material does not show the BE, $\sigma_r = -\sigma_f$ and $\beta(\sigma) = 0$. In the other possible extreme when the BE is so large that reverse plastic flow is experienced immediately upon unloading, $\sigma_r = \sigma_f$ and $\beta(\sigma) = 2$.

Finally, the Bauschinger energy parameter, $\beta(E)$ as defined by eqn. (2.7) is an empirical relationship designed to incorporate both stresses and strains simultaneously. Referring to Fig. 2.1, E_p encompasses the area OABDO and represents the plastic work done during prestraining. E_s is the shaded area A'BB'A' representing the plastic work saved during fully reversed deformation up to the level of the prestress. Abel and Muir considered that since E_s will always be less than E_p , the ratio $\beta(E) = E_s/E_p$ is consequently always less than unity. However, conditions can exist in which $\beta(E)$ easily exceeds unity particularly in the types of behaviour cited in refs. [17] and [18].

The choice of the definitions in equations (2.5) - (2.7) on account of their fractional formulations has the advantage of providing comparable rankings of the BE in different materials, irrespective of which parameter is used. However, these definitions are still not quantitative in that they do not provide for a suitable measure of the contributions from back stresses to which the large BE observed in some materials is attributable. For this single reason, none of the BE parameters proposed by Abel and Muir is adopted in this present study. Instead, equation (2.1) is used to study the yield lowering effect because it is interesting from the engineering point of view. Secondly, equation (2.4) is also adopted on account of its relevance to the processes of dislocation accumulation at second phase particles and to the

very origin of the internal back stresses which contribute both to the transient and permanent softening in the Bauschinger phenomenon. Furthermore, it will become increasingly evident in later chapters of this thesis that both of the relations (2.1) and (2.4) can be easily extended to more quantitative discussions of permanent softening in terms of the long range back stresses.

2.2.3 Suggested Causes

Abel and Muir [19] summarised some of Bauschinger's original observations [1] in the following manner:-

"Plastic prestrain increases the elastic limit for the deformation which is in the same direction as the prestrain. This is the effect we have come to expect and which we normally associate with work hardening. Plastic prestrain decreases the elastic limit for the deformation which is in the direction opposite to that of the prestrain".

Bauschinger's observations were made on wrought iron and Bessemer steel and were regarded for a while as an intrinsic feature of the work hardening process only in polycrystalline materials. On this premise, Masing [23] suggested that the effect could be explained by considering the development of a residual intergranular stress system arising from the heterogeneous deformation of an aggregate of differently oriented grains. The residual stress system was envisaged as directional in nature such that it aided reverse flow. This view was generally accepted by a number of investigators but when Sachs and Shoji [24] showed the existence of the BE in α - brass single crystals, some

controversy developed. As reported by Polakowski [25] the objections to Sachs and Shoji's results were based on the possibility of anisotropy and composition gradients in the α - brass crystals. The question as to whether the BE occurs during both the homogeneous deformation of single crystals and the inhomogeneous deformation of polycrystals appeared to have been definitely settled when Polakowski [25] also observed the BE in iron single crystals. Later, Buckley and Entwistle [13] carried out experiments using pure aluminum single and polycrystals and confirmed the existence of the BE in single crystals. The magnitude of the BE in the polycrystals was found to be of the order of twice the values of those observed in the single crystals at high prestresses.

The existence of the BE in single crystals does not completely discredit the early macroscopic residual stress theory; it simply indicates that additional more important processes are in fact operative, particularly with reference to internal sessile barriers. Such barriers may be intentionally introduced into the structure in the form of precipitates to enhance work hardening and strength or they could result from the interaction of glissile dislocations to form sessile ones [26]. Consequently, the more plausible and currently accepted theories of the BE are based on micromechanical concepts of dislocation - obstacle interaction.

In general, when a material is deformed plastically the deformation appears macroscopically homogeneous and uniform (the Luder's strain is an exception) but is naturally inhomogeneous at the microscopic level. The inhomogeneity may involve individual dislocations whose

generation and movement cause plastic flow, or it may involve dislocation groups and second phase particles. As a natural consequence of the inhomogeneously deformed microstructure, there will exist a form of microstructural incompatibility which results in internal stresses. The internal stresses may be viewed as short or long range in nature. These terms are more commonly used to describe ordered solid solutions and superlattices [26,32]. In these systems, the usual disordered and random arrangement of atoms at lattice sites undergo a structural rearrangement below a certain critical temperature to produce an ordered superlattice consisting of regular configurations of two atomic species. Where such a coherent atomic scheme extends over large distances, the crystal possesses long range order; this arrangement is strongly temperature dependent. However, above the critical temperature, the number of unlike neighbour atoms can still be different locally from that expected statistically. In this case, short range order exists. The use of the terms - short and long range - to describe back stresses retains the relationship to distance but does not presuppose any temperature dependence. ▽

The short range description of internal stresses refers to a rather localized activity, for instance, in the immediate vicinity of obstacles only. The long range description relates to internal stress effects which may be felt in an average sense by the overall deforming volume and which either subtracts from or adds to the flow stress in subsequent behaviour depending on the sense of loading.

In the short range mechanism, the resistance to dislocation motion is less in the reverse direction than in the forward direction.

In mechanistic terms, the array of obstacles sampled during the forward stroke have become weakened and so the reverse deformation can proceed more easily; possibly too, a small fraction of these barriers are no longer true obstacles in the sense that they may have been sheared during primary slip. In metallurgical terms, a more subtle language is used to describe the micromechanical dislocation processes. Daniel and Horne [27] attributed short range stresses and the BE during the cyclic hardening of pure copper single crystals to the reverse motion of unpaired dislocations in a structure where dislocation dipoles are plentiful. Stoltz and Pelloux [28] listed two other possible mechanisms, namely: the recovery of dislocation debris by the backward motion of jogs on screw dislocations, and the re-establishment of local order when single dislocations retrace their path through sheared ordered precipitates.

The long range stresses are viewed as averaged over the plastic volume and on this account are more dependent on the overall microscopic incompatibility and less sensitive to fine dislocation details. One origin of microstructural incompatibility is due to the Masing [25] type idea of heterogeneous deformation of differently oriented individual grains or aggregates of crystals in a polycrystalline medium. Dislocation pile-ups at grain boundaries will also cause inhomogeneity. More insight may be gained concerning the long range stresses by introducing Orowan's [29,30] concept of the BE based on the sampling of structural obstacles by dislocations.

The original paper by Orowan [30] sought answers among other things, to the causes of transient softening (the domain A'B' of the

reverse curve in Fig. 2.1) and permanent softening, $\Delta\sigma_p$.

Observing that the BE is not completely removed by heating below the recrystallization temperature, Orowan proposed that dislocation loops must form around impenetrable obstacles in the structure during the course of plastic deformation. Therefore, the BE was considered not simply in terms of back stresses due to the pile-ups of dislocations at structural obstacles but also in terms of complete loops of dislocations at these obstacles. The stress field of these loops persists during annealing treatments until the dislocations themselves are removed.

In his examination of the Orowan theory, Ashby [31] gives a good description of the role of second phase particles on the yielding process of alloys. When a dislocation moving on a slip plane under applied external tractions meets particles, the subsequent motion of the dislocation is hindered. As the applied stress is increased, the dislocation bows between the particles, and in the case of very strong obstacles which do not shear under the influence of the impressed forces, the dislocation will eventually reach an unstable semi-circular configuration. The end point of the process involves the joining of the bowed dislocation arms in the vicinity of the particles. A Frank-Read type source [32] is then generated and the dislocation leaves an "Orowan" loop around the particle as it bypasses it. The effective obstacle size increases with the applied stress and so does the number of loops left behind by dislocations bypassing the obstacles. If the number of loops are maintained, the repulsive effect of the loops on subsequent oncoming dislocations will be high resulting in work harden-

ing and a back stress. The number of loops can, however, become reduced by several possible relaxation mechanisms including cross slip and the conversion of shear loops to prismatic loops, (see Hirsch and Humphreys [33]), the shearing and fracture of particles, the decohesion of the matrix-particle interface and the climb of dislocations.

The essential question now is to examine how the Orowan mechanism coupled with the secondary relaxation processes can provide an explanation for the existence of the BE. Some recent work by Brown [34] provides an explanation along the following lines. Firstly, as a material is loaded, say, in tension, dislocations become piled up and bowed as they meet structural obstacles which depending on the amount of the imposed strain may already be surrounded by a number of Orowan loops. Some of the particles will have been sheared by dislocations during the loading. When the stress level is reduced during unloading, the bowed dislocations first back away from the hard array of particles under the influence of the back stress due to the pile-ups, and a small amount of reversible displacement may be observable. After becoming straight and bowed in the opposite sense during compression, the dislocations now sample an array of obstacles of random strength which are weaker than the array sampled previously during forward loading. Since the particles are always elastic and non deformable, upon unloading, they will have become stressed in one sense and the matrix in another due to the existence of permanent plastic strains in the matrix. This is clearly the origin of microstructural strain incompatibility. The mean stress exerted on the matrix by the unrelaxed

stresses in the particles is the long range stress and it adds to (during loading in the direction of the prestrain) and subtracts from (during reverse loading) the applied stress so that the typical plastic strain hysteresis loop is shifted along the stress axis. The long range stress concept therefore explains permanent softening and quantitatively predicts it as twice the mean matrix stress, $\langle \sigma \rangle_m$, that is:

$$\langle \sigma \rangle_m = \frac{1}{2} \Delta \sigma_p \text{ (see Fig. 2.1)} \quad (2.8)$$

As discussed previously, the short range stresses affect the transient nature and the roundedness of the reverse flow curve and are related to the statistics of reverse dislocation sampling of obstacles. The combined effect of both the short range and the long range stresses causes:-

- (a) the lowering of the reverse yield stress or the elastic limit traditionally known as the Bauschinger Effect;
- (b) the roundedness of the reverse flow curve;
- (c) the permanent softening of the reverse flow curve.

Current theories of the BE therefore rely on the concepts of these short range and long range stresses. In what follows, the pertinent previous investigations into general aspects of the BE will be reviewed in an attempt to establish the evolution and acceptability of this theory and to show the need for some of the investigations carried out in this thesis.

2.2.4 Related Studies on Aspects of the Bauschinger Effect.

Subsequent to the discovery of the Bauschinger Effect in 1881[1], Masing [23] proposed the textural or intergranular residual stress theory to explain it. The mechanical simulation of Masing's theory

will be dealt with in some detail in Chapter 3. In simple terms, the model predicts that the reverse stress-strain curve, when measured from the point of unloading, will be of the same shape as the preloading curve apart from a scaling factor of two. Masing unsuccessfully tried to verify his theory in the work reported in Masing and Mauksch [35] and in Rahlfs and Masing [36]. The works of other pioneers referred to previously, namely, Woolley [12], Buckley and Entwistle [13], Sachs and Shoji [24], Polakowski [25] and Edwards and Washburn [37] combined to establish the BE as an intrinsic feature of the work hardening process common to both single crystals and polycrystals. Before continuing further discussion on these individual researches, it would be instructive to review the types of experiments commonly used to study the BE.

The most widely employed experimental methods have been either reverse tension or reverse torsion. In reverse tension, specimens are preloaded in tension and subsequently plastically strained in compression (or vice versa). This can be realized in two ways:

(a) Tensile type cylindrical specimens suitably machined for tension and compression can be used in a carefully aligned jig mounted in a tension-compression loading machine. In order to avoid the effects of the shoulders, Buckley and Entwistle [13] suggested that the length of the reduced section of the test piece should be, at least, three times the diameter and that the strain should be measured over the middle third of this section.

(b) Alternatively, compression specimens may be machined from pretensioned samples and tested using well lubricated plattens.

Harrison et al [38] used this method (a practice the present author does not favour).

In reverse torsion, thin walled cylindrical specimens are used (Woolley [12], Kishi and Tanabe [2]) and the torque is applied first in one direction and then in the opposite direction. The shear stress-strain curves are obtainable from measurements of the applied torque versus the angle of revolution. In the reverse torsion tests, mirrors are generally used to measure the angle of twist, but in reverse tension, extension measurements are now made using strain gauge extensometers and may be conveniently plotted autographically against the load in most laboratory tension-compression testing machines.

Other methods of measuring the BE, such as the use of acoustic emission counts may well be coming to the fore. If there is an abrupt relaxation in either the localized or the long range stresses within a material, strain waves are produced which may be detected by means of sensitive piezoelectric transducers attached to the specimen. Chow and Embury [39] have used this method to study twinning in metals. The noise that is produced during these stress relaxations or by sudden dislocation slips is referred to as acoustic emission. Kishi et al [40] have associated acoustic emission peaks with the BE. Sankar et al [41] correlated acoustic emissions counted during the unloading of a specimen with the magnitude of the BE in several metals, and Siegel [42] in a recent publication showed that the amplitude of both the under-load and unload acoustic emissions increase with the coarsening of the G.P. zones and θ -type precipitates in age hardenable aluminum 6061 and 2024 alloys. This refers to increasing BE activity in coarse structures, a

property of the BE which will be discussed more fully later in this section.

The application of acoustic emission techniques to measurements of the BE appears to be at a preliminary stage at the moment and further work will be required in order to establish clearly if the magnitude of the BE in terms of the three aspects - yield lowering effect, roundedness and permanent softening - can be reliably measured using unload acoustic emission counts. Clearly, the observations discussed above would appear to support the view of the BE as a consequence of internal stresses.

Further specialized experiments: systems for bending, reverse bending and multiaxial stress states have been developed. In experiments designed to illustrate the influence of the stress state on the yield criterion and the BE, Rolfe et al [43] predeformed thick plates in plastic bending and subsequently tested standard tensile and compression samples machined from the wall thickness of the curved plates. Pascoe [44] simulated reverse bending by deforming plates in bending to the required radius, heat treating them to remove the effect of cold working and finally, flattening the heat treated samples using rollers. Following this, standard tension and compression tests were performed and the BE resulting from prestraining in bending was compared to the BE in uniaxial deformation. Also, in experiments concerned with the nature of subsequent yield surfaces, Morrison and Shepperd [45] developed the combined tension and torsion test for thin walled tubular cylinders.

Returning to the discussion of general research, Kumakura's

work [14] provides a good starting point. He studied the BE in six steels of different carbon contents and heat treated conditions as a function of the prestrain using reverse torsion and tension compression loading. His work was very comprehensive and the significant aspects of his conclusions deserve detailed treatment for general purposes.

(i) Using both stress and strain related BE parameters the BE was found to increase with the imposed strain. The β -strain increased almost linearly with the prestrain while the ratio $\sigma_F/|\sigma_r|$ increased exponentially with increasing prestrain. Irrespective of the testing procedure this increase of the BE with prestrain is in general observed, although a reduction of the rate of increase is observed at larger prestrain. Similar results have been reported in tension - compression tests [7], in bending [43], in reverse bending [44] and in hydrostatic extrusion [47].

(ii) The BE was shown to be generally smaller in the well ordered spheroidized structures than in the coarse pearlitic steels. The BE has been recently reported to increase in a similar fashion with the coarsening of the G.P. zones to a maximum level in the presence of semi-coherent precipitates in age hardenable Cu-30Ni-1Si alloy by Gupta et al [5].

(iii) For a given prestrain, the BE increased with the carbon content. Jamieson and Hood [8] obtained the same results in both plain carbon and HSLA steels; these same authors also found the BE to be independent of grain size (see also Kishi and Tanabe [2]) but to increase with the manganese content. Columbium and Vanadium in HSLA steels showed no effect on the BE.

(iv) The BE was measured in different orientations relative to the direction of prestraining. The magnitude decreased from a maximum value along the direction of the prestrain to a minimum value transverse to the prestraining direction. These results were obtained in tension and compression using test pieces whose longitudinal axes were inclined at various angles to the direction of prestrain. The prestrain was achieved by compressing a large diameter ($4 \frac{1}{3}$ " (110 mm)) blank from which tension and compression test pieces were machined. Kishi and Tanabe [2] have used these results to verify a new kinematic hardening law. The observed behaviour was attributed to the anisotropy of the material developed during the prestraining.

(v) Permanent softening was observed and its magnitude was found to be similarly anisotropic.

(vi) Low temperature ageing treatment tended to reduce the level of both the BE and permanent softening but did not completely eliminate the BE except in the case of very low carbon (.02%) steel. The effectiveness of static strain ageing depends of course on the extent of ageing (time and temperature). Li et al [46] recently carried out experiments in which prestraining was performed at a temperature in the dynamic strain ageing range followed by reverse straining at room temperature. They obtained larger reductions in the magnitude of the BE in plain carbon and HSLA steels.

(vii) In a final conclusion, Kumakura suggested that since ageing treatments do not completely remove the BE, then the BE although related to macroscopic residual stresses is mainly caused by microscopic

internal stresses and strain inhomogeneity.

In general, these conclusions apply to most metallic materials. Investigations into other aspects of the BE such as strain rate and temperature effects have also yielded interesting results. Eleiche and Campbell [48] carried out dynamic reverse torsion experiments with a rate sensitive magnesium alloy AZ61A. Specimens were first loaded in the forward path quasi-statically to different prestrains. After the desired prestrain was attained, the unloading and subsequent reverse loading strain rate was increased over and above that used in prestraining. In line with normal isotropic behaviour, the increased strain rate would be expected to increase the reverse flow strength over and above the reverse flow strength in ordinary quasi-static reverse loading. The reverse was, however, found to be true. In reverse straining at higher strain rates than those used during prestraining, the BE increased with the strain rate. The strain rate sensitivity was found to be initially negative at reverse yielding but switched and became increasingly positive with continued reverse straining. No other comparable results exist in the literature currently.

Turning to temperature effects, it is first noted that the flow stress of metallic and non metallic materials decreases with temperature during normal constant strain rate tests. Hasegawa et al [16] in the tension-compression of pure aluminum polycrystals observed the normal transient BE behaviour during initial reverse yielding. However, with continued reverse straining, a "region of constant flow stress" which increased with the temperature of deformation was observed on the reverse curves. In refs. [49] and [50], Hasegawa and his co-

workers attribute the regions of constant flow stress to the instability and dissolution of cell walls and subgrains formed during prestraining. They presented metallographical evidence which showed the formation of new cell walls and subgrains during reverse flow, although the total dislocation density decreased by about 16% at all temperatures during the early stages of reverse straining. There is, however, no evidence currently in the literature to indicate the possibility of similar behaviour in other materials.

This section can now be concluded with a brief discussion on the effect of particle strength on the reverse flow behaviour. The BE has been shown to depend on the shape and morphology of second phase particles, [5], [14] and [42]. Precisely, the BE is larger in incoherent or lamellae structures than in structures containing well ordered or spherical particles. The strength of the particles is also important in the sense that it controls the nature of the relaxation processes occurring during prestraining, as well as the amount and nature of real obstacles to reverse dislocation movements. Stoltz and Pelloux [17,28] heat treated aluminum and copper alloys to produce shearable and non shearable precipitates. In the alloys containing the shearable particles, the BE was normal in the sense of a continuously convex stress-strain curve. However, in the alloys containing the non shearable (very strong) precipitates, locally concave regimes were observed on the reverse flow curves, resulting in a rather large BE activity in these alloys. The results show that the stronger the structural obstacles to dislocation motion, the larger the transient BE, although the permanent softening does not appear to increase in

the same proportion. Recent work by Moan [20] has also shown the long range back stresses to be higher in Al-Cu alloys aged to contain θ' - particles than in the single phase alloys and in pure aluminum crystals.

The work of Wilson [51] which is important from the point of view of the inter-relationship between the long range back stresses and the BE also shows the effect of particle strength on the BE in two phase alloy systems. Wilson's alloys fell into two groups: the first group consisted of alloys which were effectively single phase and the second group included steels strengthened by a dispersion of strong non coherent particles. Representing the BE using the ratio $|\tau_r|/\tau_f$ (equivalent to $|\sigma_r|/\sigma_f$ of eqn.(2.2)), the first group of alloys showed smaller permanent softening than the dispersion hardened alloys. With comparable particle sizes, the permanent softening increased with the volume fraction of the precipitates and with similar volume fractions, it increased with the fineness of the dispersion. Again, coarse lamellae cementite in pearlite were found to be more effective long range stress generators than either equi-axed or well ordered spherical particles.

2.2.5 Engineering Significance

The general shape of the schematic stress-strain curve of Fig. 2.1 as it relates to the behaviour of real materials has been discussed. Some practical implication of this behaviour are now presented.

In many manufacturing processes which utilize cold forming, the strength of the part may be seriously impaired in service if the working stresses are in the sense of a reverse loading. The roundedness

of the reverse σ - ϵ curve may be important in structures which are designed on the basis of a tangent modulus or an allowable distortion at a given working stress. Furthermore, the permanently softened state of the reverse flow curve would result in overestimates of the design strength of structures in which the ultimate tensile strength to yield strength ratio of the monotonic flow curve is used as a design parameter.

It is noted that in many technological situations, it may be difficult to distinguish the behaviour that is exclusively due to the Bauschinger phenomenon since there may be other sources of directionality in the flow behaviour. This difficulty arises from two main features: Firstly, it is difficult to know the exact state of internal stress produced as a consequence of making the part. Secondly, the degree of anisotropy resulting from the previous processing history of the material e.g. rolling and that developed during the manufacturing of the part is also difficult to assess.

As an example of a manufacturing application, the U-O-E pipe forming process is given considerable attention in this thesis. This process involves plastic strain reversals and a rather severe cold deformation history than the other processes such as roller and spiral forming which are also used in high strength linepipe manufacture. However, in the manufacture of any large diameter thin walled pipe, it must be stated that the induced strains would be small. In the case of the 40 ins. (1016 mm) diameter and $\frac{1}{2}$ ins. (13 mm) wall thickness pipe studied in Chapter 6, the strains are unlikely to exceed 2%. Briefly, the manufacturing sequence in U-O-E pipe forming involves

plate bending into a U-shape, circumferential compressive shaping into an O-form and radial sizing by hydraulic Expansion. Every element in the pipe wall therefore undergoes a unique strain history and is subject to the influence of the BE. In selecting the U-O-E process for special study, it has to be born in mind that since the subject material of this work - the HSLA steels - find their largest market in large diameter high strength linepipe applications, the need for this type of study was clearly outstanding.

The theoretical aspects of the BE involve the analysis of reversible plasticity in terms of the micromechanics of dislocation processes and the role of structural obstacles in order to provide a better understanding of the BE as an integral part of the process of work hardening in structural materials. The microstructural approach is clearly useful in the metallurgical design of industrial alloys which rely on a combination of microstructural precipitates to achieve the required strength levels and overall integrity. Also, it enables the establishment of practical relationships between the important microstructural parameters and the macroscopic descriptions of the mechanical state of a material in terms of the plastic strain and flow stress which can be used for more realistic descriptions of material constitutive laws.

2.3 The Scope and Objectives of Present Investigations

In this chapter an attempt has been made to review the certain theoretical and practical aspects of the Bauschinger Effect in order to demonstrate the need for a quantitative study of the BE in the more

common structural steels. This thesis deals therefore with the BE in conventional plain carbon and in the technologically important series of HSLA steels. It has been stated that the existence of the Bauschinger phenomenon can be attributed to the presence of microscopic internal stresses and the incompatibility of the microscopic strains developed during the prestraining history. The utility of this approach to the study of the BE is that it indicates clearly the importance of describing material behaviour not simply in terms of the imposed macroscopic strains but also in terms of the resultant distribution in the local resistance to further plastic flow. In essence, this requires bringing together certain concepts of continuum plasticity and those of dislocation mechanics.

In this work, the BE and its descriptions in terms of changes in both the flow stress and the work hardening rate are studied in a variety of structural steels. The BE was first quantitatively measured in three HSLA steels using tension-compression tests. Next, spheroidized plain carbon steels were used to derive a simple model of the long range back stress which could be related to some well defined microstructural parameters such as the amount and form of the second phase cementite particles. The model of the BE derived for this system was then applied to the more complex HSLA steels in order to study its general applicability. At this point, it is worth noting that previous verifications of the long range back stress theory were limited to rather model microstructures and to small volume fractions and particle sizes (see Chapter 3, Section 4). Consequently, in this present study, the BE in a broad spectrum of steels containing second phases of

different morphologies is investigated. The objectives are to indicate clearly:-

- (i) the magnitude of the BE as a function of prestrain in the HSLA steels;
- (ii) the magnitude of permanent softening as a measure of the long range back stresses, and the relationship to the prestrain and the volume fraction of second phase constituents;
- (iii) the development of the microscopic BE model for steels and the verification with experimental observations. The model is based on the concepts of internal stresses and quantitative information is first presented using macroscopic and phenomenological models which show clearly, the influence of residual stresses on plastic flow behaviour;
- (iv) the magnitude of the unrelaxed strain or the level of matrix - particle incompatibility and the range of prestrains over which they are of importance;
- (v) the consequence of the unrelaxed strain in terms of the dimensional stability of the material. This was assessed by considering the dimensional changes occurring upon the straightening of 1045 steel rods by a series of small strain reversals following cold drawing to various imposed strains;
- (vi) the implications of the models used to derive the back stress from single strain reversals. Two aspects of this were considered: the reversibility of back stress hardening in continued cycling to produce symmetrical σ - ϵ hysteresis loops and the removal of back stress hardening using large prestrains to try and promote local fracture nucleation at the second phase particles.

(vii) to examine the reverse flow behaviour of a metal that exhibits a pronounced Luder's strain when the reverse loading occurs before the Luder's front has propagated across the entire gauge section. Of interest is the manner in which the BE is revealed and how the propagating Luder's front is affected. These aspects were studied using one of the HSLA steels.

The final objective was to demonstrate the use of these results in a practical engineering sense. This was achieved in the analysis of the engineering significance of the BE in the U-O-E pipe making process as an application involving both complex strain histories and the BE. The mechanics of the U-and O-stages of the pipe manufacturing process was first modelled in order to show the possible systems of macroscopic residual stresses and the stress and strain distributions existing in the pipe wall. Using this knowledge in conjunction with the experimentally simulated reverse flow characteristics of the HSLA steels, the radial expansion behaviour of the U-O pipe was predicted theoretically with the aid of a finite element program. These calculations are discussed in more detail in Chapter 6; however, the results obtained reflect the final properties of the pipe after the E-stage. This is viewed as an important accomplishment on account of the quality control problems attributed to the Bauschinger Effect in some of the literature originating from the steel companies and HSLA steel pipe manufacturers.

CHAPTER III

THEORETICAL MODELS OF THE BAUSCHINGER EFFECT

3.1 Introduction

In this chapter some specific macroscopic and microscopic models of the BE will be discussed. As a starting point, the continuum theory of plastic deformation and work hardening is briefly reviewed. The review will consider the processes of isotropic, anisotropic and kinematic hardening as well as some experimental techniques used to determine subsequent yield surfaces. Some discussion is also devoted to the so called second order effects in plasticity. In the continuum theory of plasticity, the BE is usually described in terms of the translation of the yield surface in stress space. The analytical models for yield surface translation will therefore be examined in some detail in order to demonstrate the complexity of the problem of attempting to obtain a unified theory.

There then follows a discussion of the three simple models aimed specifically at accounting for the BE. These models utilize respectively, (a) the influence of residual stresses, (b) a simulation of the deformation of a structure containing elastic and plastic phases, and (c) a family of loading (yield) surfaces in stress space which obey a non linear kinematic-isotropic hardening rule of some kind.

To conclude the chapter, microscopic models of the BE are discussed based on the concept of elastic-plastic deformation of a two phase material. The analytical expression for the mean matrix stress is derived for use in the subsequent analysis of experimental data.

3.2 Work Hardening Models of Continuum Plasticity

3.2.1 Isotropic and Kinematic Hardening Models

The major objective of the theory of plasticity is the provision of generalized laws of material behaviour in the plastic range under any loading history. This has been approached over the years by the formulation of constitutive laws either in the form of finite relations between stress and strain or in the form of incremental stress-strain relations. The former has become known as the total deformation theory and is predictive only in cases of simple loading, e.g. in monotonic loading. The incremental or flow theory, on the other hand, appears to hold more adequately for general plastic deformation. This conclusion stems from both empirical and physical considerations, namely, the fact that the final state of stress (strain) is not determined simply by that of strain (stress) but by the deformation path up to the current state. The equations of the flow theory of plasticity therefore establish a connection between the infinitesimal increments of strain and stress, the instantaneous stresses themselves and certain parameters of the plastic state. The material behaviour in a prescribed loading history is then obtained by integrating the increments of strain and stress along the deformation path. In addition to the constitutive law relating stresses to strains or their increments, the rule of work hardening defines the modifications of the initial yield condition during the process of plastic deformation.

Considering an element of a deforming solid referred to an orthogonal coordinate system x_i , the state of stress of this element can be represented by a stress point in a nine-dimensional space as σ_{ij} .

For the elastic (or rigid) perfectly plastic medium, the yield condition remains unchanged during continued plastic deformation.

Mathematically, this can be stated as:

$$f = f(\sigma_{ij}) = 0 \quad (3.1)$$

Geometrically, this equation may be interpreted in terms of a fixed convex surface in the stress space separating the elastic and plastic domains. Fig. 3.1(a) schematically illustrates this for the von Mises yield condition, drawn for the special case of plane stress.

Under these conditions, the yield surface can be expressed in terms of two principal stresses, σ_1 and σ_2 (with $\sigma_3 = 0$) as follows:

$$\sigma_1^2 - \sigma_1\sigma_2 + \sigma_2^2 = 0 \quad (3.2)$$

For the work hardening material, eqn. (3.1) may be altered to include a scalar parameter λ which increases monotonically with plastic deformation as follows;

$$f = f(\sigma_{ij}, \lambda) = 0 \quad (3.3)$$

The parameter, λ as a measure of the hardening is usually defined in terms of the plastic work increment, λ_1 , or less frequently, in terms of the Odquist's parameter [5], λ_2 characterizing the accumulated plastic deformation. Mathematically, these can be expressed as:

$$\lambda_1 = \int_0^{\epsilon_{ij}^p} \sigma_{ij} d\epsilon_{ij}^p \quad (3.4)$$

or,

$$\lambda_2 = \int_0^{\epsilon_{ij}^p} (2d\epsilon_{ij}^p d\epsilon_{ij}^p)^{1/2} \quad (3.5)$$

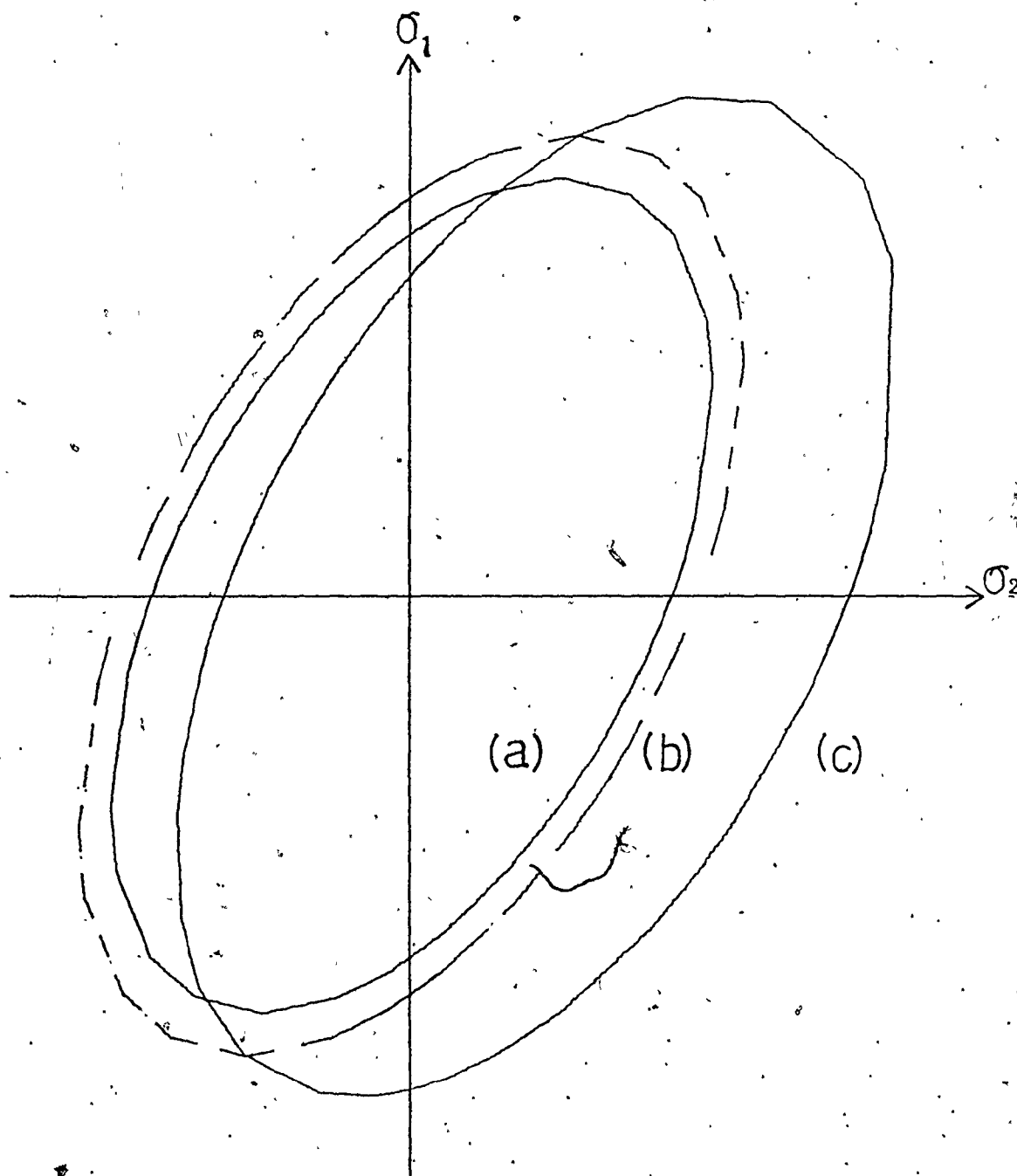


Fig. 3.1 A schematic representation of yield surfaces in plane stress: (a) Initial surface, (b) Isotropic expansion (c) Kinematic Hardening.

where ϵ_{ij}^p and $d\epsilon_{ij}^p$ are plastic strain components and the strain increments respectively. Identical results are obtained using λ_1 and λ_2 for materials obeying the von Mises yield condition. More commonly, the hardening rule expressed by (3.3) is written alternatively as

$$f = f(\sigma_{ij}) - \sigma_0^2(\lambda) = 0 \quad (3.6)$$

where σ_0 depends on λ and is readily seen as a measure of the current flow stress. Also, since the yielding of metals is known to be unaffected by the hydrostatic stress, then eqn. (3.6) can be expressed as:

$$f = f(\sigma'_{ij}) - \sigma_0^2(\lambda) = 0, \quad (3.7)$$

where $\sigma'_{ij} = (\sigma_{ij} - \frac{1}{3} \delta_{ij} \sigma_{kk})$ is the deviatoric stress tensor.

Equation (3.7) defines the rule for isotropic work hardening.

The yield surface expands uniformly and its instantaneous size is fixed by the current value of σ_0 derived from the hardening parameter, λ . This is shown schematically by the curve labelled (b) in Fig. 3.1. This conclusion and, in fact, the whole concept of isotropic hardening is at variance with observations of the BE. Therefore, to incorporate the BE, the yield condition (3.7) needs further modification to allow for a translation of the surface in the stress space as follows:

$$f = f(\sigma'_{ij} - \alpha_{ij}) - \sigma_0^2(\lambda) = 0 \quad (3.8)$$

where α_{ij} is the tensor of total translation.

The exact mathematical form of the translation tensor is still unresolved. In the original form proposed by Prager [56], the yield function excluded the term $\sigma_0^2(\lambda)$ in eqn. (3.8) and so the surface

retains its size and shape and translates like a rigid body in the stress space. The instantaneous translation was assumed to take place along the direction of the exterior normal at the stress point. On account of the flow rule, the strain increment tensor is given by

$$d\epsilon_{ij}^p = d\lambda \partial f / \partial \sigma_{ij}, \quad d\lambda > 0 \quad (3.9)$$

and the direction of the strain increment is normal to the yield surface. The translation tensor may then be represented as

$$\alpha_{ij} = c \epsilon_{ij}^p$$

or

$$d\alpha_{ij} = c d\epsilon_{ij}^p \quad (3.10)$$

where c is a constant characterizing the material. Prager's rule, (3.10), forms the basis for all kinematic hardening laws and predicts linear work hardening in the following manner:

(a) in tension: $\sigma_t = \sigma_0 + c \epsilon_p$

(b) in compression: $\sigma_c = \sigma_0 - c \epsilon_p$

where σ_0 is the initial yield stress, σ_t is the flow stress in tension measured at a plastic strain, ϵ_p and σ_c is the reverse yield stress in compression following tension.

Shield and Ziegler [57] applied Prager's rule to some particular cases including plane stress and plane strain. They found that if the yield surface in the 9-space translates in the direction of the external normal at the stress point, the two dimensional yield locus does not always do so. This loss of invariance with respect to the reductions in the dimensions of the stress was more pronounced in the case of the Tresca type material where the yield locus even deforms. Consequently,

Ziegler [58] modified Prager's rule to allow for translation in the direction of the vector connecting the centre of the yield surface with the stress point. Mathematically, this is expressed as,

$$d\alpha_{ij} = (\sigma_{ij} - \alpha_{ij}) d\mu, d\mu > 0 \quad (3.11)$$

He then proceeded to study (3.11) under some particular conditions and found that this rule applies without modification in any subspace even with the Tresca type material. However, Ziegler's rule has a serious disadvantage related to the indeterminacy of the strain increment in the corners or vertices of the Tresca yield surface.

Both the Prager and the Ziegler hardening laws appear to generalize linear work hardening in simple tension to complex states of stress. A modification to account for changes in the hardening modulus was proposed by Eisenberg and Phillips [59] who assumed that:

$$\begin{aligned} \alpha_{ij} &= c(\lambda) \epsilon_{ij}^p \\ \text{and} \\ d\alpha_{ij} &= c(\lambda) d\epsilon_{ij}^p + c'(\lambda) \epsilon_{ij}^p d\lambda \end{aligned} \quad (3.12)$$

As the hardening modulus, λ changes in the course of plastic deformation, this model may describe a non linear curve. Non linear laws of this form are of course closer to reality but are still arbitrary. The non linear kinematic hardening law of Kishi and Tanabe [2] illustrates clearly how experimental inputs may be used to characterize material behaviour in order to overcome the problem of arbitrariness. Kishi and Tanabe proposed a kinematic hardening law which utilizes the von Mises condition in the form:

$$f = \sigma'_{ij} \sigma'_{ij} - 2k(2\epsilon_{ij}^p \epsilon_{ij}^p)^{(m-1)/2} \sigma'_{ij} \epsilon_{ij}^p \quad (3.13)$$

where k and m are material parameters derived from a logarithmic fit of the yield drop, $(\sigma_f - |\sigma_r|)$ against the prestrain, ϵ_p , see Fig. 2.1. The stress, σ_f is the flow stress measured in the forward direction at a prestrain, ϵ_p and the stress, σ_r is the reverse yield stress following prestraining. The tensor of total translation, α_{ij} in eqn. (3.13) is given in terms of the cumulative plastic strain (see eqn. (3.5) as

$$\alpha_{ij} = k(2\epsilon_{ij}^p \epsilon_{ij}^p)^{(m-1)/2} \epsilon_{ij}^p \quad (3.14)$$

The law (3.14) was proposed as a result of reverse torsion and tension tests on a variety of materials. The main drawback of this rule is its mathematical complexity and the need to carry out a large number of reverse flow tests in order to establish k and m . This latter aspect is a problem common to all aspects of experimental plasticity and so does not invalidate the utility of the model. The curve labelled (c) in Fig. 3.1 schematically illustrates the processes of yield surface translation and expansion in plane stress.

To conclude this section, the theoretical work of Mroz deserves mention. In order to account for changes in the work hardening rate, Mroz [60] introduced the concept of a field of work hardening moduli into the kinematic hardening concept in place of the single parameter c as in (3.10) or the function $\sigma_0^2(\lambda)$ in (3.8). Mroz's model is discussed in further detail later in this chapter.

Other possible formulations of the kinematic hardening model, as well as their limitations, are discussed in an article by Edelman

and Drucker [61] published some years ago. Some of the more recent work permitting the translation, distortion and expansion of the yield surface is introduced below. Some of these techniques are also reviewed in an article by Shrivastava et al [62].

3.2.2 Anisotropic and Kinematic Hardening Models

Up to this point, the hardening rules discussed may be classified into three categories, namely,

- (i) Isotropic hardening;
- (ii) Kinematic hardening;
- (iii) Combined isotropic and kinematic hardening.

Implicit in the kinematic hardening concept is a form of anisotropy related to the tensor of translation, α_{ij} . In general, α_{ij} is not an isotropic tensor and so the material develops some anisotropy as a result of the hardening process.

In conventional engineering understanding anisotropy relates to the directionality of mechanical properties. An initially isotropic material may develop some anisotropy in the course of plastic deformation due to different degrees of hardening in different directions. In general, the initial yield surface may define an isotropic or anisotropic material. Hill's [63] yield criterion for the initially anisotropic material is well known;

$$2f(\sigma_{ij}) = F(\sigma_x - \sigma_z)^2 + G(\sigma_z - \sigma_x)^2 + H(\sigma_x - \sigma_y)^2 + 2L\tau_{yz}^2 + 2M\tau_{zx}^2 + 2N\tau_{xy}^2 = 1 \quad (3.15)$$

where F, G, H, L, M and N are parameters characteristic of the current

state of anisotropy. This condition deals with a metal in which the BE and kinematic hardening are negligible. In an attempt to predict the BE and the state of anisotropy from the deformation history, Yoshimura [64] proposed the yield condition given by,

$$f = \frac{1}{2} C_{ijkl} \sigma'_{ij} \sigma'_{kl} - \sigma_0^2(\lambda) = 0 \quad (3.16)$$

where the anisotropy plastic modulus, C_{ijkl} initially has the form,

$$C_{ijkl} = \frac{1}{2} (g_{ik}g_{jl} + g_{il}g_{jk}) \quad (3.17)$$

and as deformation proceeds, the metric tensor, g_{ij} becomes $g_{ij} + A\epsilon_{ij}^p$ where A is a material constant. Consequently, Yoshimura's condition for combined anisotropic and kinematic hardening may be written as,

$$f = \frac{1}{2} C_{ijkl} \sigma'_{ij} \sigma'_{kl} - B\epsilon_{ij}^p \sigma'_{ij} \quad (3.18)$$

where B is the BE modulus.

Sevensson [65] has experimentally verified that the lack of interaction between the prestrain and the yield stress in (3.18) leads to underestimates of the BE. He therefore combined the work of Edelman and Drucker [61] and that of Yoshimura to obtain

$$f = \frac{1}{2} C_{ijkl} (\sigma'_{ij} - \alpha_{ij}) (\sigma'_{kl} - \alpha_{kl}) - \sigma_0^2(\lambda) = 0 \quad (3.19)$$

and proceeded to show acceptable correlation between experiment and theory using commercially pure aluminum and 0.2% carbon steel prestrained by cold rolling [65,66]. It is worth noting that Baltov and Sawczuk [67] also proposed a similar hardening rule to Svensson's, although in this case, the anisotropy plastic modulus C_{ijkl} was

expressed as the sum of a fourth order isotropic tensor, I_{ijkl} and a tensor A_{ijkl} . The general fourth order tensor A_{ijkl} which was used to account for anisotropy was related to the strain invariants, i.e.

$$C_{ijkl} = I_{ijkl} + A_{ijkl}$$

and

$$A_{ijkl} = \bar{A} \epsilon_{ij}^p \epsilon_{kl}^p$$

(3.20)

\bar{A} is a polynomial in the strain invariants.

Most of these work hardening rules are derived from modifications to the von Mises yield criterion. To include isotropic hardening, the yield surface has been allowed to expand uniformly. The BE has been incorporated in terms of the translation of the yield surface in the stress space governed by the tensor, α_{ij} . Also, to predict anisotropy, the yield surface is allowed to rotate and distort in the stress space, governed by the parameters assigned to the tensor of plastic moduli, C_{ijkl} . The more realistic rules are, of course, those which involve a combination of kinematic hardening and either isotropic or anisotropic hardening. However, as pointed out by Shrivastava [68], these models fail to account for second order effects in plasticity. This is the subject of the next section.

3.2.3 Second Order Effects in Plasticity

Second order effects are additional complications in the search for a generalized constitutive law for the work hardening solid. The crux of this problem appears to be associated with the observed cases of axial strain accumulation during the torsioning of cylindrical specimens [69]. Second order effects have been investigated in an

article by Freudenthal and Gou [70]. In addition to the problem of axial strain accumulation during torsion, these authors discussed the drastic reduction of the strain hardening resistance in tension of aluminum, copper and titanium produced by the superposition of a low frequency cyclic strain component. In steel and nickel, this effect was found to be less pronounced. Also, when an annealed cylindrical aluminum specimen prestrained in cyclic tension and compression was subjected to a small steady torque, the shear strain increased progressively in the direction of the torque. This situation is analogous in the reverse sense to the phenomenon referred to as cyclic creep where in the cyclic plastic torsion of specimens constrained within a fixed grip distance, lateral buckling results on account of the induced axial strains. In the absence of end constraints, the axial deformation is accompanied by lateral contraction characteristic of tensile plastic deformation, and the axial plastic strain increases in magnitude with the number of cycles of strain reversals.

Since neither the commonly used theories of yielding due to Tresca and von Mises nor the kinematic hardening rules discussed earlier predict these second order effects, particularly the incidence of axial strains occurring in a bar subjected to pure torsion, additional modifications to the yield condition are necessary. The general approach has been to introduce a non-symmetric yield condition as was done, for example, by Freudenthal and Gou [70]. Non-symmetry was achieved by the inclusion of terms in the third stress invariant, J_3 defined by

$$J_3 = \frac{1}{3} t_{ij} t_{jk} t_{kl}$$

where

$$t_{mn} = (\sigma_{mn} - \alpha_{mn}) \quad (3.21)$$

introduces the Bauschinger phenomenon. Non analytic functions of the type by Freudenthal and Gou are very complex to deal with mathematically. Accordingly, Shrivastava [68,71] and Mroz [72] have proposed a non-symmetric but analytic yield function. In the general form, Shrivastava's formulation simply introduces non-symmetry in terms of J_3 as an additional term in Svensson's result given earlier in eqn. (3.19).

Generally, these work hardening laws are not necessarily predictive. However, once experimental measurements of certain parameters of the models have been made, then the models can display some of the features of observed behaviour. To illustrate this point, a brief survey of the experimental nature of subsequent yield surfaces is included in the next section.

3.2.4 Subsequent Yield Surfaces

Typically, the yield condition defines a convex surface in the stress space. All points inside the surface ($f(\sigma_{ij}) < 0$) represent conditions of elastic loading and unloading whereas the points on the surface represent the combinations of the stress components, σ_{ij} required to initiate further plastic flow if one or more of the stress components are increased. All variations of stresses prescribed on the yield surface result in neutral loading. If a material was previously overstrained beyond initial yielding into the plastic range by any method of loading, and then subsequently reloaded by the same or a different system of

stresses, the new yield point belongs to a different surface in the stress space. This surface always depicts the influence of the prestraining history in terms of:

- (a) isotropic work hardening by a uniform expansion,
- (b) anisotropy by means of distortions and rotations,
- (c) kinematic hardening (i.e. the BE) by translation, and,
- (d) the ability to accommodate second order effects.

At this point, it is worthwhile mentioning two other features relating to the shape of the yield surface which have received a great deal of attention in the literature. These are the development of corners on the yield surface and the so called cross effects. The latter refers to whether the maximum yield stress in a direction perpendicular to that of the prestrain is unaltered by the prestraining. On the other hand, corners describe singularities on the yield surface where the normality condition for the plastic strain increment is not always obeyed in terms of a unique outward pointing normal.

In the experimental determination of initial and subsequent yield surfaces, a minimum of two stress components are necessary. In his study of plastic stress - strain relations and subsequent yield surfaces in aluminum alloys, Ivey [73] used non-proportional combined tension and torsion loading of cylindrical thin walled tubes. Ivey's results, shown plotted in Fig. 3.2, have been used for a number of authors, notably, Balton and Sawczuk [67], Svensson [65] and Shrivastava [68] to compare with theoretical postulations. The data of Fig. 3.2 illustrates some of the work hardening processes discussed previously. Ivey's subsequent yield surfaces showed a pronounced BE and had translated outside the

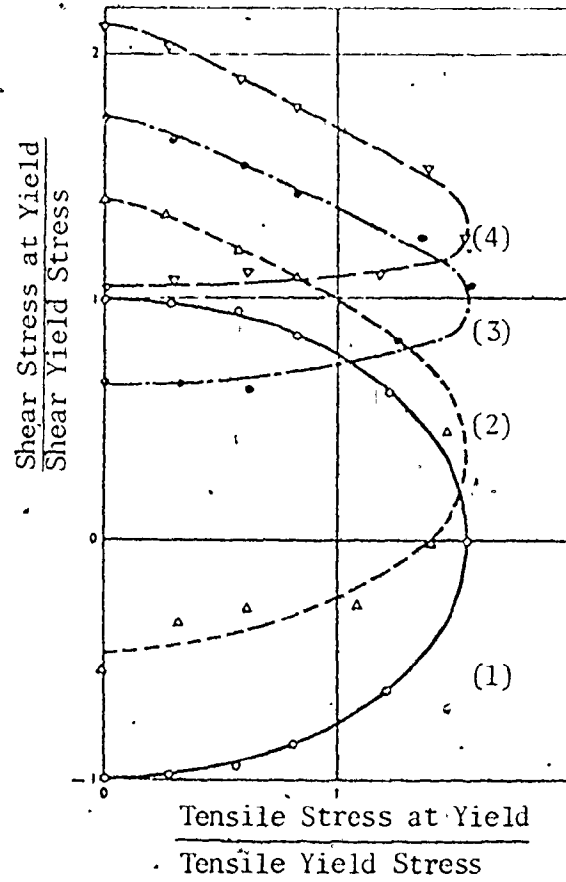
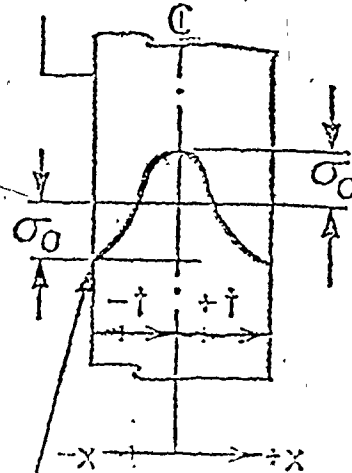


Fig. 3.2

Initial and subsequent yield surfaces of Al. (19S) alloy, Ivey [73].

- (1) Initial yield surface.
- (2) 1st subsequent yield surface.
- (3) 2nd subsequent yield surface
- (4) 3rd subsequent yield surface.

TEST PIECE



RESIDUAL STRESS DISTRIBUTION

Fig. 3.3

Macroscopic residual stress model of the Bauschinger Effect.

initial shear stress - tensile stress origin. The subsequent yield loci also appeared to have shrunk in size (negative expansion) and showed anisotropy in the form of distortions. Furthermore, no cross effects or distinct corners were observed with this alloy. In a recent article, Phillips and Wang [74] have proposed a work hardening rule which generalizes the lack of cross effect for any type of loading. The analytical model has been verified experimentally on commercially pure aluminum, oxygen free copper and brass. A large BE was also evident from the experimental data. However, as will be evident from the work in some of the references cited below, many materials do show the phenomenon referred to as cross effect. These observations therefore illustrate the difficulty involved in the problem of attempting to obtain a unified constitutive law for material behaviour.

Shiratori et al [75,76,77 and 78] have published a number of reports on the subsequent yield surfaces of annealed brass [75,76] and of annealed aluminum (17S) alloy [77,78]. In the work reported for annealed brass, the subsequent yield surfaces were also found to translate and distort, but at variance with Ivey's observations, sharp corners and cross effects were also observed. The corners were most pronounced in the general case of proportional preloading in the direction $\sigma_1/\sigma_2=1$; i.e. equal biaxial tension. A flattening of the surface on the diametrically opposite side to the prestress point was also reported indicating the non-symmetric nature (second order effect) of the yield surface. In the work reported in [77,78] for the aluminum alloy, similar results were obtained except that the corners degenerated virtually to a well rounded nose of high curvature. Williams and Svensson [79] also reported similar results to Shiratori's for thin walled tubes of 1100-F aluminum

alloy tested using non-proportional loading paths in combined tension - torsion - compression.

With respect to the BE, the observed translation of the subsequent yield surfaces shows the appropriateness of the kinematic hardening concept. Shiratori et al in [75] characterized the BE in terms of the yield surface translation by locating and measuring the displacements of the instantaneous centre of the yield locus from the original stress origin and showed that the BE increased monotonically to a saturation level with prestrain. However, it is not possible to unambiguously quantify the direction of translation in the published results on account of the anisotropic distortion and rotation of the yield surface. Attempts by Michno and Findley [80] to experimentally verify the Prager [56] (see eqn. (3.10)) and the Ziegler [58] (see eqn. (3.11)) kinematic hardening laws indicate that the translation of the subsequent yield surface, at least in SAE 1017 annealed carbon steel does not obey either model although the agreement was closer to the Ziegler than the Prager model.

In general, the kinematic hardening models discussed previously permit the macroscopic plasticity theory to allow for the BE in terms of a translation of yield surfaces. They differ in the interpretation of the coupling effect of the translation tensor, α_{ij} and the plastic strain components, ϵ_{ij}^p . The second order tensor, α_{ij} has been referred to in the literature as the residual stress or micro-stress tensor [70,71]. However, α_{ij} may represent some measure of internal stresses, but it does not purport to provide an insight as to the physical nature of the BE. It is instructive to consider some continuum and microscopic models of the BE at this stage in order to study the description of internal stresses in

both types of models. The continuum models utilize either an assumed distribution of macroscopic residual stresses in a test piece or a phenomenological interpretation of kinematic hardening. On the other hand, the microscopic model is based on the inhomogeneity of the plastic strain distribution in the material and the consequences in terms of internal stresses. The macroscopic models are first presented in what follows.

3.3 Phenomenological Models of the Bauschinger Effect

The purpose of this section is to present three phenomenological models of the BE derivable from the foregoing descriptions of work hardening continuum plasticity. In general, the treatment is limited to the observed forward and reverse flow behaviour in unidirectional straining. As noted previously, the plastic deformation of materials results in the development of internal stresses. These internal stresses arise from several sources. A relatively insignificant source of internal stresses is due to the inhomogeneous deformation of individual grains. More important, however, is the presence of second phase particles in the material. These particles interfere with the homogeneous deformation of the matrix and internal stresses are developed. The internal stresses may be modelled in the macroscopic sense by assuming a non uniform residual stress distribution in a test piece. For an exact analysis, a detailed knowledge of the residual stress distribution is necessary and this is clearly a very complex matter. On this account, the present models provide a simplified version which can at best, only show the gross characteristics of the behaviour of real materials. The

objective here is simply to show the type of results that can be obtained and how these results can be used to improve our understanding of the BE.

3.3.1 Model Based on Macroscopic Residual Stresses

A mathematical function can be used to describe the variation of residual stresses with distance across the test piece. Equilibrium is satisfied by ensuring that following uniaxial straining and unloading, the resultant residual stress distribution gives a zero axial load and bending moment. It is now proposed that the specimen is loaded in the reverse direction and the resulting stress-strain behaviour calculated on the basis of the superposition of the assumed residual stress distribution in a uniformly distributed applied stress field. It is further assumed that the normal stress-strain behaviour of the material is known and consequently, the objective here is to assess how this is modified by the residual stress.

In the unloaded state a function of the form,

$$\sigma = \sigma_0 \cos(\pi x/t) \quad (3.22)$$

is selected and this distribution is shown schematically in the diagram in Fig. 3.3. The parameter, σ_0 may be chosen as some fraction of the yield strength of the material recorded at the end of prestraining; x and t are defined in Fig. 3.5. The calculated stress-strain behaviour upon reverse loading for different values of σ_0 is given in Chapter 5 which deals with analytical and experimental results.

Friedel [81] has employed a statistical description of residual stresses which can also be used to study the BE. His model is mathe-

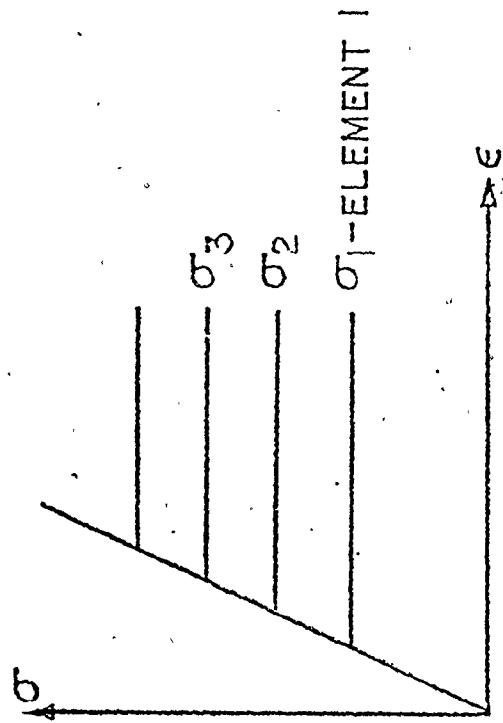
atically more complex and also requires a detailed knowledge of the residual stress distribution in order to provide anything more than a gross phenomenological behaviour.

3.3.2 The Masing Type Hardening Model

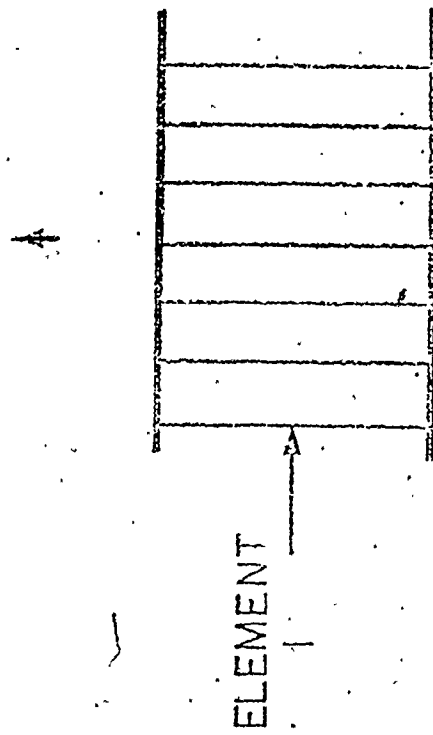
Masing's [23] view of polycrystalline deformation which has been discussed at length in a recent article by Asaro [82] envisaged a solid as composed of n geometrically identical elastic/plastic elements each having a different yield strength, $\sigma_1, \sigma_2, \dots, \sigma_n$ as shown in Fig. 3.4. The elements are connected in parallel and are elastic-perfectly plastic. On account of the differences in the yield strengths, during loading into the plastic range, some elements will become plastic while others are still elastic. The material behaviour is predicted by monitoring the yield points of the individual elements and the imposed strain. It is easy to see that during any plastic deformation process, each element will in general experience a different stress. Thus, after prestraining and unloading, a pattern of residual stresses will exist and some elements will be in tension while others will be in compression. These differences in the stresses borne by the individual elements cause the reverse stress-strain behaviour to display the BE in the manner calculated in Chapter 5. The calculations also include the case of elastic-linear work hardening elements.

3.3.3 Mroz's Kinematic Hardening Model

The model proposed by Mroz [60] departs from the direct residual stress representation of kinematic hardening and deals with the idea of a physical translation by assigning a field of work hardening moduli



(b)



(a)

Fig. 3.4 Material modeled by a parallel connection of elastic-non-hardening elements.

which can be approximated on the material $\sigma - \epsilon$ curve with n linear segments of constant tangent moduli, E_1, E_2, \dots, E_n as in Fig. 3.5(a). In the stress space, this behaviour can be represented by a series of hypersurfaces, f_0, f_1, \dots, f_n as in Fig. 3.5(b), where the interval between the surfaces defines regions of constant work hardening moduli. In the initial state which will be assumed isotropic for convenience all the surfaces enclose the stress-strain origin O . During prestraining, initial yielding is achieved by the stress point moving from O to reach the first yield surface at A' . This produces the elastic line OA in Fig. 3.5(a). Subsequently, with increased straining, this surface translates to meet the second surface at B' and the stress-strain increment in the interval is governed by the tangent modulus, E_1 . Upon meeting the second surface, both surfaces now translate together with a tangent modulus E_2 to meet the third surface at C' (see Fig. 3.5(c)) and this represents the domain BC in Fig. 3.5(a). The process of translation is carried on in this way for all the surfaces under consideration. An exact reversal of events occurs during unloading. The reverse loading curve, shown as $CDEF$ in Fig. 3.5(a), represents unloading from the stress state depicted by Fig. 3.5(c). The model, as just described, is in complete accord with the original proposal of Mroz [60] and it will be recognized that the same loading and unloading curves could be obtained using the model of the parallel connection of elastic - perfectly plastic elements described in Section 3.2.2.

With the above model, the shape of the reverse flow curve is exactly the same as that of the forward hardening curve apart from a scaling factor of two (see Chapter 5). It is now proposed to modify Mroz's original model in the following manner: during translation in

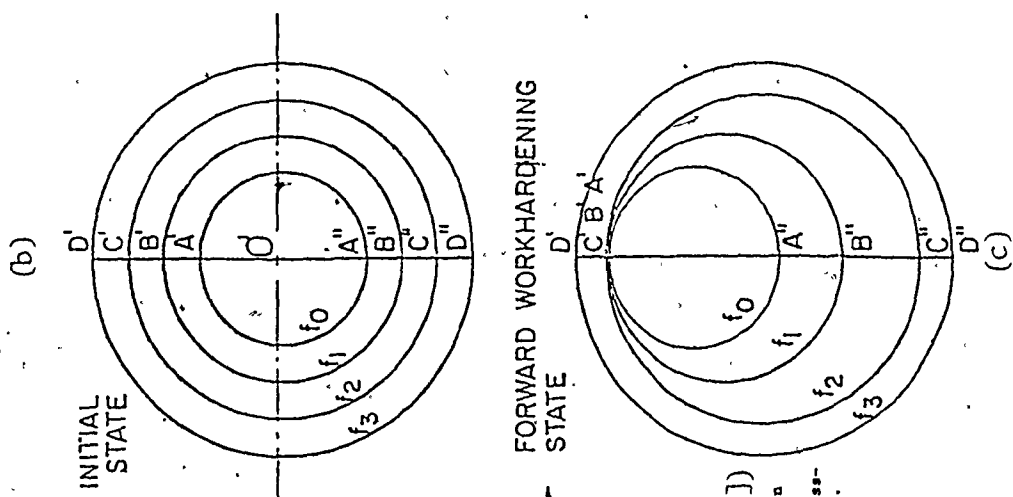
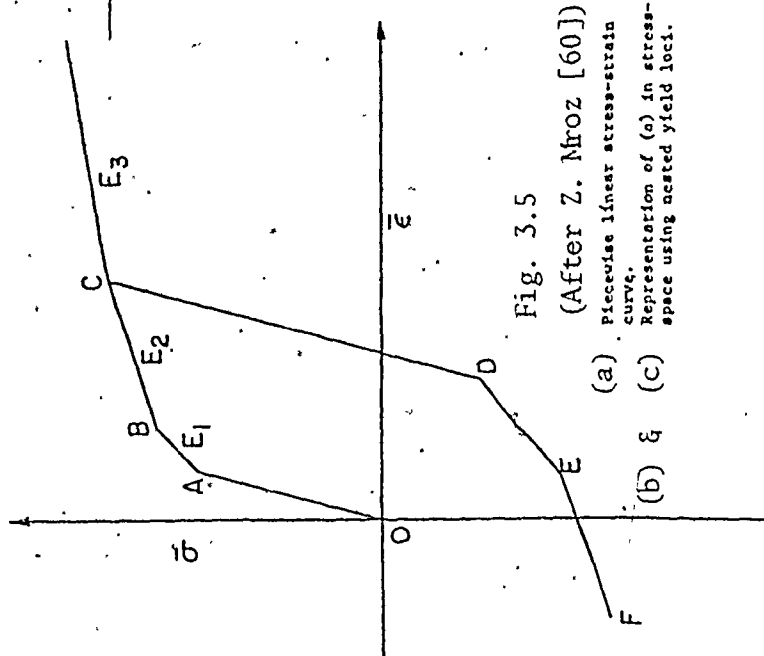


Fig. 3.5
(After Z. Mroz [60])
(a) Piecewise linear stress-strain curve.
(b) & (c) Representation of (a) in stress-space using nested yield loci.

(a)

forward loading, each surface is allowed to expand isotropically by the amount $m\Delta\sigma$ where $-1 < m < 1$, is a fraction of the stress increment $\Delta\sigma$ required to move the stress point from one surface to the other; the amount of translation in this case is $(1-m)\Delta\sigma$. This simulation of combined isotropic and kinematic hardening has considerable flexibility in that the combination parameter, m can be chosen to provide a close fit with experimental reverse flow data. The modification is compared with the original model of Mroz in the prediction of experimental behaviour in Chapter 5; some preliminary results have already been published in [83,84].

3.4 Microscopic Plasticity Models.

In Chapter 2, Section 2.3, the currently accepted cause of the BE was traced to the internal stresses produced by the microstructural incompatibility of strains particularly during the elastic/plastic deformation of two phase structures. The effect was found to be larger in materials containing second phase particles, especially of the incoherent type. This fact places direct accent on the influence of the volume fraction of these phases on material behaviour. In this section, the objectives are twofold:

- (i) to discuss some experimental observations of internal back stresses in more detail;
- (ii) to establish an analytical measure of the back stress using the microscopic model of Brown and Stobbs [85,86], and to derive and discuss the utility of the Bauschinger Effect Parameter, BEP (see eqn. (2.4)) as a measure of the BE.

3.4.1 Experimental Evidence of Back Stresses

The long range back stress theory has been developed over the years from experimental observations made on rather idealized model microstructures such as copper and aluminum single crystals strengthened with uniformly distributed precipitates of small particle sizes ($<500\text{\AA}$) and equally small volume fractions ($<1.0\%$), [85,86]. The application of these concepts to more complex systems such as steels containing not only cementite phases but also complex aggregates of precipitation strengtheners in the form of constituents of retained austenite and martensite is not well established. There is important evidence to suggest that the same concept of internal stresses is applicable in steels. In particular, the x-ray investigations of Wilson and Konnan [53] and the more recent studies of Anand and Gurland [54] indicate that a form of back stress hardening occurs in steels.

The X-ray investigations by Wilson and Konnan [53] appears to be the first direct evidence of residual lattice strains in two phase systems other than microscopic observations of high density dislocation tangles in the vicinity of particles [33,86,87,88]. In the work of ref. [53] two annealed carbon steels, 0.04% and 1.14% carbon, were tested in tension to different prestrains. Subsequent X-ray measurements of the residual transverse and longitudinal lattice strains in the unloaded specimens established clearly that compressive internal stresses were left in the ferrite matrix and that these were balanced by tensile stresses in the cementite particles. In a subsequent publication [51], Wilson showed that the average back stress, $\langle \tau \rangle_{\text{III}}$ calculated from the measured lattice strains was proportional to experimental estimates of

permanent softening, $\Delta\tau_p$ as follows;

$$\langle\tau\rangle_m = 0.53 \Delta\tau_p \quad (3.23)$$

The magnitude of $\Delta\tau_p$ was established in accordance with Orowan's [30] theory that following prestraining the back stress hardening must be removed by reverse plastic deformation prior to the creation of a new pattern of back stresses in reverse flow. Orowan had estimated that beyond a characteristic reverse strain, termed ϵ_n of 1-3%, the back stresses created during forward straining would be annihilated and a prominent permanent softening would result. Consequently, Wilson estimated $\Delta\tau_p$ at the reverse strains, ϵ_n given below at which x-ray measurements indicated zero lattice strains;

- (a) $\epsilon_n \approx 1.6\%$ in single phase materials;
- (b) $\epsilon_n \approx 3\%$ in spheroidized steel (0.74 and 1.14%C);
- (c) $\epsilon_n \approx 4.7\%$ in 0.74%C pearlite steel.

Moreover, in general, the contribution from back stress hardening was found to behave as follows:

- (a) to increase with the volume fraction of precipitates;
- (b) to increase with the incoherence of the precipitates;
- (c) to be weakly dependent on the size of the particles.

Wilson's work provided the important evidence of the development of internal stresses during plastic deformation and the consequence of the mean effect of these stresses on the reverse deformation behaviour. As will be seen in Section 3.4.2 below, the relationship in eqn. (3.23) derived from Wilson's results enables a more quantitative view of the back stress contribution to work hardening to be taken in the study of

reversible plasticity.

3.4.2 The Theoretical Derivation of the Mean Matrix Stress

In equation (3.23), $\langle \tau \rangle_m$ in shear or $\langle \sigma \rangle_m$ in uniaxial straining represents a quasi-uniform back stress developed on account of the inhomogeneous microscopic plasticity of the material. From hereon, the term mean "matrix stress" will be used in place of "back stress" because it connotes the long range nature of a stress which is felt by the complete plastic volume. Up till now, the term back stress was appropriate in terms of the localized interactions of dislocations with internal structural obstacles.

In order to derive an analytical expression for the mean matrix stress, $\langle \sigma \rangle_m$, it appears appropriate to start the discussion with two of the papers by Brown and Stobbs [85,86] on work hardening in copper-silica (Cu-SiO₂). The copper-silica system was taken as a model of the general class of dispersion hardened two phase alloys in which one phase, the SiO₂ particles can only deform elastically while the surrounding matrix of copper is plastically deformable. Using a previous model by Eshelby [89], they first sought the solution to the problem of calculating the resultant stresses in a finite body containing a volume fraction, V_f of spherical particles of radius, r_0 after a uniform shear strain, ϵ_p has been imposed [85]. The distribution of stresses inside and outside the particles was first calculated for an infinite medium. Then, an imaginary finite specimen was removed from this body in order to show the effect of external stress free surfaces. The calculations gave the following expression for the mean matrix stress;

$$\langle \sigma \rangle_m = 2\gamma\mu V_f \epsilon_p \quad (3.24)$$

where γ is Eshelby's [89] accommodation factor for the shape of the particles and μ is the elastic shear modulus of the matrix. Equation (3.24) defines the mean value of a quasi-uniform stress. The resultant of all stresses in the system is of course zero, otherwise external tractions would exist. This means that in the equilibrium state, the stresses inside the particles, $\langle \sigma \rangle_I$ are balanced by the mean matrix stress, $\langle \sigma \rangle_m$ such that;

$$\langle \sigma \rangle_I \cdot V_f + \langle \sigma \rangle_m \cdot (1 - V_f) = 0 \quad (3.25)$$

The theory does not quantify the short range internal stresses discussed in Chapter 2, Section 2.3 in a similar way but this is no drawback as these stresses possibly contribute to the BE only in the transient initial reverse flow behaviour. The mean matrix stress, on the other hand, is averaged over the entire plastic volume and being long range in nature is relatively insensitive to fine dislocation - particle details such as the size, distribution and spacing. This property is viewed as an asset in that it makes it possible to generalize the model to the more complex microstructures studied here. Furthermore, the stress, $\langle \sigma \rangle_m$ acts to increase the resistance to plastic flow in the direction in which it was originally generated but aids plastic flow in the opposite sense. On this account, it provides the greatest contribution to the BE and is eventually measurable as permanent softening. With reference to Section 2.2.3, eqn. (2.8), i.e. the work of Atkinson et al [52] and to Wilson's X-ray results in eqn. (3.23), the mean matrix stress can be related to permanent softening, $\Delta \sigma_p$ by

$$\langle \sigma \rangle_m = \frac{1}{2} \Delta \sigma_p \quad (3.26)$$

In effect, the model of internal stresses described by eqn. (3.24) is unrelaxed. If no plastic relaxation occurs around the particles i.e. no dislocation cross slip to secondary systems or climb, then the elastic stresses in the second phase particles are a precise record or a perfect memory of the imposed plastic deformation. This is clearly not possible in real materials except at very small plastic strains since in the unloaded state, the particles would then be subjected to strains of the order of the imposed plastic strains. In two other papers [86, 92], Brown and Stobbs carried out microscopic examination of their deformed Cu-SiO₂ alloy and observed the formation of secondary dislocations in addition to primary ones. The secondary dislocations were attributed to plastic relaxation processes in the neighbourhood of the particles. A detailed consideration of the dislocation relaxation processes led them to derive the relationship between the amount of the unrelaxed strain, ϵ_p^* which still persists in the structure and the imposed plastic prestrain, ϵ_p in the form [86],

$$\epsilon_p^* = \alpha \left(\frac{8|b|\epsilon_p}{\pi r_0} \right)^{1/2} \quad (3.27)$$

where b is the Burger's vector and $\frac{1}{3} < \alpha < \frac{1}{5}$ is a constant governing the strength of the hardening produced by the forest of dislocation tangles at the particles. Equation (3.24) can now be corrected to include the unrelaxed strain ϵ_p^* in place of ϵ_p . Moreover, a correction for the differences between the elastic constants of the matrix, μ and the particles, μ^* can also be introduced so that:

$$\text{and } \langle \sigma \rangle_m = 2\gamma\mu\mu^* V_f \epsilon_p^* \quad (3.28)$$

$$\mu = \mu^* / [\mu^* - \gamma(\mu^* - \mu)]$$

where μ' is the modulus correction factor. Equation (3.28) is the final form of the mean matrix stress and with reference to the relationship in (3.26) provides an estimate for the experimental measurements of permanent softening.

The relationship in eqn. (3.28) can also be corroborated using a mechanical model of elastic-plastic two phase deformation similar in form to the Masing type model in section 3.3.2. In Fig. 3.6, an "elastic" element is welded to a "plastic" element both of elastic modulus, E . No interfacial slip along the weld can occur and the volume fraction of the elastic phase is V_f . The system is now deformed in tension.

Initially, both elements deform elastically with a modulus, E and when the applied stress exceeds the yield stress, σ_0 , the plastic element yields. Following yielding at the point A, this element is considered perfectly plastic and so contributes no further resistance to forward plastic flow. Since only the elastic element now provides all the resistance to flow, the slope of the stress-strain curve is reduced to EV_f from the value E . Upon unloading, the stress applied up to the point B acts as a friction stress and reverse flow commences at C along CD after the applied stress has been reduced by $2\sigma_0$. The stress increment from the point A to B is given by the slope multiplied by the imposed plastic strain, ϵ_p as $EV_f \cdot \epsilon_p$. This increment of stress is completely due to the presence of an elastic phase in a plastically deforming material. If the same allowance as before is made for the particle shape accommodation factor, γ , the modulus correction factor μ' and for the unrelaxed strain, ϵ_p^* , the result in equation (3.28) is

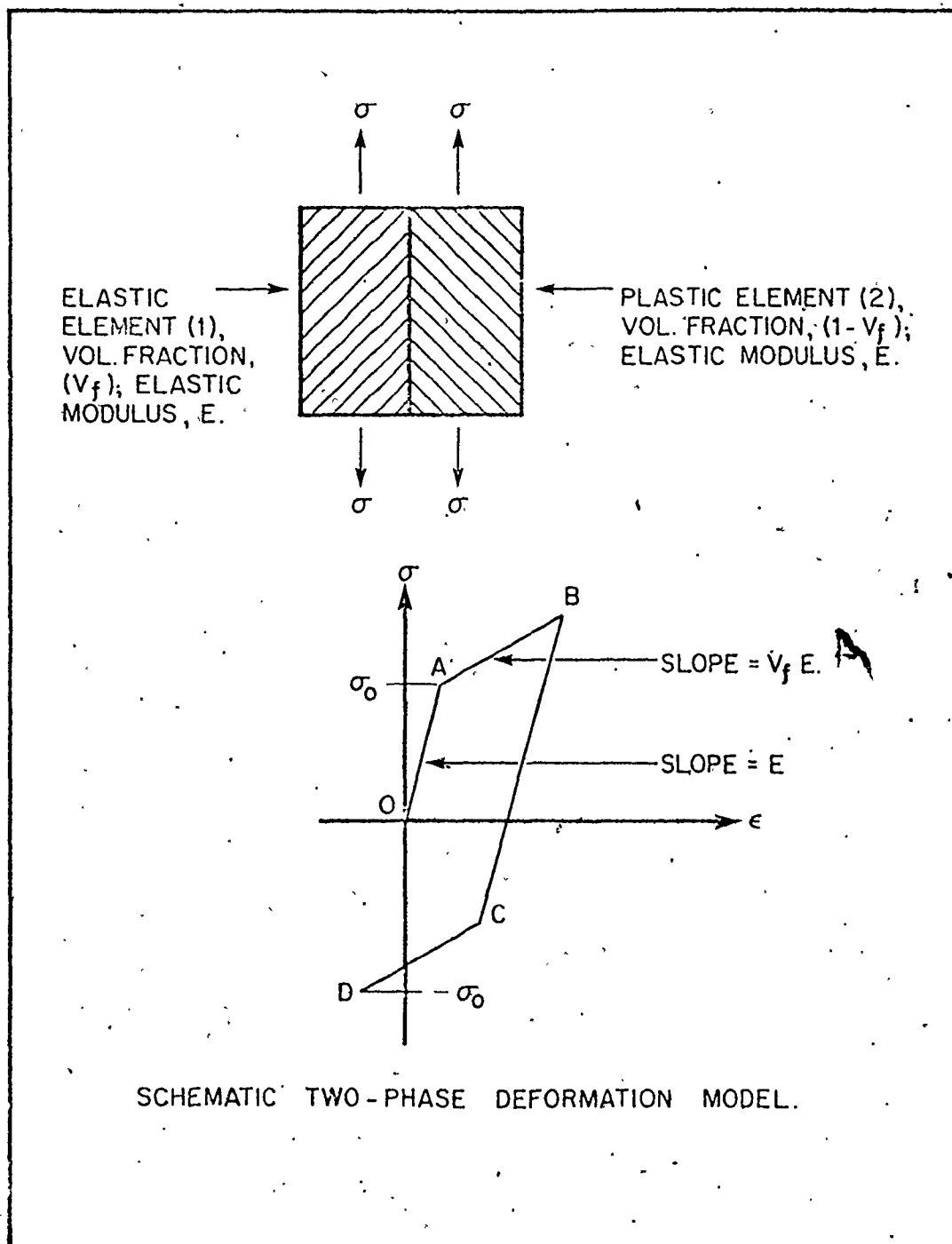


Fig. 3.6

again arrived at.

The mathematics is quite simple. The flow stress, σ , in tension beyond the point A is given by the sum of the stresses σ_0 in the plastic element and σ_1 in the elastic element, with both stresses acting in their respective volume fractions, as

$$\begin{aligned}\sigma &= \sigma_0(1-V_f) + \sigma_1(V_f) \\ &= E \epsilon_0(1-V_f) + E(\epsilon_0 + \epsilon_p)V_f\end{aligned}$$

where ϵ_0 is the elastic limiting strain and ϵ_p is the plastic strain measured in the domain A to B. Therefore, the stress increment, $\Delta\sigma$, over AB is

$$\Delta\sigma = (\sigma - E\epsilon_0) = EV_f\epsilon_p$$

Introducing γ , μ , and ϵ_p^* , this result may be written in terms of the mean matrix stress as

$$\langle\sigma\rangle_m = 2\gamma\mu V_f\epsilon_p^* \quad (3.28)$$

where $\mu = E/2$ is assumed.

Considerable attention has so far been paid to eqn. (3.28) as a measure of the level of microstructural incompatibility responsible for the internal stresses, and therefore the BE. The problem now is to study the development and the magnitude of the unrelaxed strain and its relationship to experimental values of permanent softening. This problem has, of course, received some treatment in the literature [28,52,90,91]. In [52,90] dispersion hardened single crystals of copper silica were studied. In [28] a commercial grade aluminum alloy was used while in the more recent work by Lloyd [90], polycrystals of Al-Ni and

Al-Ca were used. The particle sizes and volume fractions studied were very small compared to what is usual in structural steels. The microstructures were also carefully prepared using annealing heat treatments.

The present study is significant from the point of view of its departure from the above limitations in terms of the type, size and volume fraction of the second phases. A broad spectrum of structural steels is studied in order to generalize the observations made on these "model" microstructures to more common engineering materials. In line with the objectives of this work stated earlier, the development of the unrelaxed strain, vis à vis, the mean matrix stress with increasing plastic strain will be determined for spheroidized plain carbon steels and HSLA steels in order to provide an understanding of the BE from the point of view of its natural causes.

3.4.3 The Bauschinger Effect Parameter

It is now possible to write the complete equation for the flow stress of a material using completely metallurgical considerations. Following the method of Brown and Stobbs [86], the flow stress is the sum of three terms:-

- (a) the initial yield stress, σ_0 , known to metallurgists as the Orowan Stress;
- (b) the forest hardening stress, σ_{for} due to the localized accumulation of dislocations at the particles; this term always has a positive hardening effect in any sense of loading, and
- (c) the mean matrix stress, $\langle \sigma \rangle_m$ which is polarized to aid reverse flow.

The total forward flow stress, σ_f , is given by a scalar addition of the various terms in the form;

$$\sigma_f = \sigma_o + \sigma_{for} + \langle \sigma \rangle_m, \quad (3.29)$$

or in the complete analytical form by Brown and Stobbs [86] as;

$$\sigma_f = \sigma_o + \sqrt{3} \alpha \mu V_f^{1/2} \left(\frac{8b\epsilon_p}{\pi r_o} \right)^{1/2} + \left(\frac{8\pi b}{2 r_o \epsilon_p} \right)^{1/8} \cdot \alpha \mu V_f \left(\frac{8b\epsilon_p}{\pi r_o} \right)^{1/2} \quad (3.30)$$

where all the parameters have been previously defined. A suitable abbreviation of eqn. (3.30) is given by;

$$\sigma_f = \sigma_o + A \mu V_f^{1/2} \left[\frac{b\epsilon_p}{r_o} \right]^{1/2} + B \mu V_f \left[\frac{b\epsilon_p}{r_o} \right]^{1/2} \quad (3.31)$$

where the coefficients A and B depend on the particle shape. Following from eqns. (3.29) and (3.26), it is proposed to define a BE parameter, BEP as:

$$BEP = \frac{2\langle \sigma \rangle_m}{(\sigma_f - \sigma_o)} = \frac{\Delta \sigma_p}{(\sigma_f - \sigma_o)} \quad (3.32)$$

which is theoretically independent of the forward prestrain, ϵ_p . Inverting eqn. (3.32) and using (3.31) provides

$$\frac{(\sigma_f - \sigma_o)}{\Delta \sigma_p} = C_1 + C_2 V_f^{-1/2} \quad (3.33)$$

where $C_1 = .5$ and $C_2 = .62$ are theoretical estimates in the case of spherical particles. It also follows from a comparison of eqns. (3.29) and (3.31) that the mean matrix stress is related, in general, to the prestrain by;

$$\langle \sigma \rangle_m = \alpha_1 \sqrt{\epsilon_p}$$

Using the relationship in eqn. (3.26), then

$$\frac{1}{2} \Delta\sigma_p = \alpha_1 \sqrt{\epsilon_p} \quad (3.34)$$

The above discussion has led to the important relationships (3.32) and (3.33) which show that the BE measured in terms of the ratio permanent softening to the total work hardening in forward flow is insensitive to the prestrain but depends on the volume fraction, V_f , of the second phase particles in the material. The relation, (3.32) provides a measure of the BE in terms of its fundamental cause, that is, the effect of internal stresses measured by the mean matrix stress, $\langle\sigma\rangle_m$ or by the permanent softening, $\Delta\sigma_p$. Furthermore, this relation also involves the combined work hardening increment from all sources in the term $(\sigma_f - \sigma_o)$.

It is instructive, at this stage, to discuss an alternative descriptive definition of the Bauschinger Effect Parameter following the method of Ibrahim and Embury [9]. These authors derived the BEP from eqn. (3.29) in terms of the reverse yield strength σ_r , as:

$$(\text{BEP})^{*+} = \frac{\sigma_f - \sigma_r}{\sigma_f - \sigma_o} \quad (3.35)$$

In verifying the effects of prestrain and volume fraction on eqn. (3.35) experimentally, one needs a consistent measure of the stresses, σ_o and σ_r . Usually, on account of the often rounded nature of stress-strain curves, σ_o and σ_r are determined by an offset strain method. In the approach employed by Ibrahim and Embury, σ_r was determined by back extrapolation to the elastic line from some quasi-linear domain of the

+ The symbol (*) is used to denote the empirical nature of (3.35) compared to the theoretical BEP in (3.32).

plastic portion of the reverse flow curve. Only under special circumstances will the term $(\sigma_f - \sigma_r)$ obtained in this manner be equal to the permanent softening, $\Delta\sigma_p$. One example is the case of linear monotonic and reverse plastic flow curves. Equation (3.35) is, therefore, basically different from (3.32) derived from the Brown and Stobbs [86] model of work hardening in two phase alloys in the terms $(\sigma_f - \sigma_r)$ and $\Delta\sigma_p$. As implied earlier, the two models coincide if $(\sigma_f - \sigma_r) = \Delta\sigma_p$, but this is not generally true. However, it is shown in ref. [9] that eqn. (3.35) was independent of prestrain, as determined by forward and reverse flow tests on Armco Iron and zone refined niobium, both single phase b.c.c. metals. Some preliminary work by Filipovic [11] reports similar findings in an HSLA steel. More recently, Lloyd [90] studied the BE in very fine grained aluminum alloys containing a particle dispersion and measured both permanent softening, $\Delta\sigma_p$ in the manner indicated in Fig. 2.1 and the quantity $[(\sigma_f - \sigma_r(.2\%))]$ where $\sigma_r(.2\%)$ is the .2% reverse proof stress. A comparison of the two results showed that although the overall variation of the quantities $\Delta\sigma_p$ and $[\sigma_f - \sigma_r(.2\%)]$ with prestrain was similar, as expected, the latter method gave much larger estimates of the back stresses.

Equations (3.32) and (3.35) are quantitatively studied in this thesis. Where necessary, σ_o and σ_r are determined as proof stresses. This method allows for a comparison to be made of the parameter, $BEP^* = (\sigma_f - \sigma_r) / (\sigma_f - \sigma_o)$ over a wide domain of the reverse $\sigma - \epsilon$ curve. The variation of the BEP^* with prestrain is studied with $(\sigma_f - \sigma_r)$ measured at $\sigma_r = .1, .2$ and $.5\%$ proof stresses, and at the instant when the reverse plastic deformation is sufficiently large to enable the

measurement of the quantity $(\sigma_f - \sigma_r)$ as the permanent softening, $\Delta\sigma_p$, in the manner shown in Fig. 2.1.

3.5 Summary

This chapter has dealt with the theoretical models of the BE based on:-

- (i) Continuum plasticity including three simple models that provide a phenomenological description of the BE in uniaxial loading, and
- (ii) the microscopic model due to Brown and Stobbs which permits a quantitative view to be taken of certain aspects of the BE.

The particular aspects of these models which are studied in the thesis can be summarized as follows:-

- (a) The residual stress model: the intention here is simply to show that the origin of the BE can, at least in part, be attributed to microscopic residual stresses.
- (b) The Masing type hardening model: this is a phenomenological simulation of the deformation of two phase materials. The BE as shown by this model is also attributable to residual stresses.
- (c) Mroz's model and its modification: this model predicts the BE on the basis of kinematic hardening and is modified as part of the work in this thesis to include isotropic work hardening.
- (d) The microscopic model of Brown and Stobbs: the analytical form for the mean matrix stress derived from this model was corroborated with the results from a simple continuum model. Permanent softening has been shown to relate to the mean effect of internal stresses. These, in turn, are dependent upon the extent of prestraining and the volume fraction of second phase particles. In the results to be reported in

Chapter 5, equations (3.32) - (3.35) are first studied experimentally. Then equation (3.28) is used in conjunction with eqn. (3.26) to determine the unrelaxed strains and to study the dependence on the pre-strains.

Overiewing the theoretical continuum plasticity models of work hardening, it is clearly difficult to provide a unified theory for complex loading histories which take into account the translation, distortion and expansion of the yield surface and which can accommodate second order and cross effects. In practice, simple models which provide a phenomenological description of material behaviour are usually employed, at least to describe observed behaviours in uniaxial loading. With particular reference to the BE, both macroscopic and microscopic types of models have been presented in this chapter. The results obtained from these studies are examined in Chapter 5. In Chapter 4 which follows from here, the materials used in this work and the types of experiments performed are described.

S

CHAPTER IV

MATERIALS AND EXPERIMENTATION

4.1 Introduction

The chapter commences with a brief description of the metallurgical nature of the three classes of experimental steels. These were:-

- (i) Spheroidized plain carbon steels,
- (ii) Controlled (hot) rolled HSLA steels,
- (iii) Dual phase HSLA steels.

Then follows an account of the preliminary studies undertaken to classify the experimental materials in terms of mechanical properties. Details are then provided of the development of a reliable test device for tension-compression tests. The chapter concludes with the description of the experiments that were performed on the different materials in order to ascertain whether they displayed a number of characteristics that are collectively described in terms of the Bauschinger Effect.

4.2. Experimental Materials and Metallography

4.2.1 Plain Carbon Steels

The plain carbon steels used in this work were of the conventional carbon-manganese type, heat treatable to produce simple well characterised mixtures of ferrite and spheres of cementite. Four such steels, 1015, 1035, 1045 and 1095 were selected for this study. The steels were supplied in the form of $\frac{1}{2}$ " (13 mm) diameter cold drawn bars

and are characterised by the weight-percentage of their carbon contents. Table 4.1 provides a listing of the four plain carbon steels, their mechanical properties and their volume fraction of carbide content calculated from the chemistry.

In order to utilize the plain carbon steels as model materials, they were tested in the spheroidized condition. Spheroidization was achieved by austenitization at 900°C for 1 hr. followed by quenching in oil, tempering for various times at 700°C and furnace cooling to room temperature. The tempering times were varied for the different materials as shown in Table 4.2; the average particle diameter of the spheroidized carbides are also given. Optical micrographs of the as-received and spheroidized structures of the 1015 steel are shown in Fig. 4.1; picral was used as the etchant in order to reveal the carbides. Hereafter in this thesis the plain carbon steels will be referred to simply as spheroidized steels.

4.2.2 Controlled Rolled HSLA Steels

The structure and processing of high-strength-low-alloy (HSLA) steels are considerably more complex than those of the simple Fe-Fe₃C system of the spheroidized steels. The discussion here will therefore deal with the specific metallurgical features of the HSLA steels which have direct relevance to the BE. However, for completeness a brief review covering such areas as the technology of hot roll processing and the applications of HSLA steels is included in Appendix A of the thesis.

HSLA steels in general contain various small amounts of micro-alloying elements such as molybdenum, vanadium and columbium. The role of these elements is to promote grain refinement and a combination of

solid solution and precipitation strengthening of the final structure. In commercial production, controlled rolling above the austenite transformation temperature followed by accelerated cooling are used to produce a fine grained structure. However, the morphology of the ferrite may be either equiaxed or acicular in form. Equally important is the presence of a complicated distribution of non ferrite phases consisting of mixtures of straight carbides, precipitation carbides and carbonitrides of the microalloying elements and aggregates of martensite or retained austenite (M/A) islands. These constituents vary with the thermal history of processing and chemical compositions, and may be viewed as playing essentially the same role as the cementite spheroids in the heat treated plain carbon steels. The total volume fraction of these non ferritic phases is an important input parameter in models dealing with the BE. However, it is not certain what proportions of these particles constitute an effective distribution of hard non deformable phases relative to the softer ferrite matrix. The role of these impenetrable obstacles to dislocation motion during plastic deformation and the resultant development of short range and long range stresses were discussed at length in Chapter 2. The HSLA steels are obviously more complex in terms of their microstructure and in order to analyze their mechanical behaviour, it will be assumed that the total amount of the non ferritic material behave as isolated islands of non-deforming phases. This is an important assumption and one which to date has no unambiguous physical verification.

Figs. 4.2 (a), (b) and (c) show the optical micrographs of the three HSLA steels used in this study. Picral was again used as the

TABLE 4.1

Mechanical Properties and Volume Fractions of the
Plain Carbon Steels

Steel	Carbon (%)	Yield Strength ksi, (MPa)	Vol. Fraction of Fe ₃ C(%)	Average Y.P.E. (%) *
1015	.15	37.5 (258.6)	1.94	2.8
1035	.35	50.7 (349.6)	5.68	2.0
1045	.45	53.3 (367.5)	7.83	1.8
1095	.95	64.3 (443.3)	16.91	1.2

* Y.P.E. - Yield point elongation

TABLE 4.2

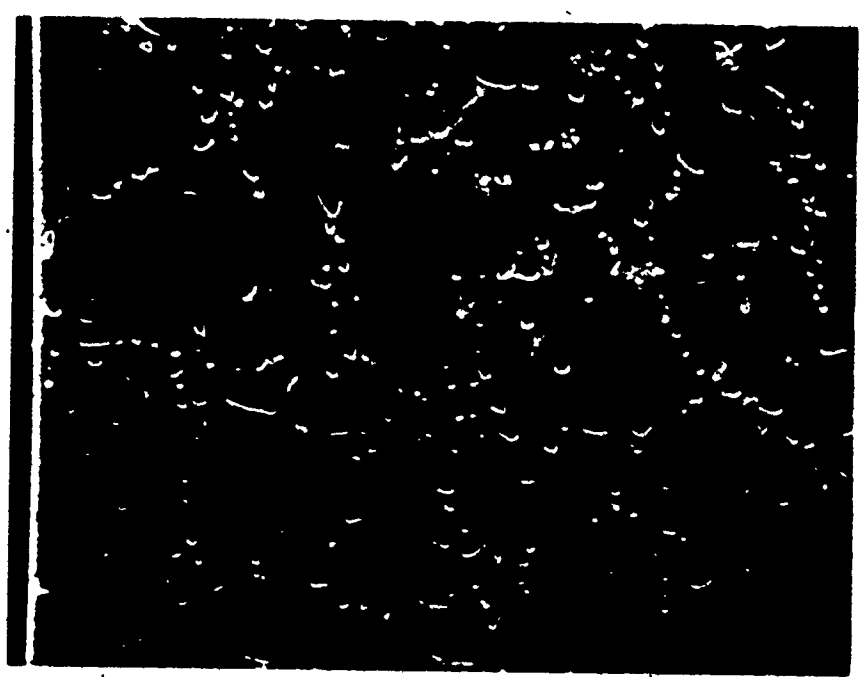
Spheroidization Tempering Schedule

Steel	Tempering time (Hrs.) at 700°C	Average Particle Dia. (µm)
1015	82	.84
1035	48	.89
1045	34	.70
1095	17	.72



(a)
As received
X600

Fig. 4.1 Optical micrographs of SAE 1015 compared in the as received and spheroidized conditions.



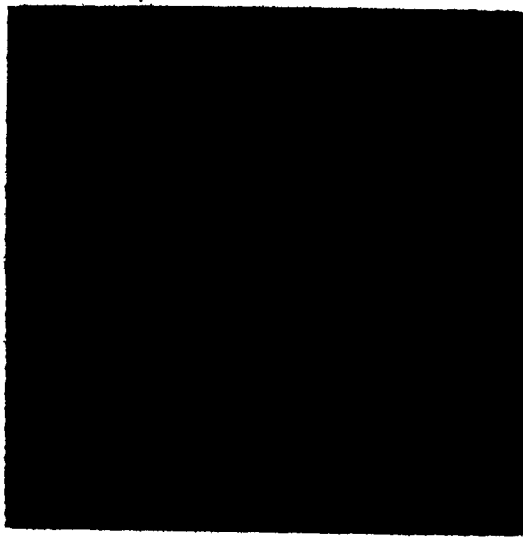
(b)
Spheroidized
X1250



Longitudinal Section,
X320.



Transverse Section,
X320.



Short Transverse,
Section, X320.

Fig. 4.2(a) Optical micrographs of the HSLA steel-A.

etchant to reveal the carbides. In each set of the figures, three separate views are shown, and these are:-

- (i) the longitudinal view containing the rolling and through thickness directions;
- (ii) the transverse view containing the transverse rolling direction and the through thickness direction;
- (iii) the short transverse view containing the rolling and the transverse rolling directions.

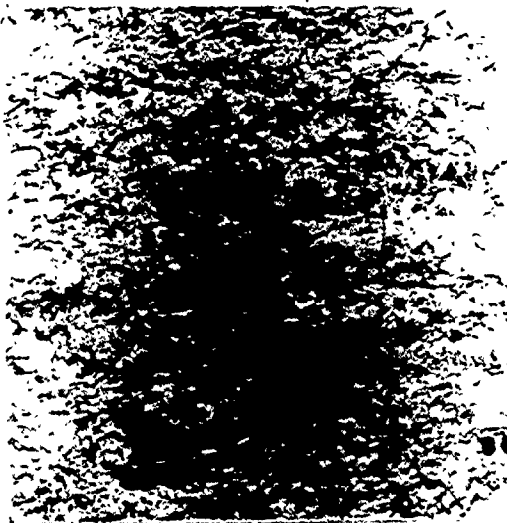
The grain structure is largely polygonal in the three steels, though some acicularity is apparent in HSLA-A. A high level of microstructural banding parallel to the rolling plane may also be seen in the HSLA-C. The three views described above are necessary due to the anisotropy introduced by the hot rolling process.

It is also observed here that the ferrite grain sizes appear to increase in the order HSLA-A-B-C. Moreover, the HSLA-B clearly has the minimum quantity of carbides and M/A islands of second phases.

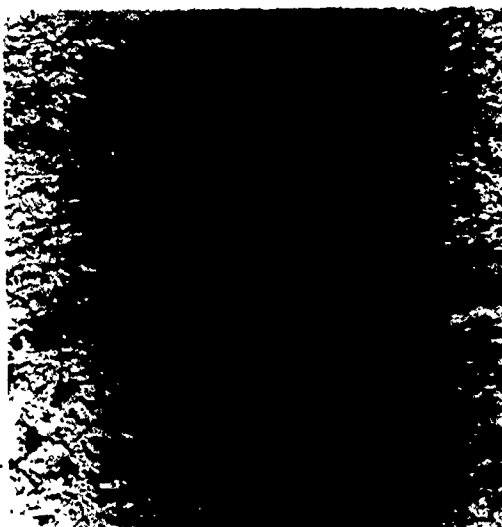
The thermal history of the controlled rolling practice used to manufacture the HSLA steels is provided in Table 4.3, and the chemical compositions in Table 4.4. Using Table 4.3, it is clear that the hot rolling practice is not significantly different in the three HSLA steels. Using Table 4.4, it is possible to argue that the combined influence of the presence of vanadium and a higher carbon content in the HSLA-C is responsible for the gross differences between the microstructural features of the HSLA-C steel and the other two steels.

The metallographical studies on the HSLA steels were limited to the qualitative analysis of the structure and to the determination of the

Longitudinal
Section, X520



Transverse
Section, X520



Short Transverse
Section, X520

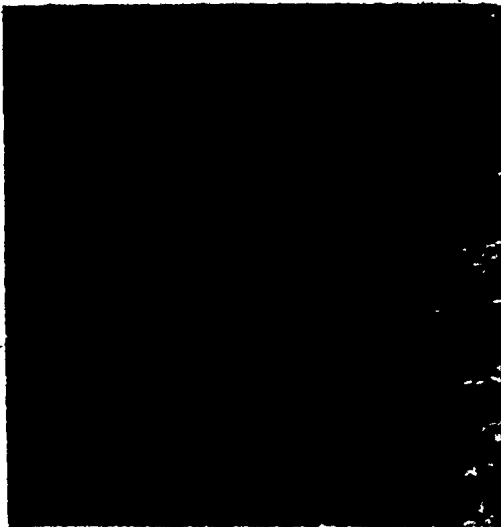


Fig. 4.2(b) Optical micrographs of the HSLA steel-B.



Longitudinal
Section, X520



Transverse
Section, X520



Short Transverse
Section, X520

Fig. 4.2(c) Optical micrographs of the HSLA steel-C.

TABLE 4.3

Rolling Practice for the HSLA Steels *

HSLA	Reheat Temp °F (°C)	Controlled Rolling Temp. < °F (°C)	Finish Rolling Temp. °F (°C)
A	2150 (1177)	1475 (802)	1360 (738)
B	2150 (1177)	1475 (802)	1370 (743)
C	2150 (1177)	1470 (799)	1380 (749)

* As received plate dimensions:

25" (635 mm) wide x 48" (1220 mm) long x 3/4" (19 mm) thick.

TABLE 4.4

Chemical Composition of HSLA and Dual Phase Steels

HSLA	C	Mn	Si	Ni	Mo	Cb	S	Cu	V	P	Al	*V _f (%)
A	.06	1.88	.27	.25	.42	.07	.008	-	-	-	-	8.0
B	.06	1.76	.25	-	.44	.056	.009	-	-	-	-	4.46
C	.09	1.56	.28	.24	-	.06	.007	.24	.08	-	-	13.2
DUAL PHASE												
D	.12	1.6	.20	-	.13	.028	.005	-	.08	.01	.048	-
E	.04	2.0	.27	-	.495	.05	.006	-	-	.013	.054	-

*V_f - Micrographic total volume fraction of non ferritic phases.

amount of non ferritic transformation products present. While the exact type and morphology of these products are unknown, an attempt was however made to determine the volume fraction of these constituents as the average ratio of the intercept lengths with the carbide areas to the lengths of ten random lines drawn on the micrographs [93]. The approximate average volume fractions calculated in the above manner are included in Table 4.4. These results will be compared in chapter 5 with alternative values obtained indirectly by interpolation. It is important to note here that the total volume fractions of the carbides and the M/A constituents are important in as much as they provide a measure of the proportion of the non deforming material present.

4.2.3 Dual Phase HSLA Steels

The dual phase steels are relatively newer types of HSLA steels. No comprehensive review of the dual phase steels exist currently in the literature. Using the work of Rashid [94] as a basis, the dual phase steels are known to contain higher volume fractions of retained austenite and martensite in addition to a precipitation hardened matrix derived from specific chemical compositions and thermal treatments of the as rolled HSLA steel in the ferrite-austenite (α - γ) transformation temperature range.

The major attraction of these materials is that they exhibit a rounded stress-strain curve with a rapid initial work hardening rate such that the increase in strength during conventional cold forming processes spans a much wider stress range than is typical in a chemically comparable conventional HSLA steel:

It is apparent that these properties can also be achieved by conventional hot rolling, however, intercritical annealing in the two phase ($\alpha+\gamma$) region of the iron-carbon diagram followed by air cooling to room temperature was used in the experimental program by Rashid [94]. In a recent review on the potential of the dual phase steel GM980X developed in General Motors for automotive applications, Rashid [95] attributes the high ductility and the increased work hardening capacity to the presence of about 10-20% volume fraction of M/A constituents and a redistribution of precipitates in the ferrite. The martensitic phases firstly introduce high dislocation densities thus providing an abundance of mobile dislocations to aid plastic flow. Secondly, microscopic internal stresses due to the volume change accompanying the formation of martensite also aids work hardening. Finally, it was speculated that the dissolution of the precipitation hardening constituents in the ferrite was responsible for the elimination of some of the dislocation barriers to initial yielding resulting in a lower yield strength in the dual phase GM980X.

Clearly, as with the conventional HSLA steels, the nature of the non ferritic transformation products is very complex and depends on the chemistry and the thermal history of processing. Thus, even if the total volume fraction of these phases can be determined, it is not unambiguously proven that the total amount of these constituents behave as hard and non deformable particles in models dealing with heterogeneous microplasticity.

The selection of dual phase steels for a part of this study was

to briefly examine whether on account of the high work hardening capacity, the reverse flow behaviour was significantly different from that of the HSLA steels. This aspect is important in regard to the utilization of dual phase steels in both fabrication operations and service conditions which involve reverse strain cycles. Table 4.4 also gives the chemical compositions of two of the dual phase steels used in this study. Steel D has a polygonal structure whereas the dual phase steel E has an acicular ferrite structure [96].

4.3 Preliminary Experimental Studies

As mentioned earlier, one of the important group of materials in this work was the three HSLA steels. In order to classify these steels, an extensive experimental programme to determine their mechanical properties was carried out. The steels were supplied as hot rolled in plate form: 3/4" (19 mm) thick, 25" (635 mm) wide and 48" (1220 mm) long.

Flat tensile specimens of nominal dimensions 3/8" (9.5 mm) x 3/16" (4.8 mm) machined from the 0°, the 45° and the 90° directions relative to the direction of rolling of the plates were used in the tests. The gauge section of the specimens measured about 3 1/2" (89 mm). At each orientation, four specimens were carefully prepared, two from the centre thickness and two from the top half thickness of the plates. This gave an average of four tests for each of the designated directions or two tests for each of the two through thickness positions.

A 10,000 lbf (45 kN) capacity standard Instron testing machine was used for this series of experiments. The crosshead speed was always 0.05"/min. (.02 mm/sec.). The extension was monitored using

a 1" (25 mm) gauge Instron extensometer and the autographic load - extension diagram was continuously plotted. The tests were stopped when the stationary point (at maximum tensile load) on the autographic machine diagram was clearly exceeded.

Most of the important tensile parameters are directly determinable using either certain key points or the complete plot of the load-extension diagram. The strain hardening index, n , however, can only be determined indirectly using empirical formulations such as,

$$\bar{\sigma} = A\bar{\epsilon}^n \quad \dots \quad (4.1)$$

where $\bar{\sigma}$ and $\bar{\epsilon}$ are representative stresses and strains and A, n are material constants. It should be noted since eqn. (4.1) is a continuous empirical power law relationship which is not obeyed for all forms of tensile flow curves, it therefore becomes necessary to clearly indicate the range of strains over which the relationship is applicable. In the usual manner, n was determined by taking a linear least squares fit of the natural logarithms of the true stresses and the corresponding true strains over a range of strains following any initial yielding discontinuities and up to the maximum tensile load. The equality,

$$\epsilon_u = n \quad \dots \quad (4.2)$$

where ϵ_u is the maximum uniform strain follows from the analysis due to Considere [97] and the use of eqn. (4.2) is often considered as a measure of the consistency of the derived n -value. As already implied, this approach is not completely rigorous because material inhomogeneities and other material and test conditions capable of limiting or extend-

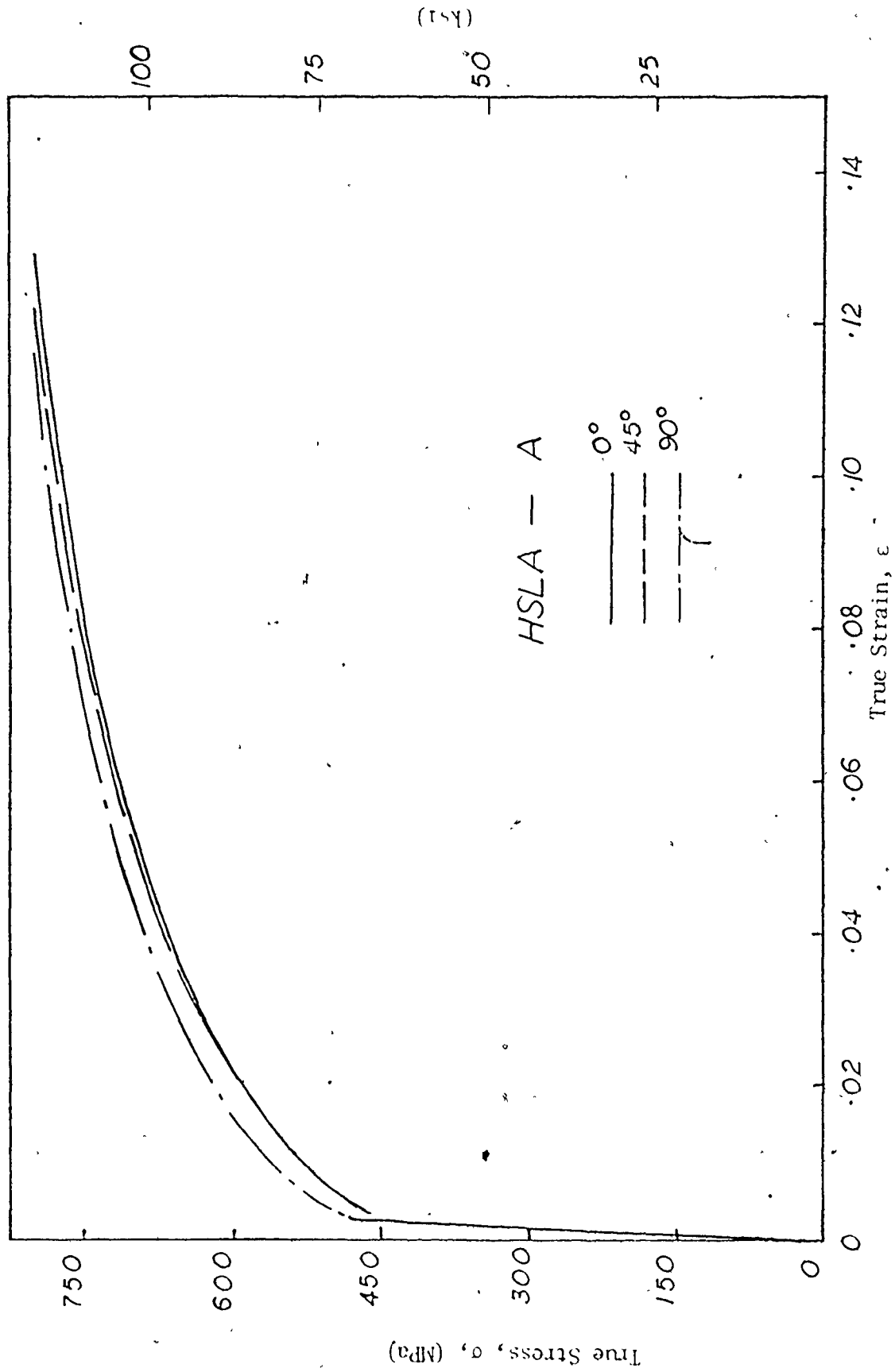


Fig. 4.3(a) Experimentally derived σ - ϵ diagrams of three differently oriented tensile samples of the HSLA-A.

ing the level of uniform plastic strain are neglected [98, 99]

Figs. 4.3 (a), (b) and (c) show the true stress-true strain plots of the HSLA steels A, B and C. It is worth noting that in each case, the 90° oriented specimens show a higher flow stress and a lower uniform strain than the 0° oriented specimens. Reviewing the chemical compositions of the three HSLA steels in Table 4.4, it will be seen that the steels do not contain any of the conventional inclusion shape control elements but appear to have been substantially desulphurised (the average sulphur content is less than .009%). However, there still exists a substantial level of anisotropy in the planar tensile properties in the curves shown in Fig. 4.3.

Table 4.5 shows the average values (of four tests) of the mechanical properties measured at each specimen orientation. The point can be made here that in view of the slight directionality of planar tensile properties, some consistency will be required in the eventual measurements of the BE parameters to ensure that the effects of anisotropy are excluded as much as possible. This fact becomes important when a measure of the BE is obtained by the stress difference between two stress-strain curves. Such stress differences or offsets, especially in the measurements of permanent softening are not necessarily very large and so only measurements from similarly oriented specimens are in fact comparable.

In the tests performed, the location of the specimen through the thickness of the plate exerted little influence on the mechanical properties of the HSLA steels A and B. In the case of the HSLA steel - C, the yield strength was consistently lower at the centre thickness than

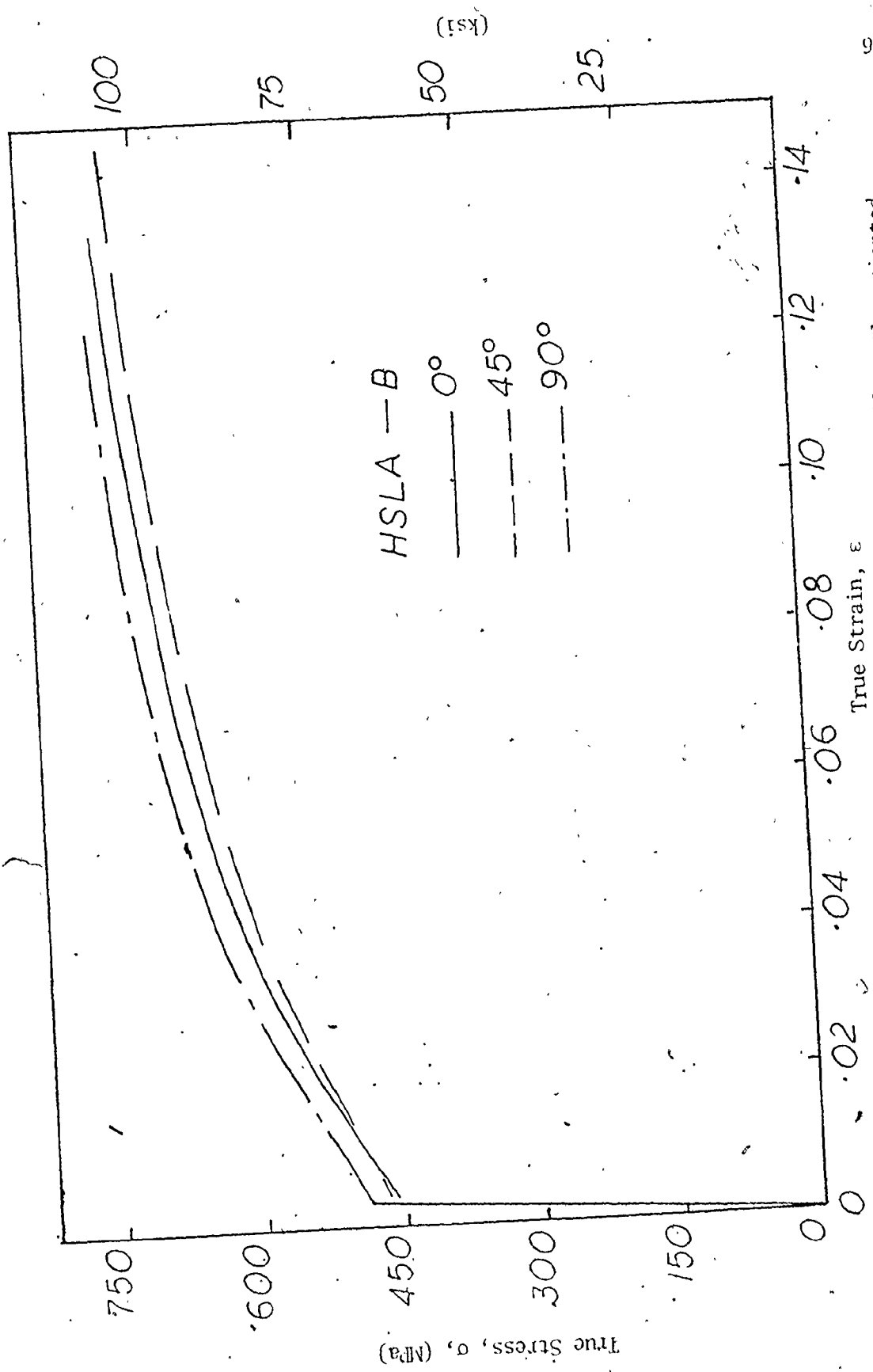


Fig. 4.3(b). Experimentally derived σ - ϵ diagrams of three differently oriented tensile samples of the HSLA-B.

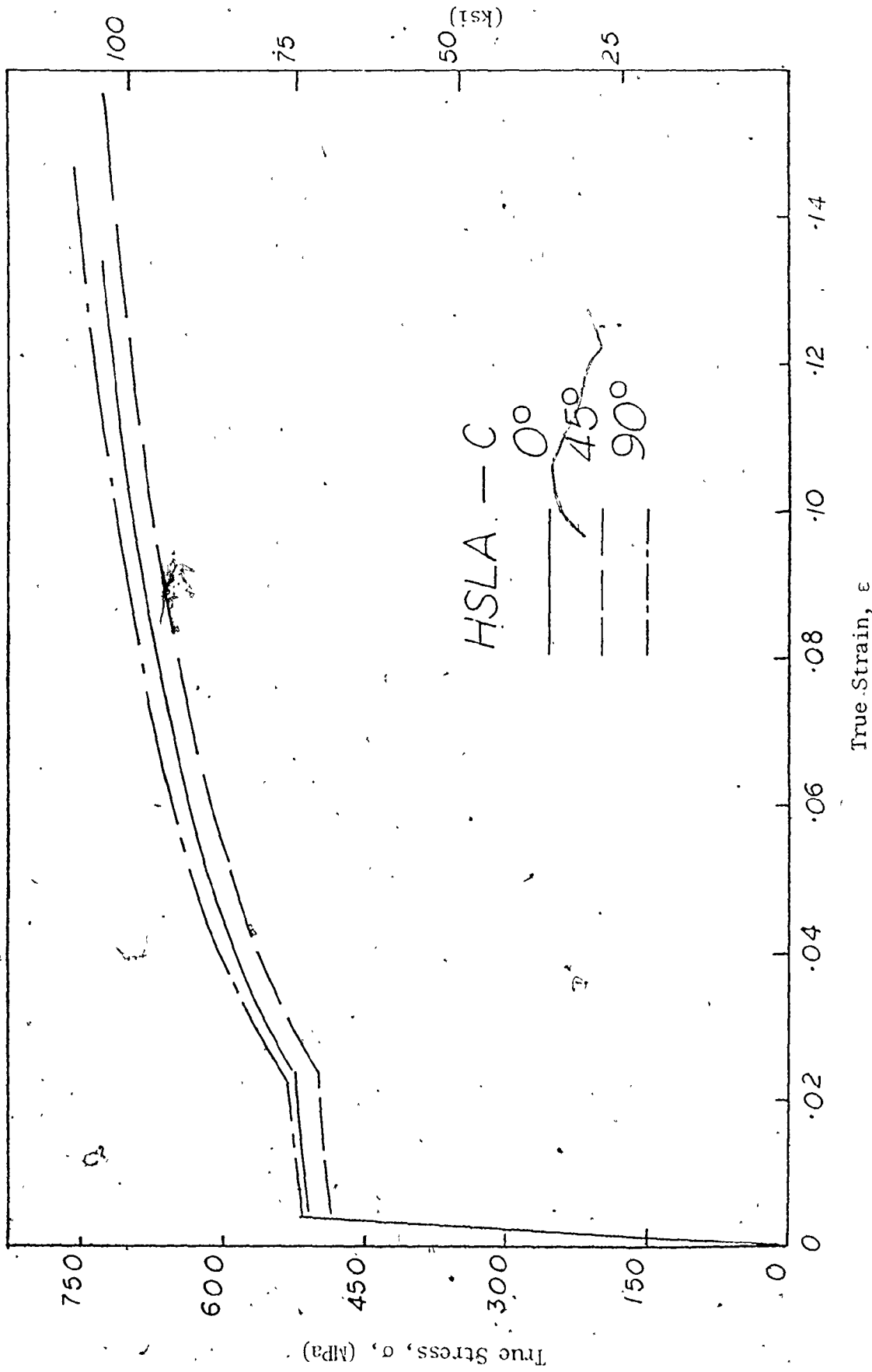


Fig. 4.3(c) Experimentally derived σ - ϵ diagrams of three differently oriented tensile samples of the HSLA-C.

TABLE 4.5
Tensile Properties of the HSLA Steels

Material and Test Direction	Yield Point Elong. (%)	Yield Stress ksi (MPa)	Ult. Tensile Strength, ksi (MPa)	Uniform Strain	Strength Coeff, ksi (MPa)	n value
0°	-	70.9 (488.8)	102.5 (707.0)	.131	166.7 (1149.4)	.170
HSLA-A 45°	-	68.3 (471.2)	103.2 (711.4)	.123	166.0 (1144.6)	.164
90°	-	76.2 (525.5)	107.3 (740.0)	.108	166.0 (1144.6)	.144
0°	-	68.0 (468.9)	94.6 (652.3)	.130	151.4 (1044.0)	.165
HSLA-B 45°	-	68.2 (470.2)	92.8 (639.8)	.150	147.1 (1014.2)	.162
90°	-	70.7 (487.5)	97.0 (668.8)	.132	153.5 (1058.4)	.159
0°	2.6	76.5 (527.5)	92.2 (635.7)	.141	148.6 (1024.6)	.168
HSLA-C 45°	2.8	73.6 (507.5)	89.7 (618.5)	.152	146.0 (1006.7)	.175
90°	2.5	77.4 (533.7)	94.3 (650.2)	.142	150.3 (1036.3)	.164

at the top half thickness; the reverse was true of the strain hardening index, n . The ultimate tensile strengths showed little variation and the uniform strain measurements showed no clear trend. These results are presented in Table 4.6 as the average of two tests for only the HSLA-C.

4.4 Tension-Compression Loading Equipment and Specimen Geometry

The Bauschinger Effect, as defined earlier, involves differential plastic flow properties in strain history related deformation. In the loading history adopted in this study, a specimen is in general prestrained in tension (or compression) by a predetermined amount and then reverse loaded in the opposite sense. The study of the three major aspects of the BE-reduced elastic limit, roundedness and permanent softening - requires an accurate determination of the reverse flow behaviour.

The rig shown in Fig. 4.4 was used for the tension-compression tests on a 20,000 lbf (90 kN) capacity Instron equipped with a backlash eliminating spring loaded screw assembly on the crosshead. Essentially, this equipment consists of two connectors, one to the load cell and the other carried on the machine crosshead with intermediate fixtures for the specimen. In tension-compression experiments, specimen buckling would appear to be the most serious problem. While it is difficult to completely eliminate the possibility of buckling in uniaxial cyclic loading, it is feasible to at least delay its incidence by means of an efficient rig and specimen design. The two major contributors to longitudinal buckling instability in this case are the presence of an initial curvature on the specimen and the eccentricity of loading.

TABLE 4.6
 Variations in through thickness tensile parameters of the HSLA Steel-C

Location of Specimen	Yield Point Elong. (%)	Yield Stress ksi (MPa)	Ult. Tensile Strength ksi (MPa)	Uniform Strain	Strength Coeff., ksi (MPa)	n value
Top	3.1	79.0(544.5)	92.6(638.8)	.150	146.5(1010.0)	.161
Half	3.3	76.6(528.4)	89.7(618.5)	.148	143.2(987.5)	.166
Thickness 90°	3.0	80.1(552.0)	94.2(649.3)	.138	149.5(1030.8)	.162
Centre	2.1	74.0(510.0)	91.8(633.1)	.131	150.7(1038.9)	.176
Half	2.2	70.5(486.4)	89.8(619.0)	.157	148.7(1025.4)	.185
Thickness 90°	1.8	74.8(516.1)	94.5(651.7)	.147	151.2(1042.6)	.166

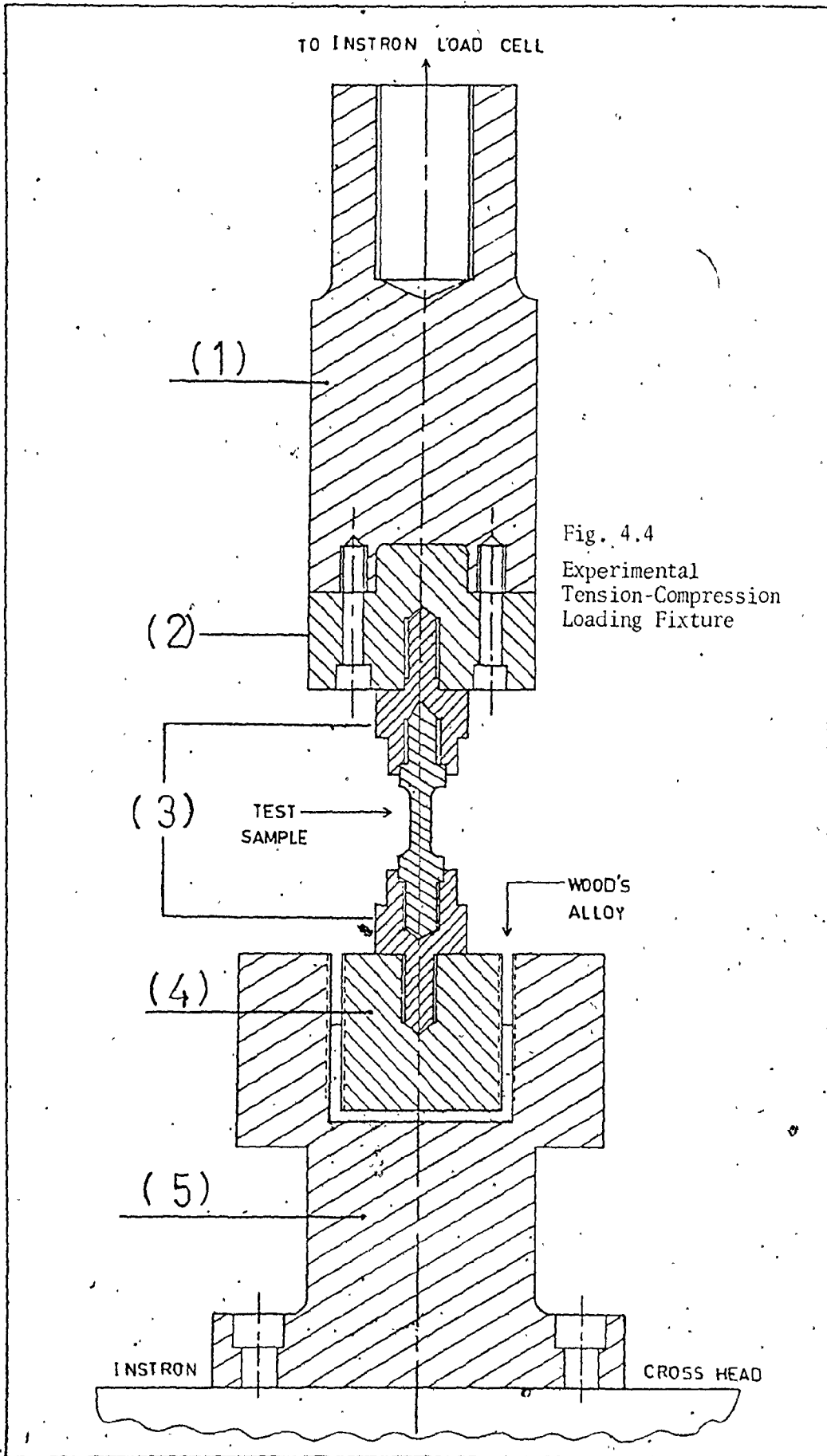
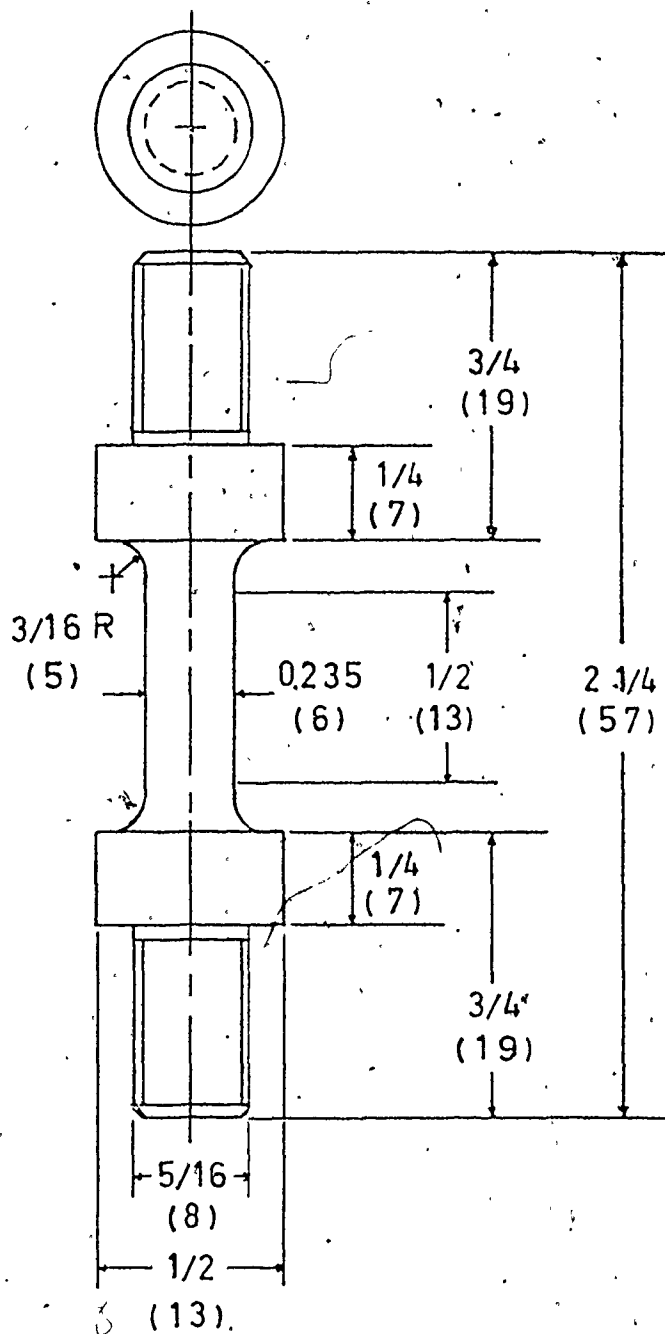


Fig. 4.4
Experimental
Tension-Compression
Loading Fixture

Specimens of geometry shown in Fig. 4.5 were carefully machined so that the shoulders fitted closely in the specimen holders, items '5' in Fig. 4.4. From the geometry of the specimen, the chosen length to diameter ratio of about 2:1 (i.e. a slenderness ratio of about 8.5) gives a theoretical Euler buckling load [100] over 100 times the anticipated loads during testing in compression. In order to determine if the machining process introduced an initial curvature in the specimens, four small flat surfaces positioned symmetrically at 90° were ground on the periphery of the shoulders of four specimens selected at random. Each specimen was placed horizontally (resting on a pair of the ground faces) on the table of an optical comparator set at $37\frac{1}{2}$ times magnification. Care was taken to align the specimen axis with the centre line of the comparator table. Each of the projected line generators of the cylindrical gauge section was measured from the datum line. The measurements of the diameter were taken every 0.005" (.13 mm) along the $\frac{1}{2}$ " (.13 mm) gauge length of the specimens. Some of the specimens showed a maximum radial taper of 0.0005" (.013 mm) along the axis but no consistent curvature was observed.

To reduce any loading eccentricity, the top specimen holder '3' in Fig. 4.4 was arranged to fit into an adjustable second holder; '2', whose machining details are shown in Fig. 4.6(a). Item '2' is connected to the holder, '1', via the clearance holes "A" which permit some lateral play in '2'. The tapped holes "B" in '2' (see Fig. 4.6(a)) carry four Allen setscrews which can be used to position the holder so that the two alignment pointers shown in Fig. 4.6(c) fitted in the top and bottom holders are brought into vertical alignment. The bottom alignment



DIMENSIONS IN INCHES & (MM)

Fig. 4.5

UNIAXIAL TENSION-COMPRESSION SPECIMEN

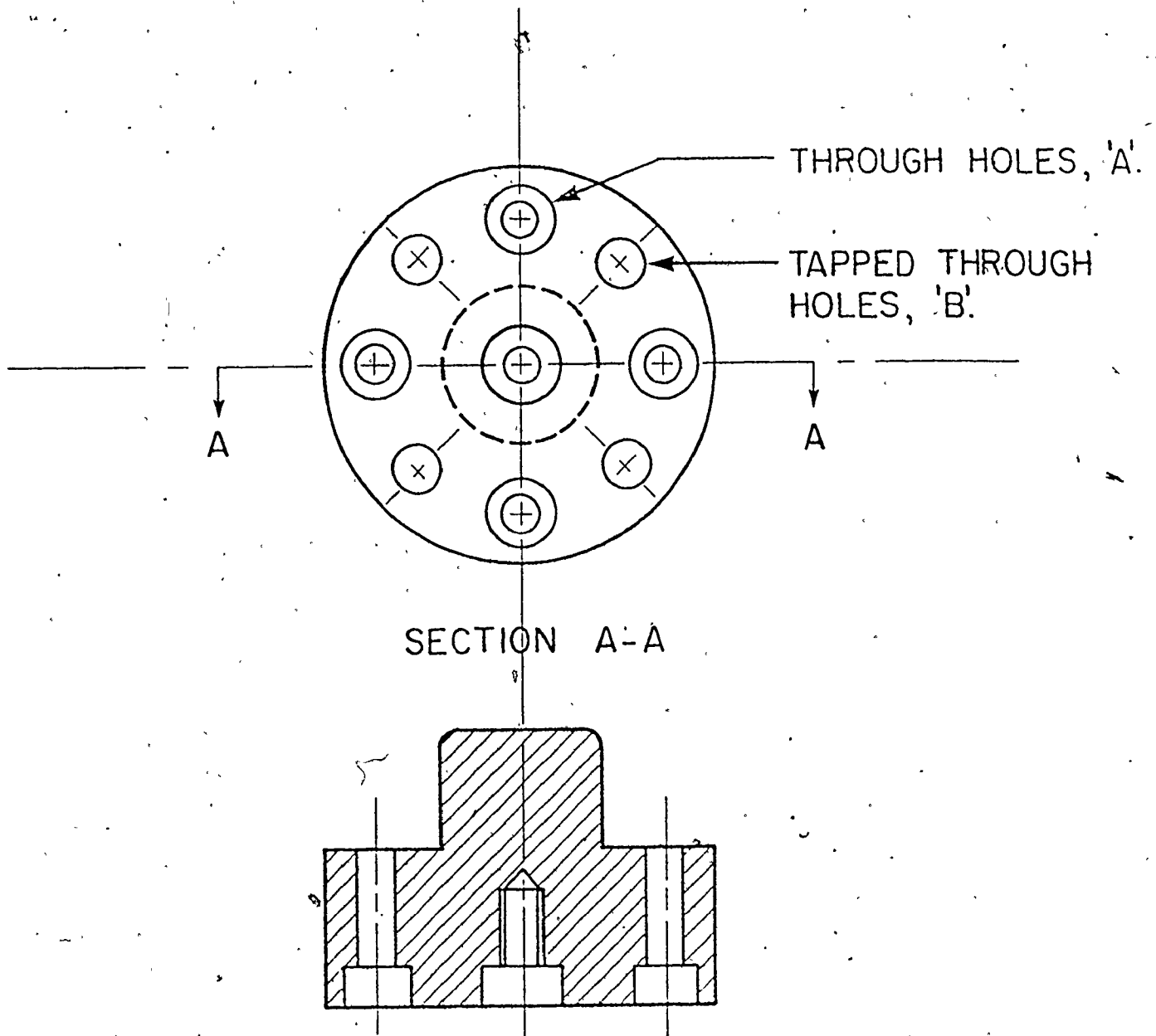


FIG. 4.6 (a)

TOP HOLDER FOR SPECIMEN
(AND ALIGNMENT POINTER)

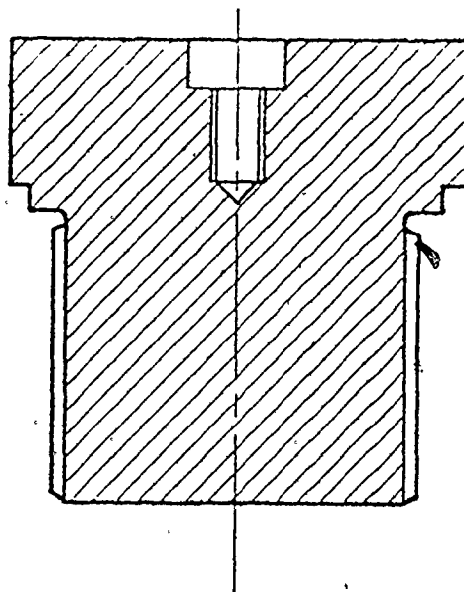


FIG. 4.6 (b)

SECTION OF BOTTOM HOLDER
FOR ALIGNMENT POINTER

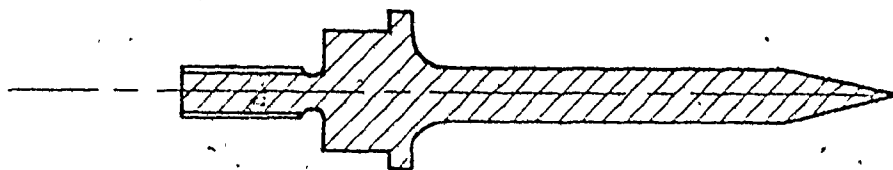


FIG. 4.6 (c)

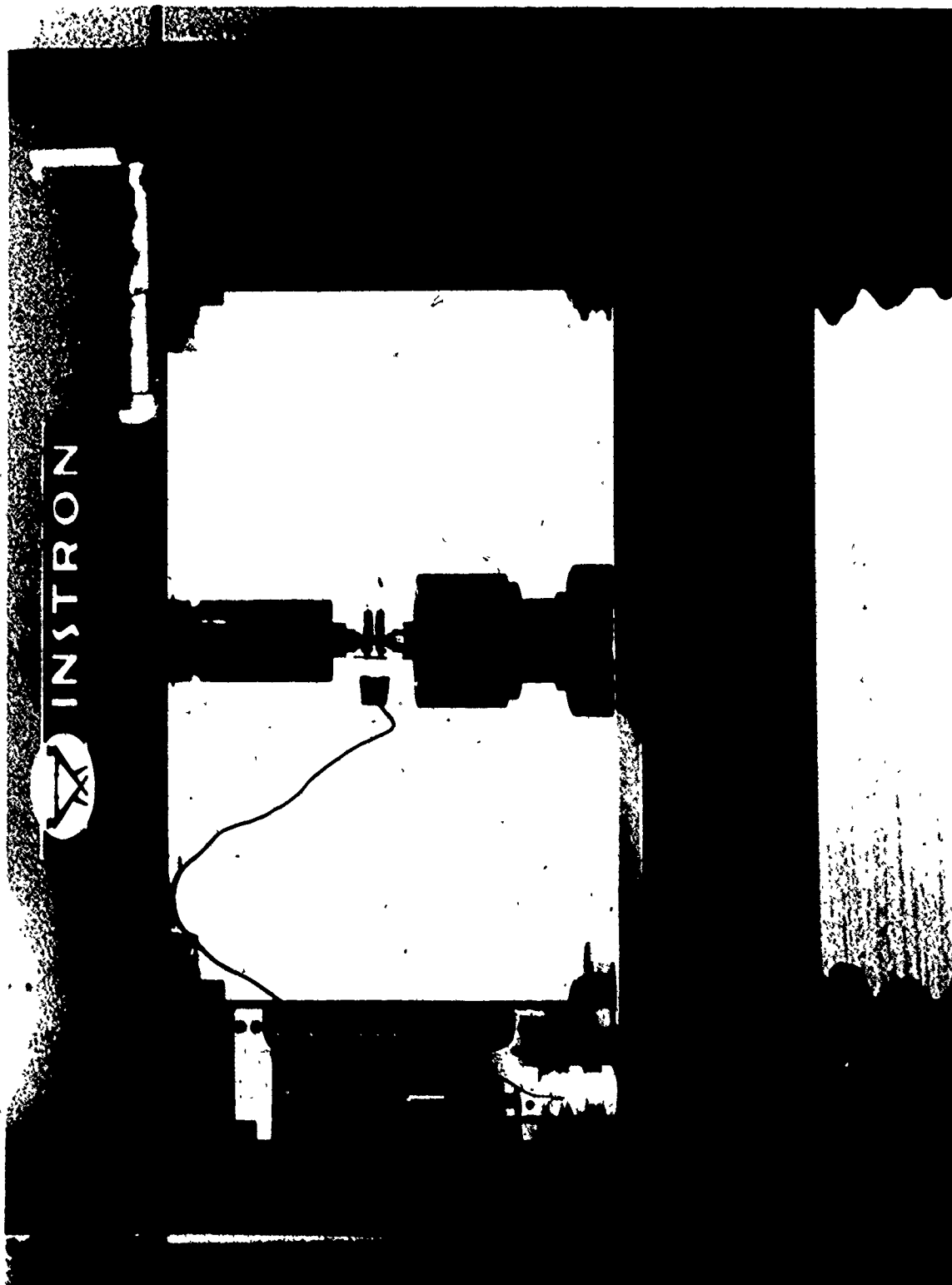
SECTION OF ALIGNMENT POINTER

pointer was carried in the holder in Fig. 4.6(b) which fits in item '5', Fig. 4.4. This was the preliminary technique adopted in the experimental set-up in order to ensure a good alignment between the specimen and the loading axis.

The actual experimental arrangement used was as shown in Fig. 4.4. An additional alignment detail may be evident in this diagram. The specimen is first fitted in the top holder. The bottom holder, floating in a molten bath of Wood's Alloy as can be seen in Fig. 4.4 is then screwed onto the specimen. The specimen is then free to align itself while the Alloy solidifies and hardens prior to testing. It is noted that the solid-liquid transformation of the Wood's metal composition used occurs between 70-79°C [101], a range of temperature too low to have any significant effects on the properties of the test sample. On account of the time needed to melt and later solidify the Wood's Alloy, it takes up to three hours to set-up and perform one complete experiment. This technique was considered acceptable as specimens tested in compression up to 6% strain showed a final curvature less than 0.005" (.13 mm). This indicates that any strains due to buckling would be negligible, of the order of < .02%.

The complete experimental arrangement is shown in Fig. 4.7. The extensometer will be recognised as a standard Instron extensometer. This was however, modified from the original ½" (13 mm) gauge length to ¼" (6 mm) by inserting two precisely ground 1/8" (3 mm) steel pads between each of the pair of extensometer arms and knife edges.

Fig. 4.7 The complete experimental tension - compression loading arrangement.



4.5 The Reverse Flow Experiments

4.5.1 Loading History, Roundedness and Permanent Softening

A typical cyclic behaviour is shown by the experimental load - extension curve, OABCDEFCHI, in Fig. 4.8. The compression domain, CDEF, shows two distinct characteristics; a reduced elastic limit, CD c.f. BC, and a well rounded plastic portion, DE.

In the experiments to determine permanent softening a cyclic path such as OABCDEF was followed i.e. prestraining along OAB followed by one reverse half cycle. In these tests the reverse flow portion of the cycle, CDEF, covered a strain of about 6%, as measured from point C. It was found necessary to employ a reverse strain of this magnitude in order to obtain a sensible measure of the permanent softening. As illustrated in Fig. 2.1 this was achieved by reflecting the reverse flow curve, about point C, into the tensile domain and measuring the offset between the curves at the stage they become parallel. Note that the complete monotonic forward hardening curve is known from previous tensile tests. A range of prestrains up to 10% was covered and for each test a new specimen was employed.

Cyclic loading tests characterised by Fig. 4.8 were performed on single specimens. In modelling certain production processes it may be necessary to ascertain the material characteristics after a second (or third, etc.) strain reversal. More will be said about this aspect in Chapter 6, where a particular pipe making operation is discussed. Some cyclic loading tests performed to study the development of symmetry in the loop shape are described in the next section, 4.5.2.

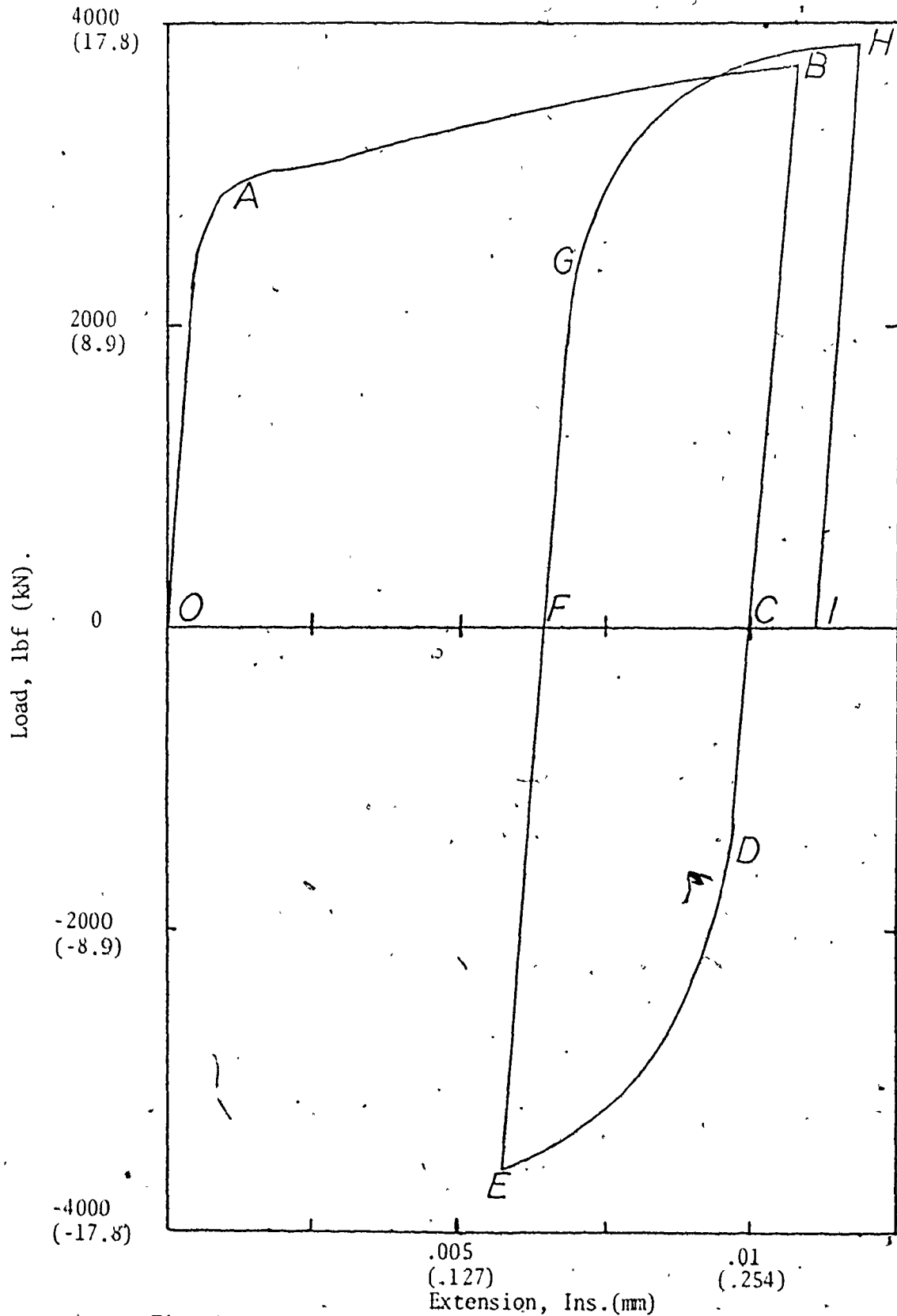


Fig. 4.8 A typical experimental reverse flow



In order to check the reproducibility of the experimental rig, the test in Fig. 4.9 was undertaken. It is clear that the respectability of the test rig would be manifest by the production of a consistent behaviour in tension and compression following elastic loading and unloading. From observing the points C and E in the tensile quadrant and the points H and J in the compression quadrant, it is evident that elastic unloading to the zero stress axis or complete unloading followed by elastic loading in the opposite sense does not have any unexpected effects on the subsequent yield behaviour except for the usual preyield microstrain and a slight elastic hysteresis loop.

4.5.2 Cyclic Loop Symmetry and Structural Damage

In Chapter 2, the development of internal stresses during the plastic deformation of alloys containing a distribution of non deformable inclusions in a soft matrix was discussed. The large BE observed in these alloys was viewed as a natural consequence of these internal stress distributions. Two additional types of experiments were undertaken in order to establish whether the distribution of internal stresses could be altered by variations in the loading path. It was pointed out in an earlier discussion that static and dynamic strain ageing experiments have been performed for the same reason.

In the method adopted here, the first set of experiments involved cyclically straining the specimen in tension and compression in order to obtain improved symmetry in the resultant tension-compression stress-strain loops. Fig. 4.10 shows four such tension-compression cyclic stress-strain curves obtained for the HSLA-steel, B. In these tests,

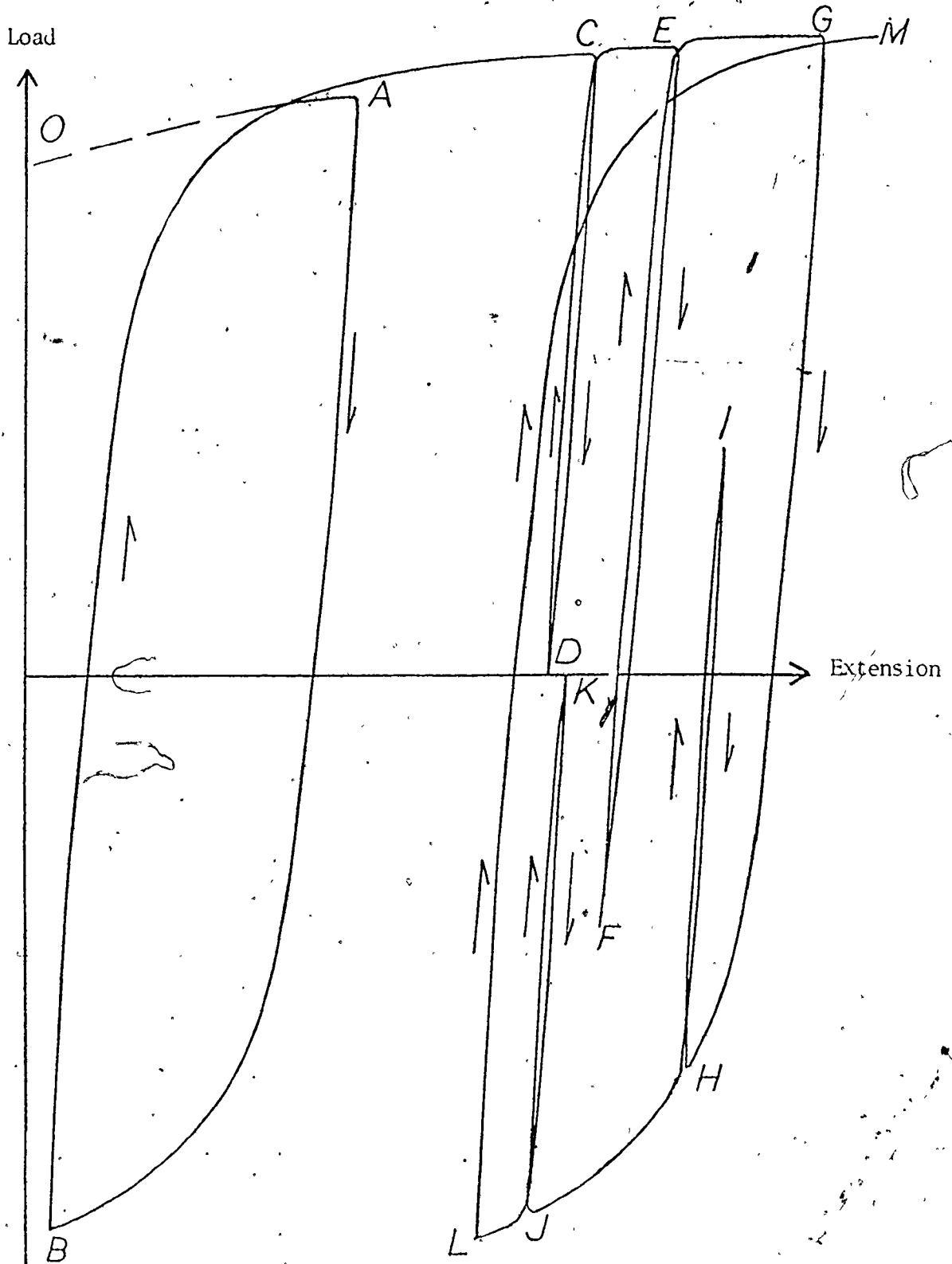
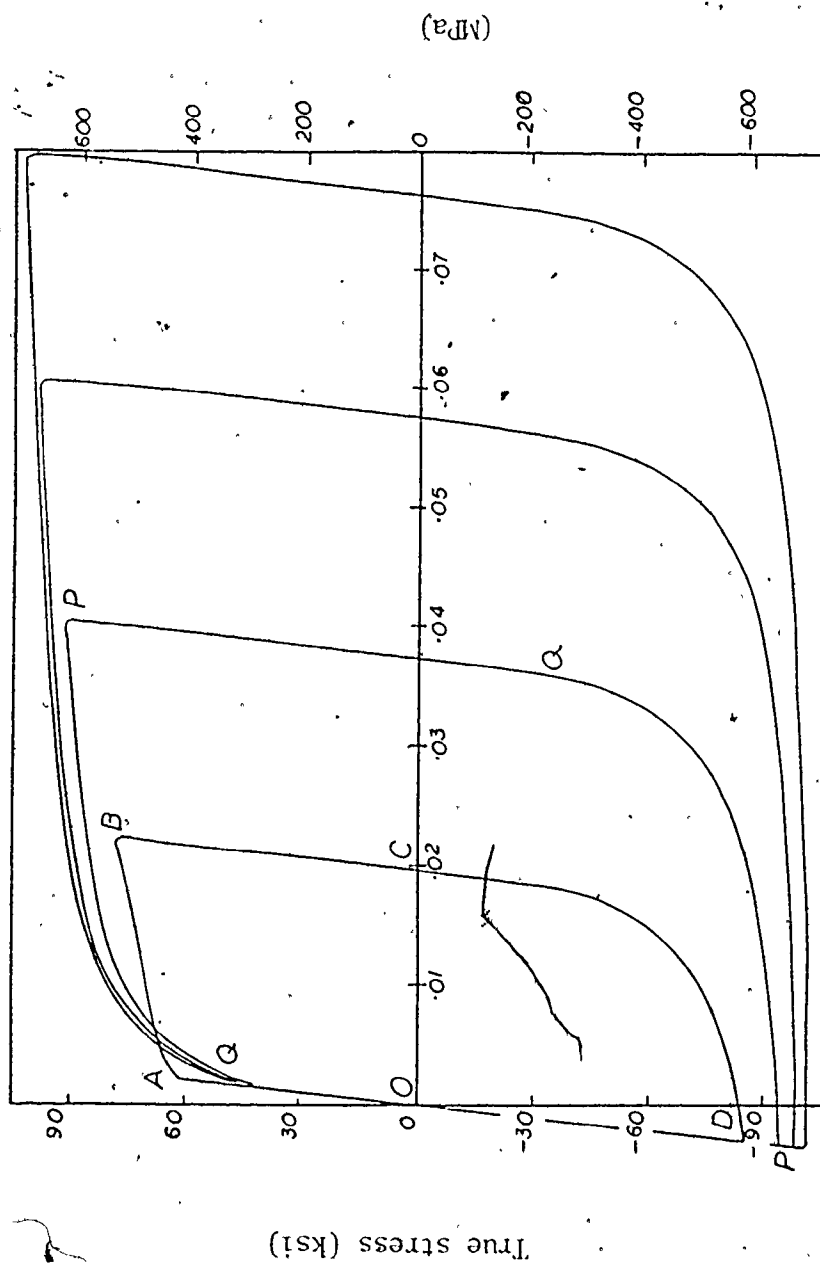


Fig. 4.9 An experimental method of assessing the reproducibility of the loading fixture in Fig. 4.4.

the strain amplitude was increased during each forward cycle and the imposed forward strain was fully reversed to zero total strain during the subsequent reverse cycle. It is evident from the discussion in Chapter 2 that on account of the polarized nature of the mean matrix stress, the influence of the internal stresses developed during each half cycle of loading would be to settle down the structure of the material and to produce identical behaviour in tension and compression after the first few loading cycles. These cyclic tension-compression tests were performed using the HSLA steel-B and the dual phase steels D and E.

Alternatively, it was argued that a reduction in internal stress levels may be realized by sufficient overstraining to cause the second phase particles to crack. The other form of possible internal structural damage is of course the decohesion of the ferrite-cementite interface. Whether these processes occur independently or simultaneously is debatable but the net effect should be to influence the reverse flow behaviour.

Overstraining was achieved by pulling 0.63" (16 mm) diameter by 2.52" (64 mm) long tensile specimens in a Tinius-Olsen machine until a conspicuously pronounced neck developed. Some specimens were also pulled to fracture and set aside for metallographic studies of structural damage close to the fracture area. The BE test pieces of Fig. 4.5 were machined from the necked specimens. Care was taken to ensure that the gauge section of the machined test pieces (termed the overstrained specimens) embraced the necked zone. These overstrained specimens were then subjected to the following strain cycles.



True Strain

Fig. 4.10 Tests for cyclic loop symmetry using the HSLA steel-B.

(i) loaded in tension to a strain of about 1%, unloaded and compressed until the reverse strain was about 2.5%; then it was unloaded and reloaded in tension a further 4.5%.

(ii) strained 3% in compression, reverse loaded in tension for about 9% and then recompressed a further 5%.

The spheroidized 1095 steel was used for this study.

4.5.3 Tests for Discontinuous Yielding in Reverse Flow

The HSLA steel-C exhibited an average yield point elongation of 2.6%. As a recap of the salient features of the yield point phenomenon (see the behaviour of HSLA-C, Fig.4.3(c)), it is noted that the Luder's strain is associated with inhomogeneous yielding and takes place at an approximately constant flow stress known as the lower yield stress. In thin tensile specimens, it is easy to see the Luder's strain propagating as a physical front or band inclined at an angle (of nearly 45°) along the specimen axis. There is also a visible geometric discontinuity at the strain front. In general, the front is not easily observed with cylindrical specimens.

Some experiments were undertaken to ascertain the behaviour during reverse flow of materials exhibiting discontinuous yielding as characterized by the propagation of Luder's bands. If a specimen is unloaded before the Luder's front has propagated through the entire gauge section, one or two questions immediately come to mind. Firstly, how is the BE exhibited (if at all) during reverse flow? Secondly, how is the discontinuous yield behaviour affected? For example, does the portion of the gauge section which has been plastically deformed during the forward loading start to deform first upon reversing the loading?

These effects are likely to be of practical significance in manufacturing processes which involve reverse strain cycles.

In order to find some answers to these questions, the following experiments were performed with the HSLA-C. In Fig. 4.11, a specimen of dimensions shown in Fig. 4.5 was loaded in the first half cycle until the mean prestrain was clearly plastic but less than the expected Luder's strain of about 2.6%. The specimen was then unloaded and reloaded in the opposite sense in the second half cycle. The reverse loading was continued until the Luder's strain reappeared before unloading.

Two specific loading programmes were used in the tests. These are demonstrated in Figs. 4.12(a) and (b). Taking Fig. 4.12(a) as an example, the first loading in tension by a prestrain of 1.35% followed the path OAB. After unloading along BC, the specimen was removed so that measurements of the diameter could be made in the manner described below. Subsequently, the same specimen was reloaded in compression along the paths CDEF, FGHI where at the point F which indicates an intermediate unloading interruption and the point I which indicates the final unloading, additional measurements of the diameter were again taken. Fig. 4.12(b) is similar to Fig. 4.12(a) except that here, the first loading is in compression. Both of these diagrams are in fact composite plots of the autographic load-extension diagrams obtained in each case from three interrupted tests - OABC, CDEF and FGHI - performed using the same specimen. Note that during the path FGHI, the reverse loading was continued until the load-extension diagram clearly indicated the beginning of work hardening, i.e. the complete exhaustion of the Luder's

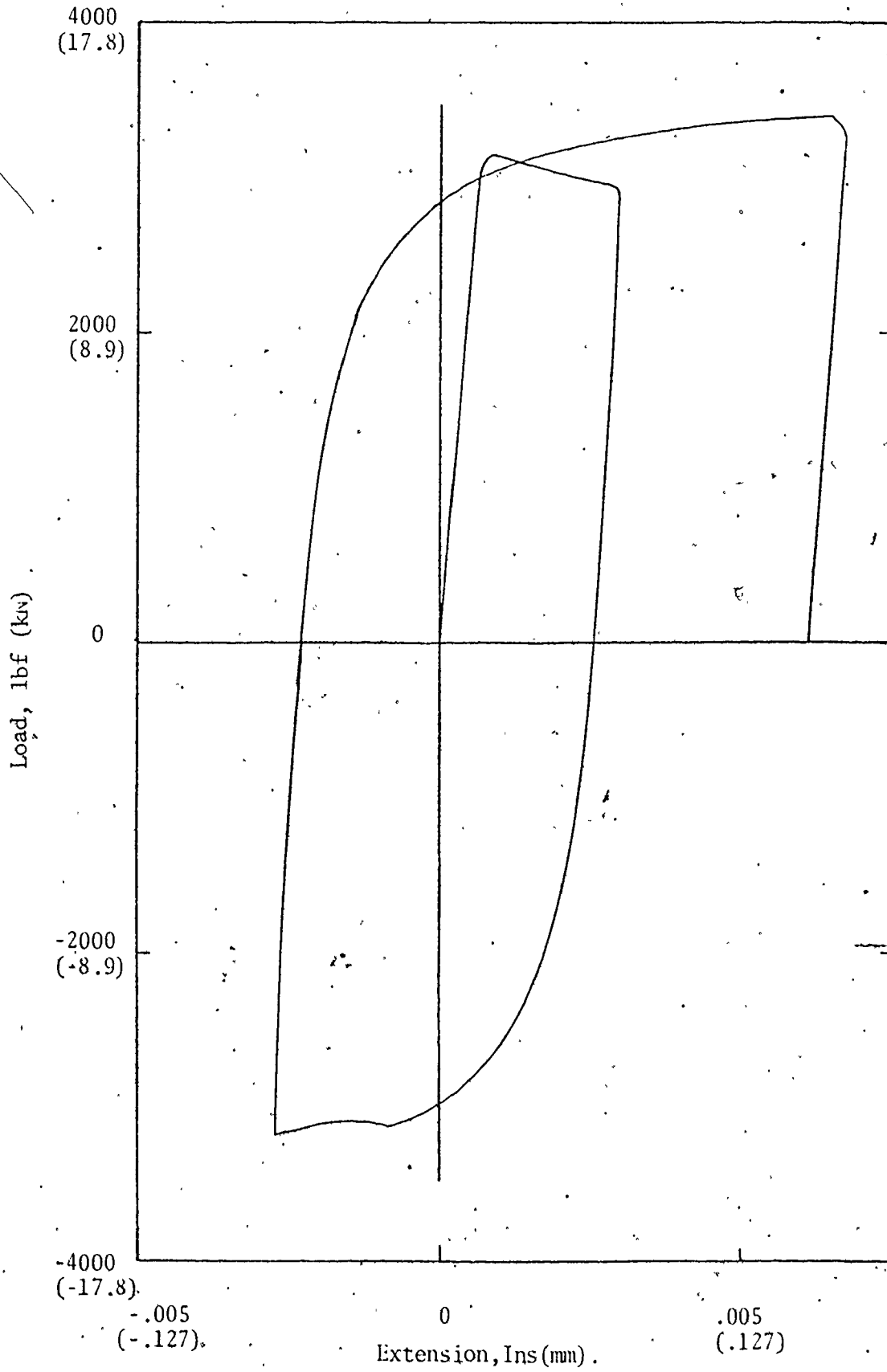


Fig. 4.11 The Ludering Effect in forward and reverse flow

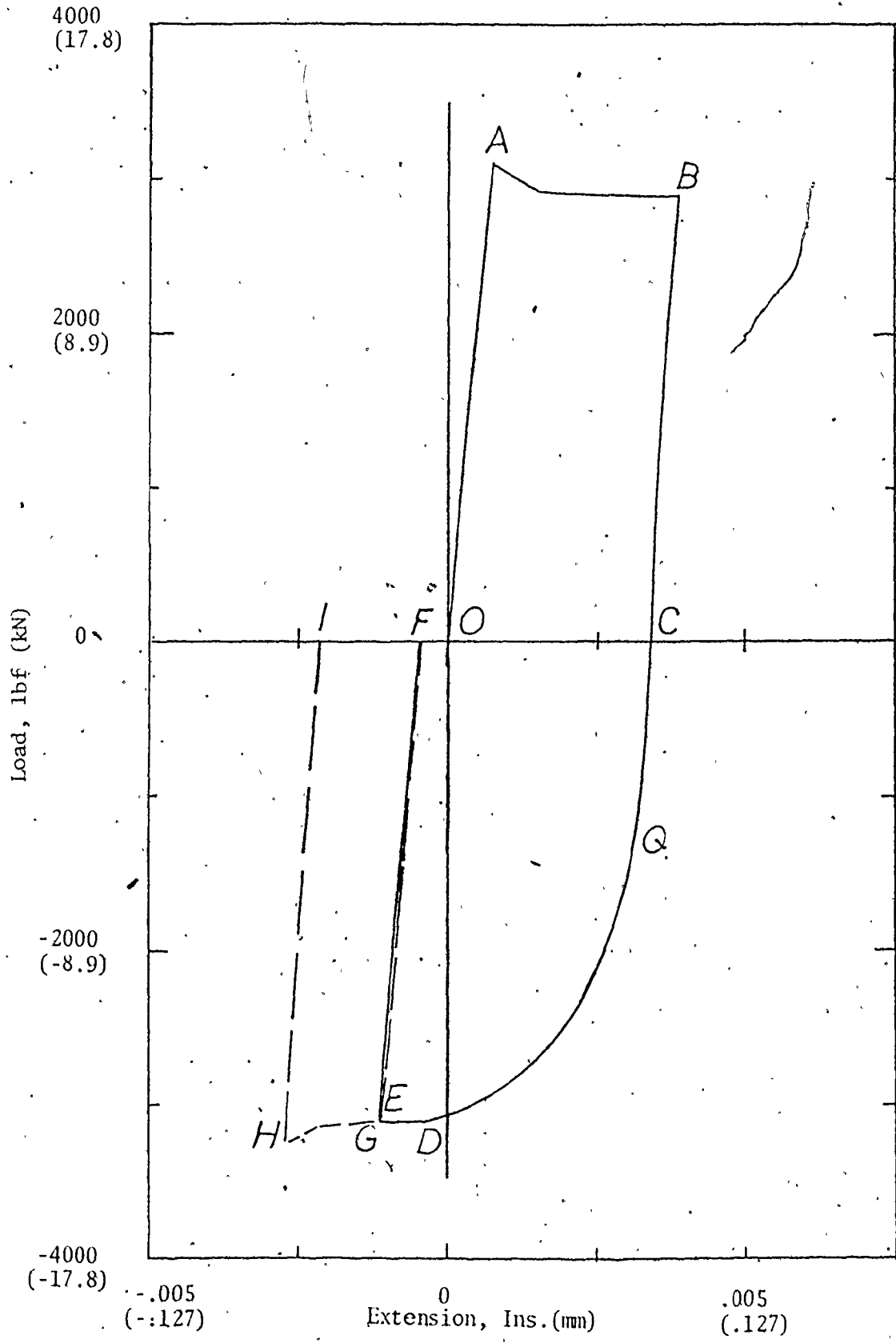


Fig. 4.12(a) Interrupted tests used to study the mechanics of Luder's strain propagation in reverse flow following a tensile prestrain.

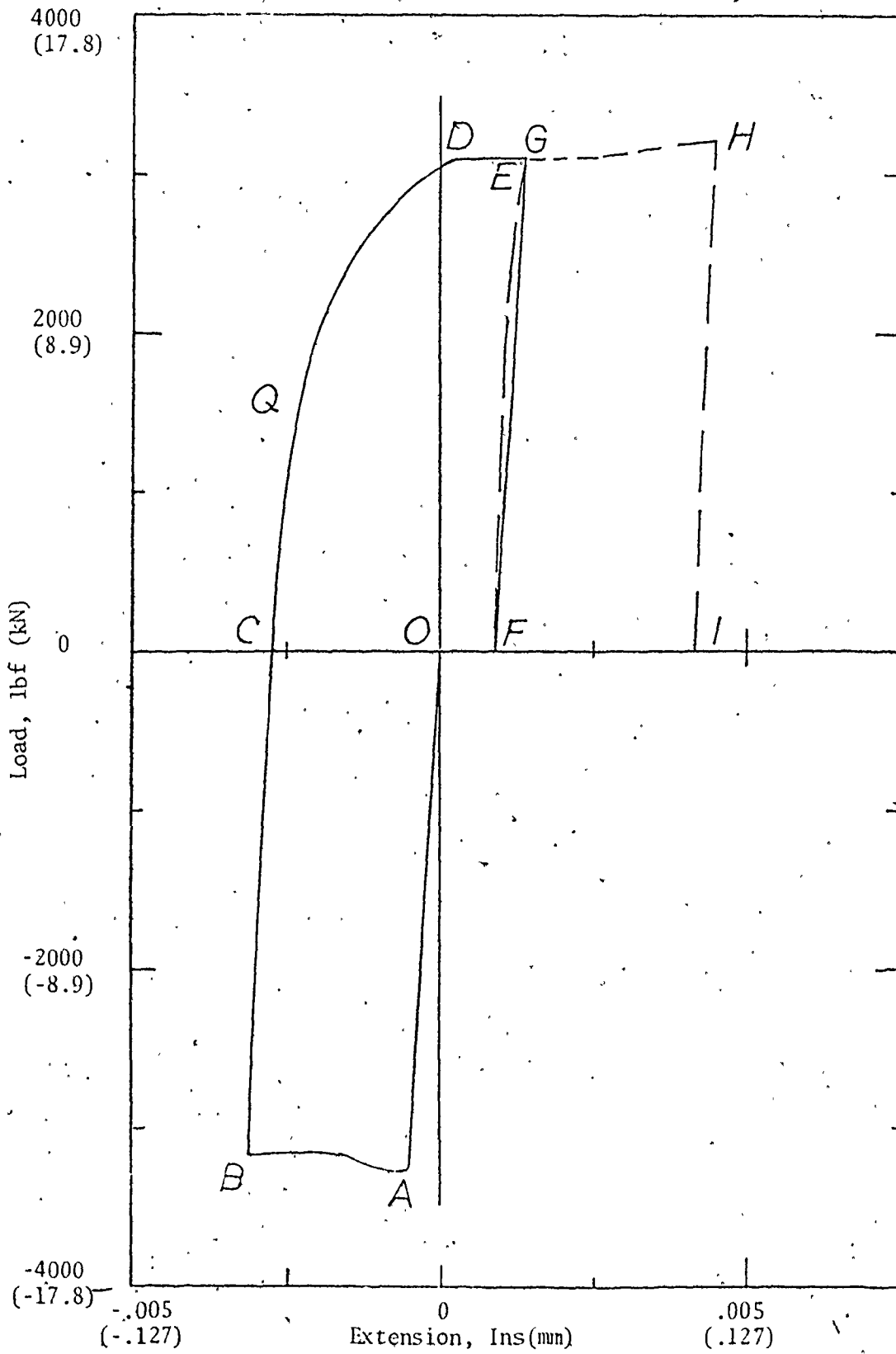


Fig. 412(b) Interrupted tests used to study the mechanics of Luder's strain in reverse flow

strains.

In order to locate the Luder's strain front during the tests, it was necessary to interrupt the loading sequence in the manner described above. Measurements of the specimen diameter at selected positions 0.05" (1.3 mm) apart were made along the $\frac{1}{2}$ " (13 mm) gauge length prior to the tests. Three additional measurements were again taken during each unloading at approximately the same position as before. In each instance, the specimen had to be removed from the experimental fixture. All measurements of the diameter were made using the optical projector set at a magnification of $37\frac{1}{2}$ times.

4.6 Experimental Results

The results obtained from all these experiments will form the subject for the discussions in the next chapter.

CHAPTER V

RESULTS AND DISCUSSION

5.1 Introduction

For convenience, this chapter is divided into three major sections. The first section (5.2) deals with the analytical results obtained during a study of the three phenomenological models of the BE proposed in Chapter 3, section 3. The objective of this portion of the study was to demonstrate, in a qualitative manner, that the magnitude of the BE is related in general to the distribution of internal stresses. In addition, an improved method for the description of experimental reverse flow data is presented.

The second section (5.3) deals with an attempt to describe the BE in structural steels along the lines of the theory developed by Brown and Stobbs using a model microstructure. In particular the form of the stress-strain curves of the three HSLA steels, A, B and C and the magnitude of the BE in these steels were determined. The objective was to relate the observed BE to the prestrain and to the microstructural parameters required by the model of Brown and Stobbs in order to establish its credibility and also to generalize the model for the more common structural steels.

An important parameter required for the detailed description of the BE in microscopic terms is the total volume fraction of second phase materials in the steels. As discussed in Chapter 4, with the structure

of the HSLA steels, a variety of mixtures of non ferritic phases are possible. For this reason, it was necessary firstly to produce a description of the BE in materials of comparable complexity, that is, polycrystals containing large volume fractions of large particles which, however, possess well characterized microstructures. The spheroidized steels were selected for this purpose. These materials have been widely studied and consist of an ideal Fe - Fe₃C system in which the choice of various carbon levels provides a wide range of volume fractions and large particles of spheroidized cementite.

It is necessary to emphasize here that the model of Brown and Stobbs utilized experimental observations and theoretical arguments limited to the deformation of single crystals of copper, which were dispersion hardened with small particles ($< 600\text{\AA}$) and low volume fractions ($< 1\%$) of silica. In the present work the maximum average size and volume fraction of particles dispersed in the polycrystalline materials investigated are of the order 9000\AA and up to 17% respectively.

From the discussion in Chapter 3, section 4.3, the following important aspects of the theory require verification:-

- (a) the dependence of permanent softening on the parameters such as the degree of the prestrain and volume fraction of the hard phases present;
- (b) the relationships between the theoretical Bauschinger Effect Parameter, the BEP in eqn. (3.32) and the prestrain and volume fraction;
- (c) the relation between the prestrain and the microscopic inhomogeneity measured by the unrelaxed strain, ϵ_p^* . The model of Chapter 3, section 4.2 is utilized here to deduce ϵ_p^* .

The experimental programme proposed in Chapter 4, section 5 was

used to derive the required data for this study of the BE. The results are discussed in section 3 of this chapter, first for the spheroidized steels and then generalized subsequently for the HSLA steels, although some of the results to be presented are plotted for convenience for both types of materials on the same diagrams.

Furthermore, later in the chapter, some consideration is devoted to the implications of the role of internal stresses in the dimensional stability of cold worked metal parts as well as the results of the tests involving the two loading programmes proposed in Chapter 4, section 5.2. These programmes were:- (i) cyclical straining for tension-compression loop symmetry, and (ii) forward and reverse loading using overstrained* specimens. The aim here was to investigate the response of the material and to interpret the data in terms of the probable effect of each type of test on the internal stresses developed within the material. Each of these later areas, although treated independently in subsections 5.4 - 5.6 comprise one major section which also includes, in section 5.7, a short discussion of experimental observations involving the behaviour of discontinuous yielding in reverse flow. The experimental aspects of this phase of the work were outlined in Chapter 4, section 5.3 and pertain only to the HSLA steel C which exhibits the yield point phenomenon.

The chapter is ended with a brief discussion of some additional data on the BE in the HSLA steels which utilize conventional experimental descriptions. For clarity, each major section is followed with a short

* Prestrained in tension until a neck is developed.

summary of the results obtained.

5.2 Phenomenological Models of the Bauschinger Effect

5.2.1 Model Based on Macroscopic Residual Stresses

This model was proposed in Chapter 3, section 3.1. The object was to study the influence of an assumed distribution of residual stresses on the macroscopic reverse flow behaviour of a specimen which had been previously strained by loading in tension. The results are shown in Fig. 5.1. It is seen that the BE is predicted firstly in terms of a reduced elastic limit in compression and secondly in terms of the roundedness of the compression stress - strain curve. These two features of the model are also seen to depend on the choice of the residual stress amplitude, σ_0 relative to the prestrain, σ_f . A more important weakness in the model is that it does not exhibit permanent softening. However, as simplified as the model is, it clearly shows that the BE is related in some way to internal stresses, represented in this instance by means of a macroscopic residual stress.

5.2.2 Hardening Model Using Elastic/Plastic Elements

One difficulty in the residual stress model described in the previous section appears to be the need to know the exact distribution of internal stresses in the material. This cannot be accomplished without a detailed analysis of the statistics of the distribution of particles, sizes, spacings and shapes as well as that of dislocation mechanisms. The model of elastic - plastic elements overcomes this drawback and simulates the inhomogeneous plastic deformation of materials in the manner that was proposed in Chapter 3, section 3.2.

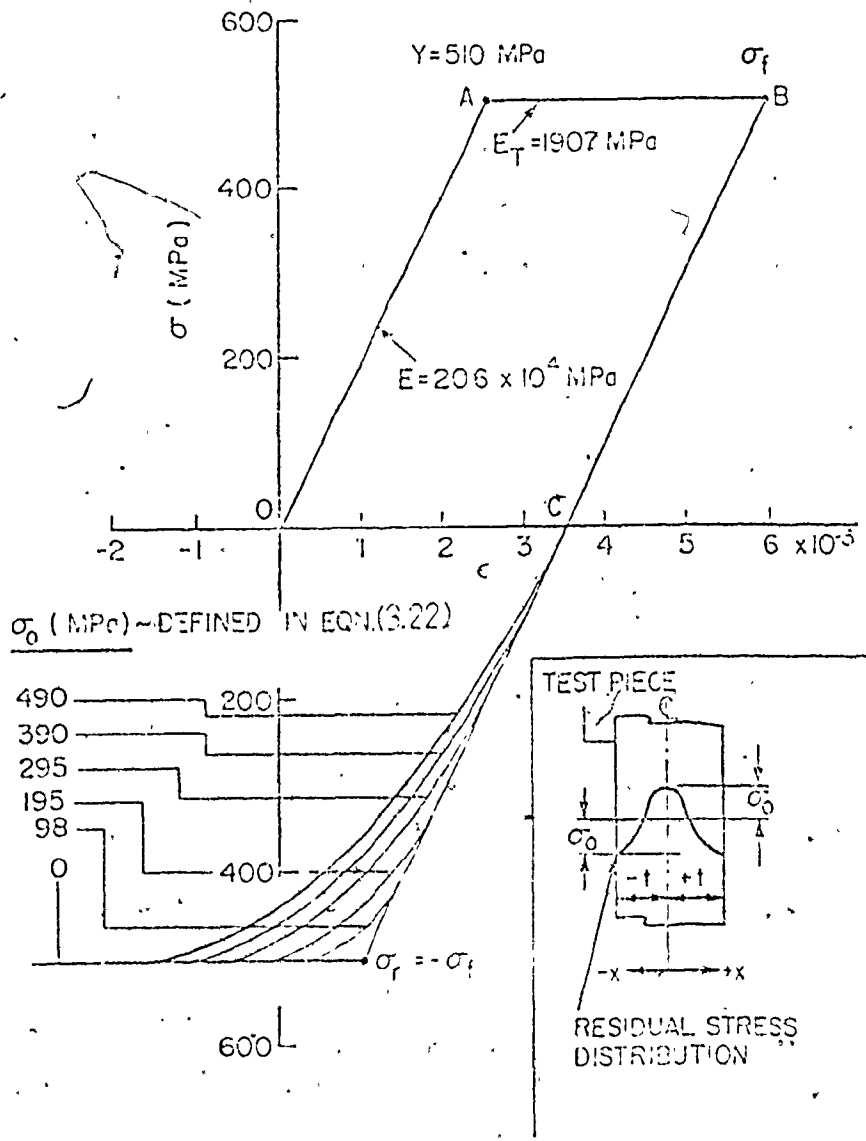


Fig.5.1 Reverse flow behaviour modified by macroscopic residual stresses.

The essential features of the model are demonstrated if two elements (1 and 2, Fig. 3.3) of yield strengths σ_1 and σ_2 ($\sigma_2 > \sigma_1$) are selected. If the structure is loaded in uniaxial tension, the first element yields at σ_1 , the strain is ϵ_1 , and the mean stress in the structure at this point is simply, σ_1 . Subsequently, element '1' is considered perfectly plastic; its flow stress is always σ_1 . Upon continued loading in tension, the element '2' yields when its stress reaches σ_2 , the strain is ϵ_2 and the mean stress on the structure is now $(\sigma_1 + \sigma_2)/2$. The flow behaviour up till this point is given by the path OAB in Fig. 5.2. For this two element (phase) system, the flow stress of the structure beyond the point B is constant at the stress value $(\sigma_1 + \sigma_2)/2$. It is noted that increasing the number of elements has the effect of rounding the plastic portion of the stress-strain curve up to the point where the last element yields and the mean stress is given by

$$(\sigma_1 + \sigma_2 + \sigma_3 + \dots + \sigma_n)/n.$$

If the two element structure is now unloaded and reloaded elastically in compression, the structure behaves elastically over a strain of magnitude $2\epsilon_1$ and the stress amplitude is $|2\sigma_1|$. At this point, the first element yields in compression at the point C, Fig. 5.2 and the mean flow stress of the structure is $[\frac{1}{2}(\sigma_1 + \sigma_2) - |2\sigma_1|]$. This defines the reverse yield strength of the structure following prestraining. Continuing the loading causes the second element to yield at the point D when its stress reaches σ_2 in compression. The additional stress increment from the point C is $2[|(\sigma_1 + \sigma_2)/2 - \sigma_1|]$ and the corresponding strain increment is $2(\epsilon_2 - \epsilon_1)$. The entire structure has now

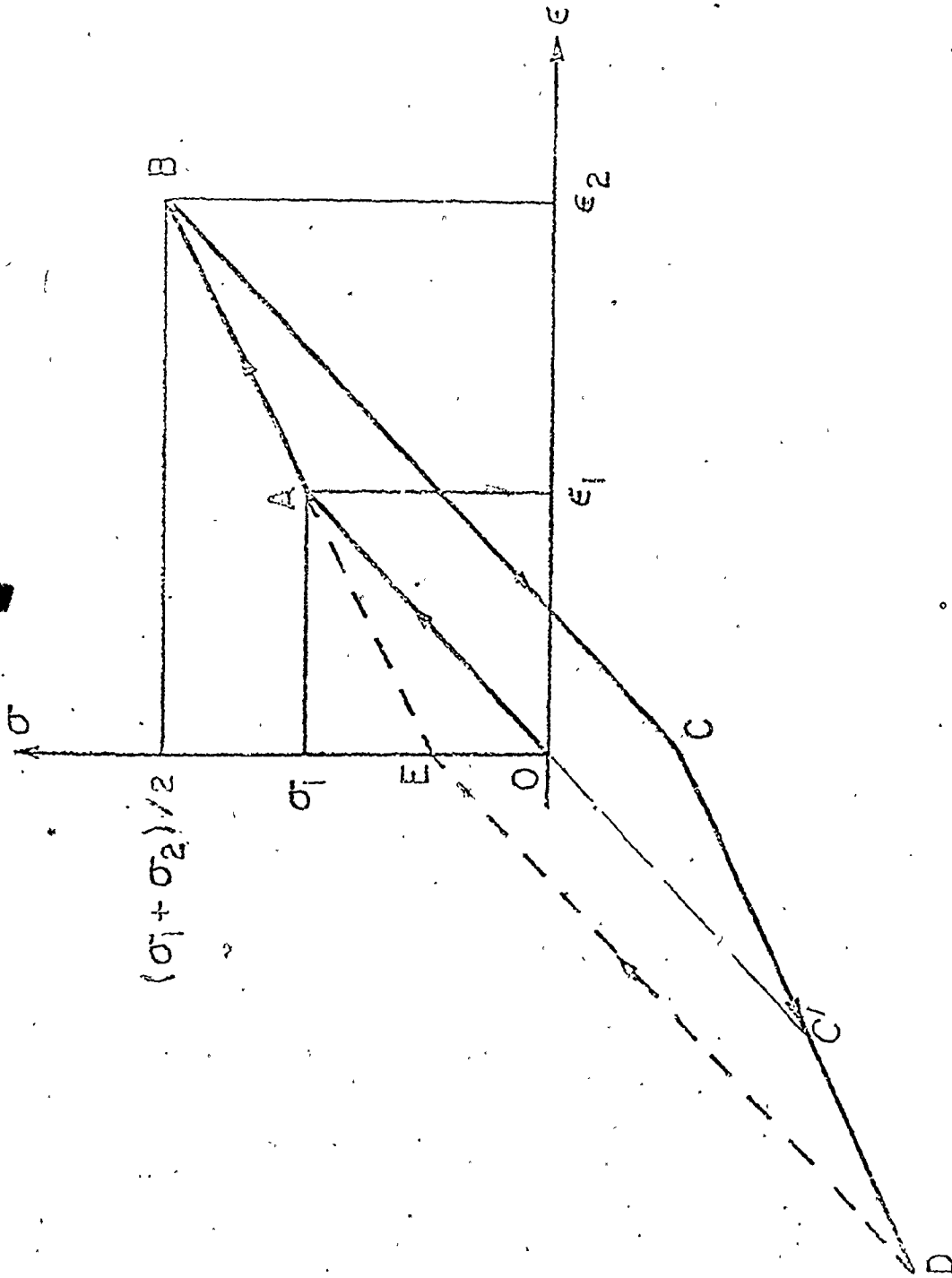



Fig. 5.2 Forward and reverse flow behaviour using two elastic/non-hardening elements. As drawn $\sigma_2 = 2\sigma_1$.



yielded. It is easy to see that following unloading to zero load, the residual stress in the element '1' is a negative quantity given by $-\frac{1}{2}(\sigma_2 - \sigma_1)$ and that in element '2' is a positive quantity, $\frac{1}{2}(\sigma_2 - \sigma_1)$. A similar differential system of residual stresses is applicable to the inhomogeneous deformation of real materials which this model simulates, that is, the particles, element '2' inherit tensile stresses and the matrix, element '1' inherits compressive internal stresses. Notice that the residual stresses are predicted by the model and no prior knowledge of these are required to calculate the reverse stress-strain curve. Moreover, the form of the reverse stress-strain curve is identical to that of the forward loading curve apart from a scaling factor of two. The following important features of the model are noted:-

(a) The slope of the stress-strain curve changes from the elastic value along OA to a less value along AB and the stress increment over AB is obtained because of the presence of an elastic volume fraction. The model shows a BE measured by $\Delta\sigma = (\sigma_B - |\sigma_C|)$ which is twice the forward hardening over AB, i.e. $2(\sigma_B - \sigma_A)$ where σ_A , σ_B and σ_C are measured at the points A, B and C respectively in Fig. 5.2.

(b) The model exhibits a roundedness which increases with the volume fraction of the elastic phase present but no permanent softening. A suitable modification to incorporate permanent softening is to allow one element, at least, to be perfectly elastic. In this case, if element '2' remained elastic, the forward hardening curve would continue beyond B with the same slope as AB. The Bauschinger stress, $\Delta\sigma$ would remain equal to $2(\sigma_B - \sigma_A)$; but it would also measure the permanent softening,

$\Delta\sigma_p$.

(c) Cycling the structure between equal stress or strain amplitudes about the origin produces symmetrical tension - compression loops of the form shown by the tension loop DEB and the compression loop BCD. The original monotonic curve OAB is preserved if the material is cycled through the origin along the path OABCC'O. In this case, the BE is only revealed in the first two half cycles but not in the third relative to the second half cycle, i.e. $|\sigma_A| = |\sigma_C'|$.

The model can be modified by allowing the individual elements to work harden. The simplest approach would be to allow all the elements to harden linearly at the same rate. As shown in Fig. 5.3, this modification shows the BE and roundedness but, again, no permanent softening. Also, there is no simple scaling factor relating the forward and the reverse curves and the structure "shakes down" to the elastic line if cycled on the basis of a fixed stress or strain amplitude about the origin.

These models are simple in form, but they have been included here in order to emphasize the relevance of residual or internal stresses to studies of the BE. In particular, they show the possible phenomenological simulation of the type of deformation of two phase structures which results in the production of internal stresses, vis à vis the BE in the important class of dispersion hardened structural alloys.

5.2.3 The Modification of Mroz's Kinematic Hardening Model

Mroz's [60] original model of the BE was discussed in Chapter 3, section 3.3. It was then proposed to introduce a modification to the model that combines the concepts of isotropic and kinematic hardening explored in the same chapter. Mroz's model was originally proposed to overcome the deficiencies shown in Fig. 5.4 of either the isotropic

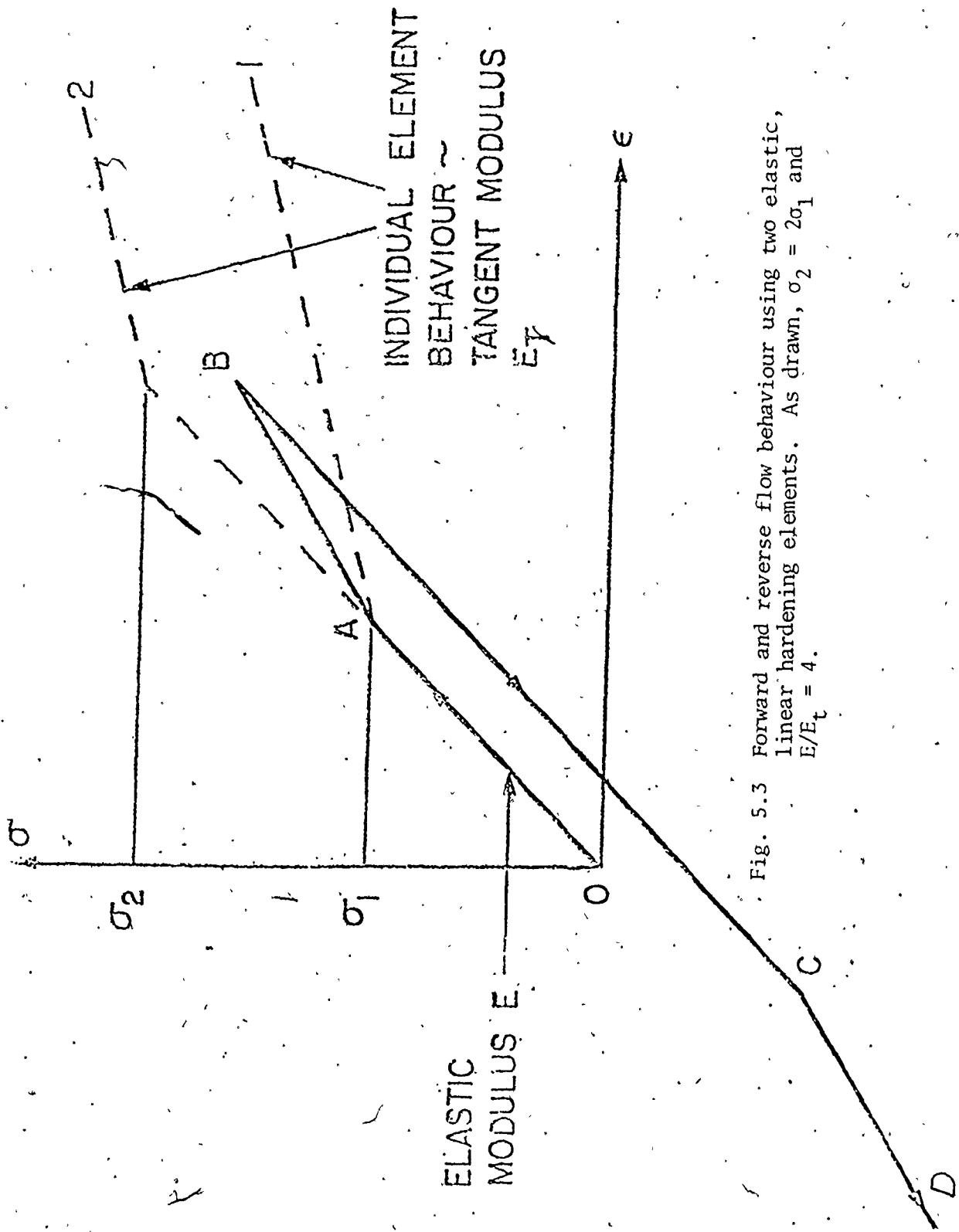


Fig. 5.3 Forward and reverse flow behaviour using two elastic, linear hardening elements. As drawn, $\sigma_2 = 2\sigma_1$ and $E/E_t = 4$.

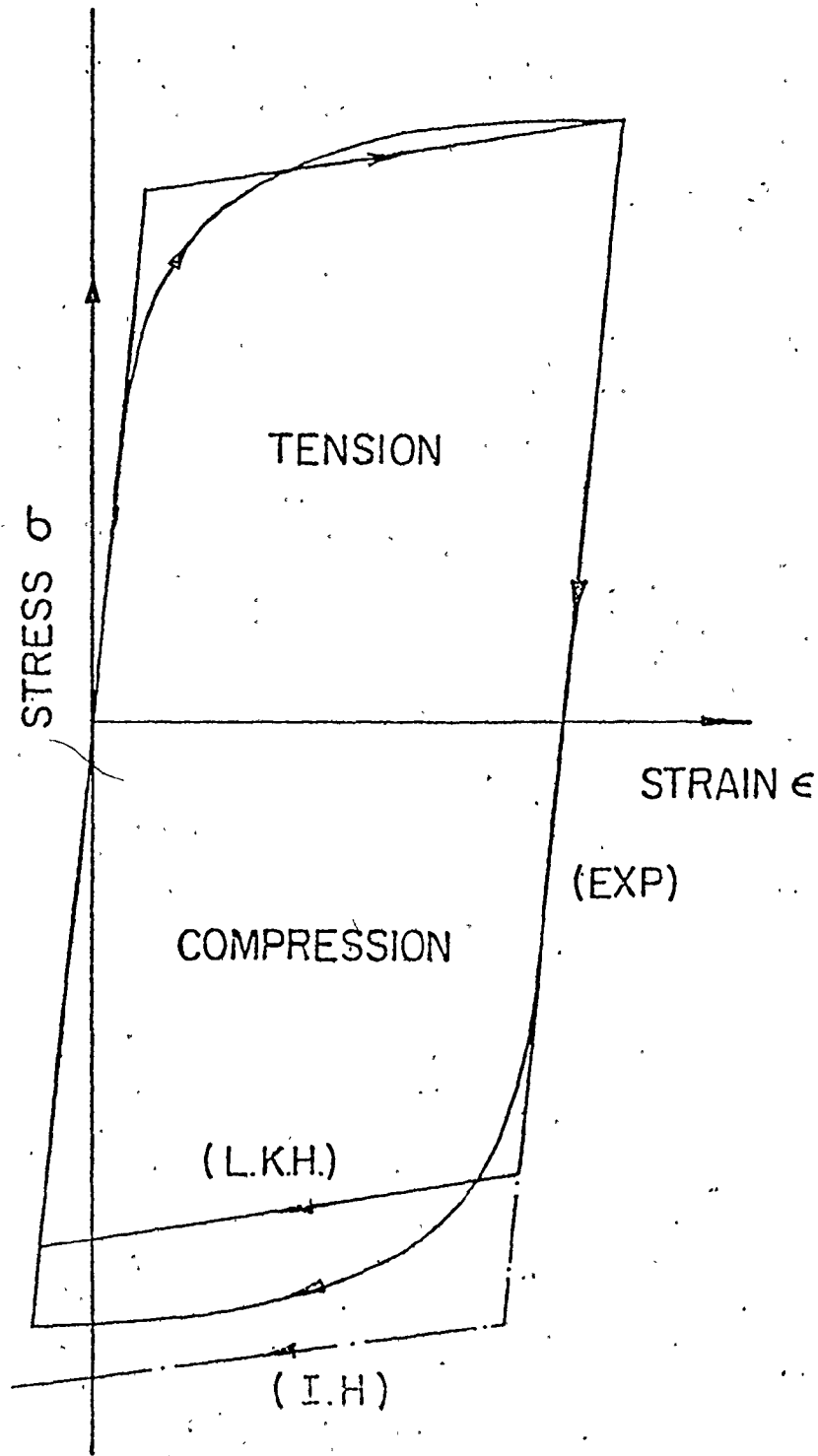


Fig. 5.4 Comparison of experimental data with an isotropic and a kinematic hardening model.

hardening (I.N.I.) rule (see eqn. (3.7)) or the linear kinematic hardening (L.K.H.) rule (see eqn. (3.10)) in the description of experimental reverse flow behaviour of materials. Mroz had also introduced the possibility that the model could further be generalized by allowing the surfaces to expand (or contract) as well as translate. This fact was utilized in this work to modify the original model of Mroz so that both isotropic and kinematic hardening take place simultaneously.

One set of results is shown in Fig. 5.5. In this diagram, an experimental cyclic curve of the HSLA steel A tested in tension to a pre-strain of about 3% before unloading and compression to zero total strain is analyzed. The case $m = 0$ corresponds to the original model of Mroz. It is evident that the modification of Mroz's model by allowing a proportioning of the work hardening stress increment, $\Delta\sigma$ into isotropic, $m\Delta\sigma$ and kinematic, $(1-m)\Delta\sigma$ components - the cases, $m = .2$ and $m = .5$ - provides an improved description of experimental data. In these results, the combination parameter, m shown on the diagram in Fig. 5.5 was chosen for the forward path; it was set to zero during reverse loading. It is to be noted that on account of the increased work hardening rate along the reverse loading curve in Fig. 5.5, it would be necessary to adjust some of the tangent moduli on the reverse path in order to obtain a closer fit with $m = .5$. In Fig. 5.6, the description of one of the symmetric cyclic loops (of the type in Fig. 4.10) of an X-80 HSLA steel extracted from ref. [11] which employed $m = .5$ for the forward path and zero for reverse loading gave an excellent fit.

The combination parameter, m , as used here, is to be selected a posteriori to give the best representation of observed behaviour. No

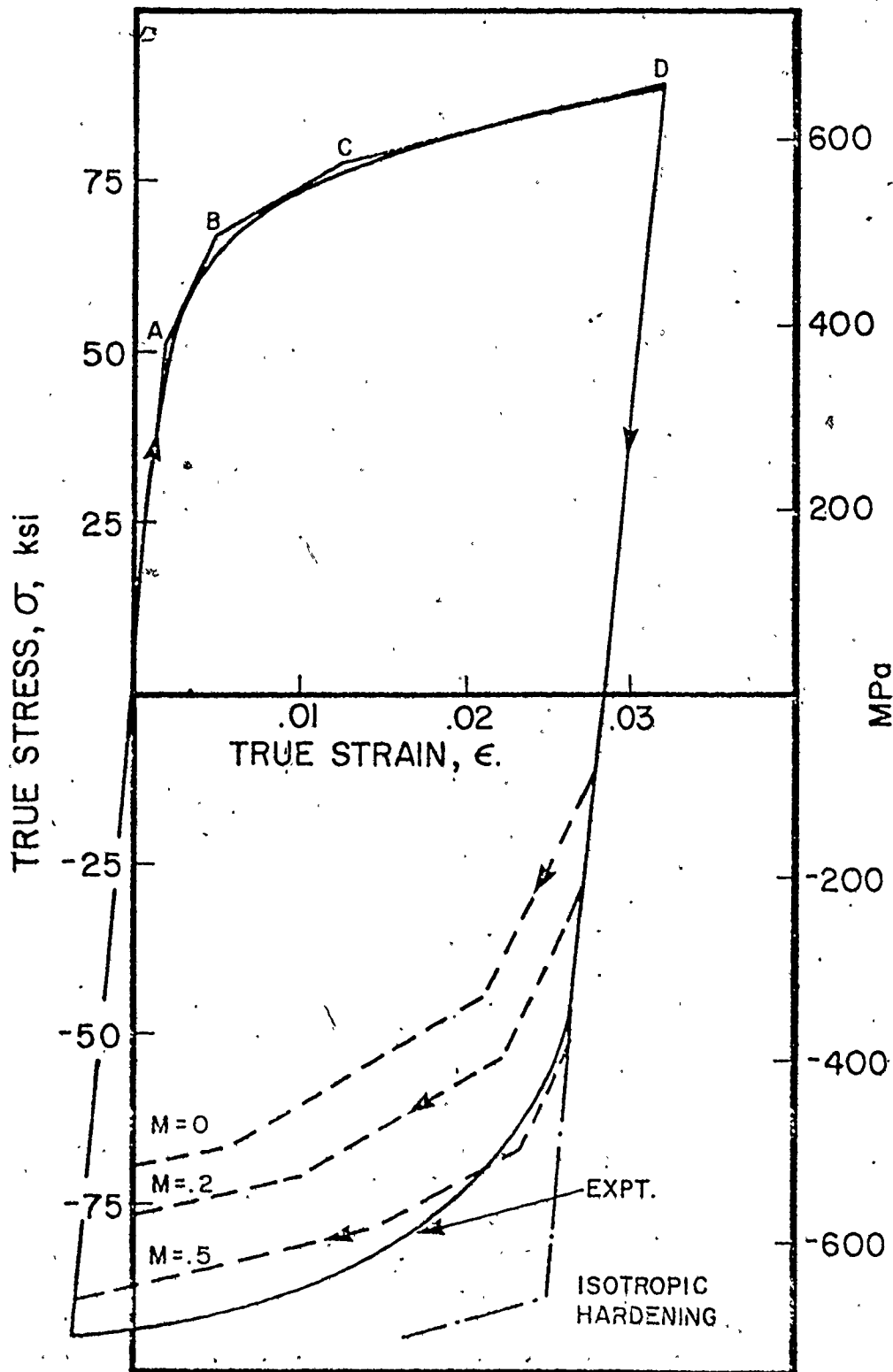


Fig. 5.5 A comparison of experimental data with the combined isotropic and kinematic hardening model for different hardening levels.

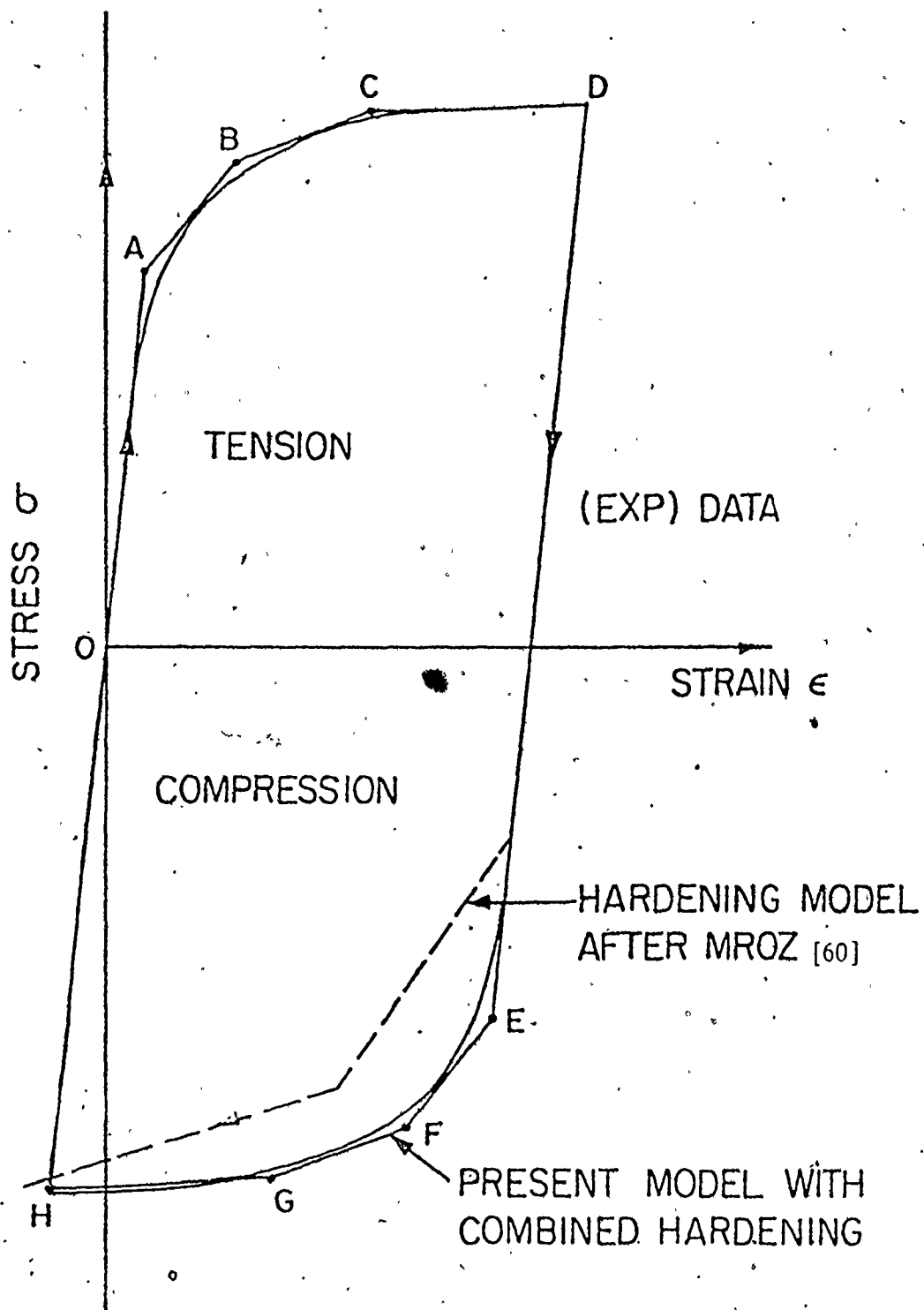


Fig.5.6 Comparison of experimental data with the combined isotropic and kinematic hardening model.

attempt has been made here to correlate the combination parameter with the physics of work hardening, and in this sense, the model is purely phenomenological. The model has the major advantage of simplifying the determination of reverse flow curves in complex loading programmes involving strain reversals. An application of the combined hardening model in the analysis of a typical pipe forming process where every element in the pipe wall possesses a unique strain history has been demonstrated in a recent article by Sowerby and Tomita [84].

5.2.4 Summary of Phenomenological Models

The continuum models discussed above have been employed to study three separate representations of the BE. The first model studied showed that internal stresses play a prominent role in controlling material behaviour. If the strain path is changed, or in this instance reversed, the influence of the internal stresses is manifested as the Bauschinger Effect. The second model was used to simulate the type of inhomogeneous plastic deformation that generates internal stresses in two phase elastic/plastic materials. The results showed that a residual stress is developed by virtue of the gradients of strain existing between the elastic and plastic phases after prestraining and unloading. Both models qualitatively predicted the BE in terms of the reduction in the compressive yield strength and the roundedness of the reverse flow curve but failed to predict permanent softening. In the final model, the BE was studied in terms of combined isotropic and kinematic hardening by introducing a modification to a model proposed by Z. Mroz [60]. The results showed an improved description of experimental reverse flow data. In the case of symmetric tension - compression cyclic loops, the

modified model yielded an excellent correlation with the experimental results obtained for an X-80 HSLA steel.

5.3 The Microscopic Model of the BE due to Brown and Stobbs

Brown and Stobbs [85,86] have attempted to describe the work hardening behaviour and the internal stresses developed in the important class of dispersion strengthened materials in terms of the dislocation structure produced at second phase particles. The essential aspects of this model were discussed in Chapter 3, section 4.

Also, in Chapter 2, section 2.1, the general discussion of the characteristics of a typical reverse flow behaviour showed that the BE involves three related aspects, namely: (i) the reduction in the elastic limit in reverse flow, (ii) a highly rounded reverse flow curve, and (iii) permanent softening. The Brown and Stobbs model essentially relates permanent softening to the mean value of internal stresses in the material. These, in turn are dependent on the extent of prestraining and on the total volume fraction of second phase particles. In this connection, the Brown and Stobbs model enables a quantitative view to be taken in which the BE is described in terms of permanent softening and the total work hardening during prestraining.

The salient features of the microscopic model, treated earlier in Chapter 3 are listed below for convenience:-

(i) From eqn. (3.34), the permanent softening, $\Delta\sigma_p$ is directly proportional to the square root of the prestrain, ϵ_p , that is, for a given material,

$$\Delta\sigma_p = \alpha_1 \epsilon_p^{1/2} \quad (5.1)$$

where α_1 scales the effect of particle shape and size.

(ii) The theoretical parameter, BEP in eqn. (3.32) was selected as a measure of the BE, that is,

$$\text{BEP} = \frac{\Delta\sigma_p}{(\sigma_f - \sigma_o)} \quad (5.2)$$

The BEP measures the Bauschinger Effect as a fraction of the total work hardening, $(\sigma_f - \sigma_o)$ due to back stresses as measured by $\Delta\sigma_p$. The BEP is theoretically independent of prestrain, and the relationship to volume fraction, V_f is evident from eqn. (3.33) written below as,

$$\frac{1}{\text{BEP}} = C_1 + C_2 V_f^{-1/2} \quad (5.3)$$

where $C_1 = .5$ and $C_2 = .62$ are theoretical constants derived in [86] for spherical particles.

(iii) Also, from eqn. (3.31), the permanent softening, $\Delta\sigma_p$ is directly proportional to the volume fraction. For a given prestrain, if the particles are of the same average size, then eqn. (3.31) may be written more simply as,

$$\frac{1}{2} \Delta\sigma_p = \alpha_2 \cdot V_f \quad (5.4)$$

where α_2 again depends on the particle shape.

(iv) Finally, permanent softening data may be used to characterize the development of strain incompatibility in the structure. This calculation requires the two phase elastic-plastic model of eqn. (3.28) in which the permanent softening, $\Delta\sigma_p$ is related to the unrelaxed strain, ϵ_p^* by,

$$\frac{1}{2} \Delta\sigma_p = 2\gamma\mu V_f \cdot \epsilon_p^* \quad (5.5)$$

Using eqn. (3.27), the expected dependence of ϵ_p^* on the prestrain, ϵ_p is of the form,

$$\epsilon_p^* = \alpha_3 \epsilon_p^{1/2} \quad (5.6)$$

Again, α_3 is a function of particle geometry.

These four major areas required detailed study in order to test the Brown and Stobbs' model for general applications. The necessary experiments were considered earlier in Chapter 4, section 5. The important input of the model requires measurements of permanent softening as a function of prestrain in different volume fractions. The above features of the model were first studied using the spheroidized steels (see Chapter 4, section 2.1) in which a well defined Fe - Fe₃C system is obtainable. It should be noted that the average particle size in Table 4.2 is reasonably constant in the four steels. The results are generalized to include the HSLA steels in section 3.2 of this chapter. However, the data for both classes of steels are plotted together in some diagrams and some cross references will be necessary.

5.3.1 Spheroidized Plain Carbon Steels

(i) Permanent Softening and the Relationship to Prestrain

A typical form of the results of the experiments for permanent softening is shown in Fig. 5.12 (see section 5.3.2) plotted for the HSLA-B. The path OAB is the tensile stress-strain curve of the material. Superimposed for comparison with this curve are four compression stress-strain curves. These have been reflected across the strain axis and plotted in the tensile quadrant. As an example, the point B shows the case of a specimen loaded in tension to a prestrain

of 5%, unloaded along B C and compressed to produce the stress-strain path CDEF. To measure the permanent softening, the stress difference typically in the region E between the curves AB B and DEF was measured at the same total strain. In this region, E, the two curves are sensibly parallel, even though still non-linear and progressive measurements of the stress offset over a strain range of 1% yielded a mean value that was used to characterize the permanent softening.

The results obtained in this manner for the spheroidized steels are shown in Fig. 5.7(a). It is noted that the 1045 steel is not included here and in most of the results that follow on account of insufficient data. The results are plotted as $\frac{1}{2} \Delta \sigma_p$ vs. ϵ_p in accordance with eqn. (3.26) in order to represent the permanent softening as a measure of the mean matrix (back) stress due to internal stresses.

These results show that the permanent softening increases with prestrain, and for a given prestrain, it increases with the carbon content or the volume fraction of cementite particles in the steel.

The relationship between permanent softening and prestrains appears parabolic from Fig. 5.7(a) in accordance with the Brown and Stobbs' model. In order to verify this conclusion explicitly, Fig. 5.7(a) is replotted in Fig. 5.7(b) as a function of the square root of prestrain. It is evident that eqn. (5.1) is obeyed, and since the size and shape of the particles are approximately equal and spherical in the three steels, the slope of the lines, α_1 , therefore shows the effect of changing the volume fraction of the second phase elements in these materials. Thus, the first important prediction of the microscopic model of the BE due to Brown and Stobbs is verified.

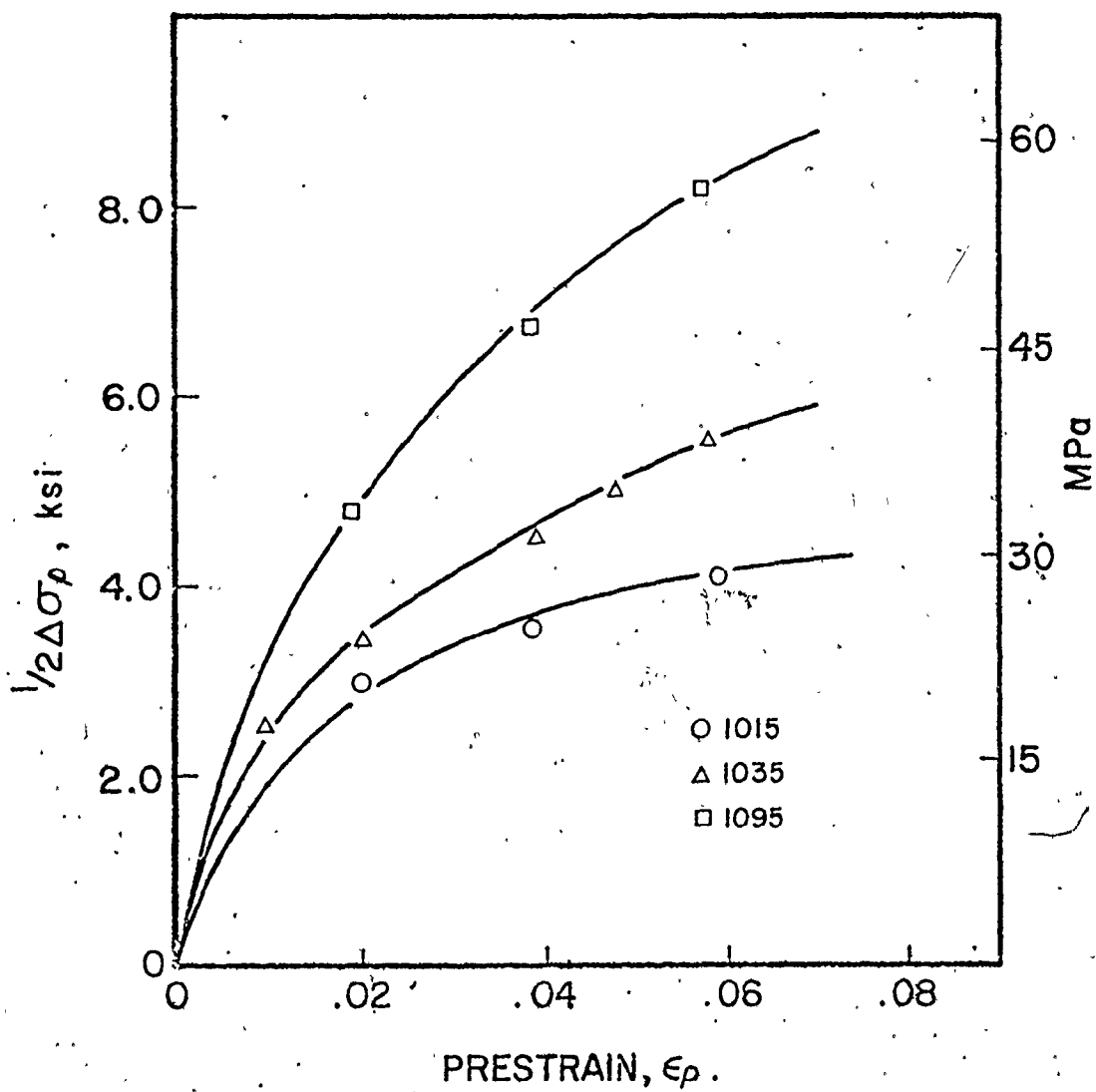


Fig. 5.7(a) Experimental measurements of permanent softening plotted as a function of prestrain for the spheroidized plain carbon steels.

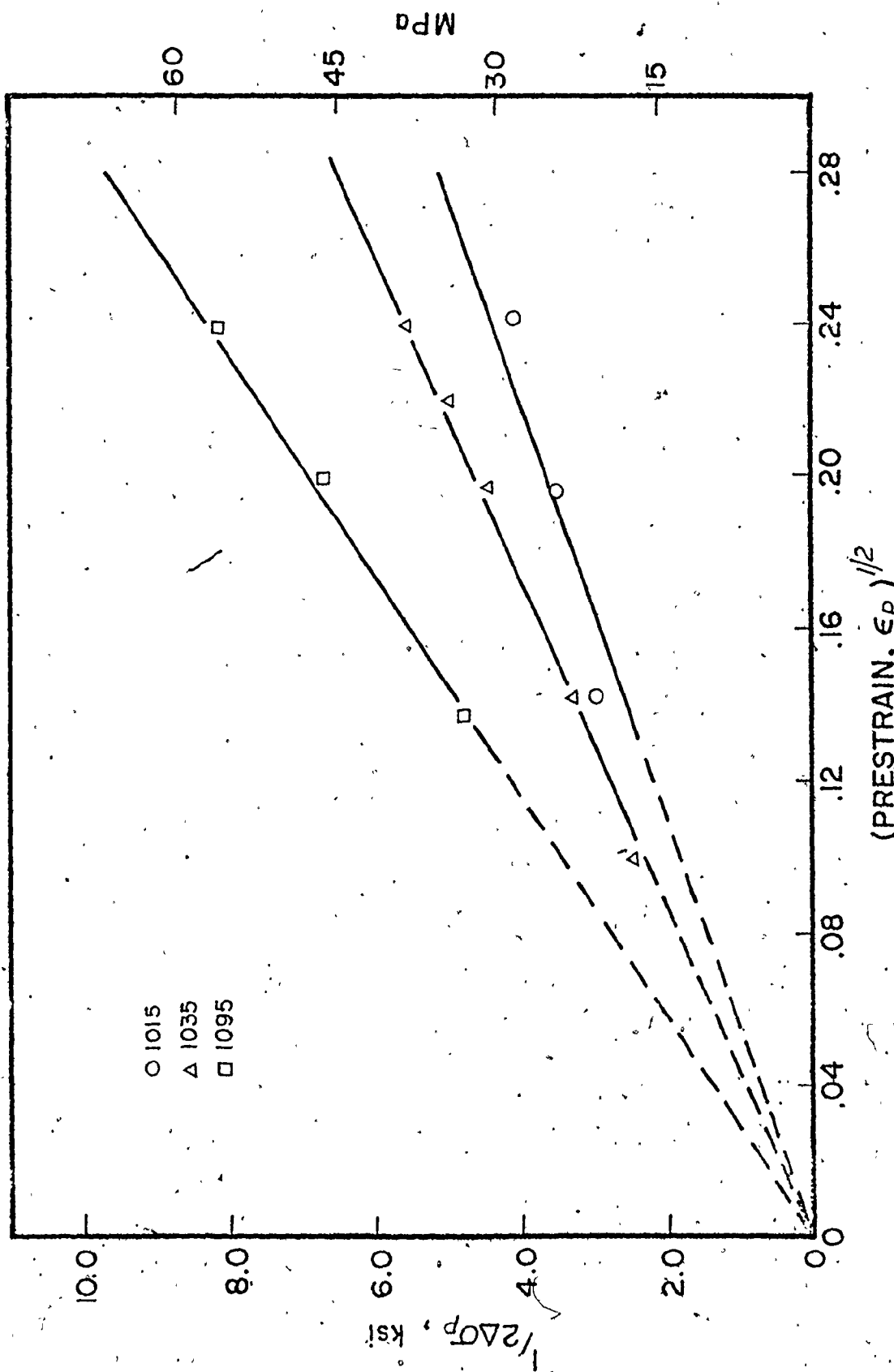


Fig. 5.7(b) A replot of Fig. 5.7(a) as a function of the square root of prestrain in order to verify the theoretical parabolic dependence of permanent softening on prestrain.

(ii) Permanent Softening and the Influence of Volume Fraction

The relationship in eqn. (5.4) is studied in Fig. 5.8 for the three spheroidized steels. The increasing carbon levels, .15% in 1015, .35% in 1035 and .95% in 1095 gave the volume fractions in Table 4.1 for these steels. Fig. 5.8 therefore shows the relationship between the measured permanent softening and the volume fraction at three pre-strain levels. The relationship is clearly linear and this verifies another important feature of the Brown and Stobbs' model given by eqn. (5.4).

It is instructive to note that although the theoretical linear relationship predicted by (5.4) is obtained, the results show what will be described as a mean threshold stress, $\langle \sigma \rangle_0$ at zero volume fraction. This aspect is not considered by the model. Both $\langle \sigma \rangle_0$ and the slope, α_2 of the lines may be observed to depend on and increase with the pre-strain. The implications of the threshold stress is discussed subsequently under item (iv) of this section.

(iii) The Bauschinger Effect Parameter, BEP and the Relationship to Prestrain and Volume Fraction.

Equation (5.2) was derived from the model as a parametric measure of the BE in terms of permanent softening and the total work hardening. The two characteristics of this parameter, that is, the BEP, namely, its independence of prestrain and the inverse relationship to $1/\sqrt{V_f}$ were also studied.

Fig. 5.9 shows the BEP plotted as a function of prestrain for the spheroidized and the HSLA steels. The results for the spheroidized steels only are important at this stage, although some of the general

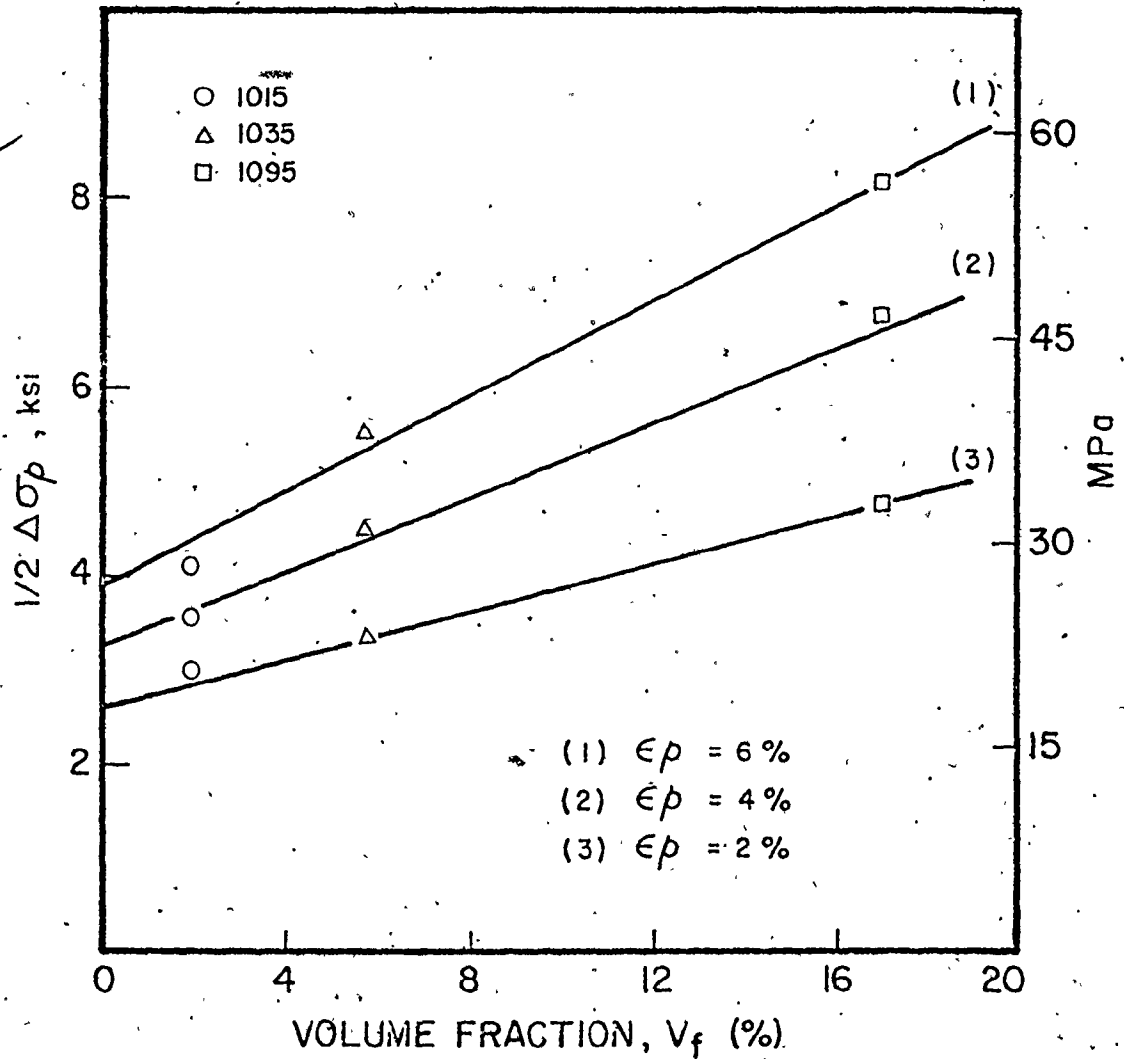


Fig. 5.8 Experimentally determined values of permanent softening plotted as a function of the volume fraction of the carbide particles in the spheroidized plain carbon steels.

remarks concerning the data will be applicable particularly to the HSLA steel C.

The spheroidized steels show high BEP values at small prestrains, but approximately constant values are obtained at higher prestrains. The results are interpretable in two parts. Firstly, at prestrains $> 4\%$, the BEP shows prestrain independence in accordance with the theory. However, at small prestrains, this relationship is not obeyed and with reference to the values of $\Delta\sigma_p$ in Fig. 5.7(a), this can only be due to the magnitude of the measured total work hardening, $(\sigma_f - \sigma_0)$. The tensile stress-strain curves of the spheroidized steels are not reported here but the steels all exhibited the type yield plateau shown by the HSLA steel-C in Fig. 4.3(c). The magnitudes of the corresponding yield point elongations given in Table 4.1 were large but decreased with increasing carbon content of the steels. Hence, the experimental measurements of the magnitude of $(\sigma_f - \sigma_0)$ obtained at small prestrains were also small and this led to the higher values of the BEP at small prestrains. It is possible to improve the results by back extrapolating the non-linear portion of the stress-strain curve from beyond the region of discontinuous yielding in order to measure a lower value of the yield stress, σ_0 at the point of intersection with the elastic loading line. However, this would introduce an arbitrary measure of σ_0 into the model, and so this technique was not adopted. However, since the BEP₀ determined at large prestrains for the spheroidized steels shows a behaviour which is approximately independent of the prestrain, it is concluded that one of the two important characteristics of the BEP is established for these materials.

The problem associated with the determination of the quantity

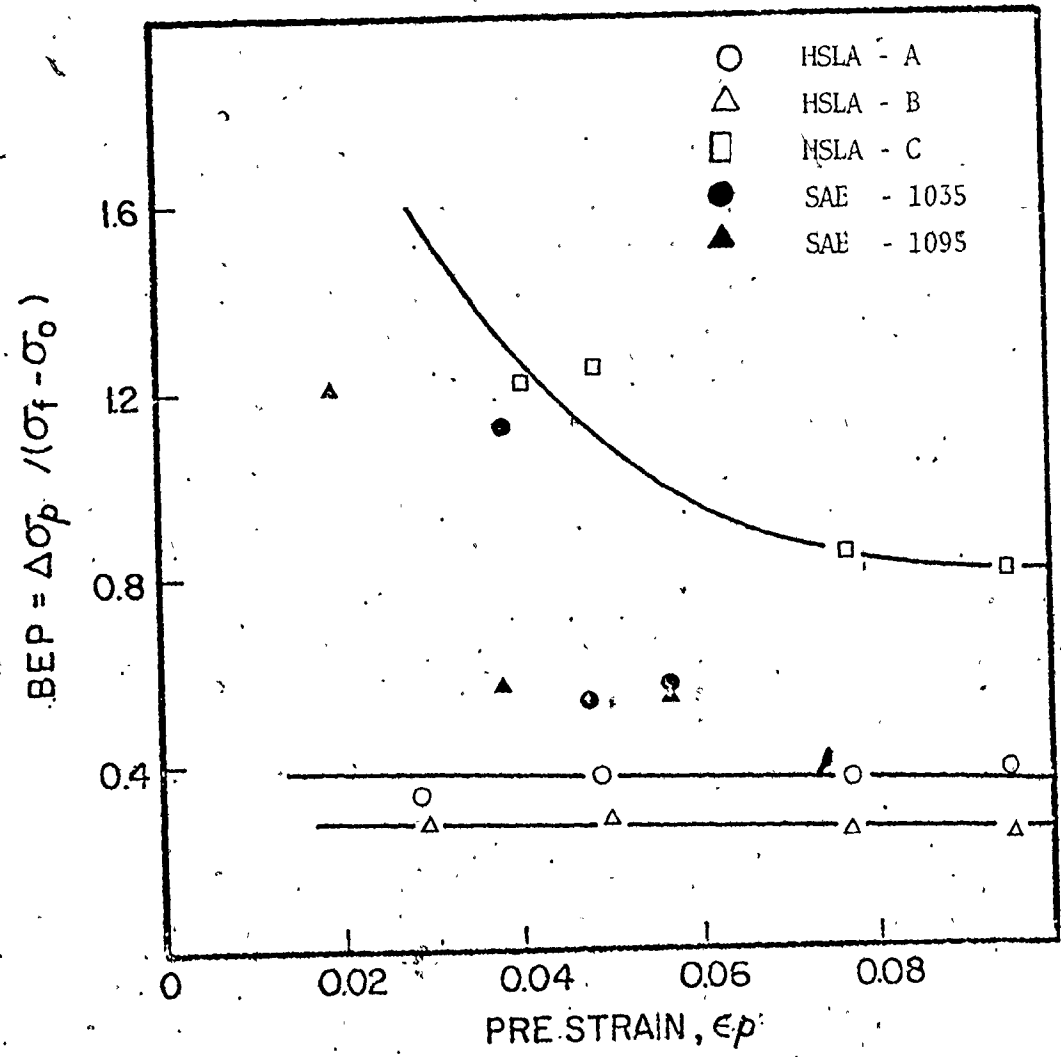


Fig. 5.9 The theoretical BEP as a function of prestrain.

$(\sigma_f - \sigma_0)$ in the case of materials which exhibit a large yield point elongation is also apparent in the diagram in Fig. 5.10 plotted to demonstrate the validity of eqn. (5.3). Only the data for the 1095 steel showed reasonable correlation with the theoretical line. Therefore, further consideration will be devoted to eqn. (5.3) and Fig. 5.10 when the results obtained for the HSLA steels are discussed in section 3.2 of this chapter.

(iv) The Development of Microscopic Incompatibility

Equation (5.5) developed in Chapter 3 was used to relate the observed permanent softening to the mean incompatibility strain, ϵ_p^* in two phase materials. For convenience, this equation is rewritten below:

$$\frac{1}{2} \Delta\sigma_p = 2\gamma\mu\mu' V_f \epsilon_p^* \quad (5.7)$$

where

$$\mu' = \mu^* / [\mu^* - \gamma(\mu^* - \mu)], \text{ and}$$

μ^* - the elastic shear modulus of the particles;

μ - the elastic shear modulus of the matrix;

V_f - volume fraction of second phase particles;

ϵ_p^* - the unrelaxed strain and

γ - Eshelby's [89] particle shape accommodation constant; γ is $\frac{1}{2}$ for spheres and $\frac{3}{4}$ for plates [102].

In order to apply the above equation, an additional assumption had to be made concerning the relative strength constants of the particles and the matrix. Since the elastic strength constant of the particles is unknown, it appears reasonable to assume that the modulus correction factor,

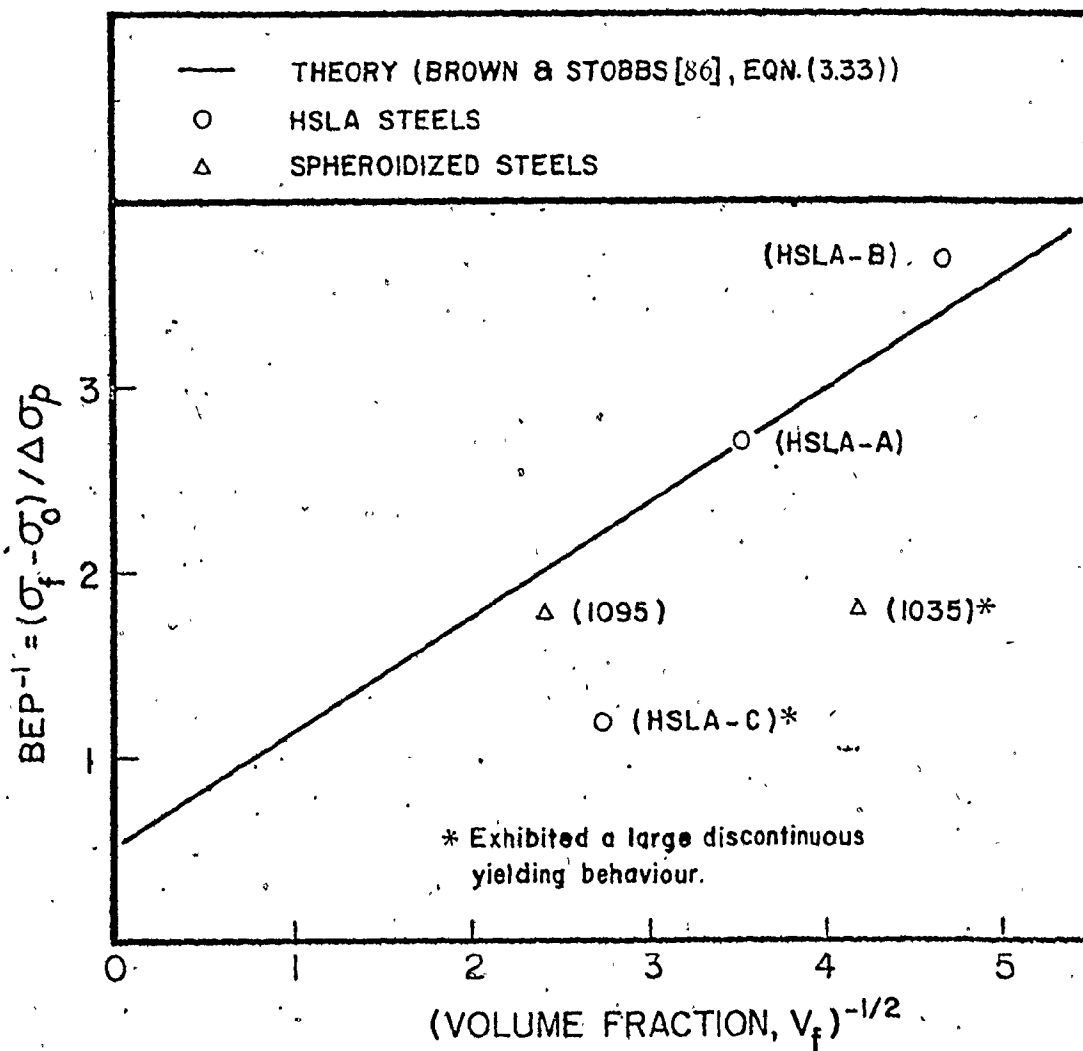


Fig. 5.10 A comparison of the experimentally determined values of the BEP with the theory due to Brown and Stobbs [86]

μ is unity. This means that during their elastic deformation, the matrix and the particles obey the same stress-strain law. Therefore, eqn. (5.7) can be approximated by

$$\frac{1}{2} \Delta\sigma_p = 2\gamma\mu \cdot \epsilon_p^* \cdot V_f \quad (5.8)$$

Now, if reference is made to eqn. (5.4) and to Fig. 5.8, it becomes evident that the slope, α_2 of the lines in Fig. 5.8 can be expressed as follows,

$$\alpha_2 = 2\gamma\mu \cdot \epsilon_p^* \quad (5.9(a))$$

Furthermore, from eqn. (5.6), the unrelaxed strain, ϵ_p^* is directly proportional to the square root of the prestrain, ϵ_p . If this behaviour is assumed, then eqn. (5.9(a)) becomes,

$$\alpha_2 = (2\gamma\mu \cdot \alpha_3) \epsilon_p^{1/2} \quad (5.9(b))$$

where α_3 from (5.6) introduces a particle size coefficient. Equation (5.9(b)) is shown plotted in Fig. 5.11(a) and the mean slopes, α_2 were determined from Fig. 5.8 for the spheroidized steels; the results for the HSLA steels are discussed in section 3.2 of this chapter. Fig. 5.11(a) is therefore a verification of the parabolic relationship between the prestrain, ϵ_p and the unrelaxed strain, ϵ_p^* as predicted theoretically by eqn. (5.6).

Having established that eqn. (5.6) is, for all practical purposes, obeyed experimentally, some consideration can now be devoted to the development of the unrelaxed strain, ϵ_p^* as a function of the imposed prestrain. To this end, it may be noted that in relating the permanent softening to volume fraction by means of Fig. 5.8 and eqn. (5.8), no

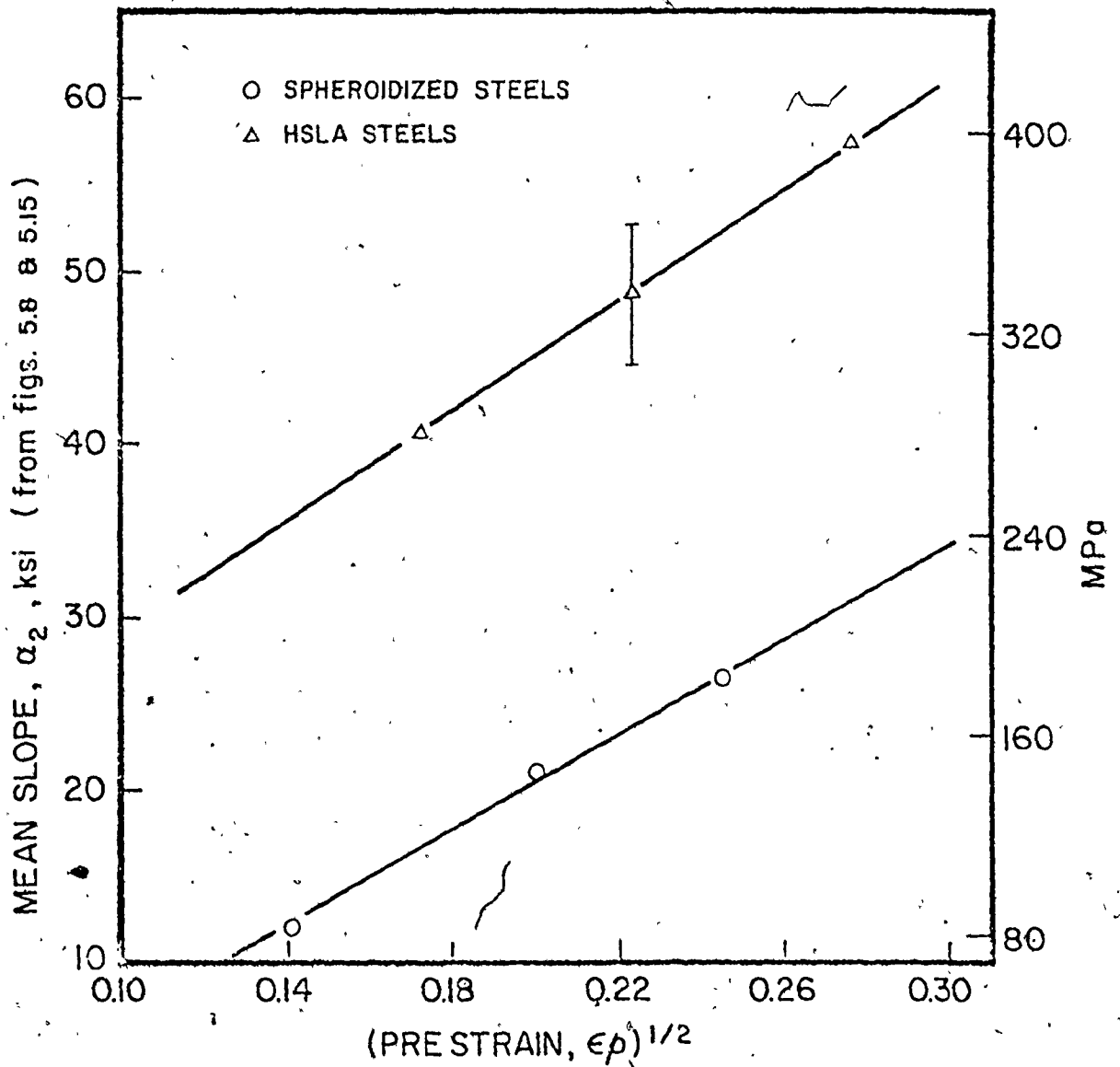


Fig. 11(a) A verification of the parabolic relationship between the prestrain and the unrelaxed strain. This diagram is derived from the data of Figs. 5.8 and 5.15 and using the model in equation (5.9).

quantitative account has been taken of α_3 , that is, the effect of the size of the second phase material in the structure of the steels. The contribution from particle size has, in fact, been considered insignificant on account of the long range nature of the internal stresses to which permanent softening is attributable. The long range concept as applied to internal stresses means that the stresses are averaged over the deforming plastic volume and as a result, the net effect of long range stresses, in this case, $\langle \sigma \rangle_m = \frac{1}{2} \Delta \sigma_p$ is insensitive to fine dislocation and particle distribution details. Furthermore, the term $(8\pi b/\alpha_3^2 r_0 \epsilon_p)^{1/8}$ in eqn. (3.30) which measures the size effect of structural particles on the flow stress of a two phase material is easily recognizable as close to unity for various practical estimates of r_0 and ϵ_p . It is therefore justifiable to neglect the effect of particle size on the permanent softening and on the unrelaxed strains which are now to be calculated. However, with reference to Table 4.2, the size of the cementite particles in the spheroidized steels are approximately of the same order of magnitude.

In order to calculate the unrelaxed strains, the shape effect of the particles was accounted for by choosing the shape accommodation factor, γ as $\frac{1}{2}$ for spherical particles in accordance with the calculations of Brown and Clark [102]. The strength constant, μ for steel was chosen as 11.3×10^6 psi (77.86 (Pa) and α_3 was set to unity. Therefore, using Fig. 5.11(a) to determine the slope, α_2 for any given prestrain, it was possible to calculate the unrelaxed strains as a function of the prestrain from eqn. (5.9). The results are shown in Fig. 5.11(b).

It is seen that the unrelaxed strains increase parabolically with

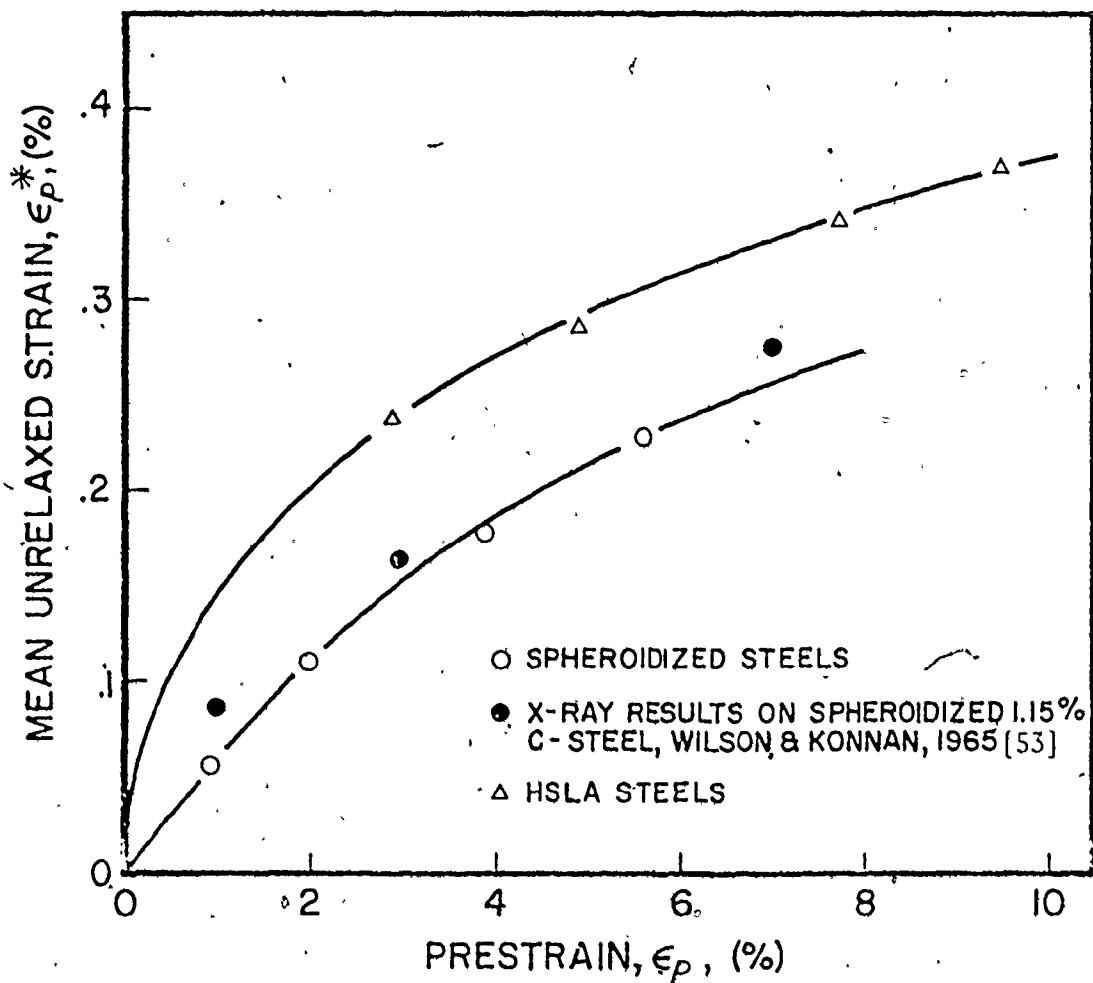


Fig. 5.11(b) The development of microscopic strain incompatibility (internal stresses) as a function of the imposed deformation in two phase spheroidized and HSLA steels.

prestrain (the parabolic relationship was verified previously using Fig. 5.11(a)). They measure the net incompatibility in the microstructure caused by internal stresses which are produced by the presence of a hard and undeformable volume fraction of second phase particles in a plastically deformable matrix.

The two diagrams of Fig. 5.11 also include the data for the HSLA steels, but at this stage, only the data for the spheroidized steels are of interest in the discussion. In order to make a quantitative comparison of the results obtained here in this present study, with those obtained by other methods three experimental points extracted from the work of Wilson and Konnan [53] are shown plotted in Fig. 5.11(b) with the results for the spheroidized steels. The agreement is excellent and of importance because of the different technique used by these authors to obtain the values of the unrelaxed strain. These authors had measured what is termed unrelaxed strains in this work by X-ray methods. Residual lattice strains were measured in a 1.15% carbon spheroidized steel at three prestrain levels. Tensile strains were found to exist in the cementite spheroids while the strains in the ferrite phase were compressive. The plotted points are the net values of the mean result of these measurements interpretable as unrelaxed strains in the context of this present investigation.

As stated earlier, this work was undertaken, in part, to generalize the Brown and Stobbs' model for structural steels. Some of the aspects of the model studied here have previously been investigated by Atkinson et al [52] for their ideal system (single crystals of copper-silica) of dispersion hardened materials. The volume fraction of the

particles was small, < 1% and the maximum particle size was 600\AA . In this thesis, it is noted that, in addition to the complexity of the morphology of the particle phase, the maximum volume fraction studied is about 17% and the maximum particle size is about 9000\AA . Despite these differences, the results obtained here are qualitatively in good accord with those reported by Atkinson et al [52] for the copper - silica system of small particles. Although Atkinson et al obtained the Perfect Memory Solid (PMS) behaviour between ϵ_p^* and ϵ_p in tests conducted in liquid nitrogen (-196°C), the room temperature tests to which the results presented here are comparable showed hardly any evidence of perfect memory behaviour. Perfect Memory Solid (PMS) behaviour may be defined by a one to one relationship between ϵ_p^* and ϵ_p which was prominent at low temperatures in the copper - silica systems at small prestrains. In this case, the strains in the particles are exactly the same as the imposed prestrain so that the particle deformation history retains a "perfect memory" of the macroscopic deformation imposed. In the steels studied here, it would appear that the plastic relaxation processes produced by local dislocations motion in the vicinity of the particles become active even at small prestrains. Consequently, the ϵ_p^*/ϵ_p relationship in Fig. 5.11(b) shows an approximately parabolic behaviour even at small prestrains. Stoltz and Pelloux [28] have also calculated what was termed critical unrelaxed strains in a system of commercial quality precipitation hardened aluminum alloys. The critical unrelaxed strains were calculated using an equation of the type in (5.7). Their results also qualitatively agree with the results presented here.

In view of the results in Fig. 5.8 in which a threshold mean

stress, $\langle \sigma \rangle_0$ is shown to exist at zero volume fraction, it appears necessary to modify eqn. (5.7) for systems in which the modulus correction factor, u is of the order of unity to read as follows:-

$$\langle \sigma \rangle_m (= \frac{1}{2} \Delta \sigma_p) = \langle \sigma \rangle_0 + 2\gamma u V_f \epsilon_p^* \quad (5.11)$$

This modification introduces the threshold mean stress, $\langle \sigma \rangle_0$ which for the Fe - Fe₃C system studied is not necessarily negligible compared to the measurements of permanent softening. The origin of the threshold mean stress, defined by $\langle \sigma \rangle_0$ in eqn. (5.11) cannot be fully explained in the context of the work. It may relate to the existence of an initial incompatibility due to the previous deformation processing of the materials, particularly in manufacturing. However, it is seen in Fig. 5.8 that the threshold mean stress increases with prestrain (from about 2600 psi (18 MPa) at 2% to about 3900 psi (27 MPa) at 6%). On this account, the origin of the stress, $\langle \sigma \rangle_0$ would appear to be unconnected with either the initial incompatibility introduced during the deformation processing in manufacturing or the transformation strains produced by heat treatments, as these would have the same effect for different pre-strain levels. It is also likely that the stress $\langle \sigma \rangle_0$ could be due to the internal stresses developed by the inhomogeneous deformation of the individual grains in a polycrystalline material. However, the origin of the threshold mean stress remains, at the moment, a moot point, but it is noted that Wilson's results [51] on plain carbon steels also indicated its existence.

This completes the study of the theoretical conclusions derived from the model of work hardening in two phase materials due to Brown

and Stobbs. This model has been studied so far using the well defined Fe-Fe₃C system of spheroidized steels. In the following section, this study is extended to the HSLA steels. Prior to this, it is necessary to re-emphasize certain of the microstructural features of the HSLA steels which are relatively ill defined. Prominent among these is the exact type and morphology of the system of second phase particles which are present in these materials. The phases may consist of: (i) carbides of the Fe₃C type, (ii) carbides and carbonitrides of the microalloying elements in the steel, (iii) regions of martensite or retained austenite, and (iv) local variations and mixtures of these. It is also unresolved as to how much of these individual phases are present and what fraction of these are essentially of the strong and undeformable type. The complications arise because the distribution of the phases in the HSLA steels is not in equilibrium but is determined by the history of prior heat treatment and cooling rate. Consequently, it becomes difficult with these materials to attempt to specify different elastic constants for the particle phase(s). Hence, the assumption employed in the case of the spheroidized steels, that is, $\mu' = 1$ will again be made. Also, the total volume fraction for all the non ferritic phases estimated from the micrographs in Chapter 4 by the line - intercept - ratio method will be used. Finally, the shape of the particles in the HSLA steels require some consideration in relation to the mechanical processing of the steels. A reasonable assumption here appears to be to select disc type shapes or platelets sandwiched in the rolling plane for which the shape accommodation factor, γ in eqn. (5.8) is calculated by Brown and Clark [10] as 3/4, if the plane of the plates are located parallel to

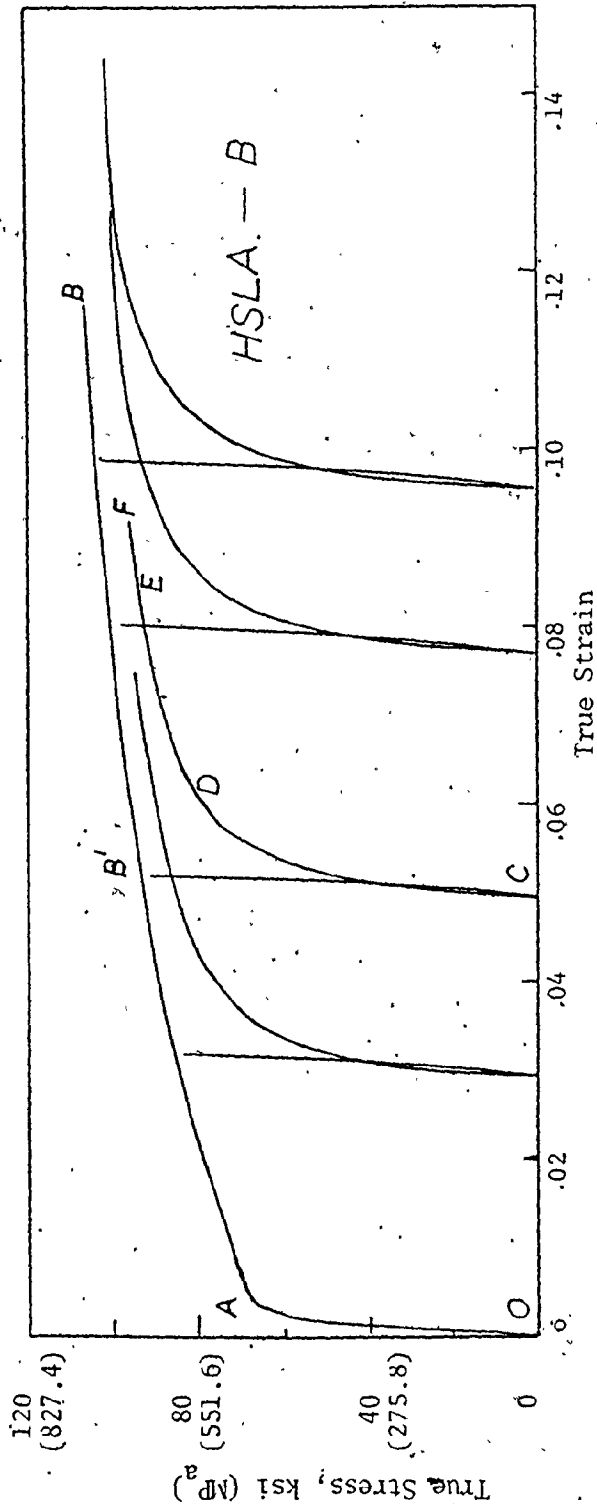


Fig. 5.12 A typical set of forward and reverse flow curves employed to experimentally determine the permanent softening.

the direction of testing.

It is instructive to refer to the tensile stress-strain curves of the three HSLA steels in Fig. 4.3. It will be evident that the HSLA-A is basically a high work hardening rate material, exhibiting a highly rounded stress-strain curve; the HSLA-B has a slightly less rounded σ - ϵ curve, showing a slight kink at yield; and the HSLA-C possesses a prominent yield point elongation of about 2½%. These characteristics are to be noted on account of their possible influence on the results to be reported below involving the application of not only the Brown and Stobbs' model to these materials but also certain results based on the empirical quantification of the Bauschinger Effect. The four areas of the Brown and Stobbs' model listed at the beginning of section 3 of this chapter will now be discussed based on the assumptions made above in relation to the HSLA steels.

5.3.2 The High - Strength - Low - Alloy Steels

Fig. 5.12 shows the results of the experiments performed to measure permanent softening in the case of the HSLA steel B. This diagram was described in detail previously in section 5.3.1 under item (i). Tests of this type were also performed for the other HSLA steels and Fig. 5.13 shows a plot of the permanent softening in terms of $\frac{1}{2} \Delta\sigma_p$ as a function of the prestrain, ϵ_p for the three HSLA steels. Replotting Fig. 5.13 in terms of the square root of the prestrain in Fig. 5.14 shows the same basic features as for the spheroidized steels in Fig. 5.7(b). It is apparent from the data that equation (5.1) is also obeyed by the HSLA steels.

The similarity of the results in Figs. 5.14 and 5.7(b) pro-

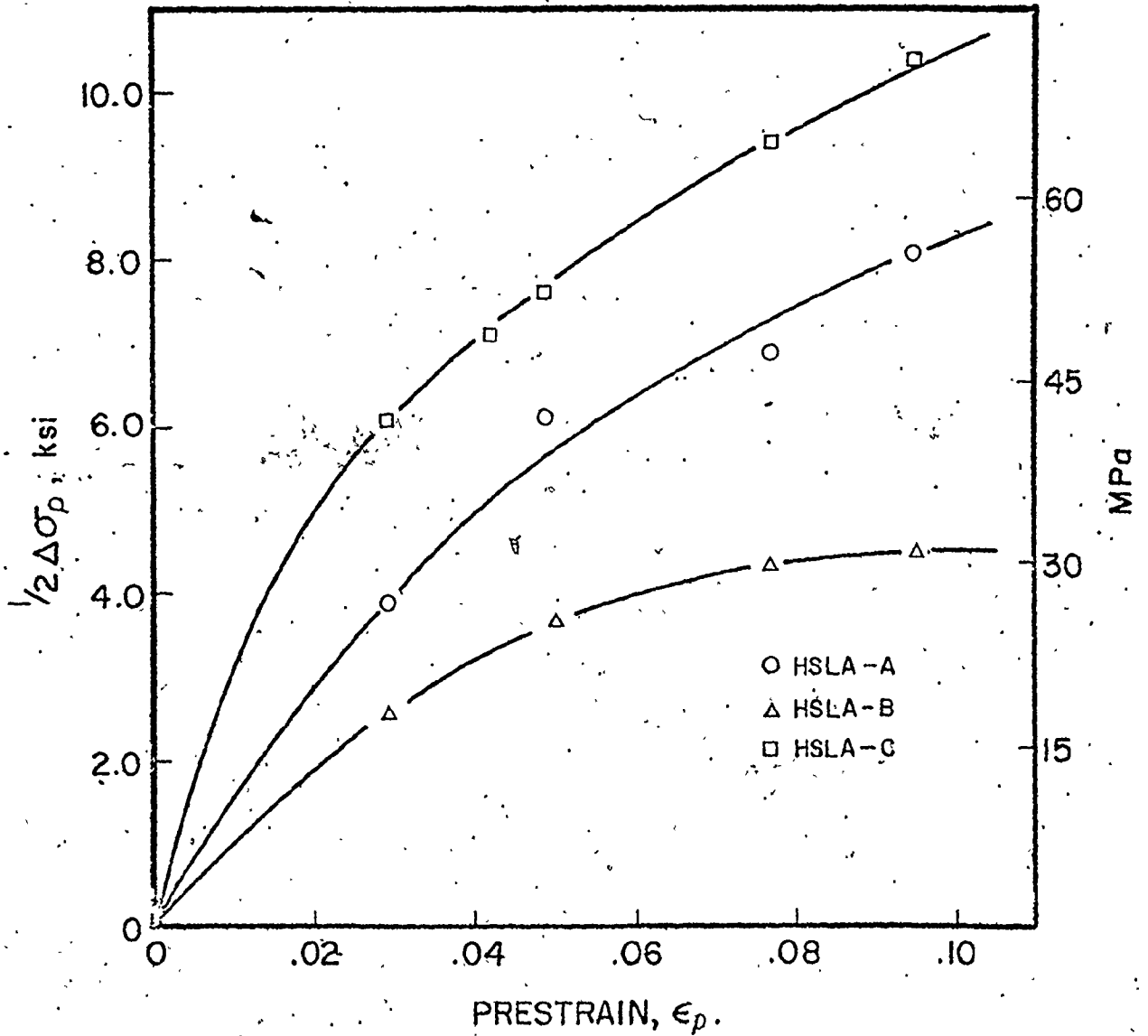


Fig. 5.13 Experimental measurements of permanent softening plotted as a function of prestrain for the HSLA steels.

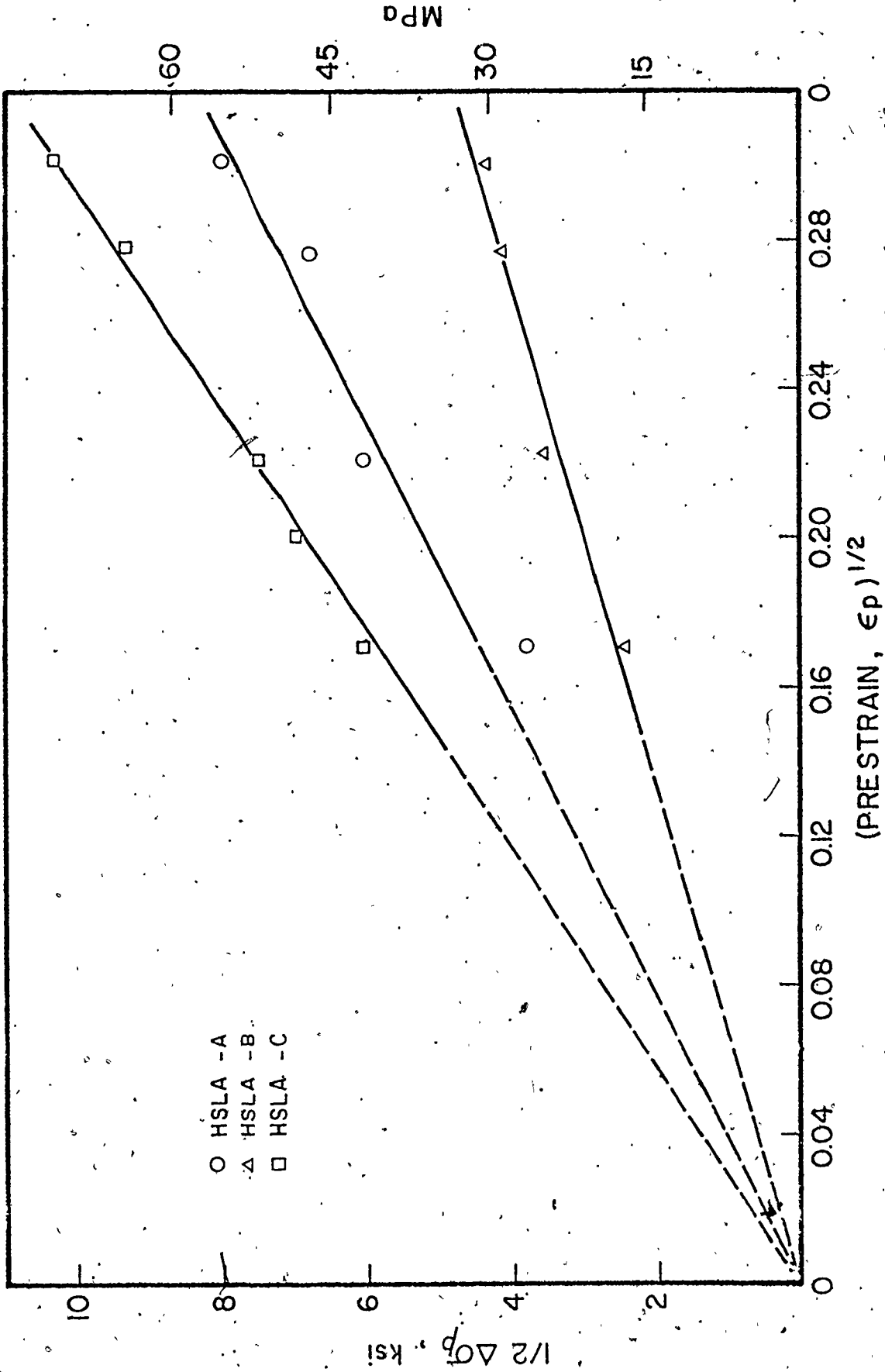


Fig. 5.14 A replot of Fig. 5.13 as a function of the square root of prestrain in order to verify the parabolic relationship of permanent softening with prestrain in the case of the HSLA steels.

vided an interesting beginning for the study of aspects of the microscopic model of the BE for HSLA steel. In preference to immediately pursuing the next aspect, namely, the influence of volume fraction, it was decided at this stage instead, to corroborate the estimates of the volume fraction of the second phase elements in the HSLA steels determined micrographically in Table 4.4 with those obtained from a comparison of the permanent softening data of the HSLA and spheroidized steels. For this purpose, an interpolation method using Figs. 5.13 and 5.8 was adopted. The magnitudes of permanent softening were interpolated at the prestrains, 2, 4 and 6% using Fig. 5.13. The values thus obtained were then used in Fig. 5.8 to further interpolate for the limits of equivalent volume fractions of the HSLA steels. The minimum and the maximum of the interpolated volume fractions obtained are compared in Table 5.1 below with the values obtained using the micrographic technique discussed in Chapter 4, section 2.2.

TABLE 5.1

Interpolated and Micrographic volume fractions of the HSLA steels.

HSLA	Volume Fraction (%)		
	Interpolated Values		Micrographic Values
	Min.	Max.	
A	2.4	10.0	8.0
B	-	1.4	4.5
C	18.0	19.0	13.2

Some discrepancy was expected in the results and while Table 5.1 does not confirm the exact order of magnitude of the volume fractions, the increasing order of the volume fractions in the two sets of data is an important information. However, it was judged preferable to use the values of volume fraction obtained by the metallographic method for the further analysis of experimental data. The plot of the observed permanent softening versus these micrographic volume fractions at three prestrain levels in Fig. 5.15 gives not only a reasonably linear trend but also indicates the threshold mean stress $\langle \sigma \rangle_0$ at zero volume fraction. These data indicate that the linear dependence of $\Delta \sigma_p$ on volume fraction as required by eqn. (5.4) is, for all practical purposes, also satisfied for the HSLA steels.

The use of permanent softening data to characterize the BE in terms of the BEP in eqns. (5.2) and (5.3) yielded the results shown previously in Figs. 5.9 and 5.10. In Fig. 5.9, the results obtained for the HSLA steels A and B excellently show the predicted independence of the BEP with respect to the prestrain. In the case of the HSLA steel C, the BEP can be interpreted as being independent of prestrain only at large prestrains. The results show again the effect of a discontinuous σ - ϵ behaviour on the parameter $(\sigma_f - \sigma_0)$ in the BEP. For the HSLA steels A and B, there is little ambiguity in the determination of $(\sigma_f - \sigma_0)$ on account of the rounded σ - ϵ tensile curve of these materials (see Figs. 4.3(a) and (b)). For the HSLA-C, the problems discussed earlier in the relation to the magnitude of $(\sigma_f - \sigma_0)$ due to the presence of the yield point phenomenon in the spheroidized steels also apply, see Fig. 4.3(c) and section 3.1, this chapter, item (iii).

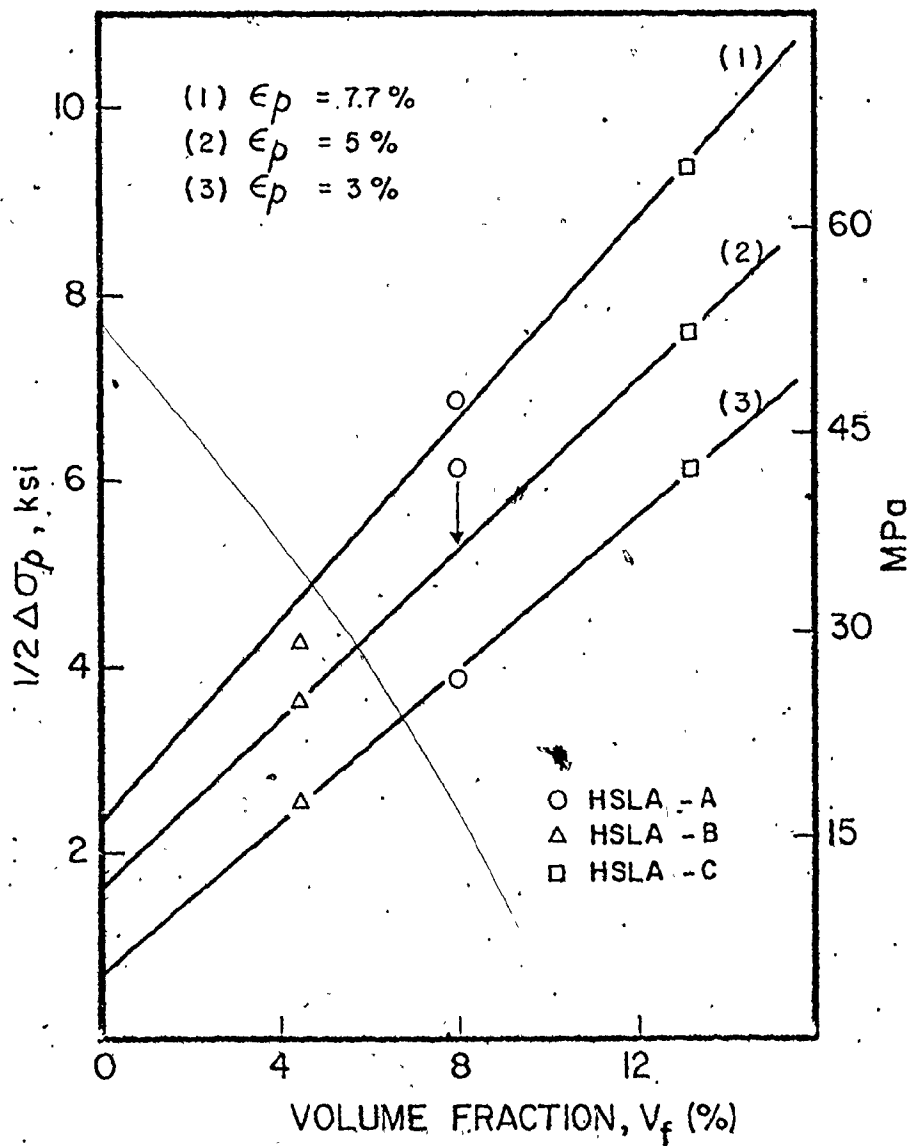


Fig. 5.15 Experimentally determined values of permanent softening plotted as a function of the total volume fraction of non-ferritic products in the HSLA steels.

The theoretical dependence of the BEP with volume fraction in Fig. 5.10 also shows that except in the case of the HSLA-C, the results are in good accord with the microscopic theory of the BE. In fact, the experimental results for the HSLA steels A and B correlate with the theory much better than those of the spheroidized steels due to the rounded nature of the σ - ϵ behaviour of these materials. It is therefore concluded that the two basic characteristics of the BEP in relation to the prestrain and volume fraction are verified both for the HSLA and spheroidized steels.

The final aspect of the Brown and Stobbs' model which relates the development of microstructural incompatibility, ϵ_p^* through the permanent softening, $\Delta\sigma_p$ to the prestrain, ϵ_p , eqns. (5.15) and (5.6) were also studied for the HSLA steels. The assumptions concerning the nature of the second phase elements in the HSLA steels were discussed at length at the end of section 3.1 of this chapter. The results on the development of the unrelaxed strain, ϵ_p^* with respect to the prestrain was plotted side by side with those obtained for the spheroidized steels in Figs. 5.11(a) and (b). Again, it is noted with reference to Fig. 5.11(a) that the theoretical relationship of eqn. (5.6) holds also for the HSLA steels. It is also noted that the calculations that led to the results for the HSLA steels assumed the model of Fig. 5.15 in order to relate the permanent softening to the volume fraction in the same manner. The different trends in the results are due firstly to the magnitude of the slopes, α_2 in Figs. 5.8 and 5.15 and secondly to the specification of $\gamma = \frac{1}{2}$ for the spherical dispersoids in the plain carbon steels and $\gamma = \frac{3}{4}$ for the disc-shaped particles assumed in the case of

the HSLA steels.

This then completes the direct study of the microscopic theory of the BE based on the model developed by Brown and Stobbs. The results obtained in the process of verifying the theory for general application to structural steels have shown that the model is valid in general although certain input parameters have to be determined with care. The theory was directly based on a macroscopic interpretation of internal stresses caused by the inhomogeneity of the deformation associated with elastic - plastic flow of two phase materials. Many structural materials fall into this class of dispersion strengthened alloys. On this account, it is useful to include some discussion on the implications of internal stresses in some practical cases and to study the consequences of the internal stresses in experiments where changes in the loading path can be introduced. However, prior to this discussion, it is necessary to summarize the salient features of the results obtained so far.

5.3.3 Summary of Aspects of the Microscopic Theory of the Bauschinger Effect

In the analyses presented so far, the BE has been studied microscopically in terms of internal stresses which arise on account of the inhomogeneous plastic deformation of a material system consisting of soft and hard phases. Certain assumptions had to be made concerning the relative strength constants of the matrix and particles. The particles in the spheroidized steels were further assumed to be spherical and to consist mainly of cementite (Fe_3C). Disc shaped particles were assumed for the HSLA steels. It was also pointed out that several types

types of particle morphologies are possible in this system. It is therefore difficult to define the amount of the non-ferritic phases which are essentially hard and undeformable or the relevant elastic constant for the particles in this case. Despite these deficiencies, the salient principles of the Brown and Stobbs' model of the BE have been quantitatively studied and successfully applied to a wide variety of structural steels.

From the results discussed so far, the important features of the Brown and Stobbs' microscopic model of the BE can be summarized as follows:-

- (a) The model applies in general to steels strengthened by a coarse dispersion of hard particles. It basically describes plastic deformation as a two phase elastic-plastic phenomenon in which the a particle phase plays a major role in determining the work hardening behaviour.
- (b) The mean effect of internal stresses developed during plastic deformation is manifested as permanent softening and this provides a quantitative means of investigating the BE.
- (c) The permanent softening is theoretically proportional to the square root of the prestrain in forward loading and to the volume fraction of second phase particles. These features have been verified experimentally for a wide range of spheroidized plain carbon and HSLA steels.
- (d) The Bauschinger Effect has been defined and measured as the fractional contribution to total work hardening due to elastic back stresses using the parameter, BEP. The theoretically predicted

invariance of the BEP with prestrain and the relationship to volume fraction have been correlated with experimental data again not only for the simple well characterized microstructures of the spheroidized plain carbon steels but also in complex HSLA steels.

(e) The origin of the Bauschinger Effect has been traced to internal stresses which arise on account of the microscopic inhomogeneity of plastic deformation. The development of this inhomogeneity, vis à vis the internal stresses was studied quantitatively in terms of unrelaxed or incompatibility strains. A simple continuum model of two phase deformation was employed for this purpose and the results were shown to be in good accord with theoretical predictions utilizing the physics of dislocation mechanisms.

5.4 Implications of Internal Stress in Cold Worked Materials

The consequences of internal stresses have wide ranging implications not only in the work hardening behaviour of materials in the manner discussed above, but also in the dimensional stability of certain cold formed metal parts. The case of spring back in which an overall change in curvature occurs when a sheet is unloaded after forming is a problem common to both the automotive and appliance industries. This has been the subject of a recent study by Duncan [103] in which the spring back in shallow draw die formed panels was shown to relate to the effect of residual stresses.

Pepe [47] has also studied the hydrostatic cold extrusion of an HSLA steel. It was found that the tensile yield strength of the extruded rods was increased while the compression yield strength was decreased. This, of course, is the classical case of the BE, however, the internal stresses developed during the deformation processing are capable of producing dimensional changes as well.

TABLE 5.2

Dimensional changes in 1045 steel rods due to straightening after Cold Drawing.

Drawing Strains $-\epsilon_d$ (%)	Recovery Strains ϵ_{rec} (%)
5.8	.14
8.3	.27
10.5	.39
11.8	.91
13.5	1.4
21.4	1.90

In a study carried out in Brazil on the dimensional changes of 1045 steel cold drawn rods [104], a series of six hyperboloid rolls were used to flexually straighten the drawn rods. Measurements were made of the diameter of the rods before and after straightening. The results, presented in Table 5.2 show that the diameters were increased after straightening by a small amount. This increase in diameter as measured by the recovery strains, ϵ_{rec} generally increased with the imposed drawing reduction, ϵ_d . In relation to internal stresses it is important that any changes in the dimensions were observed at all. While the calculated recovery strains do not measure internal stresses directly in the sense explored in this thesis, they relate to the net change in the internal stress distributions produced by the straightening operation. They also show the kind of dimensional stability problems that may be encountered on account of large internal stresses.

Further experimental evidence of the implications of the general concepts of internal stresses is provided subsequently. The discussion utilizes experimental results obtained from programmed tests in which certain variations in the loading path were introduced in order to study the consequences of internal stresses.

5.5 Implications of the Mean Matrix Stress

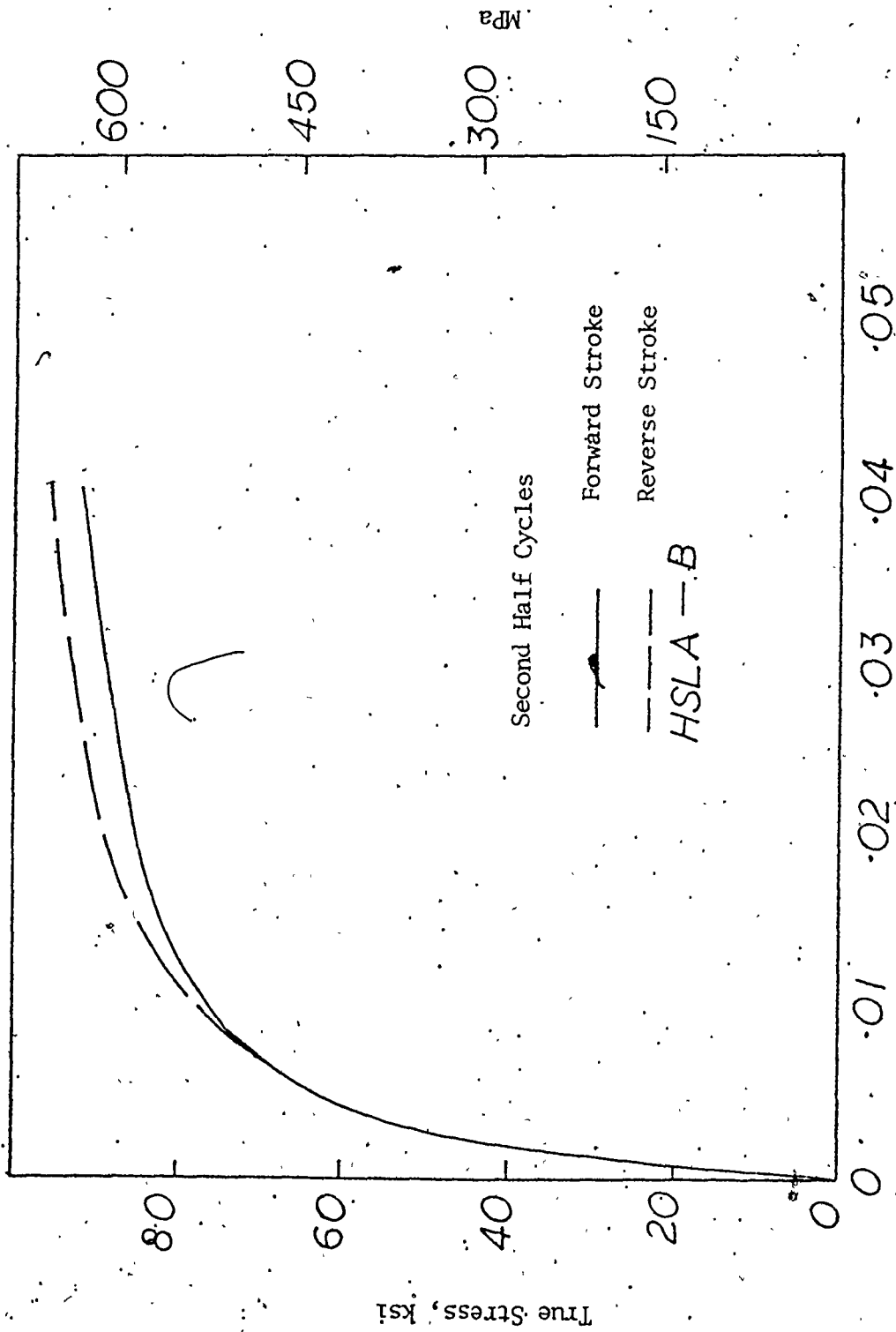
Two types of experiments were described in Chapter 4, section 5.2. In one case, a quasi - static cyclical loading programme was proposed. The second experiment involved the use of large plastic overstrains to promote structural damage. The results obtained are presented in what follows and particular attention will be paid to the implications of the concept of the mean matrix stress.

5.5.1 The Occurrence of Cyclic Loop Symmetry

The cyclic stress-strain curves presented earlier in Fig. 4.10 were obtained using a single test sample of the HSLA-B. The initial forward path was in tension and the strain amplitude was increased during the forward stroke of each of the four cycles shown.

The forward and reverse curves of Fig. 4.10 are superimposed for comparison in Figs. 5.16 (a), (b) and (c). In these diagrams, the stress-strain origin of the forward curve (the full lines) is of course the same as the origin O, in Fig. 4.10. The origin of the reverse curves (the dashed lines) was taken as the point of intersection, C of the unloading line with the strain axis. For the reverse curves then, the strain axis measures the magnitude, $|\epsilon_r|$, of the reverse strain in the direction, CO and the stress axis measures the magnitude of the compressive stress. A comparison of Figs. 5.16(a), (b) and (c), shows that the symmetry of the forward and reverse curves is improved by increasing the number of cycles; near symmetry is attained in the fourth half cycles. Figs. 5.17(a) and (b) show similar results for the dual phase HSLA steels D and E respectively. As in Fig. 4.10, cyclic symmetry is improved with the number of fully reversed tension - compression loading paths. The curves also show the expected cyclic hardening and for the dual phase steels, the high initial work hardening rate of the first forward curve (the rounded path OAB, Figs. 5.17(a) and (b)) which is the major attraction of these materials is evident.

Cyclic symmetry is to be expected as a consequence of the back stresses created during the individual half cycles of the deformation paths in Figs. 4.10 and 5.17. The internal stresses created, for instance,



Forward and reverse true strain.

Fig 5.16(a) A superimposition of the forward and reverse cyclic curves of Fig. 4.10 used to demonstrate the symmetry of the σ - ϵ loops.

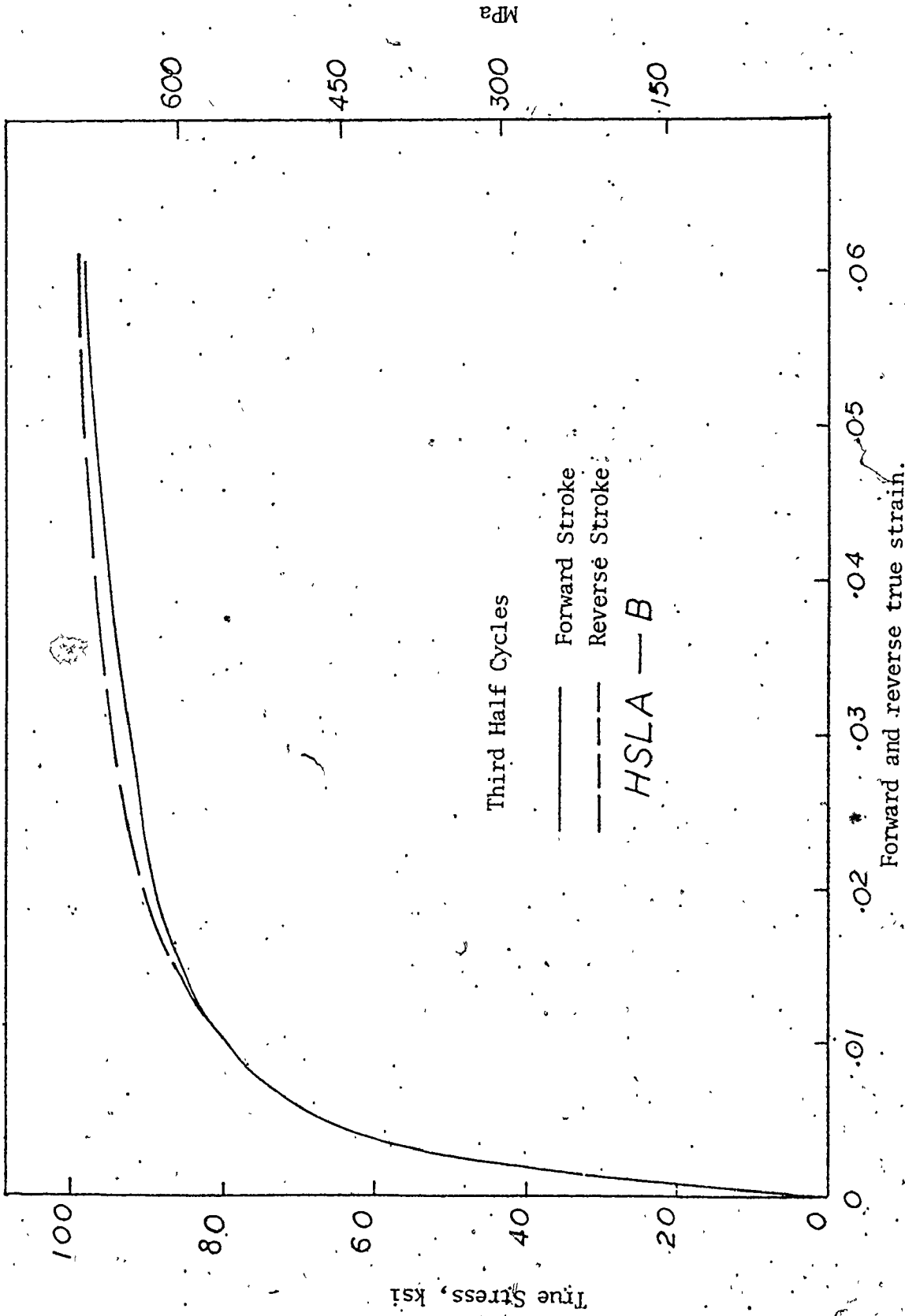


Fig. 5.16(b) A superimposition of the forward and reverse cyclic curves of Fig. 4.10 used to demonstrate the symmetry of the σ - ϵ loops.

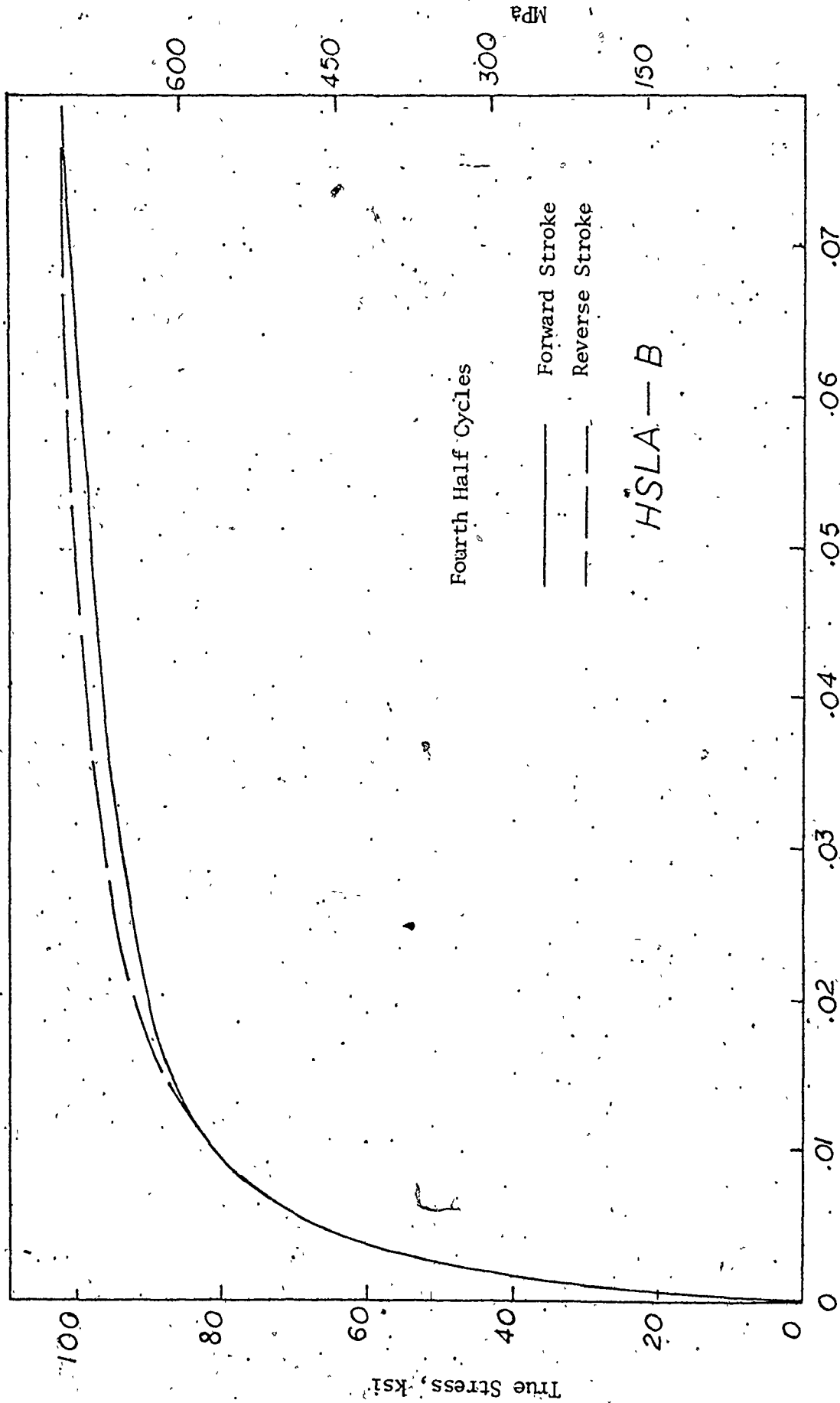


Fig. 5.16(c) A superimposition of the forward and reverse cyclic curves of Fig. 4.10 used to demonstrate the symmetry of the σ - ϵ loops.

in the forward stroke become annihilated initially prior to the creation of a new distribution during reverse straining. After the first few complete strain cycles which may be viewed as necessary to settle the structure, symmetry of the forward and reverse loops occurs. This indicates that the same order of events are taking place in the forward and reverse strokes, namely, the annihilation of previous back stresses and the creation of a new distribution. Notice that the typical point Q on the reverse curves compared to the point P shows the BE whether in tension - compression or compression - tension.

5.5.2 The Effect of Structural Damage

In the type of continued strain cycling discussed above, the pattern of internal stresses in one half cycle is reversed during the subsequent reverse half cycle. Since the internal stresses are developed by the inhomogeneity of the deformation characteristics of the matrix - particle continuum, it appears possible to reduce or even completely eliminate internal stresses by means of structural damage. If the strains are sufficiently large during prestraining, structural damage occurs in the form of particle cracking or interface voiding. This should relieve some of the particle stresses and hence reduce the magnitude of the mean stress in the matrix. Subsequent plastic response to external loads would then reflect basically, the behaviour of the matrix. This was the concept behind the experiments proposed in Chapter 4, section 5.2. The 1095 spheroidized steel was used in this experiment. Tensile necking was considered a sufficient overstrain to cause structural damage. The magnitude of the instability strain of the 1095 steel was about 10%.

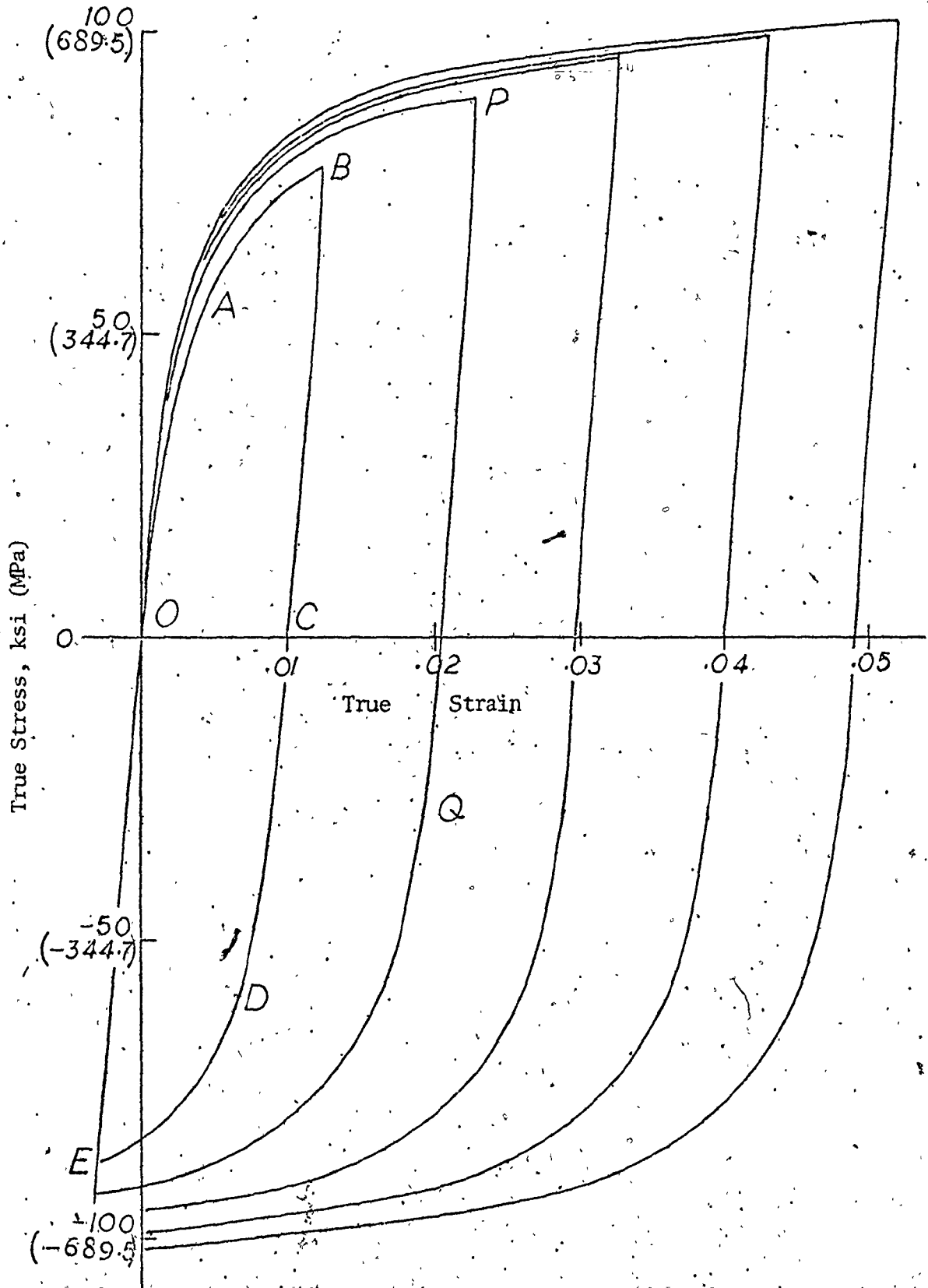


Fig. 5.17(a) The study of cyclic loop symmetry using the dual phase HSLA Steel-D.

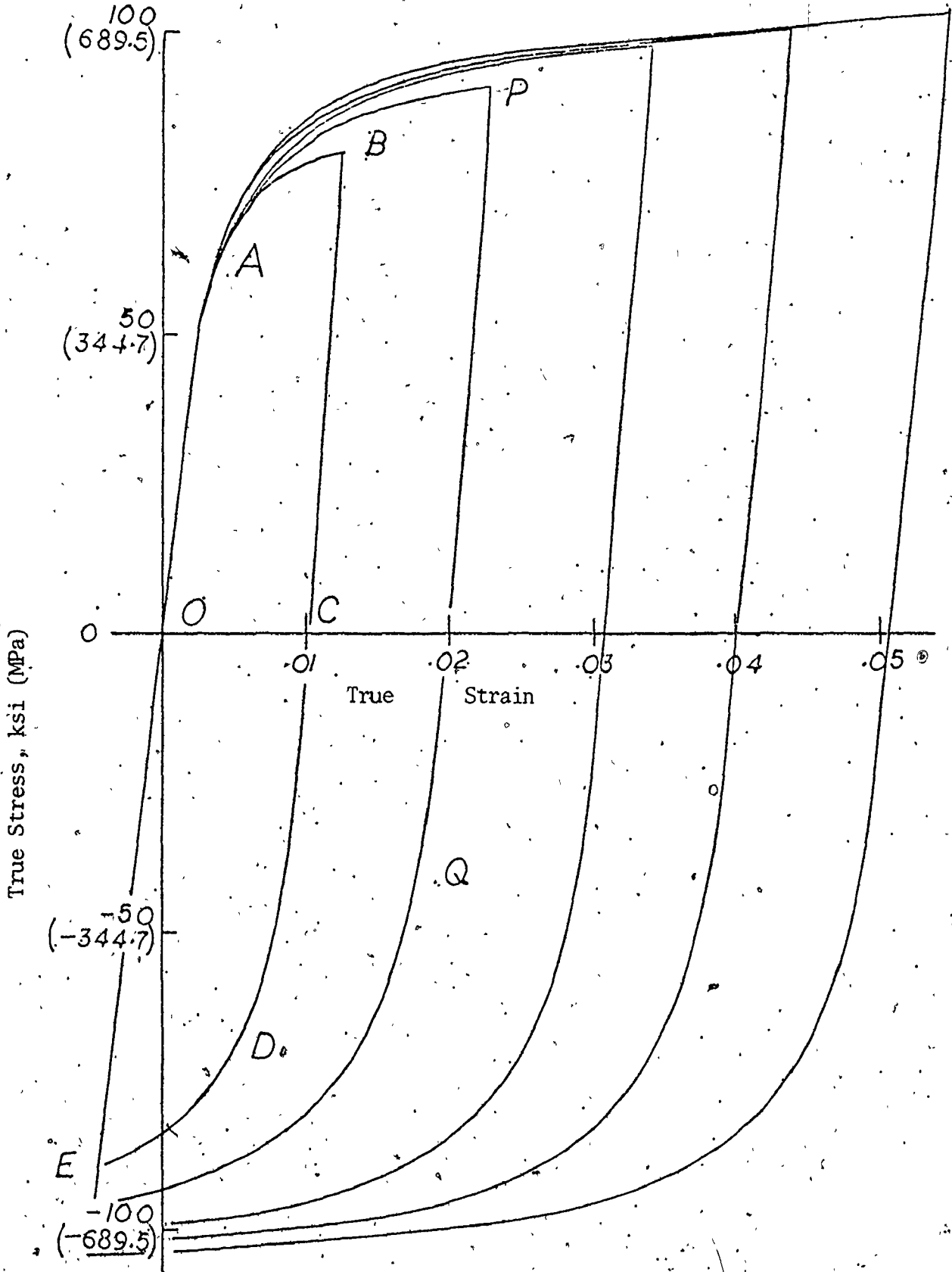


Fig. 5.17(b) The study of cyclic loop symmetry using the dual phase HSLA Steel-E.

If the overstrained specimen was pulled first in tension, then as would be anticipated, little plastic straining would take place before necking occurred (the instability strain was measured at about 1.5 - 2%). This argument is tested in Fig. 5.18(a) which shows the effect of cycling the material by pulling it first in tension to a strain just below the instability strain. The plateau AB shows that tensile instability is about to reoccur and the stress level obtained over AB is about 119 ksi (820 MPa). By comparing the points B and D, a BE is evident upon the first reversal from tension to compression. Also, an increased elastic domain, CD in compression was observed in the sense that additional experiments of the type in Fig. 5.22 reported in section 5.8 for the HSLA steels had indicated that the elastic domain of the first reversal curve of the 1095 steel was (if anything) a decreasing function of the forward prestrain. Fig. 5.18(a) also illustrates clearly the increase in the forward (tensile) strain that can be achieved during the second reversal (path FGH) into tension. No necking was visible when the specimen was unloaded from the point H.

The effect of cycling the overstrained material first in compression is shown in Fig. 5.18(b). The tensile prestress for the curve OAB in this diagram is of the order of the stress at the point A in Fig. 5.18(a). The compression path OAB therefore shows the BE. In addition, the ability to pull out the material without necking is evident from the first strain reversal in tension (CDE). The domain CDE covers a forward strain of about 8%, and this could be interpreted as a net tensile strain of about 5%. The strain cycles shown in Figs. 5.18(a) and (b) therefore illustrate how the t the

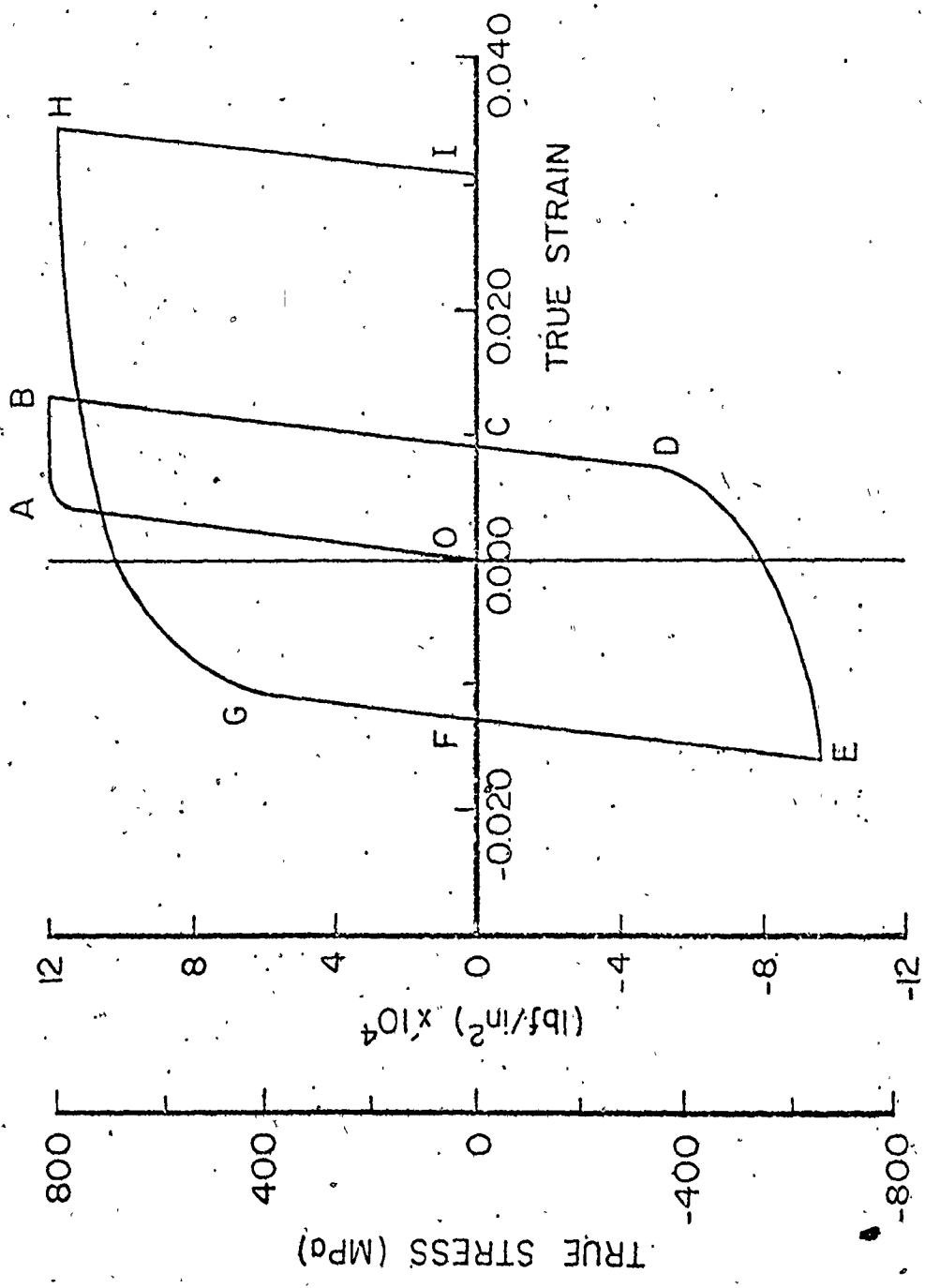


Fig. 5:18(a) The effect of cycling the overstrained material by pulling it first in tension and the reverse flow behaviour following overstraining.

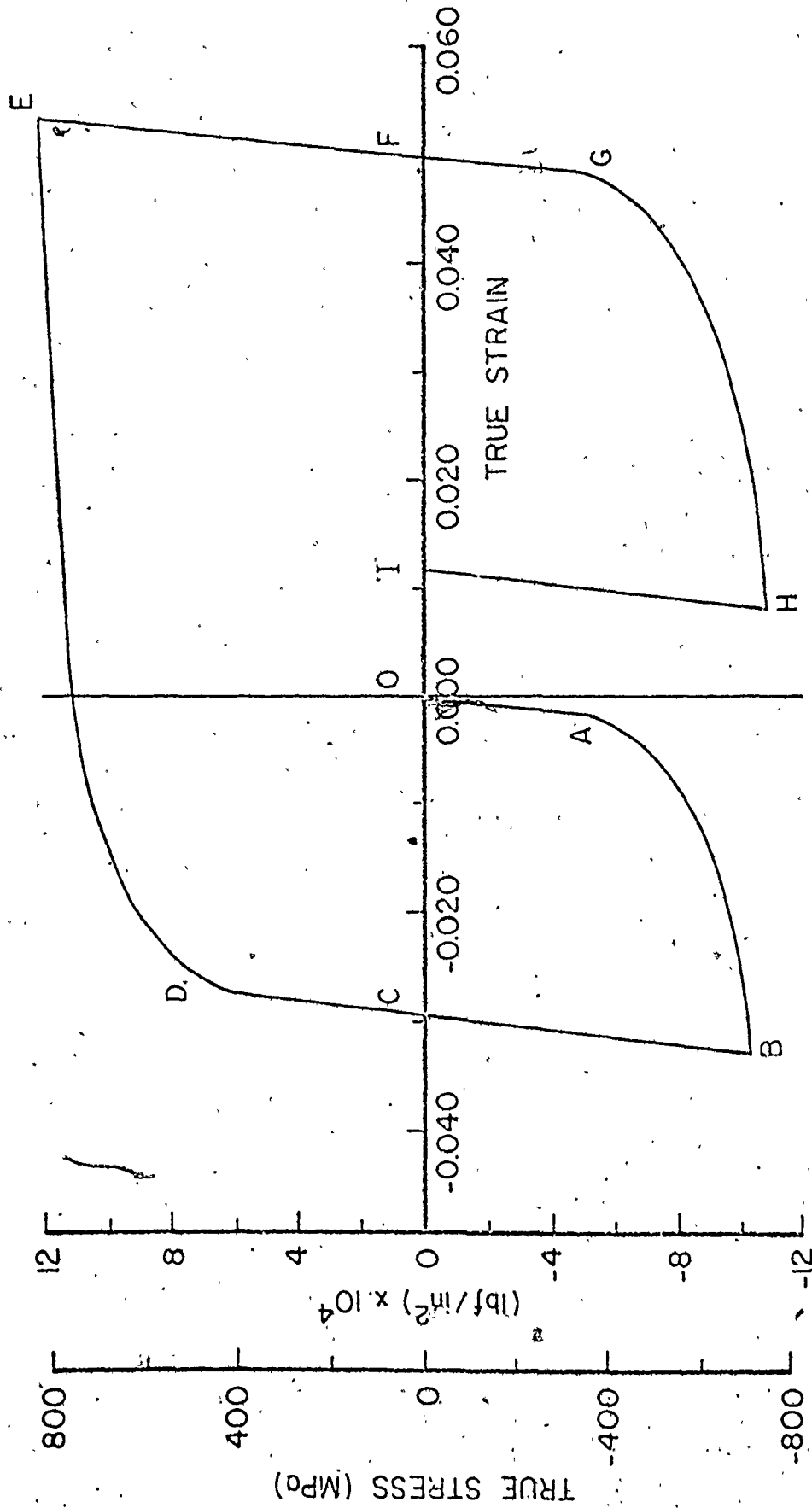


Fig. 5.18(b) The effect of cycling the overstrained material first in compression and the reverse flow behaviour following overstraining.

original overstrained material might be increased. However, there is no apparent increase in the maximum tensile flow stress of the material that can be achieved; the stress level over AB and at the point H in Fig. 5.18(a) and that at the point E in Fig. 5.18(b) all lie between 810 and 830 MPa. Also, since the extent of the initial tensile strain (the path OAB) in Fig. 5.18(a) is small, then it might be anticipated that the material behaviour during the first reversal in compression (path CDE) should be virtually identical to the first compression cycle, OAB in Fig. 5.18(b). This is born out by comparing each of these curves over the equivalent strain interval.

Returning to the subject of structural damage, the metallographical examination of some ruptured specimens did not reveal any evidence of particle cracking or interface decohesion, except in the immediate vicinity of the fractured surface. Consequently, even less structural damage is to be anticipated in the overstrained specimens, and this was found to be the case. Fig. 5.19 obtained from a careful survey of void nucleation and fracture strains in spheroidized steels [105] indicates that the detectable void nucleation strain of the 1095 steel would be of the order of 50%. Recall that the overstrain at the instant of necking was measured as about 10%. Hence, the results in Fig. 5.18 still include the influence of particle stresses as the envisaged structural damage achieved was possibly very small.

5.6 Discontinuous Yielding in Reverse Flow

The HSLA steel-C exhibited an average yield point elongation of 2.6%. In the reverse flow tests, if the prestrain in the first half cycle was less than the total Luder's strain, then the yield point

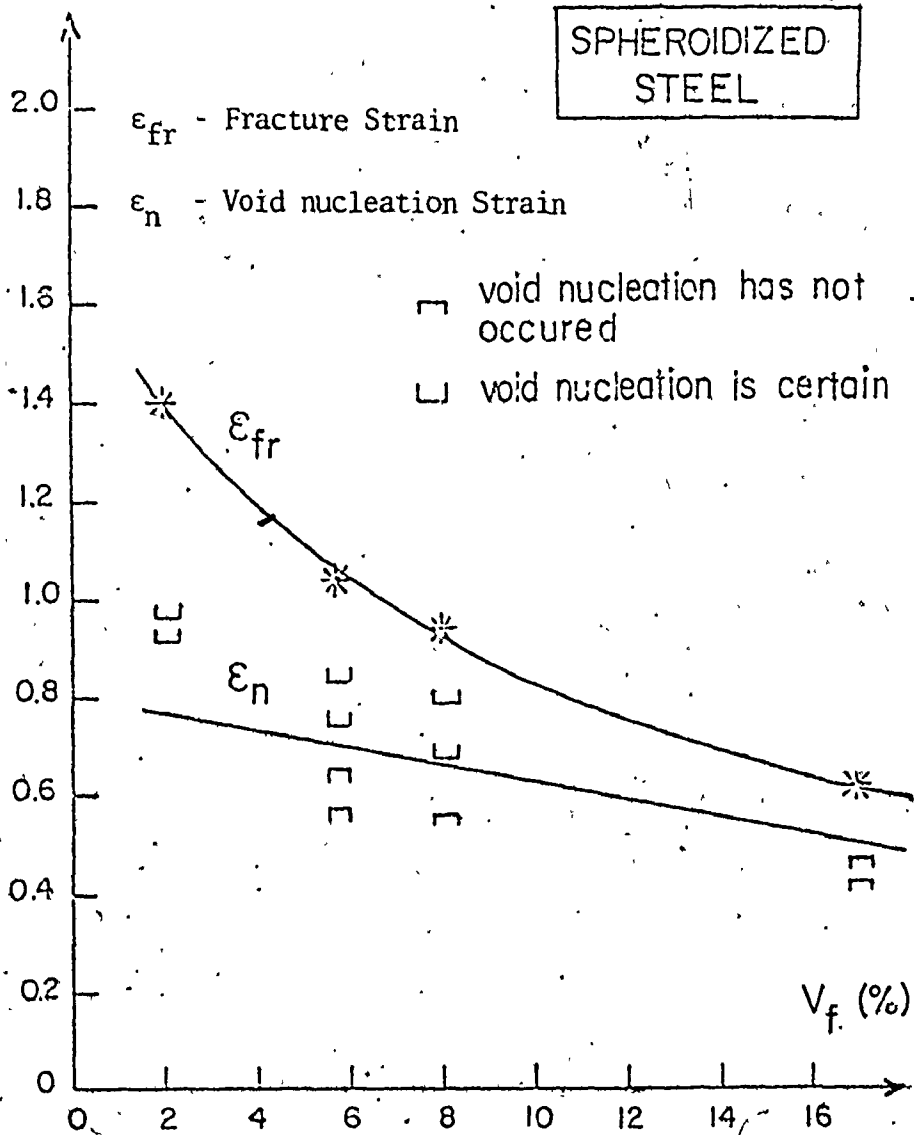


Fig. 5.19 A survey of the structural damage produced by the nucleation of voids at the second phase carbides in spheroidized steels [105].

elongation reappeared in the reverse half cycle. Also, the Luder's strains in the consecutive half cycles appear to add up to be equal to the total expected Luder's strain in monotonic loading. These observations were discussed in Chapter 4, section 5.3 using Fig. 4.11. In addition, the method of interrupted testing in Figs. 4.12(a) and (b) used to investigate the mechanics of Luder's band propagation upon load reversal was proposed. Figs. 4.11 - 4.12 must be interpreted in the true perspective of the yield point phenomenon. In this connection, reference can be made to the works of Sylwestrowicz and Hall [106], Butler [107] and Hahn [108]. Fig. 5.20 is a diagrammatic representation of the yield point deformation. From A to B, the deformation is elastic. At the point B, the upper yield point is registered and the load suddenly drops to the level C with the simultaneous appearance of the first Luder's bands. The material outside the band is plastically undeformed. If the strain is monitored using the extensometer of a given gauge length, no extension is recorded beyond the point C until the band has moved into the gauge length. Thereafter, as the front spreads over the specimen at a mean constant stress, the plateau, CD, known as the lower yield point, the extensometer measures an average extension over the gauge length. The actual extension is derived from only the portion of the gauge length through which the front has propagated. The instantaneous length embraced by the extensometer will therefore consist of the sum of plastically and elastically deformed minisections until the band has traversed the gauge length to the point D. Furthermore, no further extension is possible in the gauge area until the band has spread throughout the entire specimen. Thereafter, the deformation is

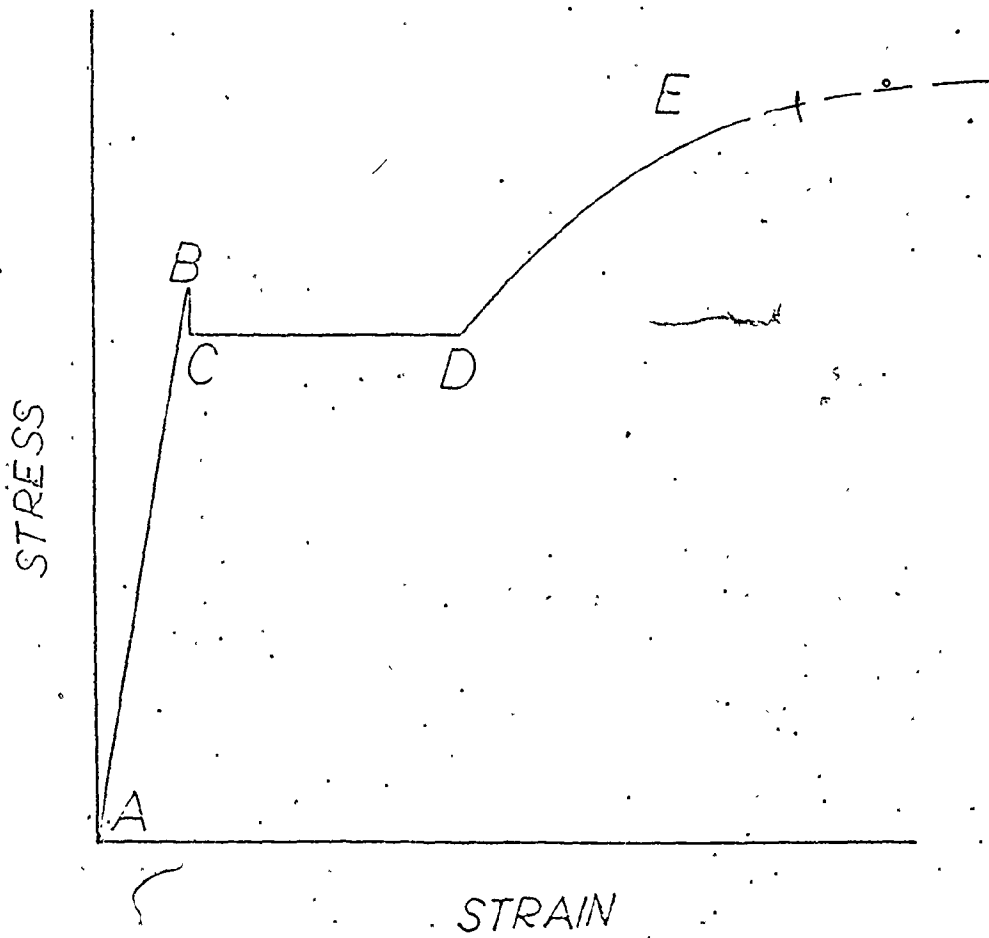


Fig. 5.20 A schematic representation of discontinuous yielding behaviour.

macroscopically homogeneous along the curve, DE.

Fig. 5.21(a) shows the results of the measurements of the profile of the diameter along the gauge section for the loading programme in Fig. 4.12(a). The curve (1) in Fig. 5.21(a) shows the measurements of the original diametral profile prior to testing. Upon loading the material in tension along the path OAB in Fig. 4.12(a), the Luder's strain propagates into the gauge length and a section of it is plastically deformed by the total amount of the Luder's strain, in this case, about 2.6%, although the recorded average tensile prestrain is about 1.35%. The curve (2) in Fig. 5.21(a) was obtained from measurements of the diametral profile following this tensile prestrain and unloading at the point C in Fig. 4.12(a).

In this section, the diameter decreases to accommodate the strain. This is evident from comparing curve (2) with curve (1) in Fig. 5.21(a) in which the instantaneous presence of a physical discontinuity across the diameter at the strain front is clearly indicated. Upon reloading in compression along the path CQD in Fig. 4.12(a), the reverse deformation firstly shows the BE in terms of a reduced elastic limit in the region Q. The domain QD of the reverse curve is highly rounded and the Luder's strain reappears in compression at the point D. Just beyond the point D, the specimen was unloaded along EF and the diametral profile of the curve (3) was determined. Three important points should be raised at this stage. Firstly, the portion of the specimen that deforms first plastically in reverse loading is the section that has already been traversed by the Luder's front. Secondly, the Luder's strain reappears and propagates in reverse loading at the instant when the original diametral profile over the

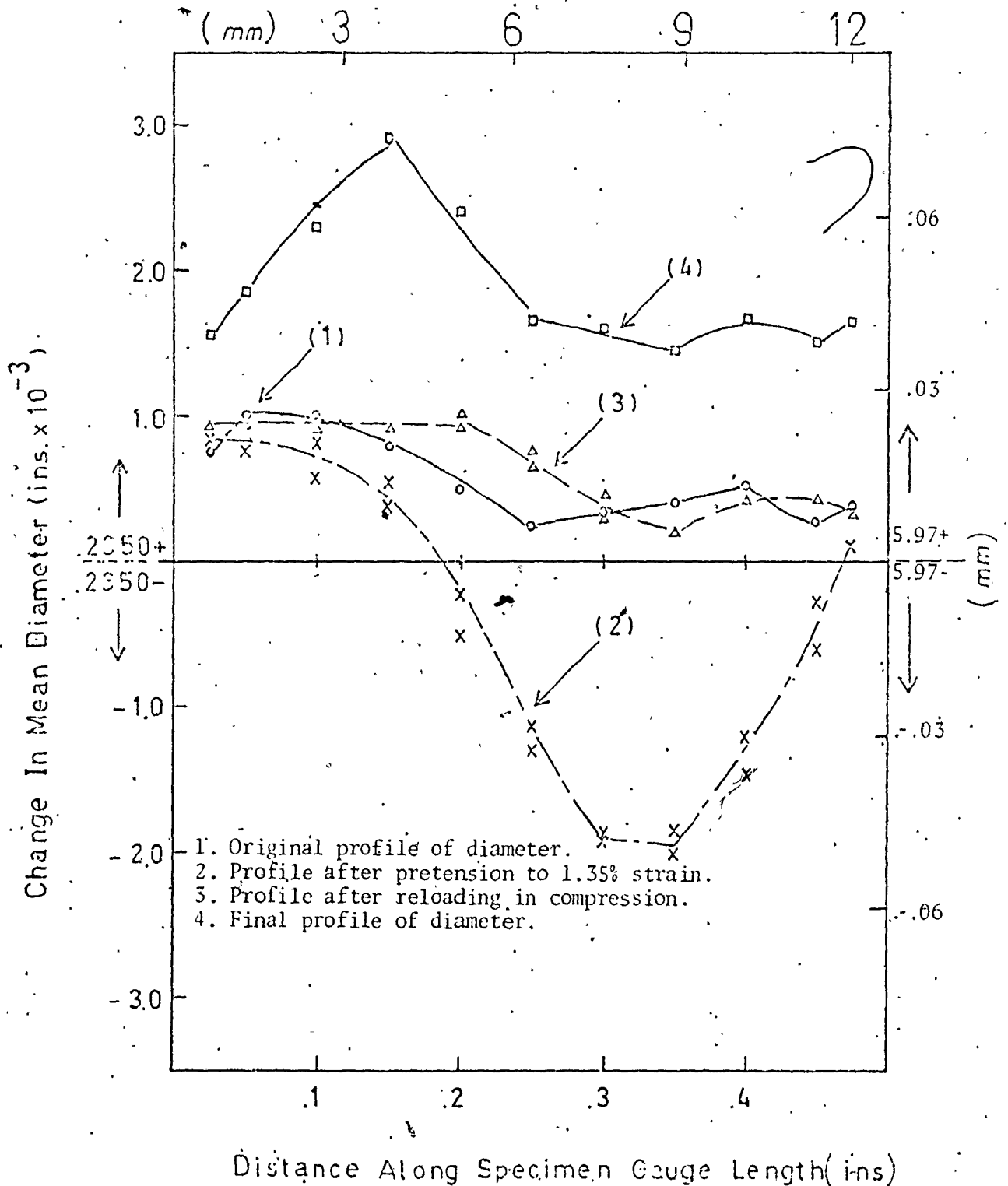


Fig. 5.21(a) The study of the mechanism of Luder's strain propagation upon loading reversal in the case of initial loading in tension.

full gauge length is reattained and the cumulative or total strain imposed is zero. The Luder's strain front propagates into the material that had not been hitherto deformed plastically. And, finally, the stress at propagation is in the order of magnitude of the initial lower yield stress. These features are all evident in the curve (3) in Fig. 5.21(a) and from observing the path CDEF in Fig. 4.12(a).

Now, reloading the material; again in compression from the point F along FGHI in Fig. 4.12(a), the Luder's strain is seen to resume to propagate upon the stress reaching the lower yield stress at the point E. In this loading cycle, all the Luder's strains are exhausted before the point H is reached and some level of work hardening appears. Soon after this work hardening was observed, the specimen was unloaded to the point I and the measurements of the diametral profile in the curve (4), Fig. 5.21(a) were taken. This curve revealed that the propagation of the Luder's strain in compression is accompanied with an increase in the diameter of the specimen. Some deformation in the section of the specimen that was first traversed by the Luder's strain front is apparent in the curve (4). This is possibly due to the strain increment imposed by the domain of work hardening in Fig. 4.12(a) just before the final unloading.

The amounts of the Luder's strains over the domains AB, DE and GI in Fig. 4.12(a) were found to add up to be equal to the total Luder's strain observed in unidirectional loading. It may also be noted that additional experiments not presented here showed that if the Luder's strain front was partially propagated first in tension (or

compression) say by an amount $\epsilon_\ell^{(1)}$ and then in compression (or tension) by an amount $\epsilon_\ell^{(2)}$, then the Luder's strain would reappear if the specimen is put back in tension (or compression) by an amount $\epsilon_\ell^{(3)}$ provided that

$$|\epsilon_\ell^{(1)}| + |\epsilon_\ell^{(2)}| < |\epsilon_\ell| \quad (5.12)$$

where ϵ_ℓ is the expected Luder's strain in continuous uniaxial loading.

If the loading in the final stage is continued in order that the strain $\epsilon_\ell^{(3)}$ completely exhausts the remaining Luder's strain, then an equality condition of the type in eqn. (5.13) below is obtained:

$$|\epsilon_\ell^{(1)}| + |\epsilon_\ell^{(2)}| + |\epsilon_\ell^{(3)}| = |\epsilon_\ell| \quad (5.13)$$

Fig. 5.21(b) shows the results of the measurements of the diametral profiles for the interrupted tests in Fig. 4.12(b) where the first loading was in compression. The mechanics of the Luder's strain propagation are of course reversed, but may be explained on the same basis as before.

The results of this investigation of Luder's strains in reverse deformation clearly answers the important question as to whether the Luder's strain and yield point elongation do occur in compression. The work by Takado and Sugie [109] also confirm, in general, the evidence presented here. In addition, the mechanics of the propagation of the Luder's strain front, either directly in compression or in general reverse flow has been studied experimentally in this work and some useful observations have been made. The final question, however, that still needs an answer, at least to the knowledge of this author, is

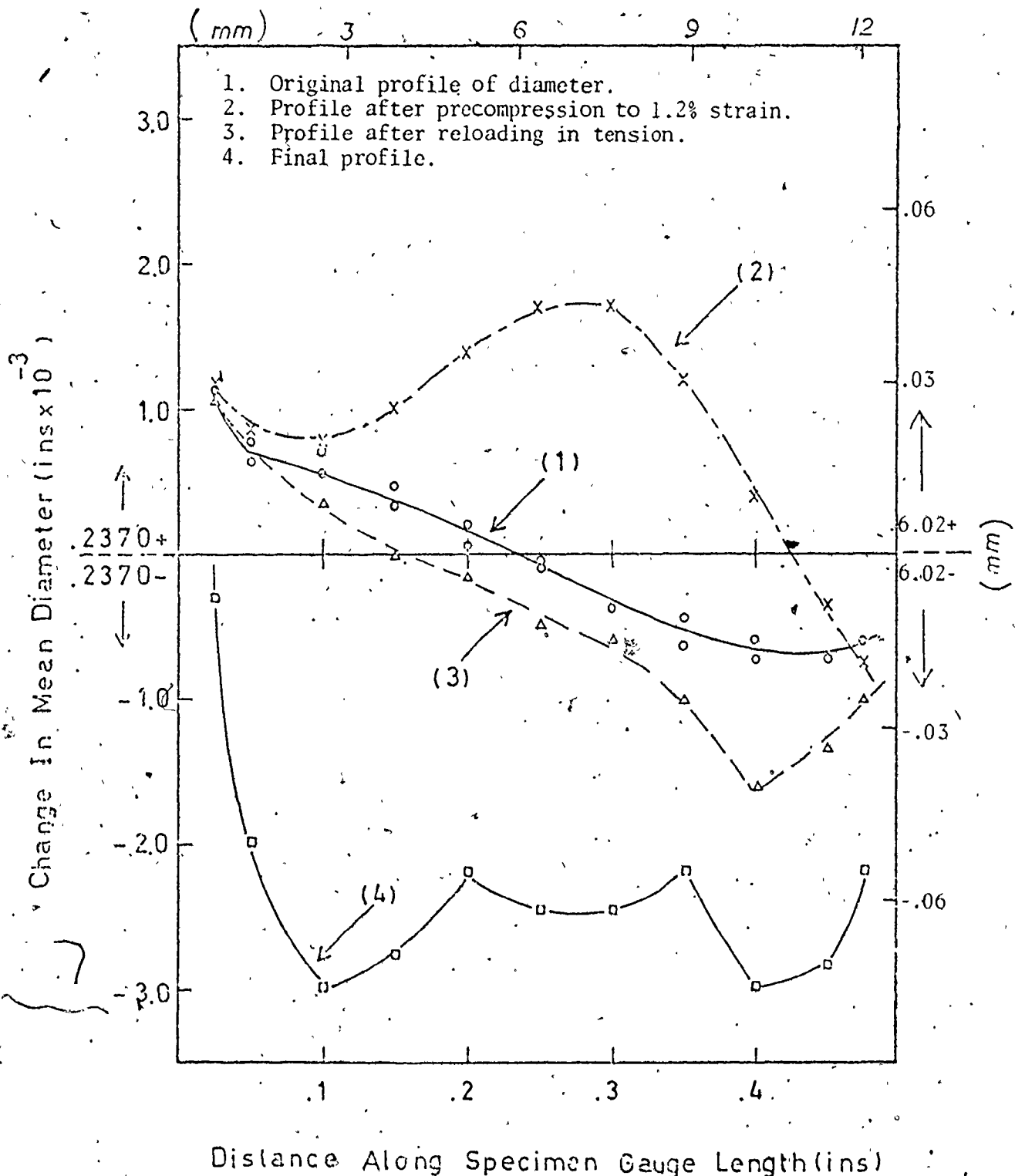


Fig. 5.21(b) The study of the mechanism of Luder's Strain propagation upon loading reversal in the case of initial loading in compression.

whether this type of discontinuous yielding is possible in multi-axial stress states. There is some qualitative evidence that this may be so from the observation of stretcher strain marks in some stretch - formed sheet metal parts. However, in general, this question appears to be currently unresolved.

The final statement can also be made here that the recording of the yield point phenomenon in compression and reverse flow reported here indicates the respectability of the loading equipment used in this work, particularly in terms of the axially of the loading system.

5.7 Summary of Results for Sections 5.4 - 5.6

(i) Implications of Internal Stresses in Cold Metal Working.

The work by Lucas [104] on cold drawn 1045 steel rods was cited with reference to the type of shape change produced by internal stresses generated during deformation processing. In this case, the internal stresses were large enough to impose a definite curvature on the drawn rods which upon straightening gave rise to measurable recovery strains. These relate to the net change in the distribution of internal stresses, but are not unrelaxed strains, ϵ_p^* in the sense that ϵ_p^* scales with the mean value of the existing incompatibility in the structure.

(ii) The Occurrence of Cyclic Loop Symmetry

In this case, some samples of the HSLA-B and dual phase HSLA steels D and E were cyclically strained first in tension, unloaded and reloaded in compression until the strain imposed during the tension half cycle was fully reversed. A minimum of four complete cycles were employed and the strain amplitude was increased during the tension stroke. In general, after the first two complete cycles, the tension and

compression curves became symmetric. The results show that when loop symmetry is attained, the internal (back) stresses created during the previous loading must be annihilated initially in which case, the BE is exhibited and a highly rounded σ - ϵ curve is produced. Then, a new pattern of back stresses are developed which aid plastic flow if the loading is again reversed. This order of events is repeated during each reversal.

(iii) Overstraining and Structural Damage

Here, it was demonstrated that overstraining by tensile necking was insufficient to produce enough structural damage in the form of particle cracking or interface voiding that would relieve the material of internal stresses. However, some positive results were presented which showed that the useful tensile strain range of the material was increased by cycling the overstrained material first compression before reloading in tension. In any case, the maximum flow stress of the material does not increase correspondingly.

(iv) Discontinuous Yielding in Reverse Flow

Some rather interesting conclusions were drawn from this study. These were:-

(a) The yield point elongation (Luder's strains) is obtainable in compression and also in general reverse loading provided, in this later case, that the prestrain during the first loading is insufficient to exhaust the expected Luder's elongation.

(b) Discontinuous yielding is related to the sense of loading, that is, the propagation of the Luder's strain front in compression increases the diameter of the portion of the specimen traversed by the front in

the case of a cylindrical specimen. It is well known that the cross sectional area decreases if the Luder's strain is propagated in tension. The strain always propagates in the direction of the material that had not been hitherto deformed plastically.

(c) Following preloading in tension with the prestrain imposed less than the expected Luder's strain, the portion of the specimen traversed by the Luder's strain front yields plastically first in compression. The compression curve shows the BE and is rounded up to the point where the Luder's strain reappears. At this point, the combined total strain is zero and the stress is of the same order of magnitude as the lower yield stress of the material.

(d) Up to the point where the Luder's strain is exhausted and the material begins to work harden, irrespective of whether this is achieved in monotonic loading or with reverse cycling, the magnitude of the Luder's strain is the same.

(e) It is necessary to investigate the occurrence of discontinuous yield behaviour in multi-axial stress states. This aspect, to the knowledge of the author has not been widely treated.

5.8 Additional Experimental Aspects of the Bauschinger Effect in HSLA Steels

In this section, additional experimental information on the BE in the HSLA steels is presented. The conventional method based on a comparison between the forward unloading flow stress and the reverse yield stress is adopted. These results are presented in order to describe the BE in more familiar terms and to devote some discussion to the aspect of roundedness.

5.8.1 Empirical Definitions

Traditionally, the BE has always been described in terms of the reduction in the elastic limit during reverse deformation following some forward plastic preloading. Using Fig. 4.8, this reduction, $\Delta\sigma$ is measured by the difference between the forward unloading stress, σ_f measured at the point B and the reverse yield stress, σ_r measured in the region D as an offset yield stress. The quantity

$$\Delta\sigma = \sigma_f - |\sigma_r| \quad (5.14)$$

has been selected in this thesis as one empirical definition of the BE. As pointed out in previous discussions, when the reverse deformation is sufficiently large, the stress difference between the continuous monotonic curve and the reverse flow curve provides for a measure of permanent softening. The permanent softening, $\Delta\sigma_p$ and the parameter, BEP defined as (see eqn. (5.2)).

$$\text{BEP} = \frac{\Delta\sigma_p}{(\sigma_f - \sigma_0)} \quad (5.15)$$

have been studied extensively in section 3 of this chapter to test the applicability of the Brown and Stobbs model [85,86] for work hardening and reversible plasticity in two-phase alloys to the general class of dispersion hardened structural steels. In this regard, eqn. (5.15) has a theoretical basis and provides a measure of the fractional contribution to total work hardening from back stresses.

A parameter, similar in form to (5.15), may be defined to incorporate the reverse yield stress, σ_r . To distinguish this from the

theoretical BEP of (5.15), eqn. (3.35) is rewritten as

$$\text{BEP}^* = (\sigma_f - \sigma_r) / (\sigma_f - \sigma_o) \quad (5.16)$$

where σ_r is defined as a proof stress. Clearly, the value of BEP^* will depend on the definition of σ_r and consequently, (5.16) is an empirical definition which does not presuppose any of the characteristics of the BEP treated earlier. Examples of studies in which eqn. (5.16) has been utilized with specialized definitions for σ_r were cited in Chapter 3, section 4.3 with respect to the work of references [9,10,11].

The definitions in eqns. (5.14) and (5.16) were used to measure the BE in the three HSLA steels. Test samples were oriented parallel and transverse to the rolling direction. Since the results for the three steels are similar in form, the data obtained for the HSLA-A and in the rolling direction only are utilized here for general discussion. The comparable results for the HSLA-A for the tests performed in the transverse rolling direction and for the HSLA steels B and C for the two orientations are included in the thesis for completeness in Appendix B.

5.8.2 The Reduction in Elastic Limit and the BEP^*

In the first instance, the BE is illustrated in Fig. 5.22 in a comparative plot of the forward unloading stress, σ_f and the reverse yield stress, σ_r as a function of the prestrain. The reverse yield stress is computed as the .2% offset yield stress and the mean initial proof yield strength of the material is shown as a basis. The pair of points ('o' and '\Delta') at a given prestrain was obtained from one test in which the complete loading followed the typical path OABCDEF in Fig. 4.8. The specimen was first loaded in tension to the required

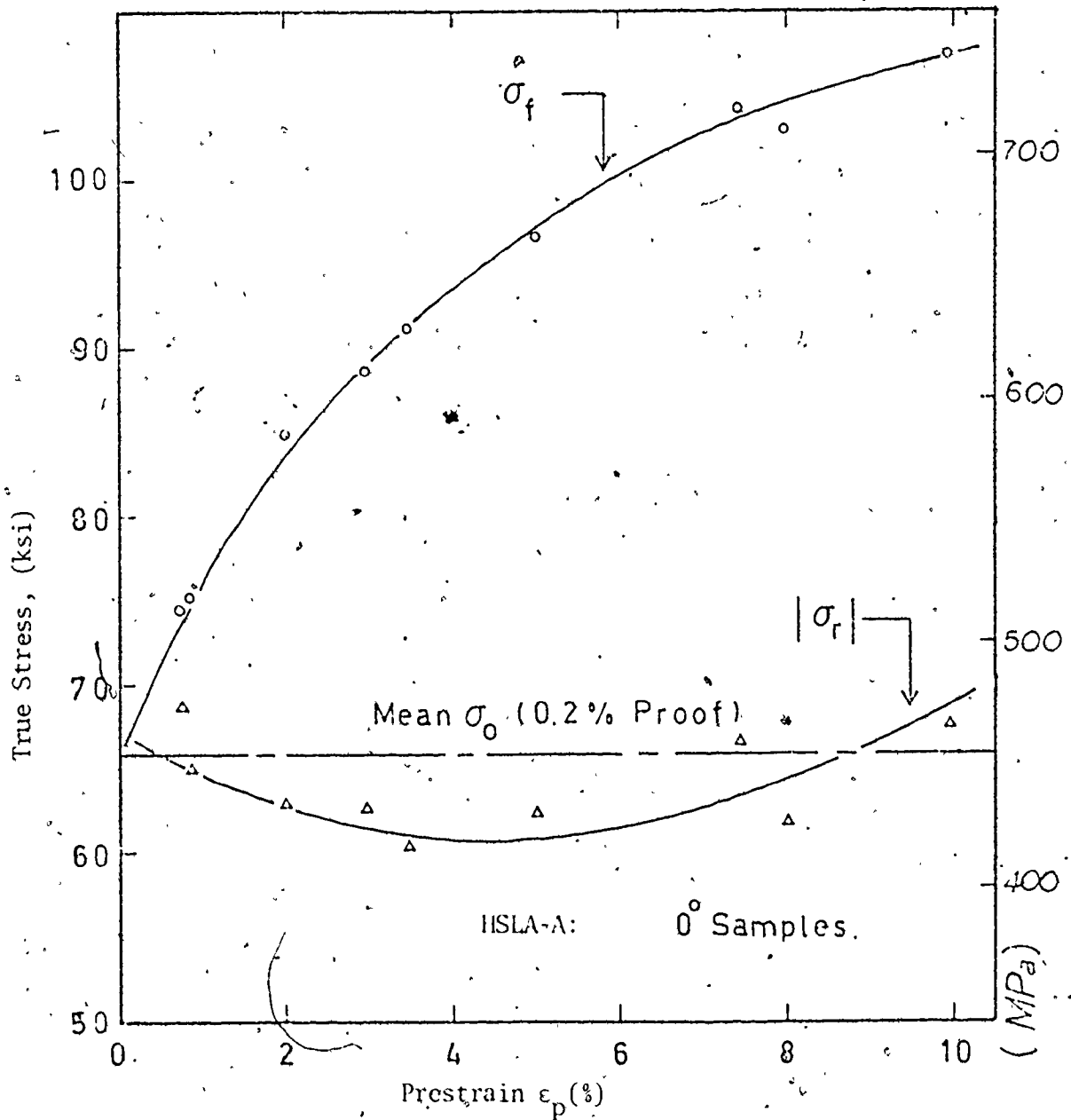


Fig. 5.22(a) A comparative plot of the tensile prestress, σ_f and the corresponding 0.2% compressive (reverse) yield stress, σ_r as a function of prestrain: The difference in the levels of the two curves measures the BE by definition.

prestrain, unloaded and compressed into the plastic range. The stresses, σ_f and σ_r were calculated on the basis of the true cross sectional areas at the points of unloading.

The results show that the reverse yield stress decreases initially to a minimum value and then increases with increased prestraining. In this connection, the results reported here are similar to those obtained by Taira et al [4].

Fig. 5.22(b) has been included for comparison to Fig. 5.22(a) in order to show the influence on experimental estimates of the BE by using a different offset strain to define the reverse yield stress. The reverse yield stress, σ_r was measured by means of the .2% offset strain in Fig. 5.22(a) while the .5% offset strain was used in Fig. 5.22(b). It is seen that the magnitude of the BE measured decreases if the offset strain used to determine σ_r is increased. The difference between the two diagrams in Fig. 5.22 are clearer if the definition in (5.14) is used to measure the BE as in Fig. 5.23. In this diagram, the measured stress difference, $\Delta\sigma = (\sigma_f - \sigma_r)$ is plotted as a function of prestrain using the four different offset yield strength definitions, that is, 0.0, 0.1, 0.2 and 0.5%. It is evident from Fig. 5.23 that with this description, the BE increases with prestrain, and for any given prestrain it decreases in magnitude if the offset strain used to define the reverse yield stress is increased. The other problem with this definition is that it is evidently difficult to provide a comparative estimate or ranking of the BE in different materials. However, Fig. 5.23 serves to demonstrate the meaning of the BE in familiar engineering concepts.

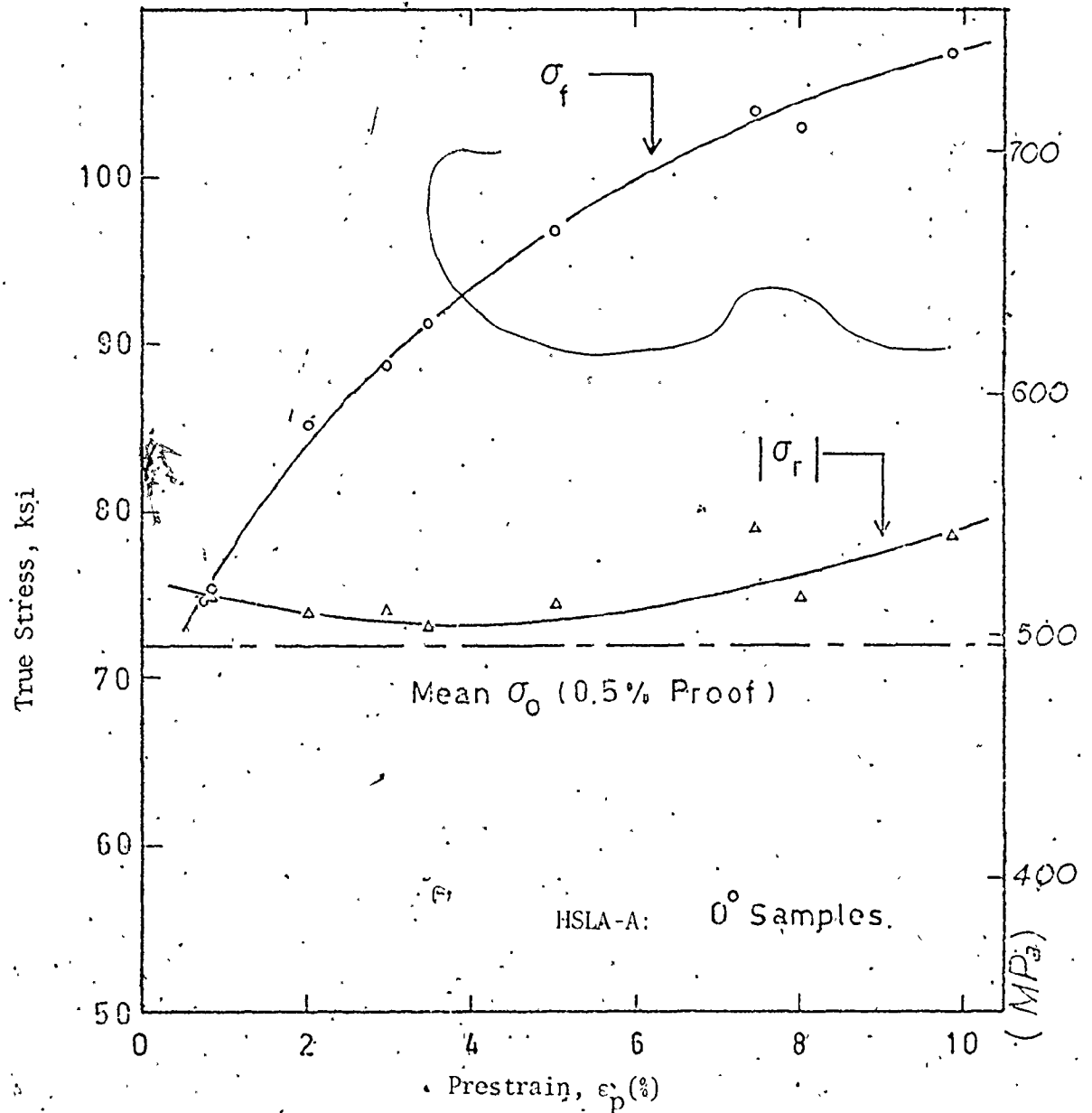


Fig. 5.22(b) A comparative plot of the tensile prestress, σ_f and the corresponding 0.5% compressive (reverse) yield stress, σ_r as a function of prestrain. In comparison to Fig. 5.22(a), this diagram shows the empirical dependence of the BE on the definition of σ_r .

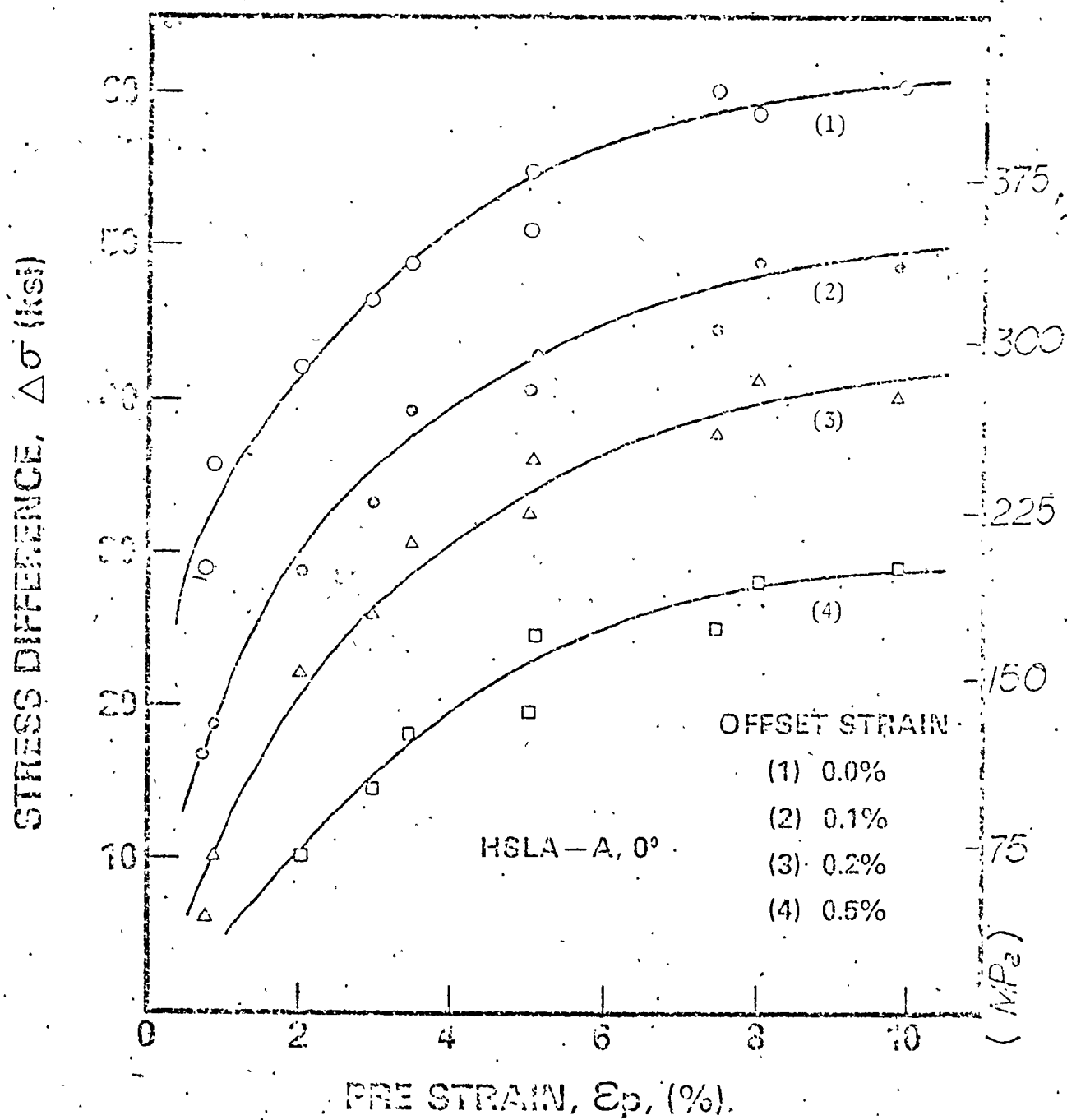


Fig. 5.23 The Bauschinger Effect measured by the stress difference, $(\sigma_f - \sigma_r)$ as a function of prestrain and using four offset strain definitions of σ_r .

The empirical parametric representation of the BE by means of BEP^* in eqn. (5.16) overcomes the problem of ranking the BE in different materials provided the stress-strain curve of the material is reasonably rounded and the same proof stress estimate of σ_r is consistently used. The need for these two conditions will be obvious from observing the measurements of BEP^* obtained in Fig. 5.24 (see also Appendix B, Figs. B.6-B.8). It is noted that the BEP^* is sensitive to the method of characterizing the reverse yield stress, σ_r . Also, higher BEP^* values are obtained in the region of small prestrains where the quantity, $(\sigma_f - \sigma_0)$ is also small, particularly for the HSLA steel C (see Fig. B.8) which possesses a discontinuous yielding behaviour.

The more interesting feature of these results is the apparent independent behaviour of the BEP^* with respect to the prestrain. This is possibly due to the similarity of this empirical definition to the theoretical BEP in eqn. (5.2). One usefulness of this parameter is that since the value of the BEP^* is reasonably constant at large prestrains, then this constant value can be utilized in classifying the BE in different materials, subject to the condition that σ_r is similarly defined in all cases.

Some comparison of the BEP with the BER^* is possible although the two parameters are essentially different. The former is directly related to the mean effect of internal stresses while the latter, although involving an arbitrary definition of σ_r appears to include not only the effect of the mean matrix stress but also the transient aspects of the BE in the region of initial reverse yielding. Also, the

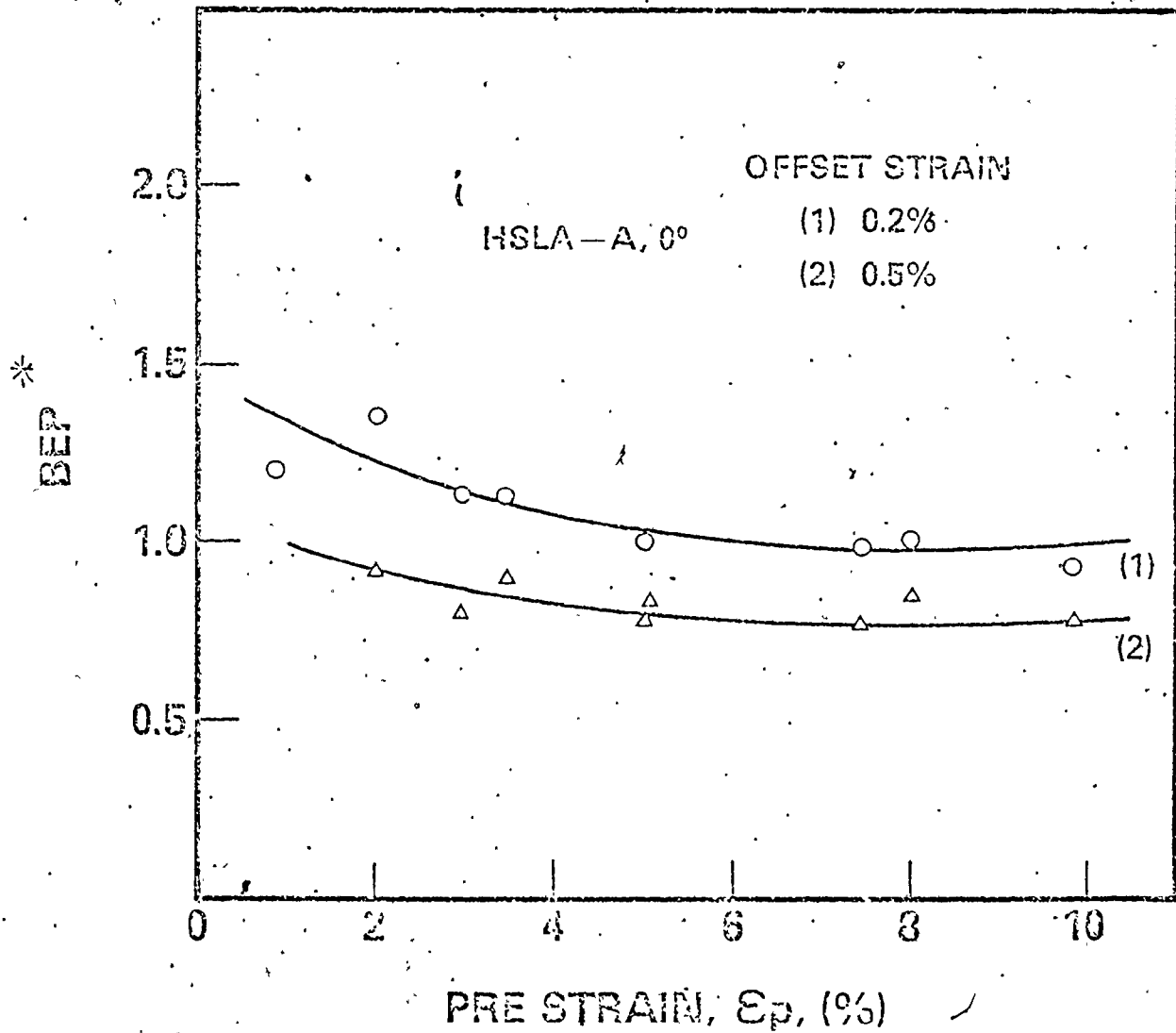


Fig. 5.24 The empirical parameterization of the Bauschinger Effect.

work by Ibrahim and Embury [9] discussed in Chapter 3, section 4.3, provided a basis for defining the BE in terms of BEP^* . These authors used the method of back extrapolation to determine σ_r and assumed that the quantity, $(\sigma_f - \sigma_r)$ thus measured was indicative of the amount of permanent softening (see Chapter 3). Their method therefore was aimed at calculating the BEP as defined in eqn. (5.15). On this account, the empirical BEP^* here is also different from that of Ibrahim and Embury.

It was mentioned that the BEP^* may involve the combined effect of the mean matrix stress and the transient aspects of the BE. Thus, the decrease in the magnitude of the BEP^* with the increase in the offset strain used to define σ_r in eqn. (5.16) could be interpreted as reflecting the roundedness of the reverse stress-strain curve. Although this aspect of the BE was not quantitatively studied in this thesis, some discussion of roundedness is considered necessary for completeness. This is done in the following section.

5.8.3 The Roundedness of the Reverse Flow Curve

For simple engineering applications, the BE, studied in terms of the reduction in yield strength upon reverse loading appears to meet the basic design requirements. For a more quantitative analysis, a consideration of permanent softening appears necessary. In between the observations of a reduced yield strength and permanent softening in reverse flow, the stress-strain curve exhibits a region of highly rounded behaviour. This is studied qualitatively in this section.

Fig. 5.25 shows four reverse stress-strain curves of the HSLA-B plotted in the tensile quadrant. If these curves are compared with the tensile stress-strain curve for this material in Fig. 4.3(b), it

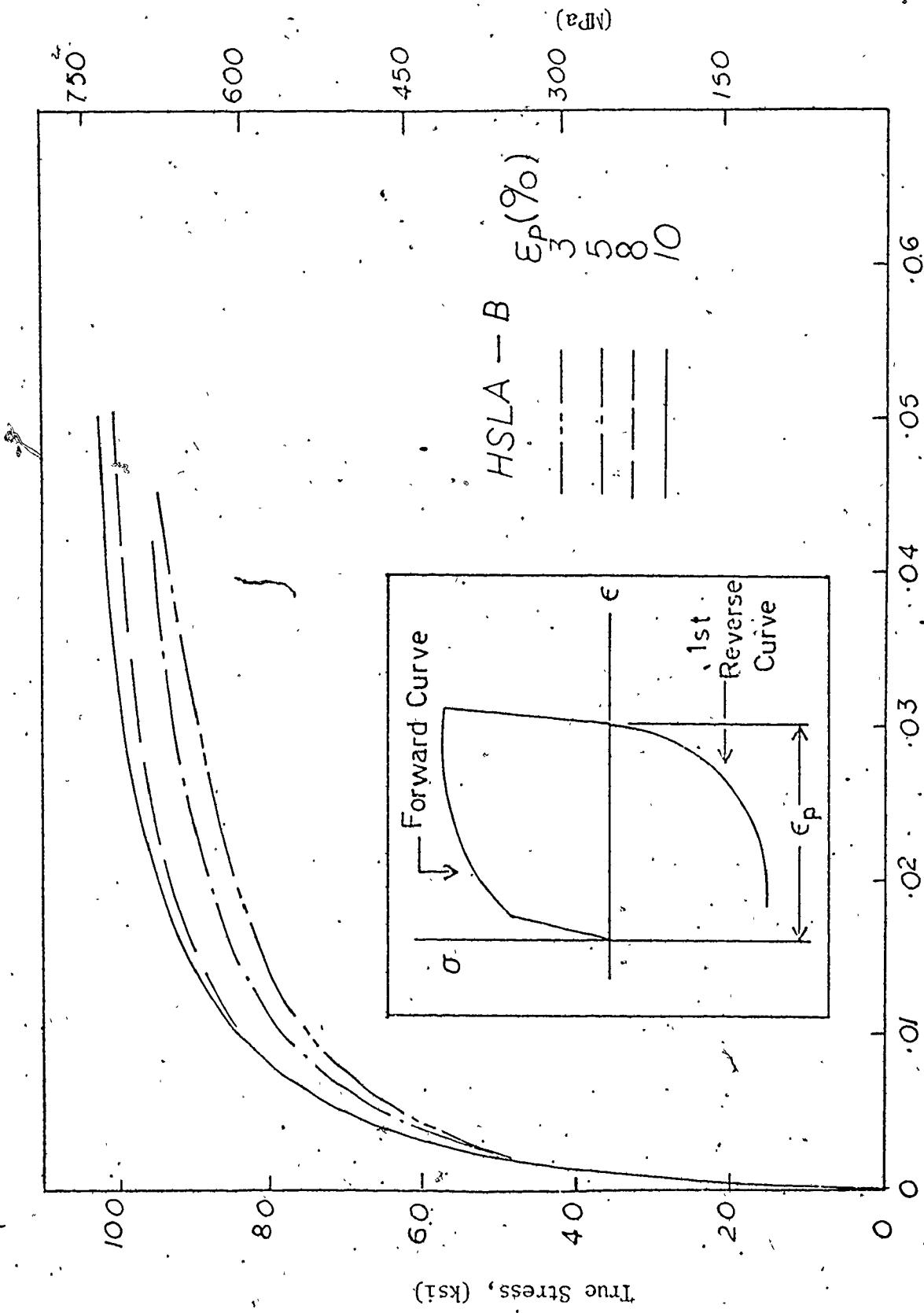


Fig. 5.25 A qualitative study of roundedness using four first reverse flow curves which are to be compared with the initial tensile curve of the material in Fig. 4.3(b).

becomes evident that the reverse curves are relatively more highly rounded initially, i.e., possess higher work hardening rates. The high roundedness has been attributed to the statistical nature of the microscopic plastic deformation mechanisms upon reverse flow [34].

In particular, the reverse processes of dislocation movements away from structural obstacles and the sampling of other obstacles and the dislocation debris created during prestraining are viewed as statistical in nature. In this connection, the study of roundedness is very complex. It is clear, however, that roundedness scales with the internal stresses generated during prestraining. On this account, it should increase with both the prestrain and the volume fraction of microscopic particles.

In view of the proportionality of permanent softening with the square root of prestrain (see eqn. (3.34)), Atkinson et al [52] represented the rounded portion of the reverse stress-strain using an empirical parabolic law of the form,

$$\sigma_r/\sigma_f = \alpha \epsilon_r^{1/2} \quad (5.17)$$

where σ_f and σ_r are measured at the same cumulative strain and ϵ_r measures the reverse strain. They postulated that by calibrating the reverse curve in this manner, the constant, α provides for some measure of the roundedness which could also be correlated with experimental estimates of internal stresses.

Roundedness was not studied in detail in this work. As is evident, preference was given to the use of experimental permanent softening data to quantitatively study the consequences of internal stresses in work hardening and material behaviour in reverse flow. This

has been treated in detail in this chapter and some practical implications of internal stresses have been discussed. In the present section, additional data on the BE have been presented which utilize the basic definition of the BE as a strength loss in reverse loading following prestraining in an opposite sense. In Chapter 6 which follows from here, some of the information presented so far is used to enlarge the study of the BE to include a practical manufacturing problem in the analysis of the U-O-E pipe making process.

The experimental data reported in this present chapter may be viewed as subject to two main sources of error, namely, the error in the initial data and that due to the variations in the measured material parameters. Where a number of repeated tests had been performed, it was found that the range of parameters (i.e. yield and ultimate strength) was less than about 4%. However, the range in the magnitude of permanent softening was about 8% of the difference measured.

CHAPTER VI

THE U-O-E PIPE MANUFACTURING PROCESS

6.1 Introduction

The U-O-E pipe making operation is a fabrication process which subjects the plate material to plastic strain reversals. Consequently, if plate materials are employed which are known to exhibit Bauschinger Effects, it follows that both producers and consumers of linepipe are interested in assessing the influence of the BE on the strength of the pipe. A truly definitive account of the straining path of each element within a plate during the pipe making operation is a formidable task. However, it is possible to go some way towards modelling a pipe making process and in so doing provide some indication of the role of the BE.

In this chapter a rather idealized version of certain stages in the U-O-E process is presented, and hence the straining path of individual elements across the wall of the pipe can be estimated. Recourse is then made to experimental data from forward and reverse flow tests on actual plate materials. It is to be noted that the reverse flow tests are designed to simulate the straining path(s) derived from the model of the pipe making process. This technique enables some assessment to be made of the strength of the pipe by predicting the expansion characteristics when the pipe is subjected to internal pressure. Results are presented for the three HSLA steels A, B and C. These are materials which have been designed for linepipe applications.

The chapter concludes with a discussion of other methods of

assessing the strength of pipes and an attempt is made to highlight the advantages and disadvantages of the respective methods.

6.2 The Mechanics of the U-O-E Process

Fig. 6.1 shows a schematic illustration of the U-O-E method of manufacturing large diameter pipes. A description of this process is given in refs. [4,110,111] and consists of basically three stages. Initially, a flat plate is bent round a 'U' shaped punch. It is then transferred to the 'O' press and compressed between two dies to obtain a near cylindrical shape and welded. Finally, the pipe may require sizing by tensile hydraulic expansion in the 'E' stage. The key words underlined above are important descriptions of the deformation modes in the pipe wall during the specified stages of forming.

The gross deformation history occurring in the pipe wall may be represented diagrammatically as in Fig. 6.2. In the outside half rim of the pipe, two complete strain reversals have occurred while in the inside half rim, one strain reversal is evident. The stress-strain response of two elements from the pipe wall, one from the outside surface and one from the inside surface is shown schematically in Fig. 6.3. Depending upon the extent of the BE and as a result of each of the strain reversals depicted in Fig. 6.3, the strength of the pipe may be impaired in the final expansion stage. Fig. 6.3 also illustrates the type of experimental reverse flow tests that had to be conducted on the plate materials. Two separate experiments are required, one to simulate the representative path OABCDEFGHI and the other for the deformation history indicated by OPQRSTUVWXYZ. The experimental strain amplitudes are determined as follows: OC and OR from bending theory and pipe geometry,

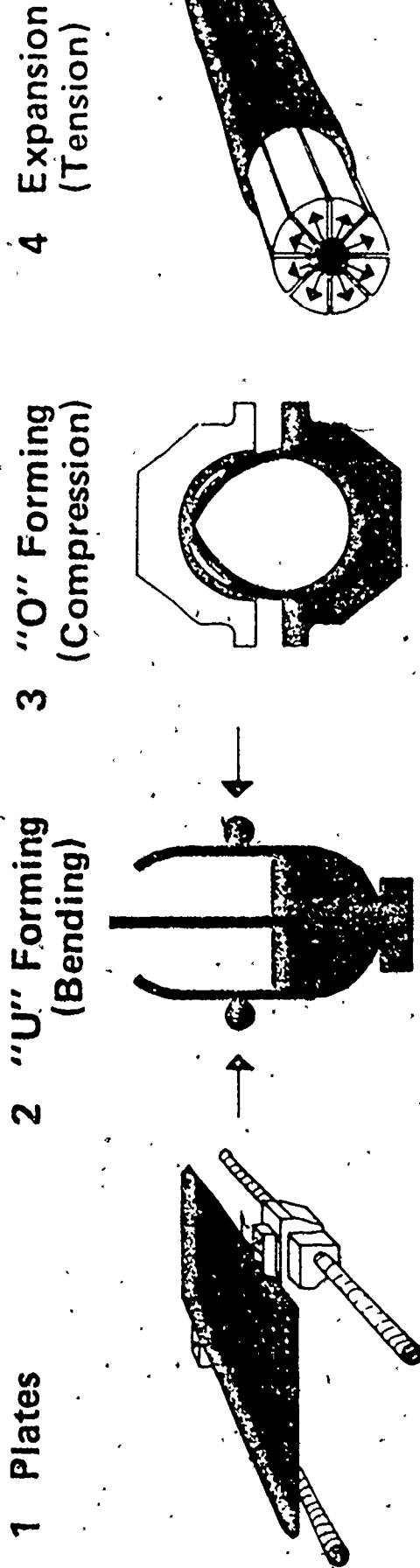


Fig. 6.1 A diagrammatic representation of the U-O-E method of pipe forming.

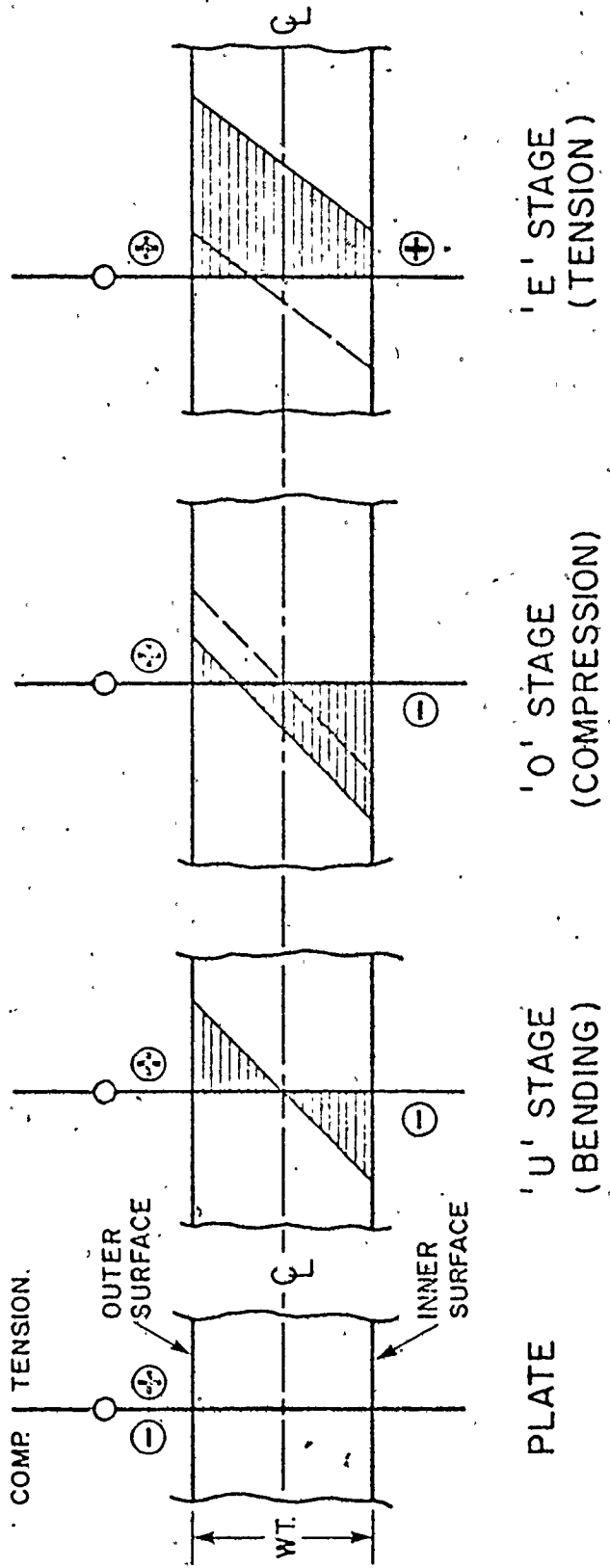


Fig. 6.2 A representation of the deformation (strain) history in the pipe wall during forming.

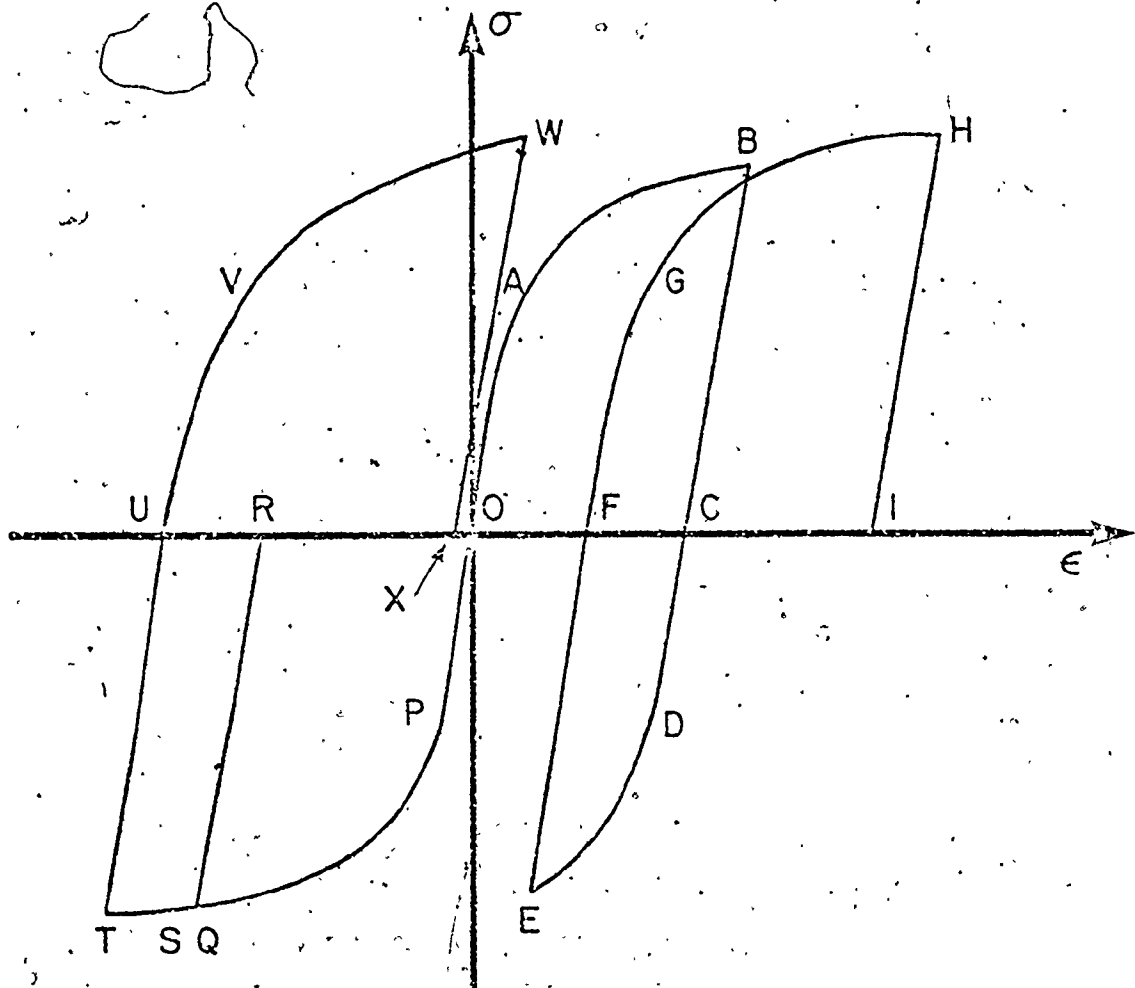
CF and RU from the amount of 'O' compression to be applied and, FI and UX from the percentage radial expansion sizing required for dimensional control. In refs. [4,38,109,110], it is indicated that practical 'O' compression and 'E' sizing strains are 1% and 1-1.5% respectively.

The experiments described above were actually performed using test samples of the HSLA steels, A, B and C in order to derive the necessary stress-strain data for the analysis of the U-O-E process with these materials. The experimental strain amplitudes employed are given in Table 6.1. It is noted that the strain for the forward paths OABC and OPQR were obtained as bending strains using an assumed pipe geometry of 40 ins. (1016 mm) diameter and 1/2 ins. (13 mm) wall thickness.

TABLE 6.1

Experimental Strain Amplitudes Employed to Simulate the U-O-E Forming of a 40" (1016 mm) x 1/2" (13 mm) pipe.

Deformation Paths (see Fig. 63)	STRAIN AMPLITUDES (%)	
	Inner Surface Element	Outer Surface Element
Bending and Unloading (OPQR, OABC)	1.2	1.2
Compression and Unloading (RSTU, CDEF)	1.0	1.0
Expansion (UVW, FGH)	2.0	2.0



INNER WALL THICKNESS DEFORMATION PATHS	OUTER WALL THICKNESS DEFORMATION PATHS
OPQR - BENDING AND UNLOADING	OABC - BENDING AND UNLOADING
RSTU - COMPRESSION AND UNLOADING	CDEF - COMPRESSION AND UNLOADING
UVWX - EXPANSION	FGHI - EXPANSION

Fig. 6.3 The schematic illustration of the deformation cycles imposed on the inside and outside surface elements of a U-O-E pipe during forming.

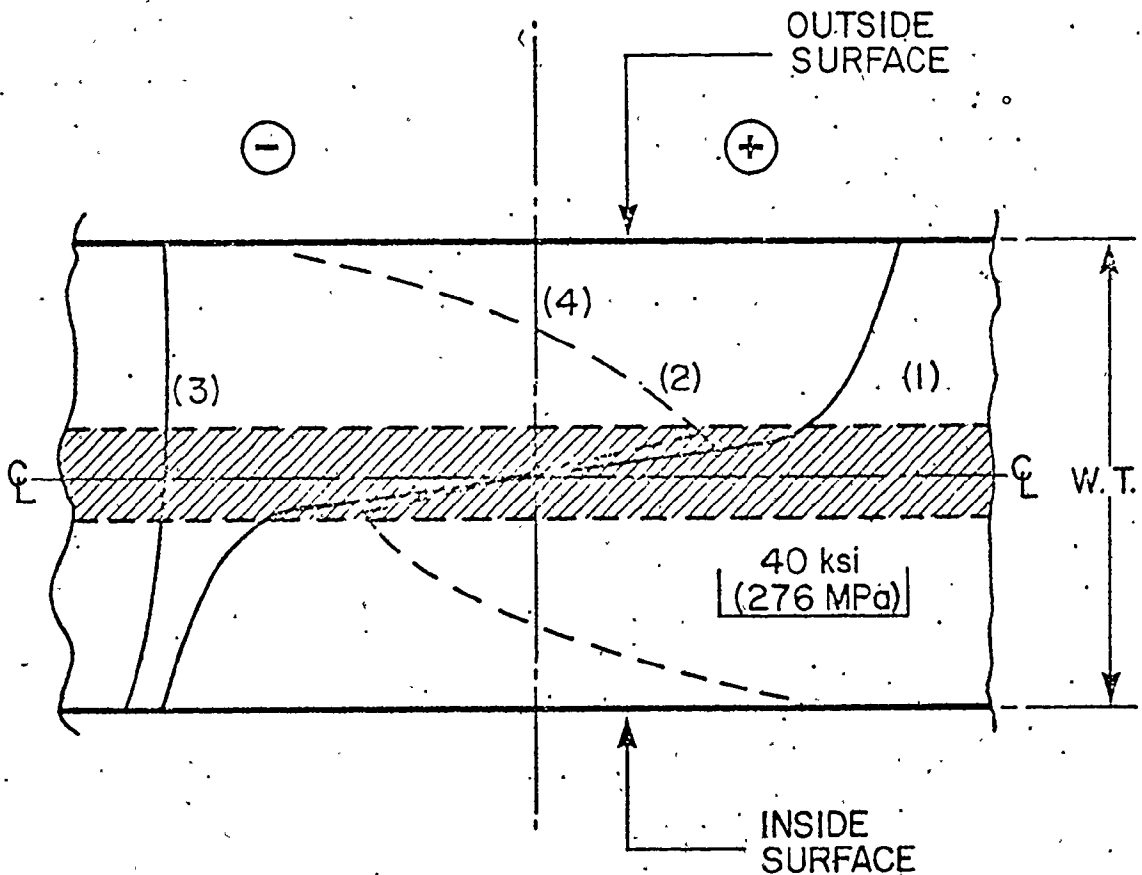
During the deformation process, each element in the pipe wall will, in general, experience a unique strain history. It will be noticed that the strain amplitudes used to simulate bending in the U stage in Table 6.1 are determined for the surface fibres of the pipe. Since the influence of the BE is known to increase in severity with the imposed plastic prestrains, the intention here is to compare the properties of a U-O-E pipe under two material conditions: one in which the maximum possible influence of the BE is implied and one in which the homogeneous stress-strain response of the initial plate is assumed and the BE is ignored. This approach was adopted in order to reduce the number of experiments needed to represent the straining process of the individual elements across the pipe wall. A phenomenological method designed to monitor the strain path of as many elements in the pipe wall as required has, however, been developed by Sowerby and Tomita [84].

Fig. 6.4 shows the stress distributions in the pipe wall during the U and O stages of forming using the HSLA-A. This diagram was obtained from a rather idealized version of the U-O process in which uniaxial and reverse flow stress-strain data were used to estimate the stress distributions. The purpose of this analysis was to show that the residual stress distribution across the pipe wall after the U and O stages of forming is almost negligible and therefore can be ignored in the analysis of the E-stage.

6.2.1 The 'U' Stage

If it is assumed that the plate experiences plain strain bending up to a radius of curvature of 20 ins. (504 mm), then the principal strains are given by:

PIPE GEOMETRY
40" (1016 mm) DIA
0.5" (13 mm) W.T.



- (1) BENDING
- (2) BENDING RESIDUAL STRESSES
- (3) CIRCUM. COMPRESSION (UNDER LOAD)
- (4) RECOVERY AFTER COMPRESSION

SHADED AREA - ELASTIC DOMAIN
 UNSHADED AREA - PLASTIC DOMAIN } AFTER BENDING

Fig. 6.4 The stress distributions and residual stresses in the pipe wall resulting from the 'U' and 'O' stages of forming. The calculations employed the pipe geometry and the uniaxial reverse flow data of the HSLA-A.

$$\begin{aligned}\epsilon_{\theta} &= -\epsilon_r = \ln(r/r_n) \\ \epsilon_z &\approx 0\end{aligned}\quad (6.1)$$

where ϵ_{θ} , ϵ_r and ϵ_z are the hoop, radial and longitudinal strains. The radius of any element in the pipe wall is given by r and r_n designates the position of the neutral layer which is assumed fixed at the centre thickness. The corresponding equivalent strain is therefore given by,

$$\bar{\epsilon} = \frac{2}{\sqrt{3}} \epsilon_{\theta} = \frac{2}{\sqrt{3}} \ln(r/r_n) \quad (6.2)$$

The strain, $\bar{\epsilon}$ calculated at twenty element locations in the pipe wall (see Fig. 6.5) was used in conjunction with the tensile stress-strain curve of the HSLA steel A to obtain the bending stress distribution numbered (1) in Fig. 6.4. Depending on the bend curvature, there may be an elastic core in the pipe wall. The position and size of the elastic core shown in Fig. 6.4 was approximated by calculating the radii from (6.2) at which the stress on the curve (1) was in the order of magnitude of the uniaxial yield stress of the material. When the moments are removed and the pipe is assumed to unload elastically, the residual stress pattern is calculated by taking the unloading moment as equal and opposite to the applied bending moment. In Fig. 6.4, the curve marked (2) shows the resultant distribution of residual stresses after this elastic spring back.

6.2.2 The 'O' Stage

In effect, upon transfer to the 'O' press, the pipe is firstly elastically bent back to return it to the radius of curvature obtained

in bending, before the imposition of plastic compression. Hence, any spring back that may have taken place during the transfer is recovered and the residual stresses are not expected to play a major role.

Furthermore, since the O-compression strains are definitely plastic, this will also have the effect of dampening the variation in residual stresses. An analogy can be made here to the case of plastic bending under superimposed longitudinal tension considered by Alexander [12] where it is shown that bending under tension almost completely eliminates the residual stresses and the elastic spring back.

The "O" stage operation is assumed to be one of uniform circumferential compression where every particle in the pipe wall deforms by the same amount; $\epsilon = -.01$ was used in this analysis. For the elements in the inner half thickness of the pipe wall, the U and O operations are considered as continuous and the elements work harden monotonically in compression. This behaviour is indicated by the continuous path, OPQST in Fig. 6.3. The elements in the outer shell on the other hand now show the first reverse loading in the true sense. The first reverse loading curve, e.g. CDE in Fig. 6.3, must then be employed to account for the BE in calculating the stress-strain response in this domain during the "O" stage deformation.

The curve marked (3) in Fig. 6.4 shows the modification of the bending stress distribution by the imposition of a uniform circumferential compression of 1%. To obtain this result, the bending strains were first calculated at twenty element locations in the pipe wall. The element locations are shown in Fig. 6.5. For the ten elements in the inner shell, the bending strains of the individual elements were added

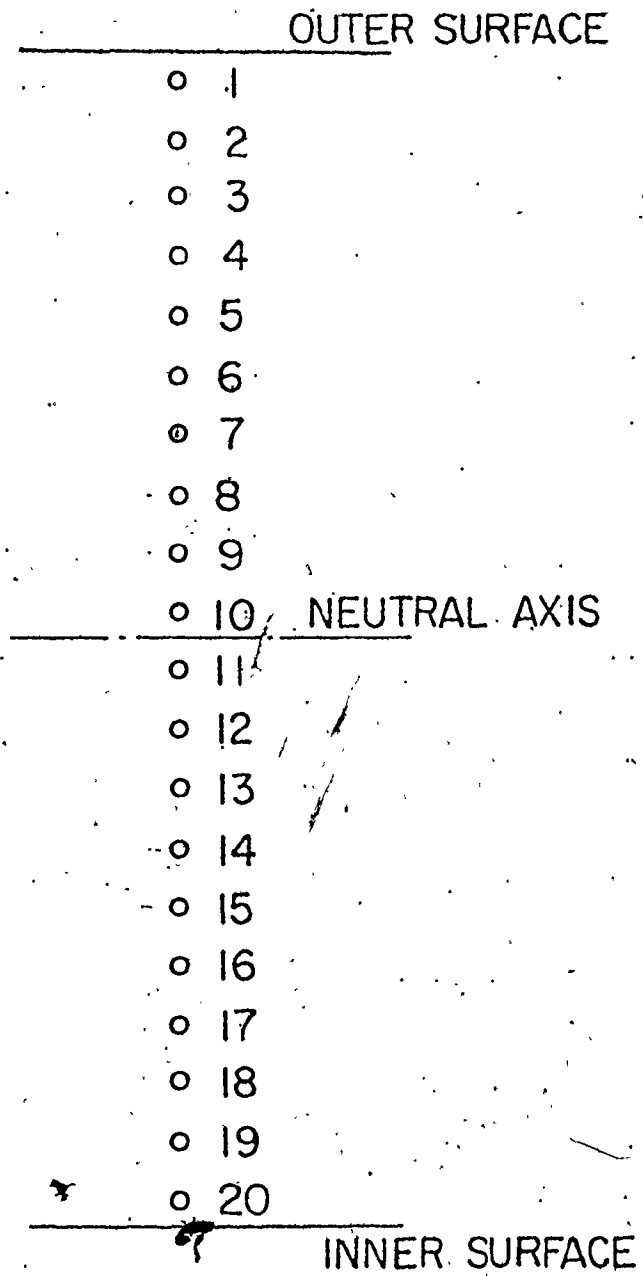


Fig. 6.5 Division of plate thickness into twenty parts.

to the total compression strain and the resultant strains were used to predict the corresponding stresses from the tensile stress-strain curve. For the ten elements in the outer shell, the first reverse experimental stress-strain curve obtained in compression after initial prestraining by 1.2% was assumed as representative of the plastic behaviour of these elements. The stresses in Fig. 6.4, curve (3) for this domain were then calculated from the first reverse σ - ϵ curve using the magnitude of the 0-compression strain, $\epsilon = -.01$. The 0-compression stress distribution (under load) in the pipe wall shows little through thickness variation indicating the dampening of residual stresses.

During manufacturing, the pipe would be seam welded at this stage and when the compression tooling is removed, the pipe will tend to recover elastically. If it is assumed that this unloading occurs in a manner such that the integral value of circumferential stress over the pipe wall produces a zero load, then the stress distribution in the wall is approximately given by the base line (4) in Fig. 6.4. It is to be noted that the preceding study of the U and O stages attempted to determine how the different domains of the pipe wall are strained and what the variations of through thickness stresses are prior to the next stage (i.e. Expansion) in the processing of the pipe. It must be recognized that the individual elements across the wall possess unique strain histories. However, for simplicity in the analysis which follows, the experimental stress-strain (history) behaviour of the two extreme surface elements will again be used as representative of individual element behaviour. As pointed out before, this method represents a kind of worst case analysis given the specific pipe geometry. The analyses up

to this point have been undertaken in order to show that residual stresses can be neglected in the calculation of expansion characteristics of the pipe in the 'E' stage of processing.

6.2.3 The 'E' Stage

It will be apparent from the mechanics of the process up to this point that only the outside portion of the pipe has undergone reverse straining in the true sense, i.e. this region has been plastically prestrained in tension during 'U' forming, unloaded and compressed during 'O' forming. During the expansion process, the outer shell will thus experience a plastic strain reversal for the second time while the remainder of the pipe will undergo reverse straining for the first time. In the present case, as indicated by the curve (4) in Fig. 6.4, the through thickness variation in residual stresses is negligible. The behaviour of the two surface elements during the expansion stage was determined using the experimental strain amplitudes in Table 6.1. The experimental paths followed were OABCDEFGHI and OPQRSTUVWXYZ in Fig. 6.3 where the segments FGH and UVW represent the expansion behaviour of the outer and inner surface elements respectively. Therefore, during the expansion, the stress-strain behaviour ascribed to the elements located at positions 1-10 in Fig. 6.5 is obtained from an experimental curve similar to FGH of Fig. 6.3 and the behaviour assigned to the elements 11-20 was derived from a curve similar to UVW.

A convenient way of studying the pressure-radial expansion behaviour is by the Finite Element Method. An FEM programme was developed analogous to that of Kitagawa and Tomita [113] which is suitable for the study of large plastic deformations in elastic-plastic materials. Since

the programme is not currently available as a publication, the basic formulations and mathematical steps are discussed in Appendix 'B' of this thesis.

The input requirements of the FEM programme include:

- (i) Element number and locations;
- (ii) Element material elastic constants;
- (iii) The pipe geometry and
- (iv) Element stress-strain behaviour.

The stress-strain curves employed were based on an approximate piecewise linear behaviour shown in Fig. 6.6. On this curve, E , E_1 , E_2, \dots, E_n are constant tangent moduli and $\sigma_1, \sigma_2, \dots, \sigma_n$ are the stresses limiting the domains of constant work hardening rate. In order to construct the finite element mesh, the pipe wall was partitioned into twenty annular and concentric elements; see Fig. 6.7(a). The element locations were as shown previously in Fig. 6.5. In addition to partitioning the pipe wall into the twenty concentric annular elements for constructing the finite element mesh, the pipe was assumed to be infinitely long so that end effects should be neglected. Plane stress deformation was assumed in which the longitudinal stress is zero, and the boundary conditions imposed are evident from Fig. 6.7(b). The annular finite element model discussed here is similar to that employed in Oden's analysis of the infinite cylinder problem, [114].

The pressure-radial expansion characteristics were calculated for two particular conditions. In the first case, the material of the pipe wall was considered homogeneous and so the stress-strain curve in monotonic loading of the original plate material was assumed to describe the behaviour of all the elements. In the second case, elements 1-10 in Fig. 6.5 were ascribed with the experimental stress-strain data of

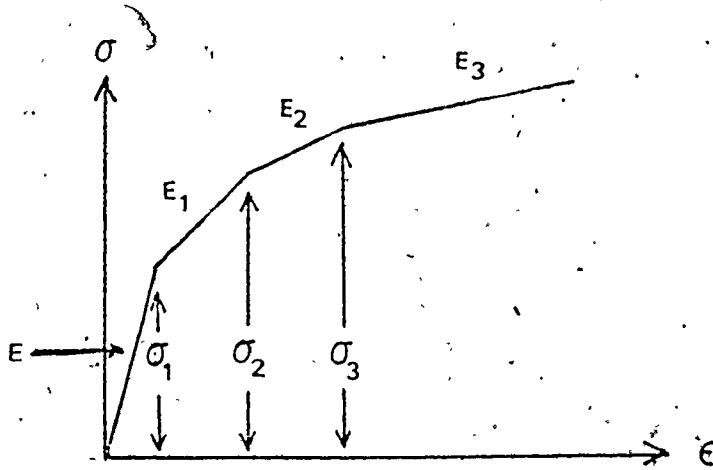


Fig. 6.6 A piecewise linear approximation method of the stress-strain curve for use in the FEM program.

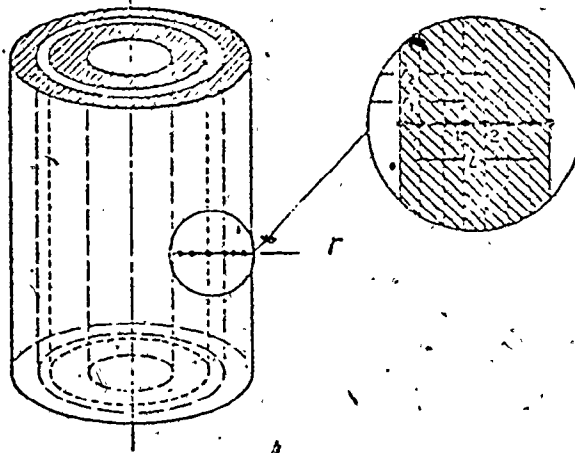


Fig. 6.7(a) The annular finite element model employed in the pipe expansion problem.

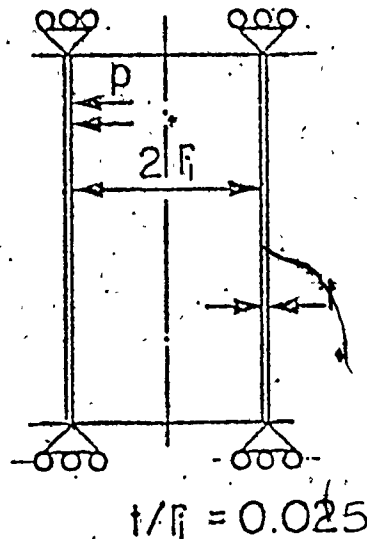


Fig. 6.7(b) The geometry and boundary conditions employed in the pipe expansion problem.

second reversal while the elements 11-20 were assigned the first reversal stress-strain behaviour. These have been previously discussed with reference to Fig. 6.3 in the expansion stage of the U-O-E process. The calculated pressure-radial expansion curves are shown in Figs. 6.8(a), (b) and (c) for the HSLA steels, A, B and C respectively. The implications of these results are discussed below, firstly in terms of the Bauschinger Effect and secondly in terms of the industrial methods of pipe strength assessment.

6.3 Discussion

6.3.1 The Influence of the BE in Pipe Making

The results in Fig. 6.8 illustrate clearly the consequences of the BE in the U-O-E process. It is seen firstly that the BE initially lowers the strength of the pipe vis à vis the homogeneous plate material and as to be expected, this is reflected by a lowering of the pressure - expansion curve for small radial expansions. However, at sufficiently large radial expansions, the U-O-E pipe shows superior strength properties, even with the BE operative, than the pipe ascribed with the homogeneous flow properties of the initial plate. This observation may be attributed to the fact that with the materials employed in this study, the effect of cyclic hardening of the type shown in Figs. 4.10 and 5.17 tends to override the detrimental influence of the BE. In the absence of this cyclic work hardening, the calculated pressure - expansion characteristics of the U-O-E pipe would always lie below the calculations based on the homogeneous behaviour of the initial plate material. It is also seen that on account of the recovery of Luder's strains in reverse flow discussed in Chapter 5,

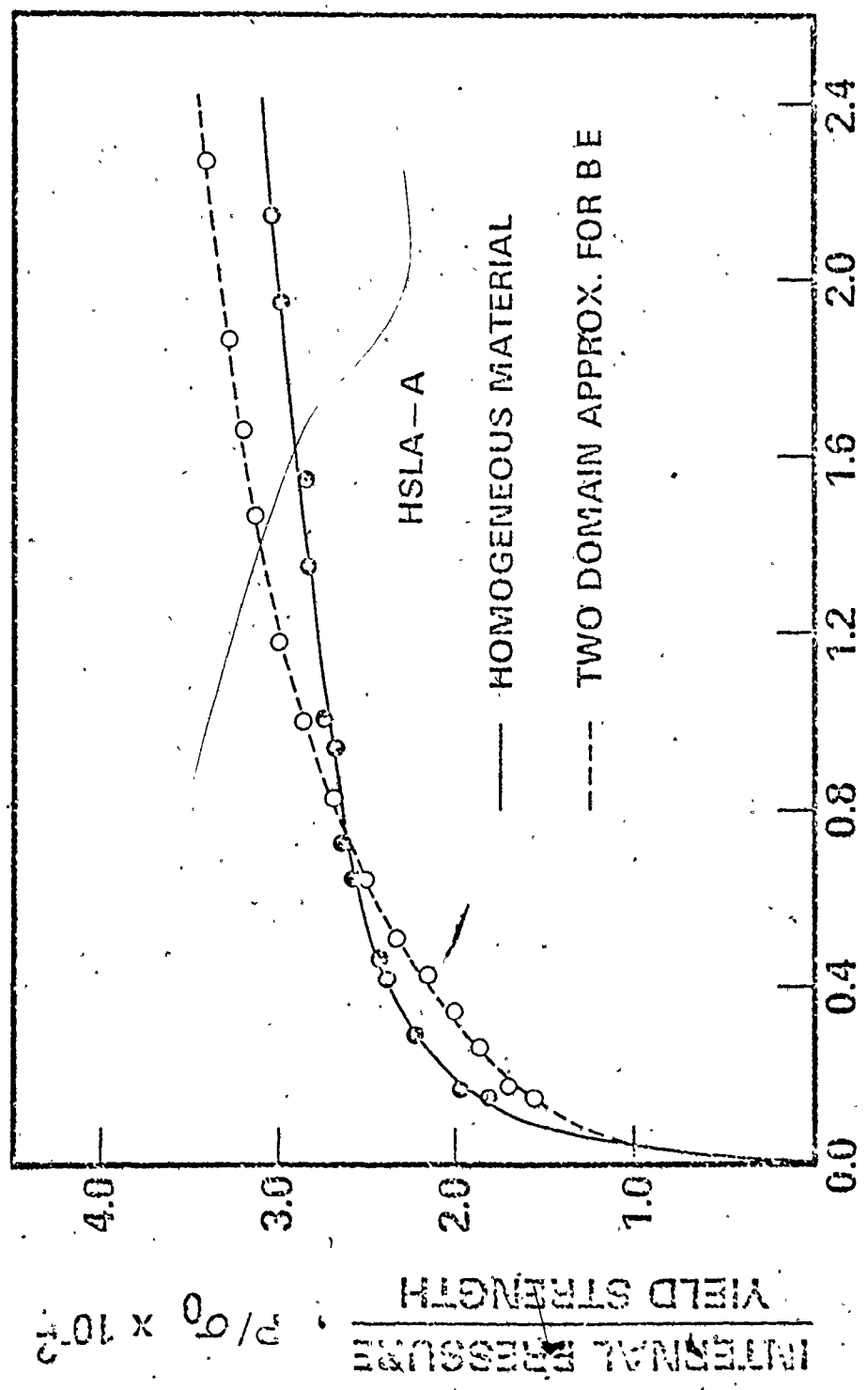


Fig. 6.8(a) Pressure-radial expansion relationship obtained by ascribing different stress-strain behaviour to the various domains of the pipe wall using the HSLA steel-A.

Section 6, the strength of the U-O-E pipe in the case of the HSLA steel-C is generally lower for the practical processing conditions chosen. It was noted previously that it is not known that Luder's strains are obtainable in loading conditions involving multi-axial stresses. However, the results presented in Fig. 6.8(c) assume that they do occur, at least in bending. It is now instructive to note that if the maximum test pressure was designed to be of the value needed to plastically expand a pipe ascribed with the yield strength and tensile flow behaviour of the homogeneous material, then two things are likely to happen:-

- (i) The HSLA materials A and B show a stronger U-O-E pipe vis a vis the parent plate for radial expansions greater than 0.5 - 0.8%. The pipe would then require a small increase in the pressure to achieve any specified displacements in excess of the cross-over expansion indicated on Figs. 6.8(a) and (b), and a much stronger pipe would result.
- (ii) If the required expansion is less than the cross-over expansions in Fig. 6.8(a) and (b), then a small increment in radial expansion would be incurred and the resulting U-O-E pipe would be, at least, as strong as the pipe ascribed with the homogeneous material behaviour. Some over sizing occurs, but this is clearly small.

The two cases discussed above apply to the behaviour of the HSLA steels A and B. In the case of the HSLA steel C, if a small radial expansion was intended, then to achieve the design pressure, unacceptably large radial expansions would occur. With respect to dimensional control during manufacturing, it may be easier to monitor the expansion pressure rather than the radial displacements during the

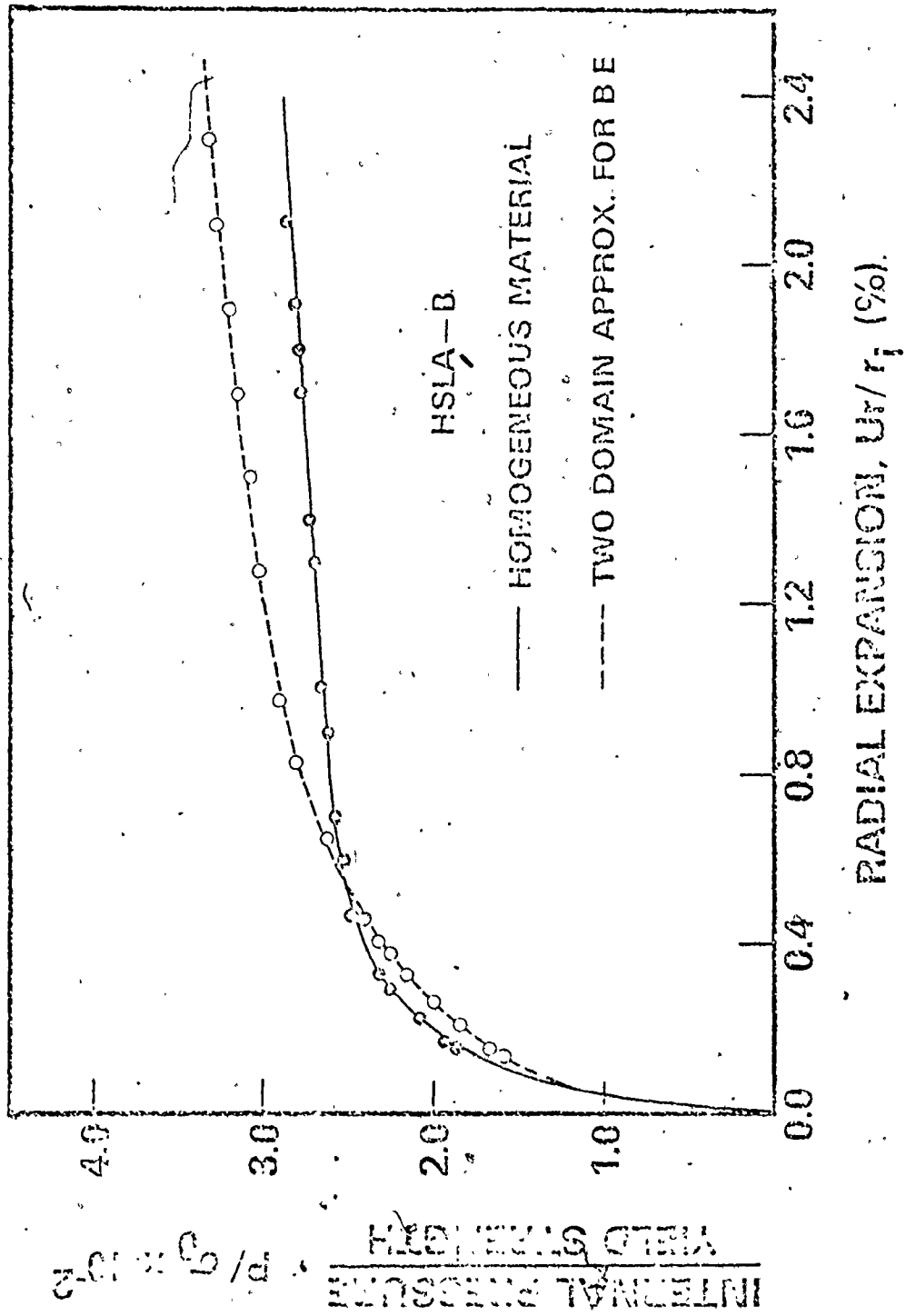


Fig. 6.8(b) Pressure-radial expansion relationship obtained by ascribing different stress-strain behaviour to the various domains of the pipe wall using the HSLA steel B.

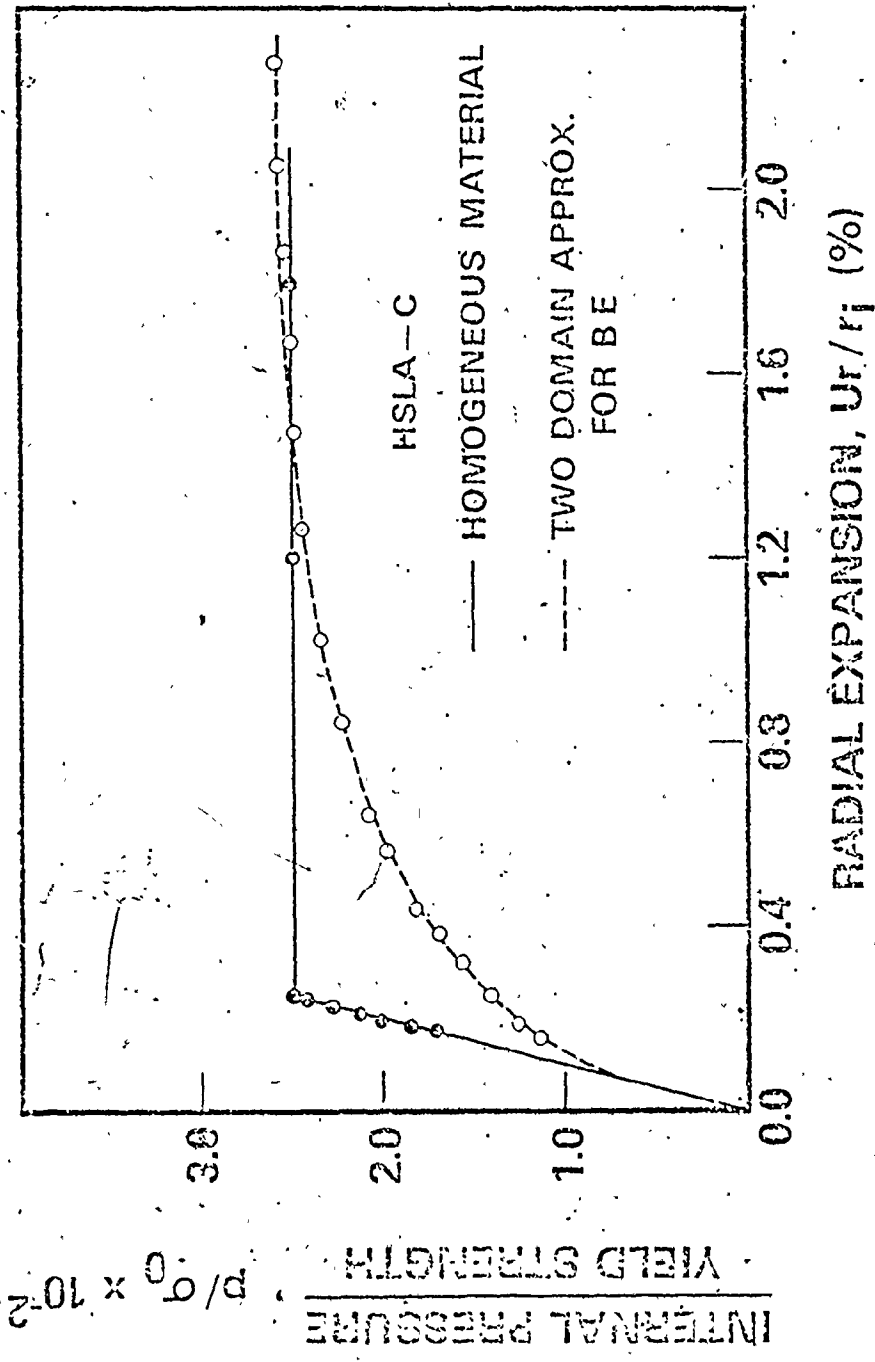


Fig. 6.8(c) Pressure-radial expansion relationship obtained by ascribing different stress-strain behaviour to the various domains of the pipe wall using the HSLA steel-C.

process. If the pressure is the control parameter, then to achieve reasonable dimensional tolerance, it would be necessary to quantitatively account for the influence of the BE as in the analysis presented here.

6.3.2 Pipe Yield Strength Assessment

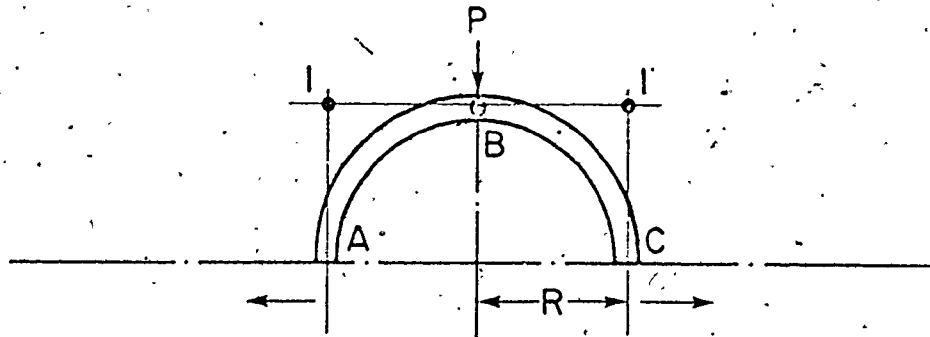
The uniaxial tensile test is the most conventional method of assessment of the basic material parameters which are widely used for specifications and design. The design strength levels of high pressure transmission pipelines are based on specifications of the minimum circumferential pipe yield strengths. It is evidently erroneous to specify the yield strength of the base plate as representative of that of the pipe in view of the strain reversals occurring during the pipe forming process from plate. The American Petroleum Institute (API) and the American Society for Testing and Materials (ASTM) recommend two methods [115] for the measurement of the tensile strength properties of the pipe. In one case, the tensile test is performed on specimens machined from a flattened transverse section of pipe full wall thickness. This method is clearly replete with the detrimental consequences of the BE firstly during the pipe manufacturing process and secondly during the unbending or straightening process of flattening. It is important to understand the consequences of the flattening process, and for this purpose, a more detailed but qualitative discussion is devoted to this aspect later in this chapter.

In recognition of the fact that the cold working introduced by flattening can alter the strength properties of the straightened coupon vis à vis the pipe material, the hydraulic ring expansion

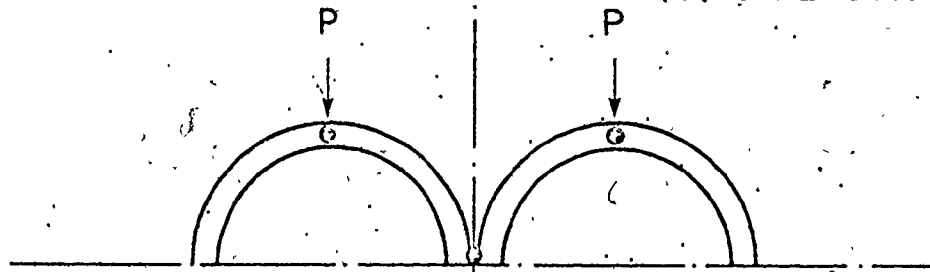
test. [115] is recommended as an alternative and more realistic method of pipe strength measurement. This test is similar in principle to the pipe - expansion process analysed above. Usually, the pressure and radial displacements (using a ring type extensometer) are monitored. Comparisons of the ring expansion and flattened strip tensile data [4,116] show that the pipe strength is generally underestimated by the later method. Furthermore, the ring expansion test data of Cotton and Thomas [116] show a clearly defined elastic domain and yield point indicating that the variations in yield stress through the pipe wall have been sensibly eliminated by the pipe mill hydrostatic expansion process.

However, in the literature from the steel and pipe manufacturers [4,117,118] attempts are still being made to predict the pipe strength from flattened strip tensile test data, mainly because of the simplicity and the inexpensive nature of the test. Some of the basic concepts of the mechanics of the flattening process are discussed below in order to show why this method of pipe strength assessment should be unequivocally disqualified. Consider, say a semi circular ring of a short longitudinal section of a pipe of mean radius, R , in Fig. 6.9 subjected to transverse flattening forces, P . In qualitative terms, the section would appear to be capable of only plastic collapse when the first plastic hinge forms at the point B to permit it to behave as a mechanism, Fig. 6.9(a). The hinge forms at the location where the bending moments are maximum. As the ends A and C slide outwards, the hinge B moves downwards in the direction of the flattening forces, P . Consequently, the arms AB and BC rotate about instantaneous centres, I and the situation in Fig. 6.9

(a) 1 PLASTIC HINGE



(b) 3 PLASTIC HINGES



(c) 7 PLASTIC HINGES

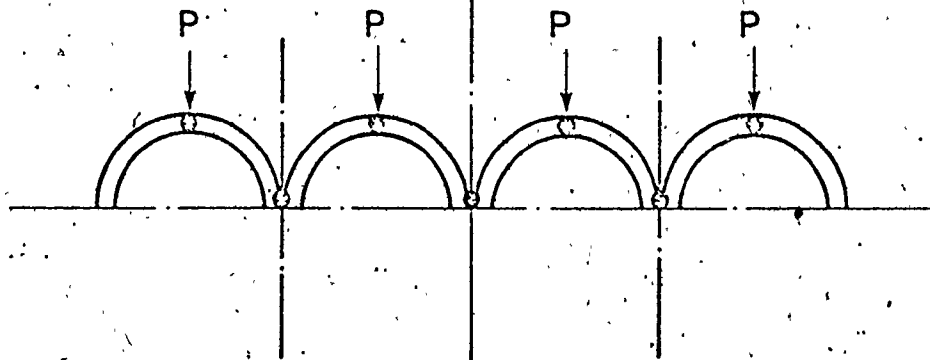


Fig.-6.9 A schematic representation of the accumulation of plastic hinges during the flattening of a transverse section of pipe.

(b) is eventually attained when two more plastic hinges begin to form. As the force, P is increased, the ring flattens to the position in Fig. 6.9(c), etc., with more plastic hinges forming. It is easy to see that at the end of the process, the flattened strip will consist of a series of highly deformed plastic hinges separated by elastic and relatively undeformed mini portions. Upon removal of the flattening forces, some spring back is to be expected and the ring can never be completely flat.

When a tensile specimen is machined from the flattened strip and tested, the deformation characteristics are bound to be grossly inhomogeneous and not amenable to any simple analysis. Moreover, the derived stress-strain data cannot be representative of that of the pipe from which the strip was cut and flattened. If the deformation during flattening was homogeneous and uniform, it would have been possible to extend the strain cycles in Figs. 6.2 and 6.3 to simulate the unbending and thereby predict the yield strength of a flattened pipe strip. However, in view of the collapse mechanism of deformation during flattening process discussed above and perhaps of other complications that might arise, in the real case, the exercise would not be of any worth.

The pressure - radial expansion curves in Fig. 6.8 are, however, reasonably quantitative and enables the prediction of the yield strength of the U-O-E pipe. In Table 6.2, the calculated nominal pipe strengths for the homogeneous and the simulated material behaviours after 1% expansion are compared with the initial plate yield strengths. The pressure, P required for 1% expansion may be obtained from Fig. 6.8 and the thin shell formula in eqn. (6.3) recommended by ASTM [115] is

used to calculate the circumferential yield stress, σ_{θ} :

$$\sigma_{\theta} = \frac{Pr_0}{t} \quad (6.3)$$

where r_0 is the outside radius of the pipe and t is the wall thickness. The result in Table 6.2 show that provided the pipe is sufficiently expanded and the base material exhibits a monotonically work hardening curve, the strength of the U-O-E pipe will be superior to that of the mother plate in spite of the BE with the materials employed in this study. If the yield point elongation exhibited by the mother plate is large as in the case of the HSLA-C, the final properties of the pipe will be relatively inferior. In this case, pipe strength levels comparable to that of the mother plate can be obtained using large radial expansions but at the expense of dimensional tolerance. It may be noted here that the high work hardening rate dual phase HSLA steels discussed in Chapters 4 and 5 would be advantageous in linepipe applications, the main reasons being the low initial yield strength, the high initial work hardening rate and the tendency to cyclically harden as evident in Fig. 5.17.

TABLE 6.2
Nominal Pipe Strengths After 1% Expansion

Material	Initial (.1%) Yield Stress, ksi (MPa)	Final Pipe Strength, ksi (MPa)	
		Homo. Matl.	Simulated Matl.
HSLA-A	65.8 (454)	72.8 (502)	76.9 (530)
HSLA-B	64.6 (445)	69.8 (481)	76.3 (526)
HSLA-C	70.4 (485)	70.4 (485)	67.5 (466)

In conclusion, it must be emphasized that the flattened strip tensile test does not yield results that are representative of pipe strength. The ring expansion test is clearly a more realistic test for pipe strength assessment. In the case where this facility is not available, then the yield strength of the mother plate, although it underestimates the pipe strength, should be confidently quoted in specifications. This is, given that the material is known to cyclically work harden. These last remarks of course apply to pipes whose mother plate material possesses a rounded stress-strain curve. Materials which exhibit a large yield plateau of Luder's strains, in the opinion of this author should rarely be employed in high strength linepipe applications.

CHAPTER VII

CONCLUSIONS

The present thesis has been concerned with aspects of the mechanical behaviour of a variety of structural steels in forward and reverse flow. Attention has been focussed on the Bauschinger Effect in these materials firstly in terms of its phenomenological description and more fundamentally, in terms of its natural causes. The latter aspect has been studied quantitatively in relation to the microstructural aspects of work hardening in dispersion hardened (two phase) alloys. The model of work hardening due to Brown and Stobbs provided a basis for the investigation of the microscopic aspects of the Bauschinger Effect. The major objective of the work was to test the applicability of the microscopic model to commercial quality structural steels and thereby provide a more general view as well as an increased understanding of the Bauschinger Effect and its consequences.

A good deal of emphasis has also been placed on the implications of the Bauschinger Effect in practical applications. In this regard, the U-O-E method of pipe fabrication was studied in detail in order to elucidate the detrimental, or otherwise, influence of reverse strain cycling and the Bauschinger Effect in the manufacture of a high strength pipe using three different grades of commercial linepipe quality HSLA steels.

The principal conclusions arising from the present study are

as follows:-

7.1 On the Phenomenological Modelling of the BE

(i) The BE observed in many materials is related in general to the production of internal stresses during the deformation of the material.

(ii) Since the main cause of the BE is attributed to the inhomogeneity in straining between the different phases of a material, macroscopic models can be developed with this concept in mind. In this present study, the simplest of these was to simulate the behaviour of a real material by assuming that it comprises of a number of elements connected in parallel, with each element exhibiting a different stress-strain behaviour. Upon unloading (to zero load) following prestraining, the model provided for a residual stress in the individual elements.

When the loading was continued in the reverse sense, the model also displayed the BE by means of a reduced level in the reverse yield strength and roundedness.

(iii) A number of work hardening models, based on the continuum theory of plasticity, have been described. The more sophisticated theories allow for distortion, translation and expansion of the yield surface and, in principle, account for the development of anisotropy and the Bauschinger Effect. However, the models are not a priori predictive and some measurements are required on the material in its deformed state.

The simple kinematic hardening model does not, in general, provide an adequate description of the BE. In this thesis, however, it is demonstrated that a simple modification of the kinematic hardening model due to Mroz [60], by combining both kinematic and isotropic hardening, can lead to an excellent representation of certain experimental reverse flow

behaviour.

7.2 On the Microscopic Model of the BE due to Brown and Stobbs. [85, 86]

(i) The effect of internal stresses developed in a material during deformation increases the flow stress of the material in the forward direction but aids plastic flow in the reverse direction. In reverse flow, the mean value of the internal stresses is measurable as permanent softening.

(ii) Using experimentally derived values of permanent softening to characterize the BE, the model of Brown and Stobbs was shown to apply in general to steels strengthened with a coarse dispersion of hard particles, i.e. spheroidized and HSLA steels. Aspects of the model which predicted certain functional relationships between the permanent softening and prestrain or volume fraction were verified. The model was then used to study the development of internal stresses in terms of the unrelaxed strain. This was also shown to be in good accord with the conclusions of the model.

(iii) The ratio of permanent softening to the total work hardening was also studied in detail as a parametric measure of the BE. The model of Brown and Stobbs required this parameter, that is, the BEP to be independent of prestrain and to vary linearly with $1/\sqrt{V_f}$ where V_f is the volume fraction of second phase particles in the material. These characteristics were shown to be obeyed very well by those materials which possess a rounded tensile $\sigma - \epsilon$ behaviour. In the case of materials which exhibit a large yield point elongation at initial yielding (and this is often found in steels), large prestrains are necessary in order to characterize the BE by means of the BEP.

7.3 Implications of Internal Stresses

(i) Internal stresses can cause dimensional instability in parts manufactured using a cold metal forming process. The case of cold drawn 1045 steel rods was cited as an example. The internal stresses produced during the drawing deformation produced a distinct curvature on the rods which upon straightening give rise to increases in the diameter of the rods.

(ii) The production of cyclic stress-strain hysteresis loops was interpreted as due to a sequence of events in which the internal stresses generated in the previous half cycle are first annihilated upon strain reversal. Following this, a new distribution of back stresses are developed ready to aid reverse flow if the loading is again reversed. This sequence of events takes place during each reversal and the cyclic curves therefore soon become symmetric with each curve exhibiting the BE in terms of a reduced yield strength and a highly rounded flow curve. On account of the continuous cycling of the structure, a direct interpretation permanent softening is not possible. All the materials tested exhibited cyclic work hardening.

(iii) It was demonstrated that overstraining by tensile necking was insufficient to produce enough structural damage in the form of particle cracking or interface decohesion to relieve the material of internal stresses. However, following this overstrain, the useful tensile strain range of the material can be increased by cycling the material first in compression before reloading in tension. Although this technique suppresses the incidence of tensile necking during the second tensile loading, the maximum flow stress of the material remains approximately

the same.

7.4 Discontinuous Yielding in Reverse Flow

(i) The yield point elongation (Luder's strains) is obtainable regardless of whether the initial loading is in tension or compression. The Luders strain is also evident in subsequent cycles providing that the accumulated plastic strain has not been sufficient to permit the Luders strain to propagate throughout the entire length of the specimen.

(ii) Discontinuous yielding is related to the sense of loading. It is shown that with cylindrical specimens, the propagation of the Luders strain front in compression increases the diameter of the portion of the specimen traversed by the front. It is well known that the cross sectional area decreases if the Luders strain is propagated in tension. The strain always propagates in the direction of the material that had not been hitherto deformed plastically.

(iii) It is shown that if a specimen is preloaded in tension (permitting partial propagation of the Luders front across the gauge length) then upon reverse loading in compression it is the portion of the specimen that has been traversed by the Luders front that yields again first. The reverse flow curve shows a BE, i.e. a reduced elastic limit and considerable rounding up to the point where the Luders front continues to propagate across the specimen. At the point of reappearance of the Luders strain, the total plastic strain (derived from the prestrain which is positive and the reverse strain which is negative) is zero and the stress at propagation is of the same order of magnitude as the lower yield stress of the material.

(iv) In monotonic loading the Luders strain is characterized on a

load - extension diagram by a constant load plateau covering a strain range, of say X%. At the end of this stage, the load increases again due to work hardening. A similar behaviour is exhibited during cyclic loading. The constant load plateau is observed in each tension and compression half cycle until the accumulated strain reaches X%, at which stage the specimen begins to work harden.

7.5 Empirical Aspects of the Bauschinger Effect

- (i) By representing the BE in conventional terms using the difference between the forward prestress and the reverse yield stress, the BE was shown to increase monotonically with the prestrain; no comparisons with the volume fraction were made in this case.
- (ii) A parametric empirical definition, the BEP^* was employed to incorporate the reverse yield stress in a parameter similar in form to the BEP. It appeared that the BEP^* behaved in a manner similar to that of the BEP with respect to variations in the level of prestraining. The magnitude of the BEP^* , however, depended on the method of characterization of the reverse yield stress. In this present study, the reverse yield stress was defined by means of the offset strain method and the magnitude of the BEP^* decreased if the offset strain was increased. Also, the behaviour of the BEP^* was observed to be rather transient at small prestrains, particularly if the material studied possessed a discontinuous stress-strain curve. It is concluded that the BEP^* is useful for a simple empirical ranking the BE in different material provided that: (a) the same definition of the reverse yield stress is used, (b) rather large prestrains can be used if the material shows the yield point phenomenon.

(iii) Some qualitative discussion was also devoted to the aspect of roundedness of the reverse flow curve. It was suggested that the roundedness increases as a function of the prestrain and the volume fraction of microscopic second-phase particles.

7.6 On a Practical Application: The Bauschinger Effect in Pipe Manufacturing

(i) The manufacturing process of a U-O-E pipe produces strain reversals in the wall thickness of the pipe material. These reversals were simulated experimentally using tension - compression loading and the data was employed to investigate the pressure - radial expansion characteristics of the pipe. The data from the HSLA steels tested show that the BE lowers the strength of the pipe vis à vis that of the homogeneous material for small radial expansions. If the radial expansion is increased, a stronger pipe, vis à vis the homogeneous plate material was obtained with two of the HSLA steels used in this study. These two steels showed a tendency to cyclically work harden which had an offsetting effect on the detrimental influence of the BE.

(ii) The third HSLA steel exhibited a rather large yield point elongation. With this steel, on account of the reappearance of Luder's strains in reverse flow, the strength of the model U-O-E pipe was lower than that of the pipe ascribed with the stress-strain behaviour of the homogeneous material. At rather impractical large levels of radial expansion, the strength levels were, however, of the same order of magnitude.

(iii) Implicit in (i) and (ii) is the fact that with the HSLA steels A and B, there is no danger of violating the dimensional specifications

during the expansion process. However, with the HSLA steel C, if the prescribed radial expansion is small compared to the Luder's strain in the material, the pipe would be relatively oversized.

(iv) Finally, the industrial methods for the assessment of pipe strength were discussed. A rather qualitative analysis was used to show that the flattened strip tensile test does not yield results that are representative of pipe strength. The ring expansion test, although more expensive was recommended as a more realistic test in this regard. The pipe pressure-expansion data also indicated that it may be safer to quote pipe strength specifications based on that of the initial plate if ring expansion test data are not available. This is given that the material is known to cyclically work harden and does not possess a discontinuous yield behaviour.

7.7 Recommendations for Further Work

(i) The observation of a threshold mean matrix stress, $\langle \sigma \rangle_0$ could not be fully explained within the context of this present study. It is proposed that the origin of this stress be further investigated in relation to its variations with prestrain, microstructural parameters and heat treatment.

(ii) A study of the Bauschinger Effect Parameters specifically in materials which exhibit large Luder's strains is recommended. This pertains to the influence of the yield stress, σ_0 on the BEP, where σ_0 is determined by the method of back extrapolation of the stress-strain curve to intercept with the elastic loading line.

(iii) It is proposed that experiments be designed in order to study

whether the discontinuous yielding behaviour observed in tension or compression loading with some steels are obtainable in multiaxial loading. The bulge test is an example of such an experiment. The necessary instrumentation would have to be sensitive to very small displacements.

(iv) The roundedness of the reverse stress-strain curve was discussed briefly in this study. The prestrain imposed and the volume fraction of the second phase material present were cited as some of the parameters controlling the extent of the rounding. It is suggested that a study of roundedness be undertaken in order to clearly elucidate the mechanism(s) of the phenomenon, the influence of mechanical and microstructural parameters and the role of internal stresses and the Bauschinger Effect.

(v) Further, two dual phase HSLA steels were employed to study the development of symmetric tension-compression loops. These are steels in which the volume fraction of the martensitic phase present in the structure has been increased by means of intercritical annealing followed by accelerated cooling. They are relatively new and have been developed to possess better forming properties. It is recommended that the formability of the dual phase steels be investigated, with some special attention paid to the hardening rates sustained during the reverse flow deformation. This is important in regard to the utilization of dual phase steels in both fabrication operations and service conditions which involve reverse strain cycles.

(vi) The question of dimensional stability was discussed briefly in the thesis. The work by Lucas [104] on cold drawn 1045 steel rods was

cited with regard to the type of gross dimensional changes produced by the internal stresses generated during the deformation processing. The cases of the development of a central burst in extruded and drawn products also appear to relate to the general problem of internal stresses. In this connection, concern has been with the development of die geometries which can lead to the generation of a tensile stress component along the axis of the extruded or drawn product. However, little work has been done to correlate this with the microstructural parameters of the material. It is recommended that some investigations be devoted to the influence of the second phase particles present in the material and the associated inhomogeneity of the straining in order to demonstrate the possible role of internal stresses. The recent review on dimensional instability by Marschall and Manrigger [134] clearly indicates that experimental techniques exist for the measurement of microplastic strains and dimensional instabilities, but so far, these have not been extensively applied to detailed microstructural features.

(vii) Second order effects, i.e., rod lengthening effects in torsion loading were also discussed in the thesis. In this regard, investigations could be undertaken to determine the role of microstructural parameters on the magnitude of the elongation and other aspects of second order effects.

APPENDIX A

METALLURGICAL AND PROCESSING FEATURES OF CONTROLLED-ROLLED HSLA STEELS

High-strength-low-alloy steels are currently finding large tonnage applications as linepipe and structural materials in the form of plates. In addition, there is a large potential market in the automotive industry for the thinner gauge HSLA steel products. For these applications, the high strength to weight ratio of HSLA steels provides the major attraction. The HSLA steels used in this present study are commercial high strength linepipe grade materials. In addition to high strength and toughness and good weldability, weight saving is also an important consideration in the selection of HSLA steels for pipelines. This is so because cost reductions are obtained on account of material savings and the relative ease of material handling, transportation and field installation. In the bulk transportation of oil and gas, HSLA steels constitute the most attractive of materials for pipelines operated in extreme climatic conditions such as Alaska, the Canadian Arctic Islands and the Arctic regions of Siberia in the USSR. Large diameter pipeline installations up to 48" (1220 mm) and 54" (1372 mm) in North America and 56" (1422 mm) in the USSR are reported to be projected for the near future [119,120].

HSLA steels derive the name from the presence of small amounts of microalloying elements such as columbium, vanadium and titanium in the composition. The role of these alloying elements is to enhance strength and toughness properties mainly through grain refinement and

precipitation hardening. The use of low carbon contents (approx. .05%) also considerably improves the weldability. The physical metallurgy of controlled rolled HSLA steels has been described in a number of excellent articles recently by Irvine et al [12], Luyckx et al [122], Gray [123] and Tither et al [124]. The results of these investigations have brought into focus some of the more important features of the complex phase transformations occurring during the hot rolling and continuous cooling of a controlled rolled HSLA steel. It is well known that precipitation hardening impairs the notch toughness of steels while increasing the yield strength. However, good overall mechanical properties are still obtainable provided certain hot rolling variables are suitably controlled. Prominent among these are the finishing temperature, the amount of deformation during hot rolling, the cooling rate and the composition. Furthermore, the existence of large volume fractions of inclusions has been a major problem in the production of HSLA steels possessing relatively little anisotropy. To reduce this directionality of mechanical properties such methods as cross rolling, desulphurization or the modification of inclusion morphology through chemical treatments with rare earth type alloys such as cerium, calcium and zirconium [121,123] are employed.

It is not the intention here to completely review the extensive literature currently available on HSLA steels. For this purpose, the complete set of the Proceedings of the "Microalloying '75" Conference [12] covering such areas as - history and theory; products, processes and linepipe; properties and applications - would provide a good starting point. Interest in this thesis has been centered on those

metallurgical aspects which clearly delineate the type and morphology of the non-ferritic constituents of HSLA steels as these are expected to influence the observed BE in these materials. To this end, it is pertinent to deal in some detail on the expected microstructures in HSLA steels following controlled rolling. In commercial production, a steel slab is reheated and 'soaked' at a high enough temperature to austenitize the steel. The hot slab is then hot rolled successively to the desired strip thickness and water spray cooled before coiling for the market. It is important to note that low finish rolling temperatures improve grain refinement and the toughness of the steel considerably; however, the risk of austenite-ferrite ($\gamma - \alpha$) transformation is higher at low finishing temperatures. This latter aspect is undesirable due to the sudden increase in grain size. There appears to be an optimum set of processing temperatures for a given composition. Glover [126] has shown that processing temperatures influence the yield strength as follows:-

(a) the slab reheating temperature and time determine the amount of microalloying elements taken into solution and so influences the potential for precipitation hardening. Here, it is noted that it is not necessary to completely solutionize the microalloying precipitates. As pointed out by Heitmann et al [127], the retention of some undissolved precipitates in the prior austenite during soaking retards the $\gamma - \alpha$ transformation and leads to the use of lower and more convenient finishing temperatures.

(b) the finishing temperature determines the grain size through its relationship with the $\gamma - \alpha$ transformation and austenite recrystalliz-

ation temperatures.

(c) the final coiling temperature and cooling rate influences the rate of precipitation (through diffusion) of the carbides and carbonitrides of the microalloying elements and so affects the yield strength and the toughness of the as rolled HSLA steel plate.

Grain sizes in the as rolled HSLA steel are more or less a close copy of the final austenite grain size during controlled rolling. One reason, therefore for the widespread use of microalloying elements, particularly columbium, is to retard austenite recrystallization and transformation thereby inhibiting grain growth. On cooling, provided the cooling rate is sufficiently high, any untransformed austenite converts directly to martensite. Consequently, a variable mixture of ferrite, martensite, cementite and precipitated carbides and carbonitrides may be expected in HSLA steels. Such in fact is the case and the resulting microstructures are broadly classified as either polygonal or acicular in form. Some typical microstructures are described in refs. [127,128].

In this work, the cementite, the complex austenite - martensite (M/A) islands and the precipitated carbides and carbonitrides were viewed as essentially playing the same roles as the cementite spheroids in the spheroidized C-Mn steels discussed earlier in Chapter 4. In this connection, the total amount or some fraction thereof of these particles constitute a distribution of a hard and non deformable second phase relative to the matrix which consists mainly of softer ferrite. The particle morphologies in the HSLA and the C-Mn systems are of course different. The role played by these structural heterogeneities

in the material, from the point of view of the Bauschinger Effect, has been a major subject of this thesis. The approach has been to characterize the heterogeneity in terms of the volume fraction of second phase particles and to delineate the influence of the particles on the process of plastic deformation. It is shown that the particles generate internal stresses which in turn cause the totality of behaviours which are described, in general, as the Bauschinger Effect.

APPENDIX B

SUPPLEMENT TO CHAPTER 5, SECTION 5.8

(Experimental Aspects of the Bauschinger Effect in HSLA Steels)

In Chapter 5, section 5.8, some of the experimental measurements of the Bauschinger Effect using the HSLA steel A were presented and discussed in full. The results obtained from test samples oriented in the rolling direction of this material were employed for this discussion in order to characterize the BE in empirical terms in the HSLA steels. This appendix is included for completeness in order to present certain data similar to Figs. 5.22 - 5.24 in section 5.8 for the HSLA steels B and C. Some of the measurements to be presented were made using test samples oriented in both the rolling and the transverse rolling directions of the plates of the three HSLA steels. These are shown below, and where needed, comparisons with some of the results previously presented in Chapter 5 are indicated directly on the diagrams.

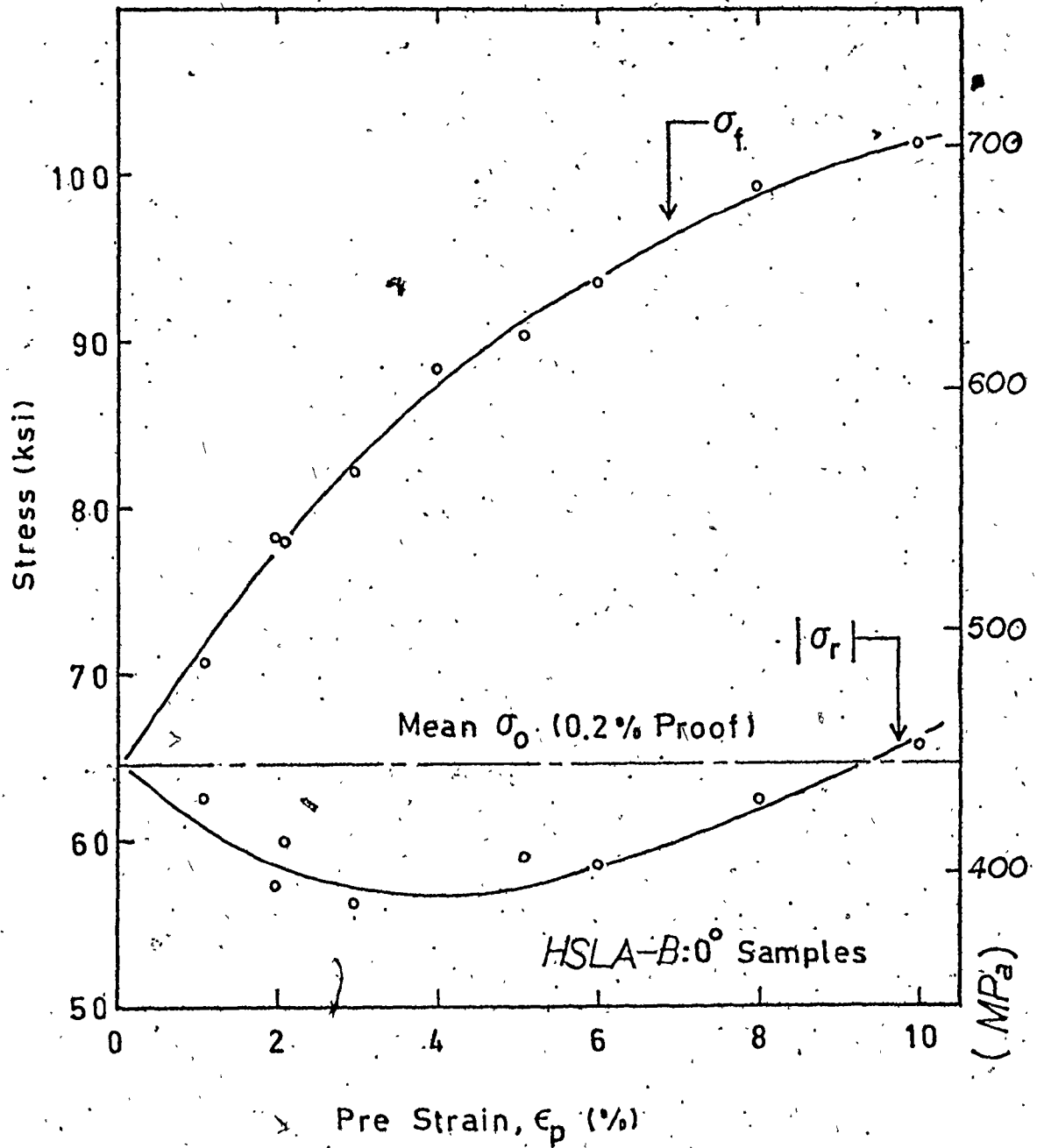


Fig. B.1 (Cf., Fig.5.22(a)) A comparative plot of the tensile prestress, σ_f and the compressive (reverse) yield stress, σ_r as a function of prestrain.

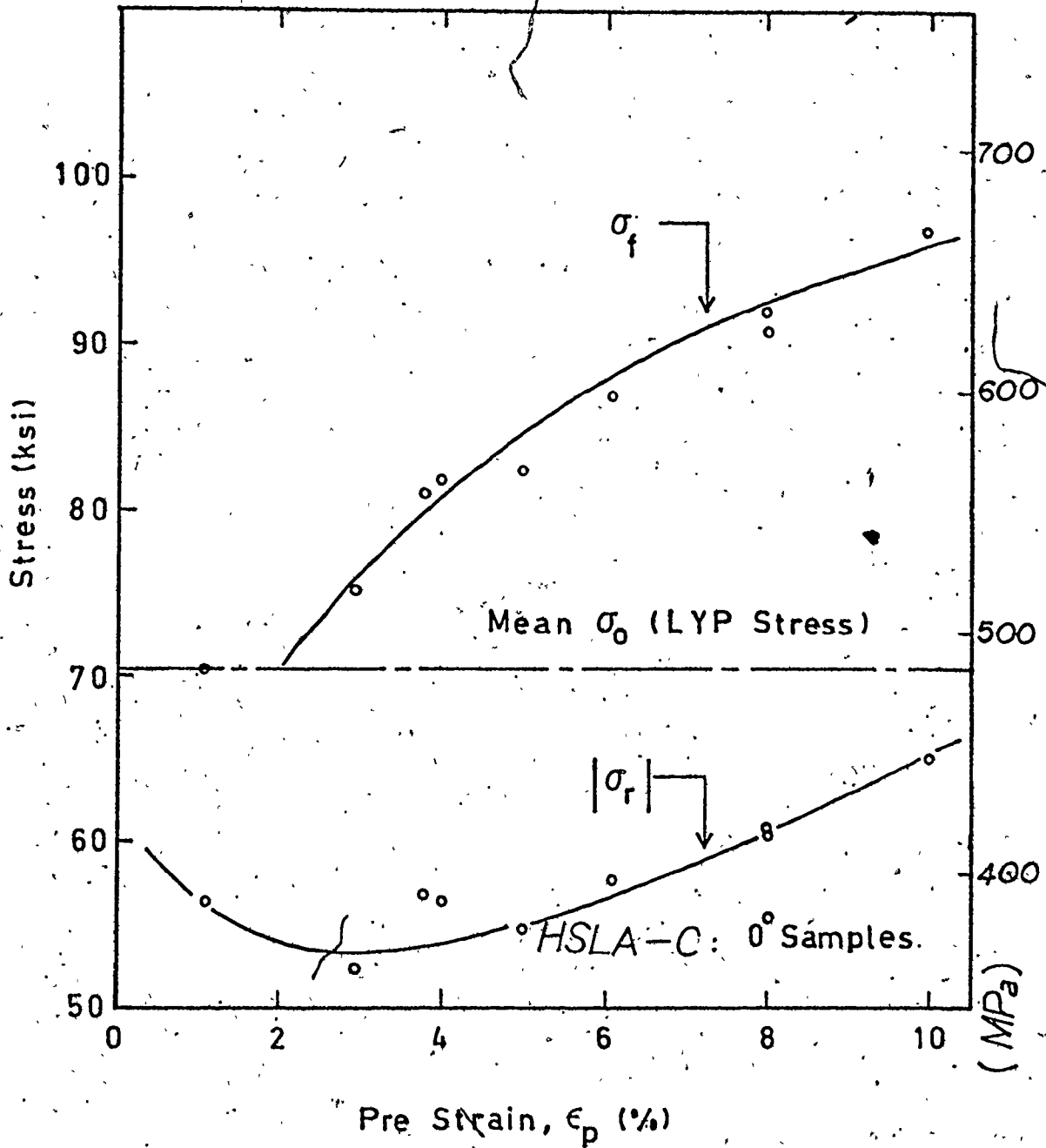


Fig. B-2 (Cf., Fig. 5.22(a)) A comparative plot of the tensile pre-stress, σ_f , and the compressive (reverse) yield stress, σ_r , as a function of prestrain.

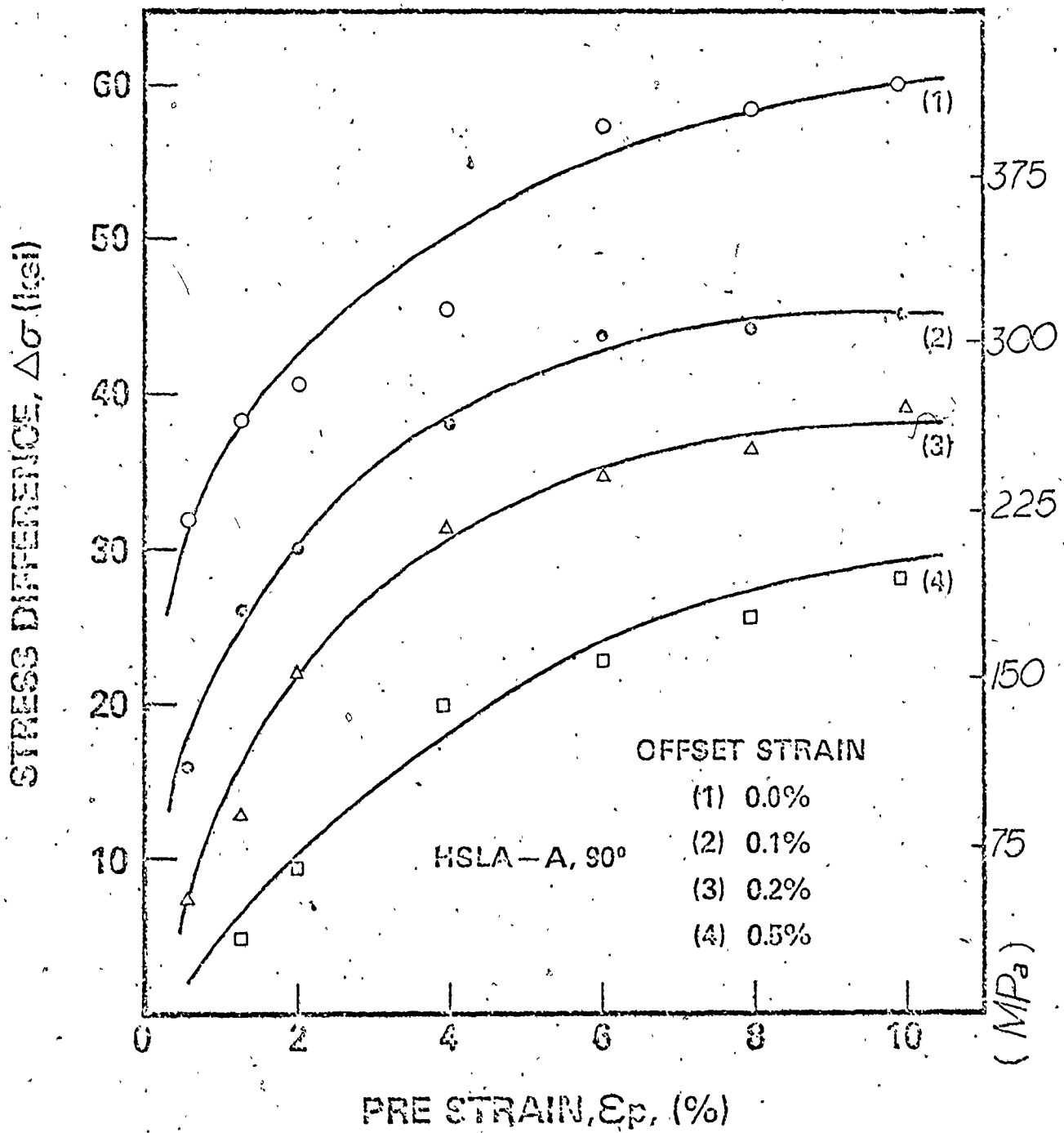


Fig. B.3 (CF., Fig. 5.23) The Bauschinger Effect measured by the stress difference, $(\sigma_f - \sigma_r)$ as a function of prestrain and using four offset strain definitions of σ_r .

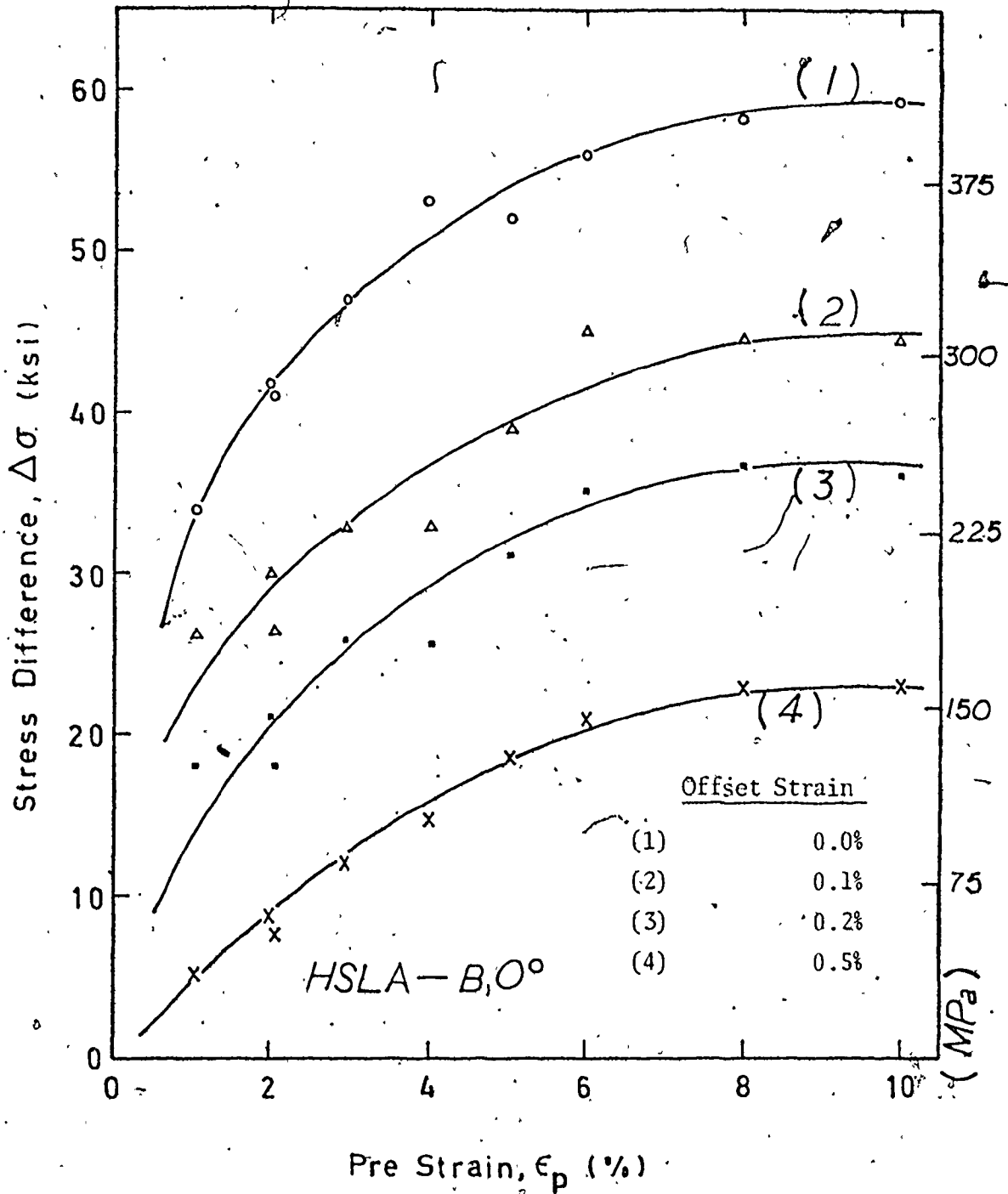


Fig. B.4(a) (Cf. Fig.5.23) The Bauschinger Effect measured by the stress difference, $(\sigma_f - \sigma_r)$ as a function of prestrain and using four offset strain definitions of σ_r .

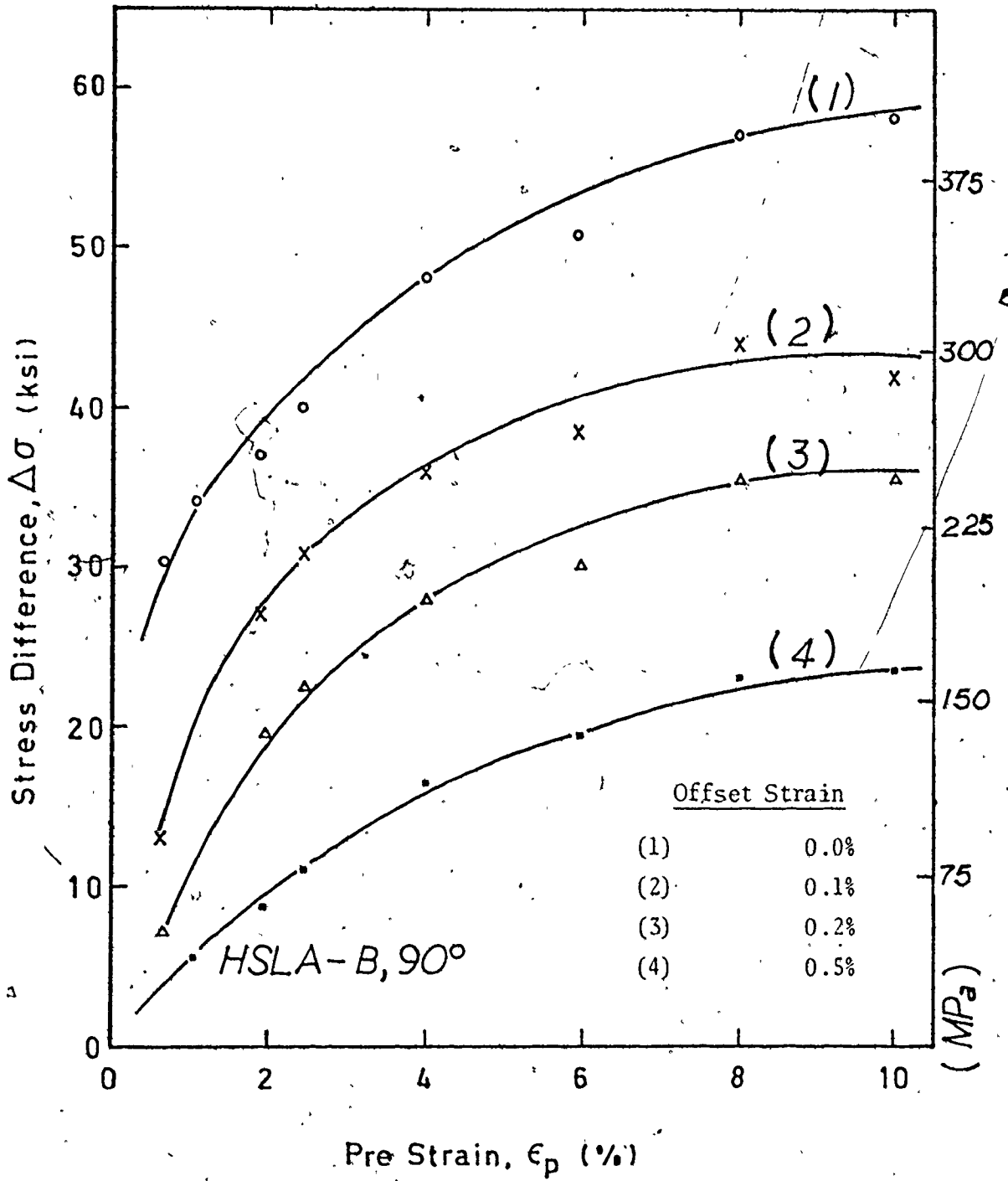


Fig. B.4(b) (Cf., Fig. 5.23) The Bauschinger Effect measured by the stress difference, $(\sigma_f - \sigma_u)$ as a function of prestrain and using four offset strain definitions of σ_r .

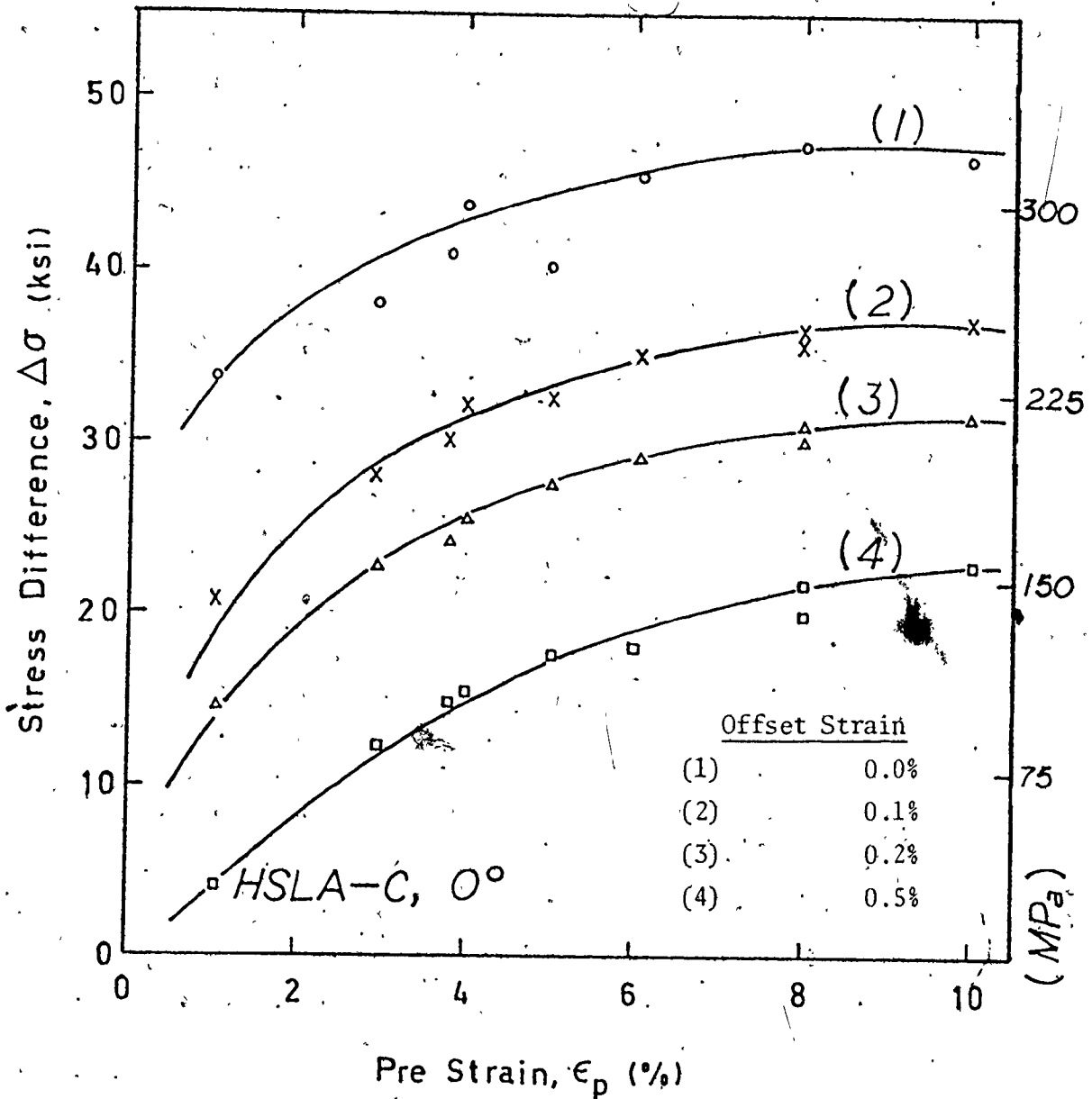


Fig.B.5(a) (Cf., Fig. 5.23) The Bauschinger Effect measured by the stress difference, $(\sigma_f - \sigma_r)$ as a function of prestrain and using four offset strain definitions of σ_r .

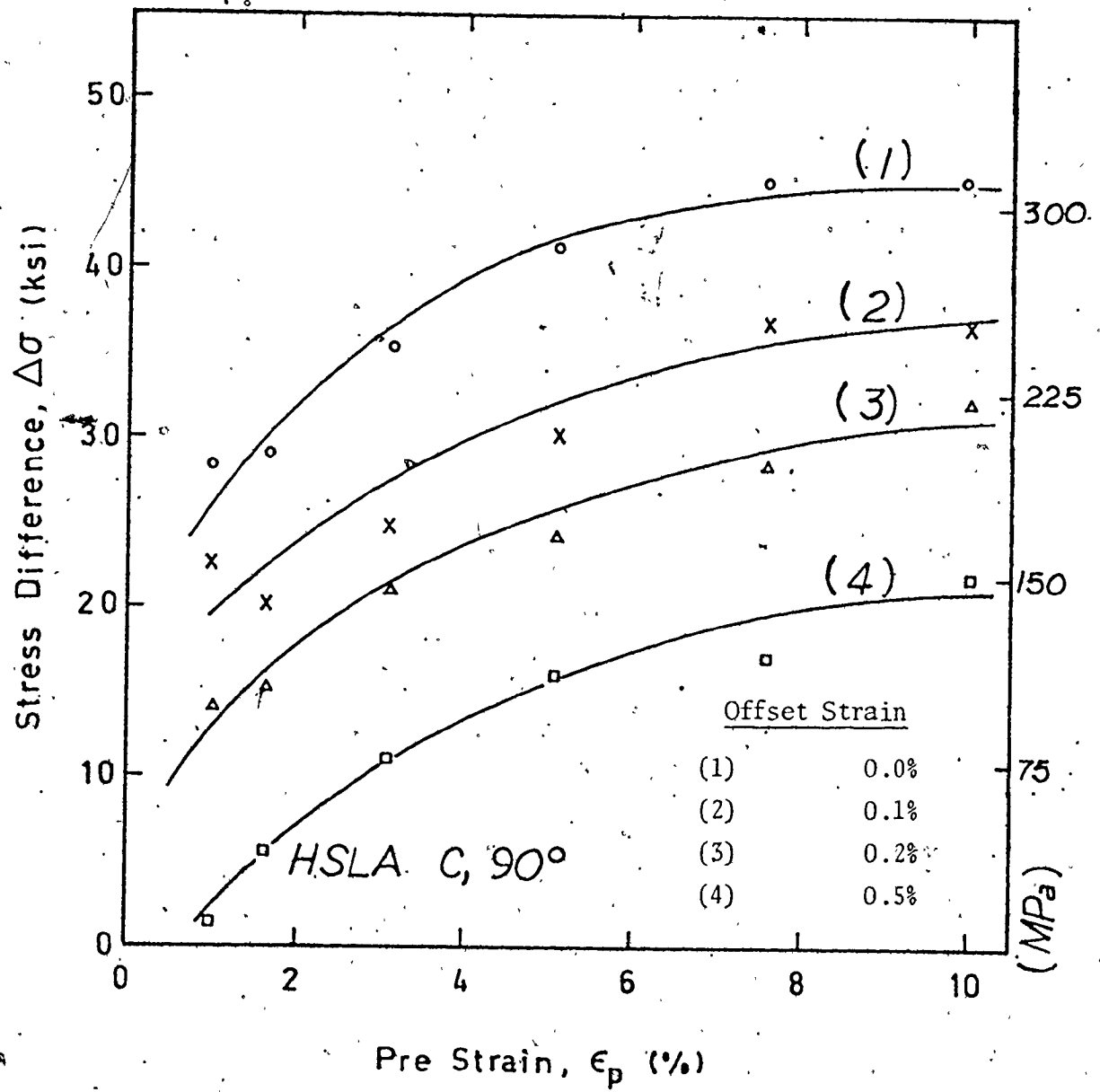


Fig. B.5(b) (Cf., Fig.-5.23) The Bauschinger Effect measured by the stress difference, $(\sigma_f - \sigma_r)$ as a function of prestrain and using four offset strain definitions of σ_r .

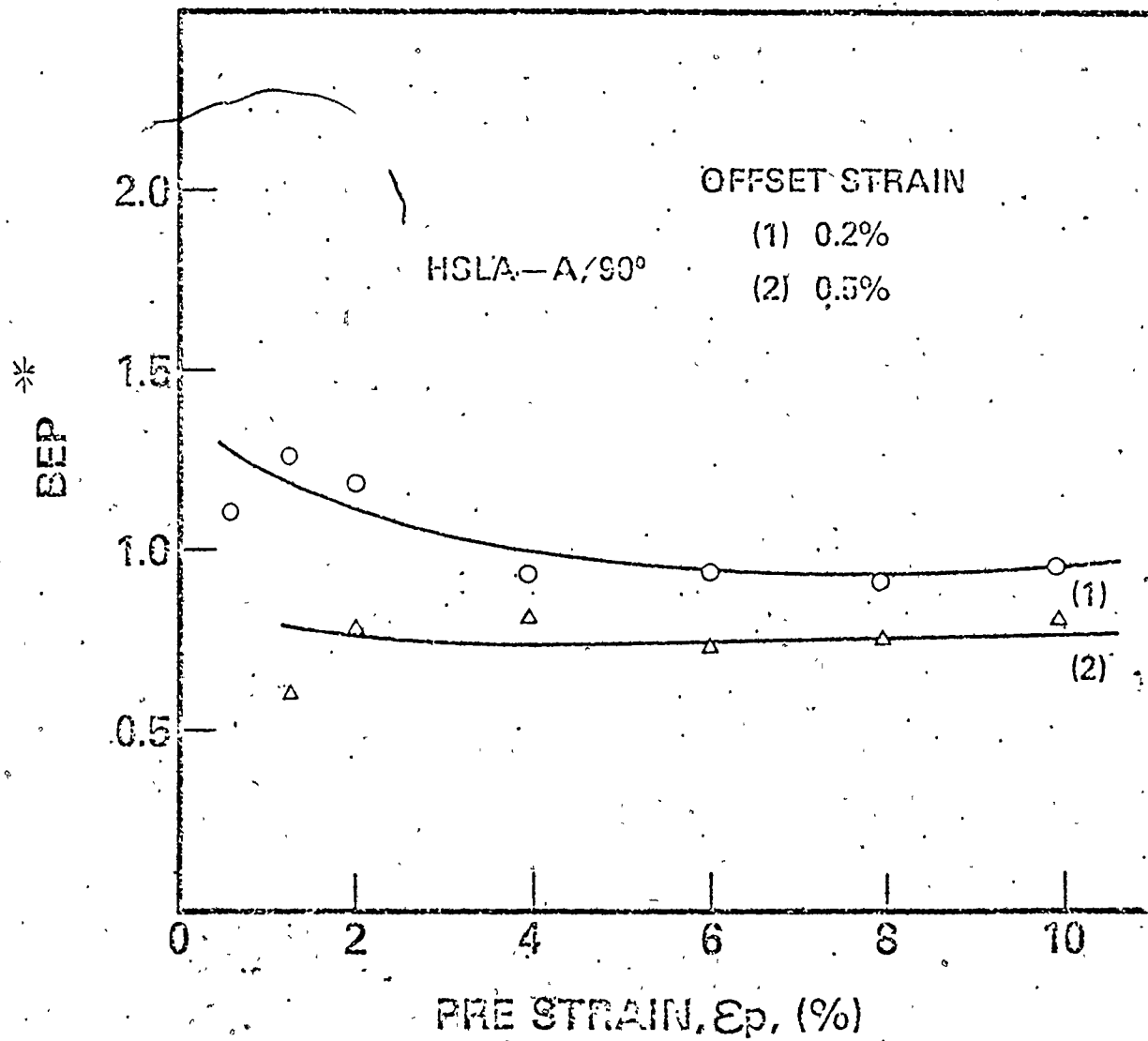


Fig. B.6 (Cf., Fig. 5.24) The empirical parameterization of the Bauschinger Effect.

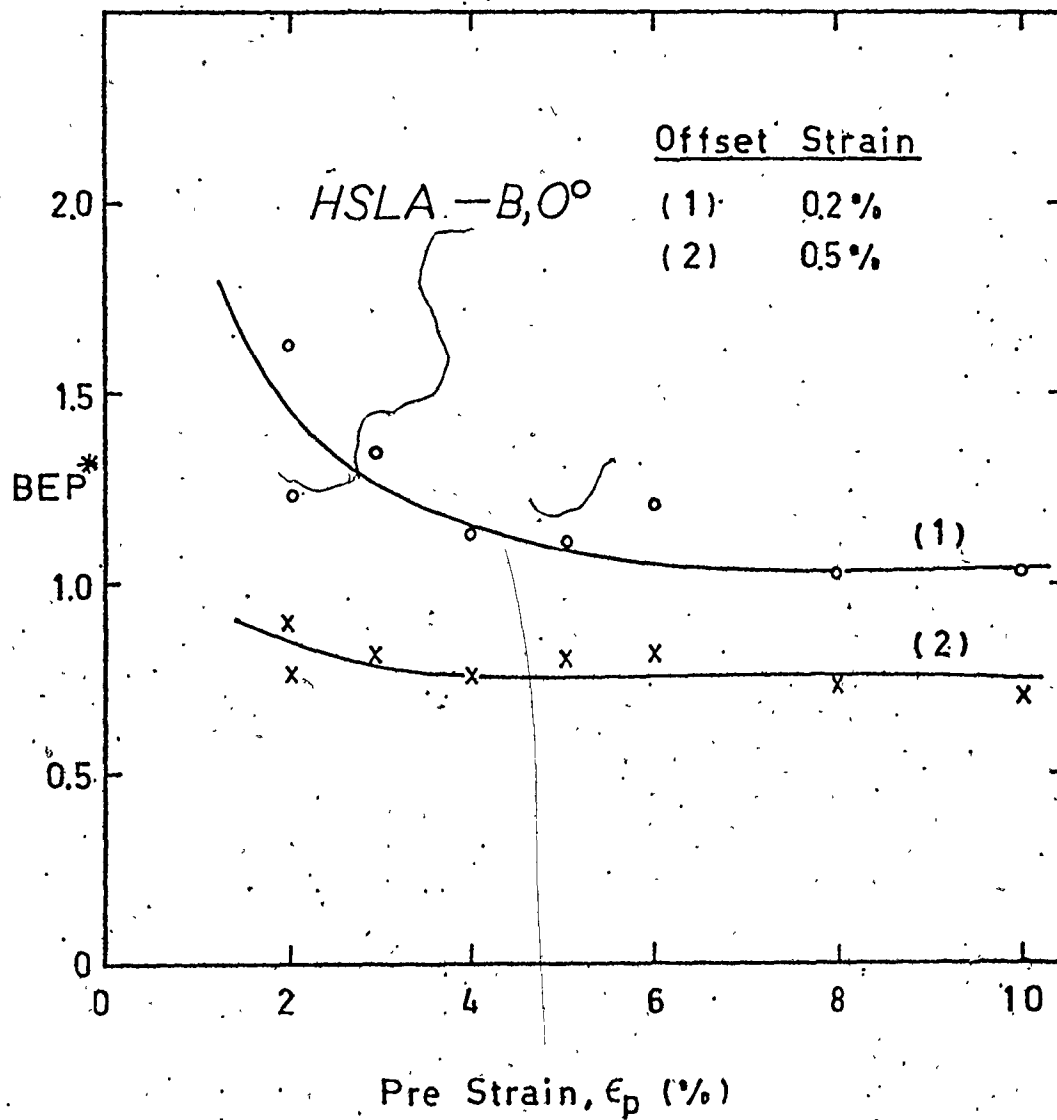


Fig. B.7(a) (Cf., Fig. 5.24) The empirical parameterization of the Bauschinger Effect.

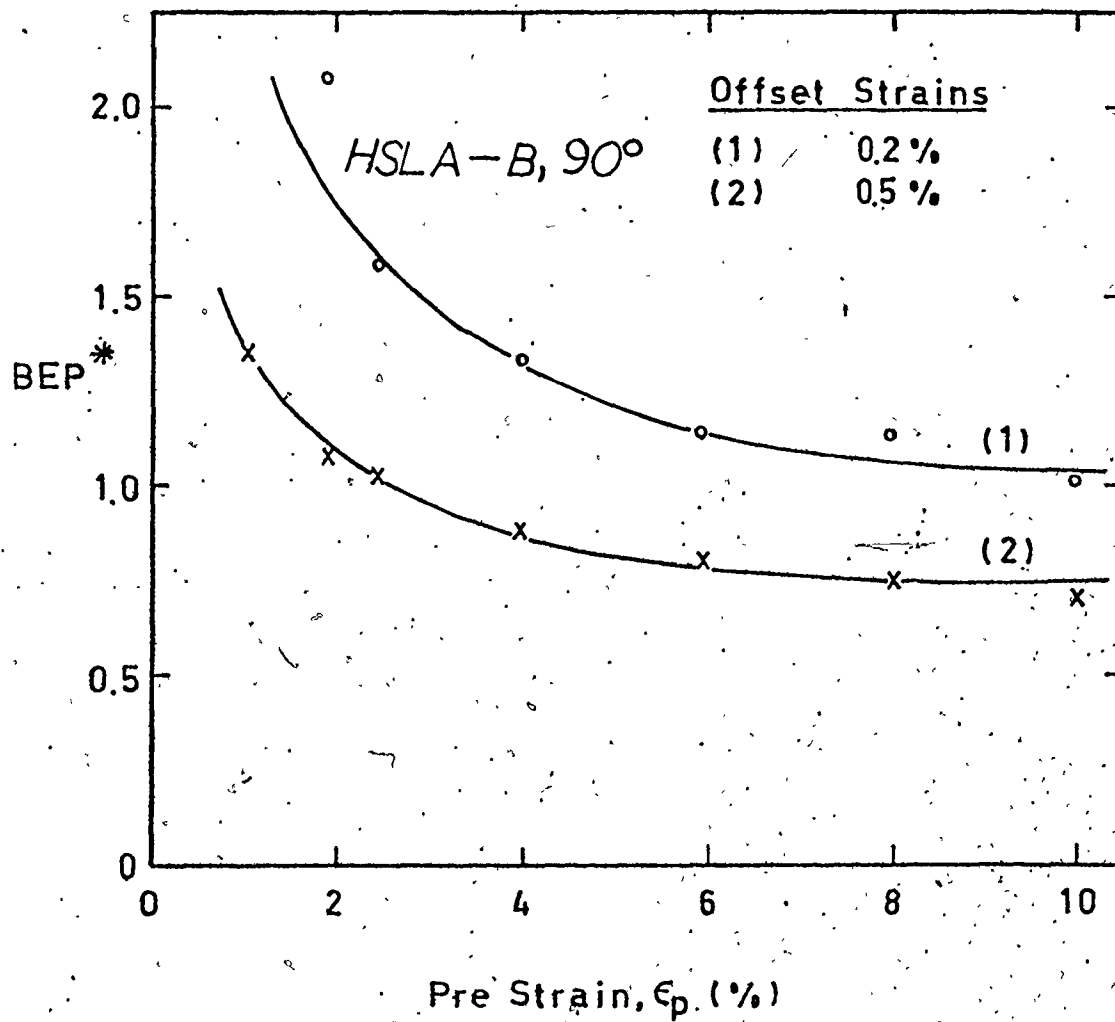


Fig. B.7(b) (Cf., Fig. 5.24) The empirical parameterization of the Bauschinger Effect.

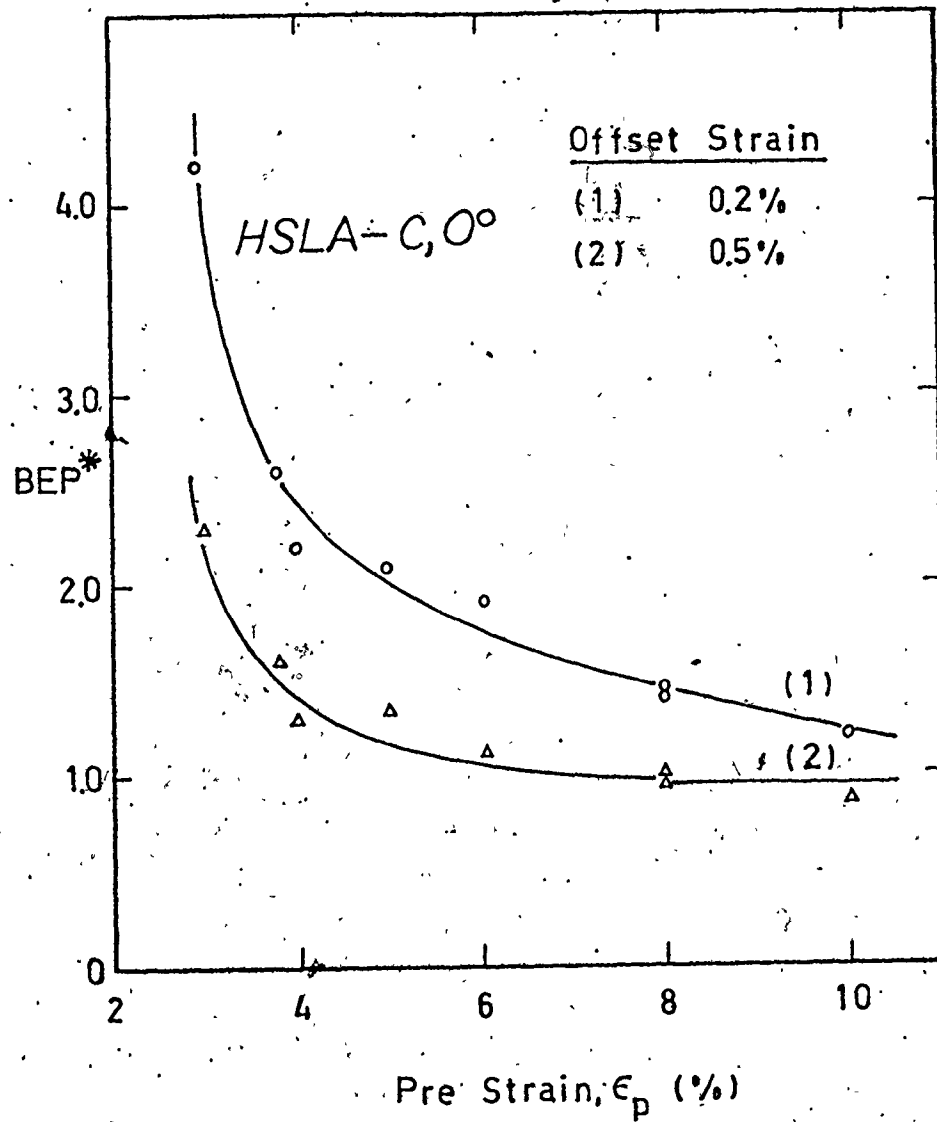


Fig. B.8(a) (Cf., Fig. 5.24). The empirical parameterization of the Bauschinger Effect.

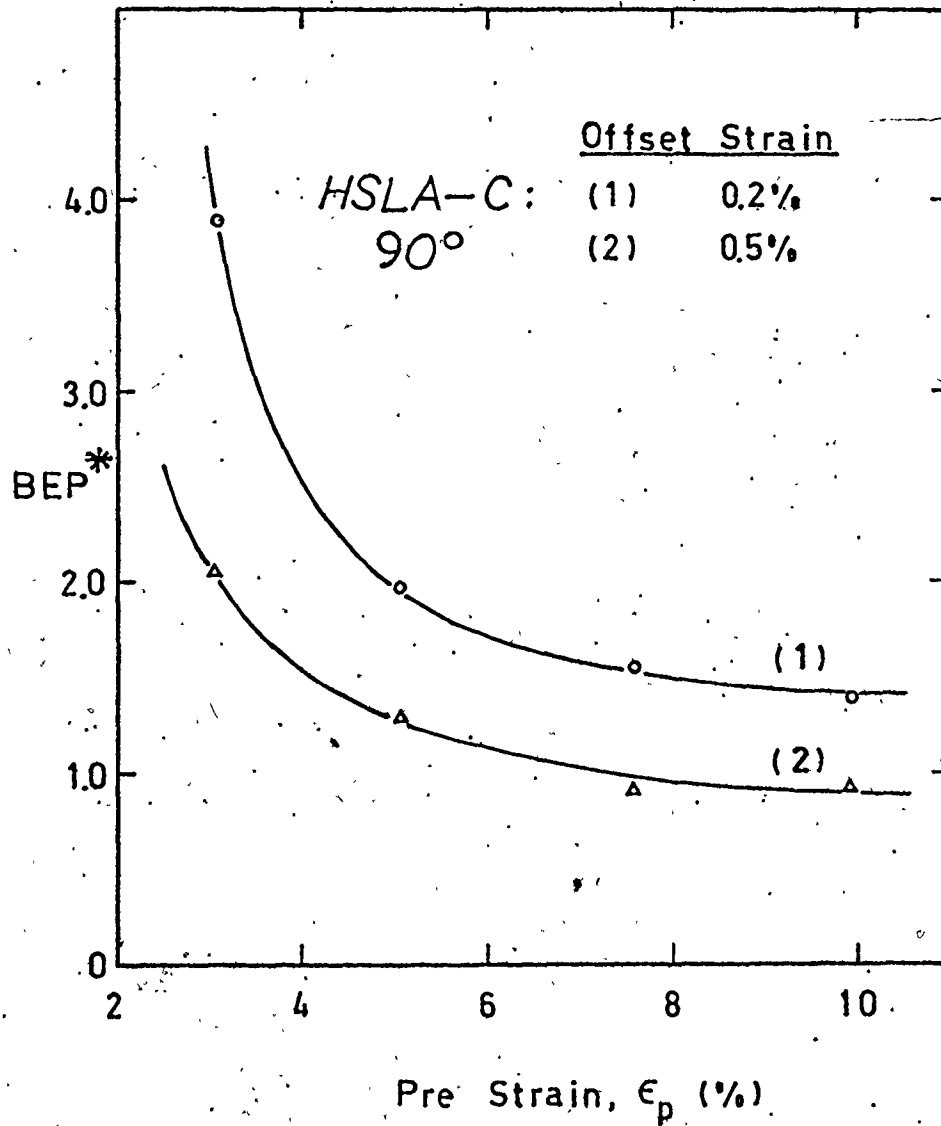


Fig. B.8(b) (Cf., Fig. 5.24) The empirical parameterization of the Bauschinger Effect.

APPENDIX-C

ELASTIC-PLASTIC AXISYMMETRIC FINITE ELEMENT
ANALYSIS OF THE PIPE EXPANSION PROBLEMC.1 Introduction

The pressure-radial expansion curves presented in Fig. 6.8; Chapter 6 on the analysis of the U-O-E pipe manufacturing process were obtained by means of a Finite Element Program. In this appendix, some of the basic mathematical preliminaries of the finite element formulation of the expansion problem are discussed. The computer program used was developed by Y. Tomita* along the lines of his previous work with Kitawawa [129,130]. The program was developed for the study of large plastic deformations in elastic-plastic materials.

In comparison with the elastic FEM analysis, elastic-plastic materials exhibit two types of nonlinearities. The first arises on account of the constitutive equation governing material behaviour while the second type of nonlinearity is geometrical in origin and relates to the large strain and displacements occurring during the deformation of the material. In the case of material nonlinearities, if the strains and displacements are small then the local distortion of a differential element can be ignored. Hence, it is usual to linearize the material constitutive law in a piece-wise manner (see Fig. 6.6) and to adopt the

* On leave of absence in McMaster University from the Faculty of Engineering, Kobe University, Japan, (1976/77).

analytical technique similar to that of the linear elastic material over the domains of prescribed linear behaviour [131]. When the problem is accompanied by geometric nonlinearities, an incremental procedure of the type explored and utilized in refs. [130,131] is essential in the finite element formulation.

This appendix presents a brief outline of the incremental FEM analysis which was employed in the pipe expansion problem in Chapter 6. The discussion is not general, and so, only the few references that appeal directly to this problem will be cited.

C.2 Mathematical Preliminaries

C.2.1 Geometric Relations

A convective coordinate system embedded in a deformation body was selected for the analysis. The coordinate system is defined for an undeformed solid which is then subjected to a known finite deformation. Then, upon the imposition of an infinitesimal deformation, incremental quantities arise which are superposed on the current configuration due to the previous finite deformation. The choice of a convective frame of reference in this instance has the advantage of simplifying the relationship between these incremental quantities.

In Fig. C.1, a point P_0 is an undeformed axisymmetric body, in this case, a pipe of unit length has the polar coordinates (r, θ, z) which coincide with the curvilinear coordinates, $X_i (i=1,2,3)$. The diagram is drawn for a constant θ -plane since the net displacements of a point in the θ -direction due to internal pressurization will be zero. The base vectors, g_i and their contravariant components, g^i at the generic material point P_0 can be defined as:

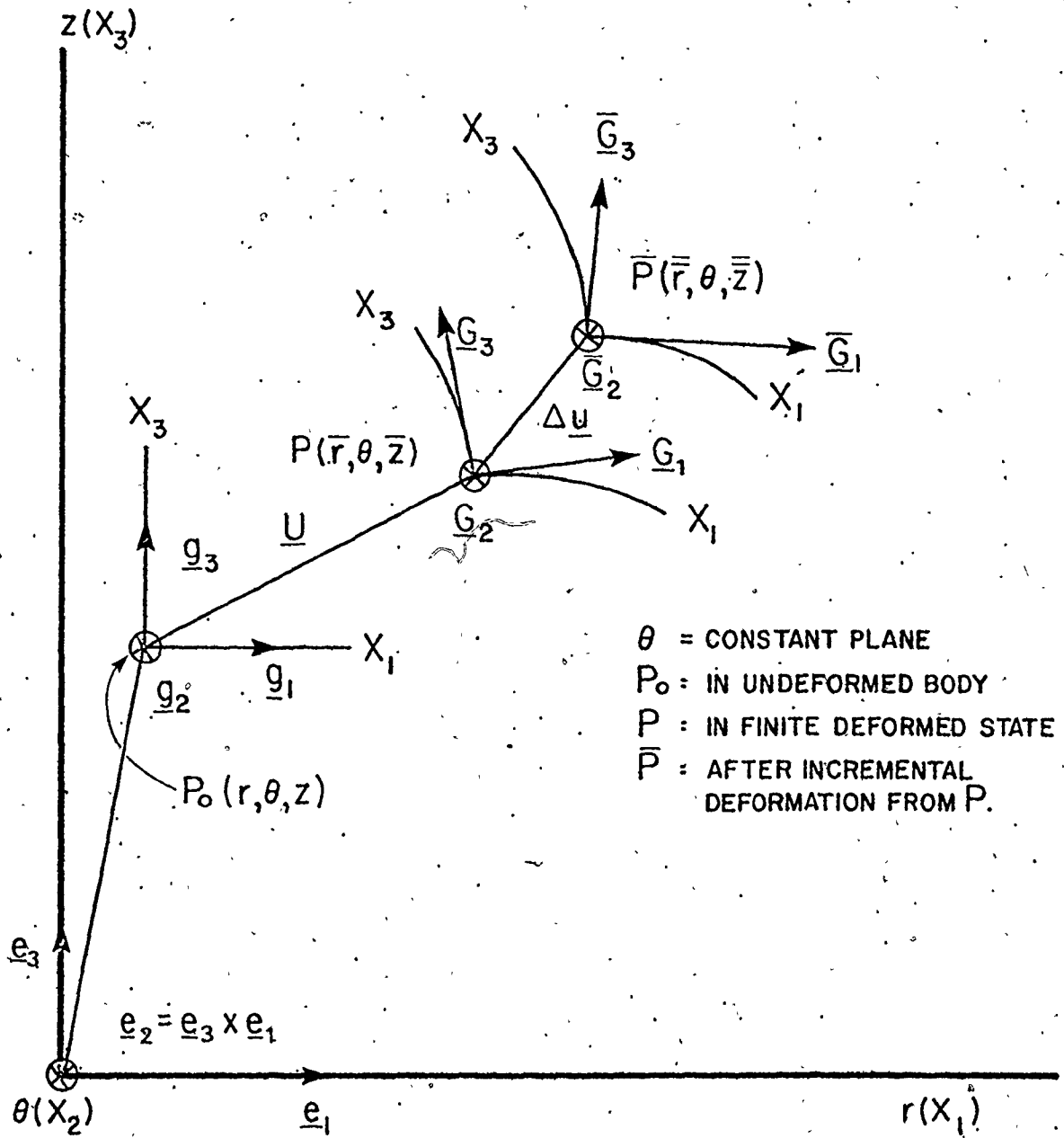


FIGURE C-1
 INCREMENTAL DEFORMATION MODEL

$$\begin{aligned} \underline{g}_1 &= \underline{e}_1; \quad \underline{g}_2 = r\underline{e}_2; \quad \underline{g}_3 = \underline{e}_3 \\ \underline{g}^1 &= \underline{e}_1; \quad \underline{g}^2 = \frac{1}{r}\underline{e}_2 \text{ and } \underline{g}^3 = \underline{e}_3 \end{aligned} \quad (\text{C-1})$$

where \underline{e}_i are unit vectors along the X_i system. The contravariant base vectors \underline{g}^i are defined by:

$$\underline{g}_i \cdot \underline{g}^j = \delta_i^j \quad (\text{C-2})^*$$

where δ_i^j is the Kronecker delta and (\cdot) signifies the scalar product of two vectors. Also, the metric tensors in the undeformed configuration are given by:

$$\begin{aligned} g_{ij} &= \underline{g}_i \cdot \underline{g}_j \\ g^{ij} &= \underline{g}^i \cdot \underline{g}^j \end{aligned} \quad (\text{C-3})^{**}$$

which are:

$$\begin{aligned} g_{11} = g^{11} = g_{33} = g^{33} = 1; \\ g_{22} = r^2; \quad g^{22} = 1/r^2 \end{aligned} \quad (\text{C-4})$$

Now, if a finite deformation is imposed, the point $P_0(r, \theta, z)$ moves to the point $P(\bar{r}, \theta, \bar{z}) \equiv P[(r+U_r), \theta, (z+U_z)]^+$ and the resultant displacement, \underline{U} is described by:

$$\underline{U} = U_i \underline{g}^i = U^i \underline{g}_i \quad (\text{C-5})$$

* The mathematical preliminaries of tensor calculus utilize the work in refs. [132,133].

** Repeated indices denote the summation convention of tensor calculus.

+ The net circumferential displacement is zero for the axisymmetric pipe expansion problem.

where the non zero displacement components are $U_1 = U_r$ and $U_3 = U_z$. The base vectors $\underline{\tilde{G}}_i(\underline{\tilde{G}}^i)$ in the current configuration of the body which are the vectors $\underline{g}_i(\underline{g}^i)$ deformed with the body are given by:

$$\begin{aligned}\underline{\tilde{G}}_i &= \underline{g}_i + U_{,i} \\ &= (\delta_i^m + U^m_{,i}) \underline{g}_m\end{aligned}\tag{C-6}$$

where $(,i)$ means differentiation w.r.t. X_i and $(|i)$ defines the corresponding covariant derivative w.r.t. X_i and based on \underline{g}_i . Also, the metric tensors in this condition are,

$$\underline{G}_{ij} = \underline{G}_i \cdot \underline{G}_j; \quad G^{ij} = (\underline{G}_{ij})^{-1}\tag{C-7}$$

A small incremental deformation now follows the finite deformation, and during this stage, the deformation of the body is geometrically described in terms of the material point $P(\vec{r}, \theta, \vec{z})$ moving to $\tilde{P}(\vec{r}, \theta, \vec{z}) \equiv \tilde{P}[(\vec{r} + U_r + \Delta U_r), \theta, (z + U_z + \Delta U_z)]$. The increment in displacements, ΔU is:

$$\Delta \underline{U} = \Delta U^i \underline{g}_i = \Delta \tilde{U}_i \underline{g}^i\tag{C-8}$$

on the basis of \underline{g}_i , or

$$\Delta \underline{U} = \Delta \tilde{U}^i \underline{G}_i = \Delta \tilde{U}_i \underline{\tilde{G}}^i\tag{C-8}$$

based on \underline{G}_i . As before in eqn. (C-6), the derivative of the incremental displacement w.r.t. X_i and based on \underline{G}_i is used to define the new base vectors $\underline{\tilde{G}}_i(\underline{\tilde{G}}^i)$ following the incremental deformation. These are given by:

$$\bar{G}_i = (\delta_i^m + \Delta \bar{U}^m | | i) G_m \quad (C-9)$$

with $\bar{G}_i \bar{G}_j = \bar{G}_{ij}$ and $\bar{G}^{ij} = (\bar{G}_{ij})^{-1}$.

It is convenient to define the derivatives, $\Delta \bar{U}^m | | i$ in covariant terms using the associated law of tensors [132] as:

$$\Delta \bar{U}^m | | i = G^{mj} \Delta \bar{U}_j | | i \quad (C-10)$$

It is now possible to define a measure of the imposed strain. The Green's strain tensor, γ_{ij} and its increment, $\Delta \gamma_{ij}$ defined by the difference of the squares of lengths before and after the deformation is used to facilitate the analysis [132,133]:

$$\gamma_{ij} = \frac{1}{2} (G_{ij} - g_{ij}) \quad (C-11)$$

$$\Delta \gamma_{ij} = \frac{1}{2} (\bar{G}_{ij} - G_{ij})$$

Substituting (C-6) in (C-7) to obtain G_{ij} and using this with (C-4) in (C-11) yields the strain components as:

$$\gamma_{ij} = \frac{1}{2} [U_i | | j + U_j | | i + U_m | | i U^m | | j] \quad (C-12)$$

The strain increments, $\Delta \gamma_{ij}$ are obtained by taking the increments of the displacements in (C-12) as:

$$\Delta \gamma_{ij} = \frac{1}{2} [\Delta U_i | | j + \Delta U_j | | i + \Delta U_m | | i U^m | | j] \quad (C-13)$$

Equations (C-12) and (C-13) can be written in terms of the partial derivatives of the displacement and its increments based on the (r, θ, z)

system. If $(U_1, U_2, U_3) \equiv (U_r, \theta, U_z)$, then,

$$\begin{aligned} U_1|_1 &= U^1|_1 = U_{r,r}; U_1|_3 = U^1|_3 = U_{r,z} \\ U_2|_2 &= r \cdot U_r; U^2|_2 = U_r/r; U_3|_1 = U^3|_1 = U_{z,r} \\ U_3|_3 &= U^3|_3 = U_{z,z} \end{aligned} \quad (C-14)$$

where $()_r$ and $()_z$ denote partial differentiation w.r.t. r and z .

Using (C-14) in (C-12) gives the strain components below in (C-15):

$$\begin{aligned} \gamma_{11} &= \gamma_{22} = U_{r,r} + \frac{1}{2} [(U_{r,r})^2 + (U_{z,r})^2]; \\ \gamma_{22} &= \gamma_{\theta\theta} = rU_r + \frac{1}{2} (U_r)^2; \gamma_{\theta\theta}^* = U_r/r + \frac{1}{2} (U_r/r)^2; \\ \gamma_{33} &= \gamma_{zz} = U_{z,z} + \frac{1}{2} [(U_{r,z})^2 + (U_{z,r})^2] \\ 2\gamma_{13} &= 2\gamma_{rz} = (U_{z,r} + U_{r,z}) + (U_{r,z}U_{r,r} + U_{z,z}U_{z,r}) \end{aligned} \quad (C-15)$$

where $\gamma_{\theta\theta}^*$ is the physical component of the hoop strain. From (C-13), the incremental strain components are:

$$\begin{aligned} \Delta\gamma_{11} &= \Delta U_{r,r} + \Delta U_{r,r} U_{r,r} + U_{z,r} \Delta U_{z,r} \\ \Delta\gamma_{22} &= r\Delta U_r + U_r \Delta U_r \\ \Delta\gamma_{33} &= \Delta U_{z,z} + U_{r,z} \Delta U_{r,z} + U_{z,z} \Delta U_{z,z} \\ 2\gamma_{13} &= (1 + U_{z,z}) \Delta U_{z,r} + (1 + U_{r,r}) \Delta U_{r,z} \\ &\quad + (U_{r,z} \Delta U_{r,r} + \Delta U_{z,z} U_{z,r}) \end{aligned} \quad (C-16)$$

After every incremental deformation, total strain is obtained by adding the increments of strain to the current value.

To utilize the above analysis, a continuous description of the displacement is necessary. In view of the type of deformation expected during the radial expansion of a pipe, it was proposed to define the displacement using the form:

$$U = \alpha + \beta r \quad (C-17)$$

such that the displacement is a linear function of the current radius only. The radius, r describes the current location of any of the twenty elements into which the pipe wall was divided, see Fig. 6.5. The system of concentric annular elements employed to define the one dimensional finite element mesh was also shown in Fig. 6.7. It is noted using Fig. C-2 that the radial displacement, U_r and the current radius, r are similarly defined. This fact enabled the use of the isoparametric element concept [131] in the final definition of the displacement function which facilitates some of the integrations in the calculations, particularly, those in eqn. (C-31).

C.2.2. The Constitutive Equation

An incremental stress-strain law of the type in eqn. (C-18) below was assumed:

$$\Delta \tau^{ij} = E^{ijkl} \Delta \gamma_{kl} \quad (C-18)$$

where $\Delta \tau^{ij}$ and $\Delta \gamma_{kl}$ are incremental stress and strain tensors referred to the convective coordinate system based on \tilde{G}_i ; E^{ijkl} is the tensor of elastic-plastic moduli. It is necessary that the constitutive law

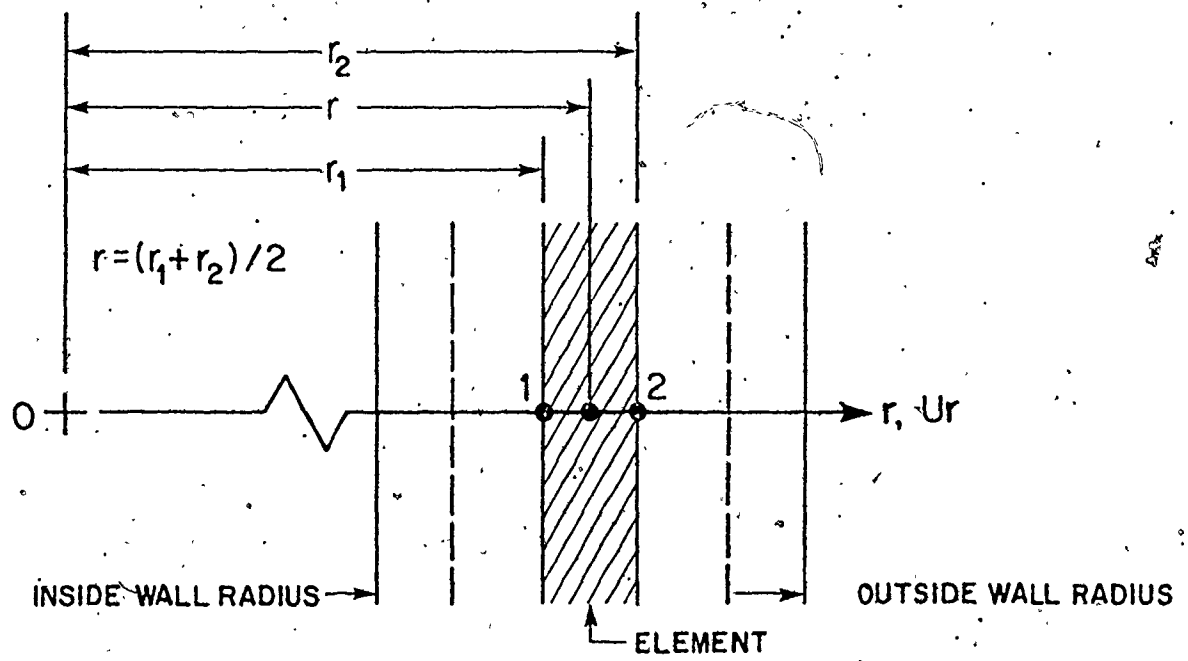


FIGURE C-2

LOCATION OF A FINITE ELEMENT IN THE PIPE WALL.

is invariant under a change in coordinate system. The quantities $\Delta\tau^{ij}$ and $\Delta\gamma_{kl}$ have this property of frame indifference, but it is still possible to violate the yield condition if rigid body rotations occur. In this connection, it is more appropriate to use the Jaumann stress increment, $J\Delta\tau^{ij}$ [129] in the constitutive law. This is defined by:

$$J\Delta\tau^{ij} = \Delta\tau^{ij} + (G^{\ell j}{}_{\tau}{}^{ki} + G^{\ell i}{}_{\tau}{}^{kj}) \Delta\gamma_{k\ell} \quad (C-19)$$

Using (C-19) in (C-18) gives

$$J\Delta\tau^{ij} = D^{ijkl} \Delta\gamma_{k\ell} \quad (C-20)$$

where D^{ijkl} is defined below in eqn. (C-22). Ignoring the couple effects due to elastic (e) and plastic (p) strain components give:

$$\Delta\gamma_{ij} = \Delta\gamma_{ij}^{(e)} + \Delta\gamma_{ij}^{(p)}$$

If Hook's law is assumed for the elastic part, then the elastic part of (C-20) is:

$$J\Delta\tau^{ij} = B^{ijkl} \Delta\gamma_{k\ell}^{(e)}$$

where for an isotropic material of elastic constant μ and Poisson's ratio ν :

$$B^{ijkl} = \mu(G^{ik}G^{j\ell} + G^{i\ell}G^{jk} + \frac{2\nu}{1-2\nu} G^{ij}G^{k\ell}) \quad (C-21)$$

For the plastic part, the flow rule is used to define the strain increment, that is:

$$\Delta\gamma_{ij}^{(p)} = \frac{\partial f}{\partial \tau^{ij}} \Delta\lambda, \Delta\lambda > 0$$

where f is the yield function. In ref. [129], it is shown that the tensor

D^{ijkl} in eqn. (C-20) comprises of the elastic and plastic terms derived from (C-21) and the flow rule as:

$$D^{ijkl} = B^{ijkl} - 2\mu\tau^{ij}\tau^{kl} / \left[\frac{2}{3}\bar{\sigma}^2 \left(\frac{H}{2\mu} + 1 \right) \right] \quad (C-22)$$

where the deviatoric stress τ^{ij} is given by

$$\tau^{ij} = \tau^{ij} - \frac{1}{3} G^{ij} G_{rs} \tau^{rs}$$

and $\bar{\sigma}$ is the representative stress given by

$$\bar{\sigma}^2 = \frac{3}{2} \tau^{ij} \tau_{ij}$$

The constant H in (C-22) is derived from the tangent moduli, E_t defined on a uniaxial $\bar{\sigma} - \bar{\epsilon}$ diagram by:

$$H = \frac{2}{3} \left\{ \frac{2\mu E_t (1+\nu)}{2\mu(1+\nu) - E_t} \right\}$$

H will change from one linear domain to another on the $\bar{\sigma} - \bar{\epsilon}$ diagram, see Fig. 6.6. The final form of (C-18), using (C-19), (C-21) and (C-22) is as follows:

$$\Delta\tau^{ij} = (B^{ijkl} - F^{ijkl} - \alpha Q^{ijkl}) \Delta\gamma_{kl} \quad (C-23)$$

where F^{ijkl} is the term in brackets in the r.h.s. of (C.19), Q^{ijkl} is the r.h.s. of (C-22) and $\alpha = 0$ for elastic loading and 1 for plastic loading. B^{ijkl} is given by (C-21).

C.2.3. The Virtual Work Principle

The principle of virtual work is used widely in the Finite Element Method in order to obtain a balance between the internal (strain) energy of a deforming body and the mechanical work expended on it. In

incremental terms, Kitagawa and Tomita. [129] express the virtual work principle, assuming volume constancy, in the following way:

$$\int_V (\Delta \tau_{ij} + \tau_{im} \Delta \bar{U}_j ||_m) \delta \bar{U}_i ||_j \cdot dV$$

$$= \int_S \Delta P_i^i \delta \bar{U}_i ds \quad (C-24)$$

where V and S denote volumetric and surface integrations, $\delta \bar{U}_i$ is the increment of virtual displacements referred to G_i and ΔP_i^i is the applied external force vector on the surface element ds also based on G_i .

C.2.4 Matrix Notations for the FEM model

From eqn. (C-16), the incremental strain components, $\Delta \gamma_{ij}$ are expressible in matrix form as:

$$\{\Delta \gamma\} = [A] \{\Delta U\} \quad (C-25)$$

where

$$\{\Delta \gamma\}^T = \{\Delta \gamma_{11} \quad \Delta \gamma_{22} \quad \Delta \gamma_{33} \quad 2\Delta \gamma_{13}\},$$

$$\{\Delta U\}^T = \{\Delta U_r \quad \Delta U_z\},$$

Also, $\{ \}$ denotes a column vector and $[A]$ is a two dimensional matrix derived from (C-16) as:

$$[A] = \begin{bmatrix} (1 + \frac{\partial U_r}{\partial r}) \cdot \frac{\partial}{\partial r} & \frac{\partial U_z}{\partial r} \cdot \frac{\partial}{\partial r} \\ (r + U_r) & 0 \\ \frac{\partial U_r}{\partial z} \cdot \frac{\partial}{\partial z} & (1 + \frac{\partial U_z}{\partial z}) \cdot \frac{\partial}{\partial z} \\ [(1 + \frac{\partial U_r}{\partial r}) \cdot \frac{\partial}{\partial z} + \frac{\partial U_r}{\partial z} \cdot \frac{\partial}{\partial r}] & [(1 + \frac{\partial U_z}{\partial z}) \cdot \frac{\partial}{\partial r} + \frac{\partial U_z}{\partial r} \cdot \frac{\partial}{\partial z}] \end{bmatrix}$$

The covariant derivatives, $\Delta \bar{U}_j ||_i$ in eqn. (C-10) are also expressible in matrix form as:

$$\{\gamma\} = [C] \{\Delta U\} \quad (C-26)$$

where $\{\gamma\}^T = \{\Delta \bar{U}_1 ||_1 \Delta \bar{U}_2 ||_2 \Delta \bar{U}_3 ||_3 \Delta \bar{U}_1 ||_3 \Delta \bar{U}_3 ||_1\}$,

and:

$$[C] = \begin{bmatrix} \left(1 + \frac{\partial U_r}{\partial r}\right) \cdot \frac{\partial}{\partial r} & \frac{\partial U_z}{\partial r} \cdot \frac{\partial}{\partial r} \\ (r + U_r) & 0 \\ \frac{\partial U_z}{\partial r} \cdot \frac{\partial}{\partial z} & \left(1 + \frac{\partial U_z}{\partial z}\right) \cdot \frac{\partial}{\partial z} \\ \left(1 + \frac{\partial U_r}{\partial r}\right) \cdot \frac{\partial}{\partial z} & \frac{\partial U_z}{\partial r} \cdot \frac{\partial}{\partial z} \\ \frac{\partial U_r}{\partial z} \cdot \frac{\partial}{\partial r} & \left(1 + \frac{\partial U_z}{\partial z}\right) \cdot \frac{\partial}{\partial r} \end{bmatrix}$$

Similarly, the covariant derivatives of the virtual displacement increments, $\delta \bar{U}_i ||_j$ which appear in eqn. (C-24) are expressible in matrix form as:

$$\{\delta\} = [C] \{\delta U\} \quad (C-27)$$

where $\{\delta\}^T = \{\delta \bar{U}_1 ||_1 \delta \bar{U}_2 ||_2 \delta \bar{U}_3 ||_3 \delta \bar{U}_1 ||_3 \delta \bar{U}_3 ||_1\}$,

$$\text{and } \{\delta U\}^T = \{\delta U_r \delta U_z\}.$$

The terms appearing in the virtual work eqn. (C-24) are now rewritten in matrix form. The first of these is $\Delta \tau^{ij} \delta \bar{U}_i ||_j$. $\Delta \tau^{ij}$, as defined in (C-18) involves the stress-strain matrix, [E] which from (C-23) is comprised of the tensors of elastic and plastic moduli, that is:

$$[E] = [B] - [F] - \alpha[Q]$$

$$= \begin{bmatrix} E^{1111} & E^{1122} & E^{1133} & E^{1113} \\ & E^{2222} & E^{2233} & E^{2213} \\ & & E^{3333} & E^{3313} \\ \text{SYM} & & & E^{1313} \end{bmatrix}$$

$$\text{and } \{\Delta\tau\} = [E] \{\Delta\gamma\}.$$

Substituting for $\{\Delta\gamma\}$ from (C-25), gives

$$\{\Delta\tau\} = [E] [A] \{\Delta U\}$$

$$\text{where } \{\Delta\tau\}^T = \{\Delta\tau^{11} \ \Delta\tau^{22} \ \Delta\tau^{33} \ \Delta\tau^{13}\}.$$

The final form of $\Delta\tau^{ij} \delta\bar{U}_i ||_j$ is then $\{\Delta\tau\}^T \{\delta\}$,

or:

$$\begin{aligned} & ([E] [A] \{\Delta U\})^T \{\delta\} \\ & = \{\Delta U\}^T [A]^T [E] [A] \{\delta U\} \end{aligned} \quad (C-28)$$

where the matrices $\{\delta\}$ and $[C]$ in (C-27) is rearranged in the form of (C-25) and the symmetry of $[E]$ means that $[E]^T = [E]$.

The second term of (C-24) is $\tau^{im} \Delta\bar{U}^j ||_m \delta\bar{U}_i ||_j$. Using (C-10), this term becomes $\tau^{im,jk} \Delta\bar{U}_k ||_m \delta\bar{U}_i ||_j$ which is given in matrix form using (C-26) and (C-27) as:

$$\begin{aligned} & \{\gamma\}^T [S] \{\delta\} \\ & = \{\Delta U\}^T [C]^T [S] [C] \{\delta U\} \end{aligned} \quad (C-29)$$

and:

$$[S] = \begin{bmatrix} \tau_{G^{11}}^{11} & \tau_{G^{21}}^{21} & \tau_{G^{31}}^{31} & \tau_{G^{13}}^{13} & \tau_{G^{11}}^{11} & \tau_{G^{13}}^{13} \\ & \tau_{G^{22}}^{22} & \tau_{G^{32}}^{32} & \tau_{G^{23}}^{23} & \tau_{G^{21}}^{21} & \tau_{G^{23}}^{23} \\ & & \tau_{G^{33}}^{33} & \tau_{G^{31}}^{31} & \tau_{G^{31}}^{31} & \tau_{G^{33}}^{33} \\ & & & \tau_{G^{33}}^{33} & \tau_{G^{31}}^{31} & \tau_{G^{13}}^{13} \\ & & & & \tau_{G^{11}}^{11} & \tau_{G^{13}}^{13} \\ & & & & & \tau_{G^{11}}^{11} & \tau_{G^{13}}^{13} \end{bmatrix}$$

SYM.

The final term on the r.h.s. of (C-24) is:

$$\Delta P_i^i \delta \bar{U}_i = \{\Delta P\}^T \{\delta U\} \quad (C-30)$$

where $\{\Delta P\}^T = \{\Delta P_r \ \Delta P_z\}$ is the incremental force vector.

Using (C-28), (C-29) and (C-30), the final matrix form of (C-24) is then:

$$\int_V \{ \{\Delta U\}^T \{ [A]^T [E] [A] + [C]^T [S] [C] \} \} dV \\ = \int_S \{ \Delta P \}^T dS \quad (C-31)$$

or $\{\Delta U\}^T [K] = \{\Delta F\}^T$

where $[K] = \int_V ([A]^T [E] [A] + [C]^T [S] [C]) dV$

and $\{\Delta F\}^T = \int_A \{ \Delta P \}^T dS$

[K] is the element stiffness matrix which is assembled in the usual

manner [131] to obtain the global stiffness matrix and ΔF is the increment of the applied force at the element nodes calculated from the internal pressure. Equation (C-31) is the final model employed in the FEM program to determine the pressure - expansion curves in Fig. 6.8.

C.3 The FEM Program

As mentioned before, a pipe of geometry, 40" (1016 mm) diameter and 0.5" (13 mm) wall thickness was assumed in the analysis. The wall thickness was divided into twenty annular and concentric elements for the construction of the FEM mesh. Plane stress deformation (axial stress equal to zero) was assumed and the boundary conditions were previously discussed with reference to Fig. 6.7(b). Also, in Chapter 6, the input parameters of the FEM program were listed. These included the specification of the elastic modulus, Poisson's ratio and the initial yield stress for all the elements. In addition, experimental stress-strain curves, described by means of piece-wise linearization as in Fig. 6.6 were employed to describe individual element behaviour during elastic-plastic loading. It was necessary to use experimentally derived reverse flow data in certain cases in order to account for the BE. The program also accepts estimates of residual stresses, but in this instance, these were set to zero in accordance with the results of Fig. 6.4.

The output information of the program consists firstly of the printing of the input data and the calculated element locations. This is followed with a printout of the calculated nodal forces, the corresponding nodal displacements, the applied internal pressure and the current radius of the inside wall of the pipe. The diagrams in Fig. 6.8 were then derived from these latter set of data.

The output also includes the stress and strain data of all the twenty elements in the pipe wall. Four types of stresses and strains are calculated: (i) the Euler stress and Green's strain, τ^{ij} and γ_{ij} , (ii) the physical components of stress in the Cartesian system of coordinates, (iii) the physical components of stresses in polar coordinates, and (iv) the representative stress and strain. The output may be controlled so that printing is performed after a specified number of computation cycles until the prescribed maximum pressure or iteration limit is reached. The listing of the FEM computer program is included below in this appendix.

C.4 Listing of FEM Program

See Pages 267 - 279

S

```

C MAIN PROGRAM
C ELASTIC PLASTIC FINITE ELEMENT PROGRAM
C FOR AXISYMMETRIC RADIAL PIPE EXPANSION

COMMON X(50),Y(50),NCD(50,2),RR(50),SGM1(50),EEP(50),TDG(50,4),
1 TDG(50,4),TG(50,3),DEP(50,4),EP(50,4),U(50),CE(50,9),O(50,7),
2 T(50),DSGM(50),DEEP(50),EPP(50),PG(50),XR(50),DXR(50),OO(50,7),
3 TP(50),CTG(50,4),UR(50),UX(50),YG(50),UG(50),DUP(50)
4 ,R1(50,3),E1(50,3),Y1(50,7)
PAY=3.141593

C ENTER ELASTIC MODULUS POISSONS RATIO AND ELASTIC LIMIT
C WRITE INPUT DATA

READ(5,9)YM1,PR1,YY
9 FORMAT(3F12.0)
WRITE(6,400)YM1,PP1,YY
400 FORMAT(1H,2HE=,E18.8,3HU=,E18.8,2HY=,E19.8)
G=YM1/(1.-(+PP1)/2.0)

C ENTER OUTSIDE AND INSIDE RADIUS OF PIPE
C ENTER THE NUMBER OF ELEMENTS

READ(5,500)RO,RI,N
500 FORMAT(2F10.0,I4)
C COMPUTE ELEMENT LOCATIONS
NPOIN=N
NELEM=N-1
DF=(RO-RI)/FLOAT(N-1)
C ELEMENT COORDINATES AND LOCAL NUMBERING SYSTEM
DO 503 I=1,NPOIN
503 X(I)=0.0
CRD=RO-RI
DD1=CRD/20.0
Y(I)=RI
DO 40 I=2,21
40 Y(I)=Y(I-1)+DD1
C WRITE ELEMENT NUMBER AND LOCATIONS
WRITE(6,508)(I,X(I),Y(I),I=1,NPOIN)
508 FORMAT(1H,I4,2E15.7)
DO 504 I=1,NELEM
504 NCD(I,1)=I
NCD(I,2)=I+1
C WRITE ELEMENT SYSTEM OF NODAL NUMBERING
WRITE(6,509)(I,NCD(I,1),NCD(I,2),I=1,NELEM)
509 FORMAT(1H,3I4)
DO 507 I=1,NPOIN
507 YG(I)=Y(I)
UG(I)=0.0
CONTINUE
NKN=NPOIN
MMH=2
C TOTAL NUMBER OF NODES AND DEGREES OF FREEDOM
WRITE(6,401)NKN,MMH
401 FORMAT(1H,2I5)

C INITIALIZATION
C MATRIX=0

```



```

FC=0.0
FC=0.0
DO 21 I=1,NELEM
  EPP(I)=0.0
  RP(I)=0.0
  SGM1(I)=0.0
  EEP(I)=0.0
  CR(I)=0.0
  UX(I)=0.0
  CTDG(I,4)=0.0
  TDG(I,4)=0.0
  DO 22 J=1,3
    TCG(I,J)=0.0
    CTDG(I,J)=0.0
    TG(I,J)=0.0
  22 CTG(I,J)=0.0
  DO 23 J=1,4
    CEP(I,J)=0.0
    EP(I,J)=0.0
  23 CONTINUE

```

```

C READ AND WRITE INDIVIDUAL ELEMENT MATERIAL PROPERTIES
C --THREE LEVELS OF TANGENT MODULI, STRENGTH LIMITS
C AND RESIDUAL STRESSES
C CONVERSION OF RESIDUAL STRESSES TO EQUIV. STRESSES

```

```

  RG(I)=(Y(I)+Y(I+1))/2.0
  READ(5,520)E1(I,1),E1(I,2),E1(I,3),Y1(I,1),Y1(I,2),Y1(I,3),TG(I,2)
  WRITE(6,520)E1(I,1),E1(I,2),E1(I,3),Y1(I,1),Y1(I,2),Y1(I,3),TG(I,2)
520 FCOMAT(7F10.0)
  TCG(I,1)=-TG(I,2)/3.0
  TCG(I,3)=0.0
  TCG(I,4)=-TG(I,2)/3.0
  SGM1(I)=SCPT(TG(I,2)+TG(I,2))
  TG(I,2)=TG(I,2)/RG(I)/RG(I)
  TCG(I,2)=2.0*TG(I,2)/3.0
  R1(I,1)=SGM1(I)/Y1(I,1)
  R1(I,2)=SGM1(I)/Y1(I,2)
  R1(I,3)=SGM1(I)/Y1(I,3)
21 CONTINUE

```

```

C START
C III=1
C FIRST INCREMENT OF INTERNAL PRESSURE
  CK=300.0
  GO TO 4
3 CONTINUE
  III=III+1
  CK=50.0
4 CONTINUE
  DO 68 I=1,NNN
    IF(I)=I
68 U(I)=0.0

```

```

C CALCULATION OF ELEMENT STIFFNESS MATRIX
C ASSEMBLY INTO GLOBAL FORM -SUBROUTINE -FEM-
  CALL FEM(III,PR1,G,NNN,MMN,NELEM,PAI)
  ITP=NNN
  M2=MMN+MMN-1

```

```

CC 39 I=1, IIP
IIP=IP(I)
CC 39 J=1, M2
30 CC(I, J)=C(IIP, J)
U(I)=2.0*PAI*YG(I)*JK

```

```

C SOLUTION OF STIFFNESS EQUATION SUBROUTINE -SOLVE-
CALL SOLVE(MMM, NNN)

```

```

C CALCULATE THE RESULTANT STRESS AND STRAIN INCREMENTS
C SUBROUTINE STRESS
C CALL STRESS(NELEM, YM1, PR1)
C AMOUNT OF NEXT PRESSURE INCREMENT
C INCREMENT MUST NOT VIOLATE YIELD CONDITION

```

```

RM1=4.0
IF(III=-1) 700, 701, 703

```

```

700 RM1=2.0

```

```

701 CONTINUE

```

```

NPMIN=NELEM

```

```

IEM=0

```

```

CC 201 K=1, 3

```

```

CC 200 I=1, NPMI

```

```

IF(R1(I, K)-C.995) 260, 260, 200

```

```

260 CONTINUE

```

```

IEM=IEM+1

```

```

W1=TDG(I, 1)+DTDG(I, 1)

```

```

W2=TDG(I, 3)+DTDG(I, 3)

```

```

W3=TDG(I, 2)+DTDG(I, 2)

```

```

RGR=RG(I)+UR(I)

```

```

W2=RGR*W2

```

```

W3=RGR*W3

```

```

W4=TDG(I, 4)+DTDG(I, 4)

```

```

YY=Y1(I, K)

```

```

SGM1=SQRT(1.5*(W1*W1+W2*W2+W4*W4+2.0*W3*W3))

```

```

SGM1=SGM1-SGM1(I)

```

```

GAMMA=OSGM(I)*CSGM(I)-2.0*SGM1(I)*SGM1-SGM1*SGM1

```

```

R3=(GAMMA+SQRT(GAMMA*GAMMA+4.0*OSGM(I)*CSGM(I)*(YY*YY-SGM1(I)*
1 SGM1(I))))/(2.0*OSGM(I)*CSGM(I))

```

```

IF(R3-RM1) 180, 180, 220

```

```

180 RM1=R3

```

```

220 CONTINUE

```

```

200 CONTINUE

```

```

RMIN=RM1

```

```

EPSR1=0.0

```

```

CC 24 I=1, NELEM

```

```

EPSR=DEEP(I)*RMIN

```

```

IF(EPSR1-EPSR) 25, 25, 26

```

```

25 EPSR1=EPSR

```

```

26 CONTINUE

```

```

24 CONTINUE

```

```

201 CONTINUE

```

```

IF(IEM, RE, 0) GO TO 27

```

```

EPSR=EPSR/2

```

```

IF(EPSR1-EPSR) 27, 27, 28

```

```

28 RMIN=RMIN*EPSR/EPSP1

```

```

27 CONTINUE

```

```

R=RMIN

```

```

C SUBROUTINE KKKKA CALCULATES AND PRINTS FOR EVERY
C ELEMENT, THE STRESSES AND STRAINS

```

```

C      CALL KEKKA(NELEM, P, PAI, G, III)
C      RENEW DISPLACEMENTS AND COORDINATES
C      DO 30 I=1, NNN
C      T(I)=T(I)*R
C      U(I)=U(I)*R
30    CONTINUE
C      DO 31 I=1, NPOIN
C      UG(I)=UG(I)+T(I)
31    YG(I)=YG(I)+T(I)
C      IF(III.EC.1) GO TO 450
C      IMC=2
C      ICC=40
C      IMM=IMC
C      IIK1=III/IMM
C      IIK2=III-IMM*IIK1
C      IF(IIK2.EC.0) GO TO 450
C      GO TO 451
450   CONTINUE

C      PRINT ELEMENT NUMBER TOTAL RADIAL DISPLACEMENT,
C      THE RADIAL COORDINATE THE INCREMENTAL NODAL
C      FORCE AND THE DISPLACEMENT
C      DO 32 I=1, NPOIN
C      WRITE(6, 209) I, UG(I), YG(I), U(I), T(I)
209   FCRTAT(1H, I4, 4E12.5)
32    CONTINUE
451   CONTINUE
C      FC=FC+U(1)
C      FC=PO+R*CK

C      PRINT TOTAL FORCE, INTERNAL PRESSURE AND
C      RADIAL DISPLACEMENT
C      WRITE(6, 511) III, FO, FC, UG(NPCIN)
511   FORMAT(1H, I4, 3E15.7)
C      RESET FOR THE NEXT INCREMENT OF PRESSURE
C      IF(III.NE.ICC) GO TO 3
C      STOP
C      END
C      SUBROUTINE FEM(III, PRI, G, NNN, MM4, NELEM, PAI)

C      CALCULATION AND THE ASSEMBLY OF THE STIFFNESS MATRIX
C      DIMENSION TH(2,2), TE(2,2), GLE(2,2), GUE(2,2), C(4,4), T(3,4),
1A(4,4), E(3,3), SE(4,4), CE(4,4), PD(4,4), BA(3,4), ESA(3,4), BPA(4,4),
2SBDA(4,4), CA(4,4)
C      REAL MU, MU1
C      COMMON X(50), Y(50), NCC(50,2), RR(50), SGM1(50), EEP(50), TDG(50,4),
1DTDG(50,4), TG(50,3), DEP(50,4), EP(50,4), U(50), CE(50,9), O(50,7),
2T(50), DSGM(50), DEEP(50), EPP(50), PC(50), XP(50), CXR(50), OO(50,7),
3IP(50), CTG(50,4), UR(50), UX(50), YG(50), UG(50), CUR(50)
4, P1(50,3), E1(50,3), YRZ(50,3)

C      MM42 IS THE BAND WIDTH OF THE STIFFNESS MATRIX
C      INITIALIZE GEOMETRIC PARAMETERS
C      MM42=4MM+MMH-1
C      DO 60 I=1, NNN
C      DO 60 J=1, MMH2
60    C(I, J)=0.0
C      DO 100 LL=1, NELEM

```

```

0  UG = RG(LL)
    UR = UR(LL)
    UX = UX(LL)
0  TC - CONVECTIVE DEVIATORIC STRESSES
    TC(1,1) = TCG(LL,1)
    TC(1,2) = TCG(LL,2)
    TC(2,1) = TCG(LL,2)
    TC(2,2) = TCG(LL,3)
0  ST - EQUIV. STRESS
    ST = SGM1(LL)
0  TE - CONVECTIVE STRESSES
    TE(1,1) = TEG(LL,1)
    TE(1,2) = TEG(LL,2)
    TE(2,1) = TEG(LL,2)
    TE(2,2) = TEG(LL,3)
    Y1 = Y(LL)
    Y2 = Y(LL+1)
    Y3 = 1.0 / (Y2 - Y1)
    A1 = RG + UG
    A2 = 1.0 + UR
0  GL - COVARIANT METRIC TENSORS
    GL(1,1) = A2 * A2
    GL(2,2) = A1 * A1
    GL(1,2) = 0.0
    GL(2,1) = 0.0
0  GU - CONTRAVARIANT METRIC TENSORS
    GU(1,1) = 1.0 / A2 / A2
    GU(2,2) = 1.0 / A1 / A1
    GU(1,2) = 0.0
    GU(2,1) = 0.0
    H1 = G * (1.0 - PR1)
    MU1 = 1.0 - PR1
0  DE - ELASTIC STRESS - STRAIN MATRIX
    DE(LL,1) = MU * GUE(1,1) * GUE(1,1)
    DE(LL,2) = MU * (MU1 * GUE(1,2) * GUE(1,2) + PR1 * GUE(1,1) * GLE(2,2))
    DE(LL,3) = MU * GUE(1,1) * GUE(1,2)
    DE(LL,4) = MU * GUE(2,2) * GUE(2,2)
    DE(LL,5) = MU * GUE(1,2) * GUE(2,2)
    DE(LL,6) = MU * 0.5 * (MU1 * GUE(1,1) * GUE(2,2) + (1.0 + PR1) * GUE(1,2) * GUE(1,2))
1)  DE(LL,7) = 0.0
    DE(LL,8) = 0.0
    DE(LL,9) = 0.0
    IF (R1(LL,1) - 0.995) 14,14,15
0  EXAMINE AND LIMIT STRESS POINT TO RANGE OF CURRENT
0  TANGENT MODULUS
15  ET = E1(LL,1)
21  IF (R1(LL,2) - 0.995) 20,20,21
    ET = E1(LL,2)
31  IF (R1(LL,3) - 0.995) 32,32,31
    ET = E1(LL,3)
32  CONTINUE
20  CONTINUE
0  CALCULATION OF THE PLASTIC STRESS-STRAIN MATRIX
    YM1 = 2.0 * G * (1.0 + PR1)
    H = ET * YM1 / (YM1 - ET)

```

```

S1 = 0.0
S2 = 0.0
S3 = 1.0
DO 200 I = 1, 2
DO 200 J = 1, 2
S1 = S1 + T0(I, J) * GLE(I, 1) * GLE(I, J)
S2 = S2 + T0(I, J) * GLE(I, 2) * GLE(I, J)
S3 = S3 + T0(I, J) * GLE(I, 3) * GLE(I, J) + 2.0
F1 = S1 * DER(LL, 1) + S2 * DER(LL, 2) + S3 * DER(LL, 3)
F2 = S1 * DER(LL, 2) + S2 * DER(LL, 4) + S3 * DER(LL, 5)
F3 = S1 * DER(LL, 3) + S2 * DER(LL, 5) + S3 * DER(LL, 6)
F = 4.0 * S1 * SY * H / 9.0 + F1 * S1 + F2 * S2 + F3 * S3
DE(LL, 1) = DE(LL, 1) - F1 * F1 / F
DE(LL, 2) = DE(LL, 2) - F1 * F2 / F
DE(LL, 3) = DE(LL, 3) - F1 * F3 / F
DE(LL, 4) = DE(LL, 4) - F2 * F2 / F
DE(LL, 5) = DE(LL, 5) - F2 * F3 / F
DE(LL, 6) = DE(LL, 6) - F3 * F3 / F
DE(LL, 7) = F1 / F
DE(LL, 8) = F2 / F
DE(LL, 9) = F3 / F
14 CONTINUE
DE(LL, 1) = DE(LL, 1) - 2.0 * TE(1, 1) * GUE(1, 1)
DE(LL, 2) = DE(LL, 2) - 2.0 * TE(1, 2) * GUE(1, 2)
DE(LL, 3) = DE(LL, 3) - TE(1, 2) * GUE(1, 1) - TE(1, 1) * GUE(1, 2)
DE(LL, 4) = DE(LL, 4) - 2.0 * TE(2, 2) * GUE(2, 2)
DE(LL, 5) = DE(LL, 5) - TE(2, 2) * GUE(1, 2) - TE(2, 1) * GUE(2, 2)
DE(LL, 6) = DE(LL, 6) - TE(1, 2) * GUE(1, 2) - (TE(1, 1) * GUE(2, 2) + TE(2, 2) * GUE(1, 1)) / 2.0
C INITIALIZATION AND CALCULATION OF ELEMENT STIFFNESS MATRIX
DO 50 I = 1, 4
DO 51 J = 1, 3
51 R(I, J) = 0.0
DO 52 K = 1, 4
CE(I, K) = 0.0
A(I, K) = 0.0
SE(I, K) = 0.0
52 BD(K, I) = 0.0
50 CONTINUE
C B-STRAIN - DISPLACEMENT MATRIX
B(1, 2) = A2
B(2, 1) = A1
C A-DISPLACEMENT-NODAL DISPLACEMENT MATRIX
A(1, 1) = (Y2 - Y3) * Y3
A(1, 2) = (RGR - Y1) * Y3
A(2, 1) = -Y3
A(2, 2) = Y3
C E-FINAL ELASTIC-PLASTIC STRESS-STRAIN MATRIX
E(1, 1) = DE(LL, 1)
E(1, 2) = DE(LL, 2)
E(2, 2) = DE(LL, 4)
DO 53 I = 1, 2
DO 53 J = 1, 2
53 E(I, J) = E(I, J)
C CE-INCR. COVARIANT DERIVATIVE-DISPL. MATRIX
CE(1, 2) = 1.0 / A2
CE(2, 1) = 1.0 / A1
C SE-STRESS MATRIX

```

```

SSE(1,1)=TE(1,1)
SSE(2,2)=TE(2,2)
SSE(1,2)=A2
SSE(2,1)=A1
DO 54 I=1,2
DO 54 J=1,2
S=0.0
DO 55 K=1,2
55 S=S+E(I,K)*A(K,J)
54 BEA(I,J)=S
DO 56 I=1,2
DO 56 J=1,2
S=0.0
DO 57 K=1,2
57 S=S+E(I,K)*BEA(K,J)
56 EBA(I,J)=S
DO 58 I=1,2
DO 58 J=1,2
S=0.0
DO 59 K=1,2
59 S=S+BEA(K,I)*EBA(K,J)
58 BEBA(I,J)=S
DO 70 I=1,2
DO 70 J=1,2
S=0.0
DO 71 K=1,2
71 S=S+BEBA(I,K)*A(K,J)
70 BEBA(I,J)=S
DO 72 I=1,2
DO 72 J=1,2
S=0.0
DO 73 K=1,2
73 S=S+BEBA(I,K)*BEBA(K,J)
72 BEBA(I,J)=S
DO 74 I=1,2
DO 74 J=1,2
S=0.0
DO 75 K=1,2
75 S=S+BEBA(I,K)*A(K,J)
74 CA(I,J)=S
DO 76 I=1,2
DO 76 J=1,2
S=0.0
DO 77 K=1,2
77 S=S+CA(K,I)*SPCA(K,J)
76 C(I,J)=C(I,J)+S
T2=1.0+2.0*(EP(LL,4))
T1=SQRT(T2)
RGP=A1
DO 78 I=1,2
DO 78 J=1,2

```

C-ELEMENT STIFFNESS MATRIX

```

C 78 C(I,J)=2.0*PAI*RGP*T1*C(I,J)/Y3
C ASSEMBLY OF GLOBAL STIFFNESS MATRIX
DO 30 MM=1,2
DO 30 KK=1,2
MMI=MOD(LL, KK)
NNJ=MOD(LL, +1)

```

```

NN=MMK-PMI+NNJ
30 C(MMI,NI)=C(MMI,NI)+C(KK,NI)
100 CONTINUE
RETURN
END
SUBROUTINE KEKKA(NELEM,R,PAI,G,III)

```

C CALCULATION AND WRITING OF STRESS - STRAIN DATA

```

DIMENSION GLE(2,2),TG(2,2),DEE(2,2),TE(2,2),TER(2,2)
DIMENSION GUE(2,2)
COMMON X(50),Y(50),NCD(50,2),RR(50),SGM1(50),EEP(50),TDG(50,4),
1CTDG(50,4),TG(50,3),DEP(50,4),EP(50,4),U(50),DE(50,9),D(50,7),
2Y(50),CSGM(50),CEEP(50),EPP(50),RG(50),XP(50),DXP(50),OC(50,7),
3IP(50),DTG(50,4),UR(50),UX(50),YG(50),UG(50),CUR(50),
4R1(50,3),E1(50,3),Y1(50,3)
IMC=5
IP*=IMC
IIK1=III/IMC
IIK2=III-IP*IIK1
C RENEW FIELD VARIABLES
DO 1 L=1,NELEM
CUR(L)=R*CUR(L)
UX(L)=UX(L)+CUR(L)
L1=L
L2=L+1
UP(L)=UP(L)+0.5*(T(L1)+T(L2))*R
CSGM(L)=CSGM(L)*R
DO 3 I=1,3
DTDG(L,I)=R*DTDG(L,I)
DTG(L,I)=T*DTDG(L,I)
TG(L,I)=TG(L,I)+DTG(L,I)
3 CONTINUE
DO 30 I=1,4
DEP(L,I)=R*DEP(L,I)
30 EP(L,I)=EP(L,I)+DEP(L,I)
RGR=RG(L)
UGR=UR(L)
UFU=UX(L)
A1=RGR+UGR
A2=1.0+LPU
C METRIC TENSORS
GLE(1,1)=A2*A2
GLE(2,2)=A1*A1
GLE(1,2)=0.0
GLE(2,1)=0.0
GUE(1,1)=1.0/A2/A2
GUE(2,2)=1.0/A1/A1
GUE(1,2)=0.0
GUE(2,1)=0.0
C CONNECTIVE STRESSES
TE(1,1)=TG(L,1)
TE(1,2)=TG(L,2)
TE(2,1)=TG(L,2)
TE(2,2)=TG(L,3)
S=0.0
DO 50 I=1,2
DO 50 J=1,2
50 S=S+GLE(I,J)*TE(I,J)
S=S/3.0

```

```

DO 51 I=1,2
DO 51 J=1,2
C DEVIATORIC STRESSES
51 TDC(I,J)=TE(I,J)-GUE(I,J)*S
TDC(L,1)=TDC(1,1)
TDC(L,2)=TDC(1,2)
TDC(L,3)=TDC(2,2)
C INCREMENT OF GREENS STRAIN
DEEP(L,1)=DEEP(L,1)
DEEP(L,2)=DEEP(L,2)
DEEP(L,3)=DEEP(L,2)
C INCREMENT OF EQUIV. STRESS
DSG(L)=DSG(L)
DEEP(L)=0.0
C INCREMENT OF EQUIV. STRAIN
DEEP(L)=DEEP(L)*R
C EQUIV. STRAIN
EP(L)=DEEP(L)+DEEP(L)
EPP(L)=DEEP(L)
GG=-2.0*GLE(1,2)*TE(1,2)+GLE(1,1)*TE(1,1)+GLE(2,2)*TE(2,2))/3.0
TDC(L,4)=GG/(1.0+2.0*EP(L,4))
S=GG*GG
DO 60 I=1,2
DO 60 J=1,2
DO 60 K=1,2
DO 60 L=1,2
60 S=S+GLE(I,J)*GLE(K,L)*TDC(I,K)*TDC(J,L)
C EQUIV. STRESS
SGM1(L)=SQRT(1.5*S)
C PHYSICAL STRESS COMPONENTS IN POLAR COORDINATES
TER11=TE(1,1)*A2*A2
TER22=TE(2,2)*A1*A1
TER12=0.0
XG=2.0
CX=COS(XG)
SX=SIN(XG)
C PHYSICAL STRESSES IN RECTANGULAR COORDINATES
TER(1,1)=CX*CX*TER11+SX*SX*TER22-2.0*CX*SX*TER12
TER(1,2)=(CX*SX*(TER11-TER22)+(CX*CX-SX*SX)*TER12
TER(2,1)=TER(1,2)
TER(2,2)=SX*SX*TER11+CX*CX*TER22+2.0*CX*SX*TER12
R1(L,1)=SGM1(L)/Y1(L,1)
R1(L,2)=SGM1(L)/Y1(L,2)
R1(L,3)=SGM1(L)/Y1(L,3)
C CALCULATION OF PRINCIPAL STRESS
WA=TER(1,1)+TER(2,2)
ROOT=SQRT((TER(1,1)-TER(2,2))*(TER(1,1)-TER(2,2))+4.0*TER(1,2)*
1 TER(1,2))
TER01=0.5*(WA+ROOT)
TER02=0.5*(WA-ROOT)
R=TER(1,1)-TER(2,2)
IF (R.EQ.0.0) GO TO 10
TER3=2.0*ATAN(2.0*TER(1,2)/R)*160.0/PAI
GO TO 11
10 TER3=45.0
11 CONTINUE
ENG=EP(L,2)*2.0
IF (I.IK2.EQ.0) GO TO 502
GO TO 500

```



```

502 CONTINUE
TK=EP(L,4)
EP3=EP(L,3)/RGR/RGR
EP4=ENG/RGR

```

```

C WRITE RESULTS--CONVECTIVE STRESSES AND STRAINS,
C PHYSICAL STRESSES IN POLAR AND RECTANGULAR COORDINATES,
C PRINCIPAL STRESSES AND EQUIV. STRESSES AND STRAINS

```

```

WRITE(6,204)L,TG(L,1),TG(L,3),TK,TG(L,2),EP(L,1),EP(L,3),ENG,
1 TER(1,1),TER(2,2),TER(1,2),TER11,TER22,TER12,SGM1(L),
2 EP3,EP4,TER1,TER2,TER3,EP4
204 FORMAT(1H,J3,5H T11=,E12.5,5H T22=,E12.5,5H T33=,E12.5,5H T12=,E1
12.5,5H T11=,E12.5,5H T22=,E12.5,5H T33=,E12.5,5H T12=,E1
2.5,5H TYY=,E12.5,5H TXY=,E12.5,5H RXX=,E12.5,5H RYY=
3,E12.5,5H RXY=,E12.5,5H SGM=,E12.5,5H DSG=,E12.5,5H DEP=,
4 E12.5,5H S11=,E12.5,5H S22=,E12.5,5H CAT=,E12.5,5H DEP=,E12.5)

```

```

500 CONTINUE
1 CONTINUE
RETURN
END

```

```

SUBROUTINE STRESS(NELEM,YM1,PR1)

```

```

C CALCULATION OF STRESS AND STRAIN INCREMENTS

```

```

DIMENSION GLE(2,2),GUE(2,2),GTE(2,2),DEE(2,2),DTG(2,2)
COMMON X(50),Y(50),NCD(50,2),RG(50),SGM1(50),EEP(50),TDG(50,4),
1CTDG(50,4),TG(50,3),DEP(50,4),EP(50,4),UX(50),UE(50,9),O(50,7),
2T(50),DSGM(50),DEEP(50),EPD(50),RG(50),XP(50),CXR(50),OO(50,7),
3IP(50),DTG(50,4),UR(50),UX(50),YG(50),UG(50),CUP(50)
4,R1(50,3),E1(50,3),Y1(50,3)

```

```

C INITIALIZATION OF GEOMETRIC PARAMETERS

```

```

EO 1 L=1,NELEM
RGR=RG(L)
UGR=UR(L)
UPU=UX(L)
A1=RGR+UGR
A2=1.0+UPU
GLE(1,1)=A2*A2
GLE(2,2)=A1*A1
GLE(1,2)=0.0
GLE(2,1)=0.0
GUE(1,1)=1.0/A2/A2
GUE(2,2)=1.0/A1/A1
GUE(1,2)=0.0
GUE(2,1)=0.0
N1=L
N2=L+1
CUR(L)=(T(N2)-T(N1))/(Y(L+1)-Y(L))
CLRX=CUR(L)
CUG=0.5*(T(N2)+T(N1))

```

```

C INCREMENTAL STRAIN

```

```

DEE(1,1)=A2*CURX
DEE(1,2)=0.0
DEE(2,1)=0.0
DEE(2,2)=A1*CUG

```

```

DEP(L,1)=DEE(1,1)
DEP(L,2)=DEE(1,2)
DEP(L,3)=DEE(2,2)
ENG=2.0*DEE(1,2)

```

C INCREMENTAL STRESS

```

DTE(1,1)=DE(L,1)*DEE(1,1)+DE(L,2)*DEE(2,2)+DE(L,3)*ENG
DTE(2,2)=DE(L,2)*DEE(1,1)+DE(L,4)*DEE(2,2)+DE(L,5)*ENG
DTE(1,2)=DE(L,3)*DEE(1,1)+DE(L,5)*DEE(2,2)+DE(L,6)*ENG
DTE(2,1)=DTE(1,2)
DTG(L,1)=DTE(1,1)
DTG(L,2)=DTE(1,2)
DTG(L,3)=DTE(2,2)
BTB=0.0
DO 4 I=1,2
DO 4 J=1,2
BTB=BTB+GLE(I,J)*DTE(I,J)
4 CONTINUE
BTB=BTB/3.0
G3=1.0+2.0*EP(L,4)
G33=1.0/G3
DEP(L,4)=-3.0*DE1*G3*BTB/YM1
IF(R1(L,1)-0.995) 21,21,22
22 CONTINUE
ATA=GLE(1,1)*TG(L,1)+2.0*GLE(1,2)*TG(L,2)+GLE(2,2)*TG(L,3)
ATA=ATA/3.0
ATB=DE(L,7)*DEE(1,1)+DE(L,8)*DEE(2,2)+DE(L,9)*ENG

```

C COMPUTE THE INCREMENTAL AXIAL STRAIN

```

21 DEP(L,4)=DEP(L,4)-G3*ATA+ATB
CONTINUE
C INCREMENTAL DEVIATORIC STRESS
DO 5 I=1,2
DO 5 J=1,2
5 DTD(I,J)=DTE(I,J)-GUE(I,J)*BTB
DTDG(L,1)=DTD(1,1)
DTDG(L,2)=DTD(1,2)
DTDG(L,3)=DTD(2,2)
S=BTB*BTB
DTDG(L,4)=-BTB*G33
DO 6 I=1,2
DO 6 J=1,2
DO 6 K=1,2
DO 6 N=1,2
6 S=S+DTD(I,J)*DTD(K,N)*GLE(I,K)*GLE(J,N)
INCREMENTAL EQUIV. STRESS
SGM(L)=SQRT(1.5*S)
S=DEP(L,4)*DEP(L,4)*G33+G33
DO 7 K=1,2
DO 7 J=1,2
DO 7 N=1,2
DO 7 M=1,2
7 S=S+GUE(K,J)*GUE(H,N)*DEE(J,N)*DEE(K,N)
INCREMENTAL EQUIV. STRAIN
DEP(L)=SQRT(2.0*S/3.0)
1 CONTINUE
RETURN
END

```

SUBROUTINE SOLVE(M,N)

SOLUTION OF THE STIFFNESS EQUATION FOR LOCAL DISPL.

DIMENSION IK(50), JK(50)
 COMMON X(50), Y(50), ACC(50,2), RR(50), SGM1(50), SEP(50), TDG(50,4),
 10 TDG(50,4), TG(50,3), DEP(50,4), EP(50,4), U(50), DE(50,9), O(50,7),
 27(50), DSGY(50), DEF(50), EPP(50), PG(50), XP(50), DX(50), OO(50,7),
 31P(50), DTG(50,4), UR(50), UX(50), YG(50), UG(50), CUP(50)

INITIALIZE

1 CC 1 I=1, N
 IK(I)=1
 NP1=N-M+1
 2 CC 2 I=NP1, N
 JK(I)=N
 NP=N-M
 3 CC 3 I=1, NP
 JK(I)=I+NP-1
 M1=M+1
 4 CC 4 J=M1, N
 IK(J)=J-M1+1
 JKJ=JK(1)

CHOLESKY DECOMPOSITION

10 CC 10 J=2, JKJ
 M1J=M-1+J
 C(1, M1J)=C(1, M1J)/O(1, M)
 11 CC 11 I=2, N
 IKI=IK(I)
 JKJ=JK(I)
 MKI=M-K+1
 12 CC 12 J=IKI, I
 S=0.
 C1=C(I, J)
 13 CC 13 K=IKI, J1
 MKK=M-I+K
 MKJ=M-K+J
 S=S+O(I, MKI)*O(K, MKJ)
 M1J=M-I+J
 14 CC 14 C(I, M1J)=C(I, M1J)-S
 IF(I, EQ, N) GO TO 17
 M1=M1+1
 15 CC 15 J=I1, JKI
 MKJ=IK(J)
 IF(I, EQ, IKJ) GO TO 16
 S=J.
 M11=M1-1
 16 CC 16 K=I+J, I11
 MKK=M-I+K
 MKJ=M-K+J
 S=S+O(I, MKI)*O(K, MKJ)
 M1J=M-I+J
 17 CC 17 C(I, M1J)=(O(I, M1J)-S)/O(I, M)
 GO TO 17
 18 CONTINUE
 M1J=M-I+J
 19 CC 19 C(I, M1J)=C(I, M1J)/O(I, M)
 20 CONTINUE
 21 CONTINUE

C BACKWARD SUBSTITUTION

```

U(1)=U(1)/C(1,M)
DO 20 K=2,N
S=0.0
IKI=IK(I)
I1=I-1
DO 21 K=IKI,I1
MIK=M-I+K
21 S=S+C(I,MIK)*U(K)
20 U(I)=(U(I)-S)/C(I,M)
T(N)=U(N)

```

C FORWARD SUBSTITUTION

```

DO 30 K=2,N
I=N-K+1
JKI=JK(I)
S=0.0
I1=I+1
DO 31 L=I1,JKI
MIK=M-I+L
31 S=S+C(I,MIK)*T(L)
30 U(I)=U(I)-S
IIP=4

```

C CALCULATION OF NODAL FORCES

```

DO 50 I=1,IIP
IIPP=IP(I)
S=0.0
JJK=JK(IIPP)
IKI=IK(IIPP)
DO 51 J=IKI,JJK
MIJ=M-IIPP+J
51 S=S+C(I,MIJ)*T(J)
50 U(IIPP)=S
RETURN
END
      6400 END OF RECORD

```

REFERENCES

1. Bauschinger, J., *Civiling N.F.*, 27, 289, (1881). *Min. Proc. Inst. Civ. Eng.*, London, 87, 463, (1886).
2. Kishi, T. and Tanabe, T., *J. Mech. Phys. Solids.*, 21, 303, (1973).
3. Kishi, T. and Gokyu, I., *Met. Trans.*, 4 (1), 390, (1973).
4. Taira, T., Osuka, T. and Ishida, Y., *Manusc. 15th Mech. Working and Steel Processing Conf.*, Pittsburg. Pa., Jan. 1973.
5. Gupta, P.S. and Kodali, S.P., *Trans. JIM*, 17, 264, (1976).
6. Gupta, P.S. and Kodali, S.P., *Scripta Met*, 10, 111, (1976).
7. Milligan, R.V., Koo, W.H. and Davidson, T.E., *J. Basic. Eng.*, 480, June, (1966).
8. Jamieson, R.M. and Hood, J.E., *JISI*, 46, Jan. (1971).
9. Ibrahim, N. and Embury, J.D., *Matl. Sci. Eng.* 19, 147, (1975).
10. Ibrahim, N., Ph.D. Thesis, McMaster Univ., Hamilton, Canada, (1974).
11. Filipovic, A., M. Eng. Thesis, McMaster Univ., Hamilton, Canada, (1976).
12. Woolley, R.L., *Phil. Mag.*, 44, Ser. 7 (353), 597 (1953).
13. Buckley, S.N. and Entwistle, K.M., *Acta Met.*, 4, 352, (1956).
14. Kumakura, S., *Bull. JSME*, 11 (45), 426, (1968).
15. Abel, A., M. Sc. Thesis, McMaster Univ., Hamilton, Canada, (1965).
16. Abel, A. and Ham, R.K., *Acta Met.*, 14, 1489, (1966).
17. Stoltz, R.E. and Pelloux, R.M., *Scripta Met.*, 8, 269, (1974).
18. Hasagawa, T. and Yakou, T., *Scripta Met.*, 8, 951, (1974).
19. Abel, A. and Muir, H., *Metals Australia*, 4 (8), 267, (1972).
20. Abel, A. and Muir, H., *Phil. Mag.*, 26, 489, (1972).
21. Abel, A. and Muir, H., *Phil. Mag.*, 27, 585, (1973).

22. Mban, G.D., Ph.D. Thesis, McMaster Univ., Hamilton, Canada, (1977).
23. Masing, G., Wiss. Veroff. Siemens-Konzern, 3, 231, (1923),
Ibid., 5, 135, (1926).
24. Sachs, G. and Shoji, H., Z. Phys., 45, 776, (1927).
25. Polakowski, N.H., Research, 5(3), 143, (1952).
26. Honeycombe, R.W.K., Plastic Deformation of Metals, Edward
Arnold Ltd., (1968).
27. Daniel, R.C. and Horne, G.T., Met. Trans., 2, 1161, (1971).
28. Stoltz, R.L. and Pelloux, R.M., Met. Trans., 7A, 1295, (1976).
29. Orowan, E., in Symp. on Internal Stresses in Metals and Alloys,
Inst. of Metals, p. 451, (1948).
30. Orowan, E., in Internal Stresses and Fatigue of Metals, Ed.:
G.M. Rassweiler and W.L. Gnebe, p. 59, Elsevier, N.Y., (1959).
31. Ashby, M.F., in Strengthening Methods in Crystals, Ed.: A. Kelly
and R.B. Nicholson, Wiley, N.Y., p. 113, (1971).
32. Smallman, R.E., Modern Physical Metallurgy, 2nd. Ed., Butter-
worths, (1963).
33. Hirsch, P.B. and Humphreys, F.J., in Strengthening Methods in
Crystals, Ed.: A. Kelly and R.B. Nicholson, Wiley, N.Y., p. 189,
(1971).
34. Brown, L.M., Scripta Met., 11, 127, (1977).
35. Masing, G. and Maksud, W., Wiss. Veroff. Siemens-Konzern, 5,
142, (1926).
36. Rahlfs, P. and Masing, G., Z. Met., 41, 454, (1950).
37. Edwards, E.H. and Washburn, T., J. Metals, 200, 1239, (1954).
38. Harrison, T.C., Weiner, R.T. and Fearnough, G.D., JISI, 334,
May, (1972).
39. Chow, P. and Embury, J.D., Private Communication, Fac. of Eng.,
McMaster Univ., Hamilton, Canada, (1977).
40. Kishi, T., Tanaka, H., Horiuchi, R., Obata, Y. and Aoki, K.,
Scripta Met., 9, 1023, (1975).

41. Sankar, N.G., Frederick, J.R. and Felbeck, D.K., *Met. Trans.*, 1, 2979, (1970).
42. Seigel, E., *Acta Met.*, 25, 383, (1977).
43. Rolfe, S.T., Haak, R.P. and Gross, J.H., *J. Basic Eng.*, 403, Sept.(1968).
44. Pascoe, K.J., *J. Strain Anal.*, 6(3), 167, (1971).
45. Morrison, J.L. and Shepherd, W.M., *Proc. Inst. Mech. Engrs.*, London, 163, 1, (1950).
46. Li, C.C., Flasck, J.D., Yaker, J.A. and Leslie, W.C., "On Minimizing the BE in Steels by Dynamic Strain Ageing", *Private Com.*, (1977).
47. Pepe, J.J., *Metals Eng. Quart.*, 43, Nov.(1974).
48. Eleiche, A.M. and Campbell, J.D., *Expt. Mech.*, 281, Aug.(1976).
49. Hasegawa, T., Yakou, T. and Karashima, S., *Mats. Sci. Eng.* 20, 267, (1975).
50. Hasegawa, T., Yakou, T., Shimizu, M. and Karashima, S., *Trans. JIM*, 17, 416, (1976).
51. Wilson, D.V., *Acta Met.*, 13, 807, (1965).
52. Atkinson, J.D., Brown, L.M. and Stobbs, W.M., *Phil. Mag.*, 30, 1247, (1974).
53. Wilson, D.V. and Komman, Y.A., *Acta Met.*, 12, 617, (1964).
54. Anand, L. and Gurland, J., *Met. Trans.*, 7A, 191, (1976).
55. Kachanov, L.M., *Foundations of the Theory of Plasticity*, North-Holland Publ. Co., London, 80, (1971).
56. Prager, W., *Proc. Instn. Mech. Engrs.*, 169, 41, (1955).
57. Shield R.T. and Ziegler, H., *ZAMP*, 9(a), 260, (1958).
58. Ziegler, H., *Quart. Appl. Maths.*, 17, 55³, (1959).
59. Eisenberg, M. and Phillips, A., *Acta Mechanica*, 5, 281, (1948).
60. Mroz, Z., *J. Mech. Phys. Solids*, 15, 163, (1967).
61. Edelman, F. and Drucker, D.C., *J. Franklin, Inst.*, 251; 581, (1951).

63. Shrivastava, H.P., Mroz, Z. and Dubey, R.N., *ZAMM*, 53, 625, (1973).
64. Hill, R., "Math. Theory of Plasticity", OUP, (1950).
65. Yoshimura, Y., Aero, Res. Inst., Univ. of Tokyo, Report No. 349, (1959).
66. Svensson, N.L., *J. Mech. Engg. Sci.*, 8, (2), 162, (1966).
67. Svensson, N.L., *J. Inst. Metals*, 94, 284, (1966).
68. Balfov, A. and Sawczuk, A., *Acta Mechanica*, 1(2), 81, (1965).
69. Shrivastava, H.P., Ph.D. Thesis, Univ. of Waterloo, Canada, (1973).
70. Swift, H.W., *Engineering*, 165, 253, (1947).
71. Freudenthal, A.M. and Gou, P.F., *Acta Mechanica*, 8, 34, (1969).
72. Shrivastava, H.P., Mroz, Z. and Dubey, R.N., *Acta Mechanica*, 17, 137, (1973).
73. Mroz, Z., Shrivastava, H.P. and Dubey, R.N., *Acta Mechanica*, 25, 51, (1976).
74. Ivey, H.J., *J. Mech. Engg. Sci.*, 3(1), 15, (1961).
75. Phillips, A. and Wang, A.J., *Trans. ASME, J. Appl. Mech.*, 97E, 378, (1975).
76. Shiratori, E., Ikegami, K. and Hidehara, O., *Bul. JSME*, 11 (45), 413, (1968).
77. Shiratori, E., Ikegami, K. and Kaneko, K., *Bul. JSME*, 16 (100), 1483, (1973).
78. Shiratori, E., Ikegami, K., Yoshida, F., Kaneko, K., and Shigeyuki, K., *Bul. JSME*, 19(134), 877, (1976).
79. Shiratori, E., Ikegami, K., and Yoshida, F., *Bul. JSME*, 19 (136), 1122, (1976).
80. Williams, J.F. and Svensson, N.L., *J. Strain Analysis*, 5(2), 128, (1970).
81. Michno Jr., M.J. and Findley, W.N., *J. Engg. Matls. Tech., Trans. ASME*, p. 25, Jan. 1975.
82. Friedel, J., in "Internal Stresses and Fatigue of Metals", p. 220, Elsevier, N.Y., (1959).

82. Asaro, R.J., *Acta Met.*, 23, 1255, (1975).
83. Sowerby, R., Tomita, Y. and Uko, D.K., MWRG Report No. 89, Faculty of Engg., McMaster Univ., Hamilton, Canada (1976).
84. Sowerby, R. and Tomita, Y., *Int. J. Mech. Sci.*, 19, 351, (1977).
85. Brown, L.M. and Stobbs, W.M., *Phil. Mag.*, 23, 1185, (1971).
86. Brown, L.M. and Stobbs, W.M., *Phil. Mag.*, 23, 1201, (1971).
87. Humphreys, F.J. and Hirsch, P.B., *Proc. Roy. Soc., London, Series A*, 318, 72, (1970).
88. Stewart, A.T. and Martin, J.W., *Acta Met.*, 23, 1, (1975).
89. Eshelby, J.D., *Proc. Roy. Soc., London*, 241(A), 376, (1957).
90. Lloyd, D.J., *Acta Met.*, 25, 459, (1977).
91. Gould, D., Hirsch, P.B. and Humphreys, F.J., *Phil. Mag.*, 26, 1353, (1974).
92. Brown, L.M. and Stobbs, W.M., *Phil. Mag.*, 34(3), 351, (1976).
93. Brandon, D.G., *Modern Techniques in Metallography*, Publ. Van Nostrand, N.J., (1966).
94. Rashid, M.S., SAE Preprint 760206, Feb. (1976).
95. Rashid, M.S., SAE Preprint 770211, Feb. (1977).
96. Mooz, A., B. Eng. Project Report, Dept. of Met. & Matl. Sci., McMaster Univ., Hamilton, Canada, (1977).
97. Considere, A., *Ann des Pans et. Chaussees*, 9, 574, (1885).
98. Marciniak, Z., "Aspects of Material Formability", MWRG Report, McMaster Univ., Hamilton, Canada, Feb. (1974).
99. Hart, E.W., *Acta Met.*, 15, 351, (1967).
100. Lancaster, P.R. and Mitchell, D., *The Mechanics of Materials*, p. 219, McGraw-Hill, (1967).
101. *Metals Handbook*, Vol. 1 on Properties and Selection of Metals, 8th Edition, (1973).
102. Brown, L.M. and Clarke, D.R., *Acta Met.*, 23, 821, (1975).
103. Duncan, J.L., *Proc., Australian Conf. Manufacturing Engg.*, 11, (1977).

104. Lucas, E., (Private Communication), IAT, Porto Alegre, Rio Grande do Sul, Brazil, (1976).
105. LeRoy, G., (Private Communication), Dept. of Met. & Matl. Sci., McMaster Univ., Hamilton, Canada, (1977).
106. Sylvestrowicz, W. and Hall, E.O., Proc. Phys. Soc. B, 64, 495, (1951).
107. Butler, J.F., J. Mech. Phys. Solids, 10, 313, (1962).
108. Hahn, G.T. Acta Met., 10, 727, (1962).
109. Takada, I. and Sugie, E., Trans. ISIJ, 16, 531, (1976).
110. Nakajima, H., Mizutani, W., Kikuma, T. and Mutumoto, H., Trans., ISIJ, 15, 1, (1975).
111. Civallo, M.A., Parrini, C. and Pizzimenti, N., Proc. Micro Alloying '75 Conf., Wash. D.C., Session 2B, p. 81, (1975).
112. Alexander, J.M., Proc. Instn. Mech. Engrs., London, 173, No. 1, 73, (1959).
113. Kitagawa, H. and Tomita, Y., Proc. 21st Japan Congress of Appl. Mech., p. 243, (1971).
114. Oden, J.T., "Finite Elements of Non Linear Continuum", McGraw Hill, p. 325, (1972).
115. ASTM-A570, Annual Book of ASTM Standards, Part 4, 310, (1977).
116. Cotton, H.C. and Thomas, D.B.J., ISI, P.135, Conf. on Tube and Pipe Production, p. 12, Nov. (1970).
117. Shoemaker, A.K. and Ives, K.D., Written Discussion on Ref. [4], 15th Mech. Working and Steel Processing Conf., Pittsburg, Pa., p. 50, (1973).
118. Gładowski, R.J. and Thompson, J.M., Written Discussion on Ref. [4], 15th Mech. Working and Steel Processing Conf., Pittsburg, Pa., p. 59, (1973).
119. Gertman, S.L., "Future Canadian Pipelines", Int. Rep. PM-M-74-4, Dept. of Energy, Mines and Resources, Mines Branch, Ottawa, Canada, (1974).
120. Gondoh, H., Nakasuzi, H. and Masui, H., "Recent Progress in accicular ferrite steels for Arctic grade linepipe", Paper No. 95, 16th Annual Conf. of Metallurgists, Vancouver, Canada, Aug. (1977).

121. Irvinè, K. J., Gladman, T., Orr, J. and Pickering, F.B., JISI, 717, (1970).
122. Luyckx, L., Bell, J.R., McLean, A. and Korchinsky, M., Met. Trans. 1, 3341, (1970).
123. Gray, J.M., Metallurgy of HSLA pipeline steels, Molybdenum Corp. of America, Report No. 7201, (1972).
124. Tither, G., Coldren, A.P. and Mihelich, J.L., "Influence of processing on properties of molybdenum steels for pipelines", Climax Molybdenum Company of Michigan, Ann Arbor, Michigan, (1975).
125. "Proceedings Microalloying 75", ASM; Metals Park, Ohio, 44073, (1975).
126. Glover, G., Int. Conf. on Production Tech., Institution of Engrs. Australia, Publ. No. 74/3, 137, (1974).
127. Heitman, W.E., Oakwood, T.G. Gray, J.M. and Wilson, W.G., "An economical alternative to controlled rolled plate for pipe applications", Inland Steel Co., East Chicago, Indiana, (1975).
128. Hero, H., Uko, D.K., Filipovic, A., Sowerby, R., Duncan, J.L. and Embury, J.D., Scand. J. Met., 6 282-292, (1977).
129. Kitagawa, H. and Tomita, Y., Proc. 21st Japan Nat. Cong. Appl. Mechs, 21, 243, (1971).
130. Kitagawa, H., Seguchi, Y. and Tomita, Y., Ing.-Arch., 41, 213, (1972).
131. Desai, C.S. and Abel, J.F., Intr. to the Finite Element Method, Van Nostrand Reinhold Co., (1972).
132. Green, A.E. and Zerna, W., Theoretical Elasticity, O.U.P. 2nd Edition, (1968).
133. Flügge, W., Tensor Analysis and Continuum Mechanics, Springer-Verlag, N.Y., (1972).
134. Marschall, C.W. and Maringer, R.E., "Dimensional Instability", Pergamon Press, Oxford, 1st. Ed., (1977).